



**Swansea University**  
**Prifysgol Abertawe**

**Numerical and experimental studies of aeroelastic  
hinged wingtips**

by

Daide Balatti

Doctor of Philosophy

at

Swansea University

August 2022



# Abstract

Aeroelasticity is the science that investigates the mutual interaction between aerodynamic, elastic, and inertia forces and how this affects the static and dynamic structural response. Aeroelastic models can be defined considering different levels of fidelity depending on the models' aim. Gust loads are among the most critical cases an aircraft can encounter, and so mitigating the loads enables the design of a lighter structure, consequently reducing production and fuel consumption costs. Hinged wingtips have shown potential to improve the wing aerodynamic performance while alleviating structural loads. The aim of this work is the numerical and experimental study of aeroelastic wings with hinged wingtips subjected to gusts. Measurements from wind tunnel tests are used to validate the numerical model. Two numerical models, representative of the same aircraft with hinged wingtips subjected to gusts, were considered, a detailed and a simplified one. The latter model, due to its low number of degrees of freedom, was used for wingtip design optimisation. Gust and turbulence events cannot be measured directly, but they can be identified from in-flight measurements. Cubic B-spline functions were used for gust identification considering simulated flight data from the simplified and detailed models. Results have shown the ability of the simplified model to identify the gust and turbulence considering simulated data from the detailed model. To validate the numerical models, a gust generator was designed, installed and commissioned for the Swansea University wind tunnel. Experimental results have shown the difficulty of creating a perfect '1-cos' gust at the desired location. Two techniques to improve the '1-cos' gust were considered. In the first case, the transfer function between the vane rotation and the gust produced at the aircraft model location was identified, and its inverse was used to calculate the vane rotation. The improvements using this approach are limited by the strong nonlinearity of the aerodynamics. A parametric study of the vane rotation has shown that a more complicated vane rotation function allows '1-cos' gusts at the aircraft model location to be obtained with a mean square error two orders of magnitude smaller than the initial case. An elastic wing able to accommodate different wingtips was manufactured. Three wingtips, namely a fixed wingtip, a hinged wingtip, and a hinged wingtip with a torsional spring at the hinge were considered. Static and dynamic wind tunnel tests have shown the potential of hinged wingtips in reducing wing gust loads. Measured gust loads were used to validate the aeroelastic models.



**Declarations**

This work has not previously been accepted in substance for any degree and is not being concurrently submitted in candidature for any degree.

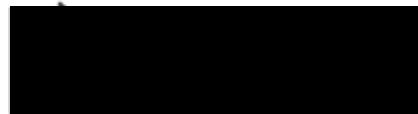
Signed



Date 03/08/2022

This thesis is the result of my own investigations, except where otherwise stated. Other sources are acknowledged by footnotes giving explicit references. A bibliography is appended.


Signed



Date 03/08/2022

I hereby give consent for my thesis, if accepted, to be available for photocopying and for inter-library loan, and for the title and summary to be made available to outside organisations.

Signed



Date 03/08/2022

The University's ethical procedures have been followed and, where appropriate, that ethical approval has been granted.

Signed



Date 03/08/2022



# Acknowledgements

I would like to express my sincere gratitude to my supervisors Prof. Mike Friswell, Prof. Hamed Haddad Khodaparast and Dr Marinos Manolesos, who have always supported, motivated and provided excellent supervision throughout this work. Their hard work, dedication and passion have been a source of my inspiration. I would also like to thank Dr Andrea Castrichini for his useful support during these years. Without their help, I would not be able to have done this work.

I am grateful to the DigiTwin consortium for supporting my research and the opportunity to collaborate with other consortium members. I would like to extend my gratitude to the Faculty of Science and Engineering at Swansea University for the financial support. Thank you to Alexandra Elbakyan for promoting accessibility in science.

I take this opportunity to thank all my friends and colleagues at Swansea University for their support and memorable journey together. Thanks to my friends in Italy who supported me from a distance.

A special thanks go to my parents and my siblings, who supported me during these years despite the distance. I realised the benefit of a simple call during a difficult moment.

Finally, my biggest thanks to my wife Kayal, whose love is a constant support in my life.





# CONTENTS

<b>Title</b>	<b>Page No.</b>
List of Figures	xiii
List of Tables	xxiv
Abbreviations	xxvii
Nomenclature	xxix
<b>1 Introduction</b>	<b>1</b>
1.1 Motivation . . . . .	1
1.2 State of the Art . . . . .	3
1.2.1 Active Load Alleviation . . . . .	4
1.2.2 Passive Load Alleviation . . . . .	5
1.2.3 Hinged Wingtip . . . . .	6
1.2.4 In Flight Gust Identification . . . . .	13
1.2.5 Wind Tunnel Testing of Gust Load Alleviation . . . . .	17
1.3 Thesis Outline . . . . .	21
1.4 Aims and Research Outcome . . . . .	22
1.4.1 Research Outcome . . . . .	23
<b>2 Aeroelastic Modelling of an aircraft</b>	<b>26</b>
2.1 Introduction to Aeroelasticity . . . . .	26
2.1.1 General Form of the Aeroelastic Equations . . . . .	28
2.1.2 Gust Model . . . . .	31
2.2 Simplified Aeroelastic Models . . . . .	33

---

2.2.1	Structural and Aerodynamic model of an Aircraft With a Straight Wing (Model One) . . . . .	35
2.2.2	Structural and Aerodynamic Model of an Aircraft With a Straight Wing and Folding Wingtip (Model Two) . . . . .	37
2.3	Validation . . . . .	39
2.3.1	Comparison of Different Models . . . . .	40
2.3.2	Model Two Gust Response . . . . .	41
2.4	Detailed Aeroelastic Model . . . . .	44
2.5	Conclusions . . . . .	46
<b>3</b>	<b>Multi-Objective Optimisation for the Worst-Case Gust Prediction</b>	<b>49</b>
3.1	Civil Commercial Aircraft Case . . . . .	50
3.1.1	Quantities of Interest . . . . .	51
3.1.2	Static Trim Solution . . . . .	51
3.2	Multi-Objective Optimization . . . . .	52
3.2.1	Optimization: Set-Up . . . . .	53
3.2.2	A. Optimal Parameters: Wingtip CM Position, Flare Angle and Wingtip Span . . . . .	56
3.2.3	B. Optimal Parameters: Wingtip CM Position and Flare Angle . . . . .	59
3.2.4	C. Optimal Parameters: CM Positions with Flare Angle Fixed at 30° . . . . .	62
3.2.5	D. Optimal Parameters: CM Positions with Flare Angle Fixed at 20° . . . . .	64
3.2.6	Flutter Speed . . . . .	66
3.3	Conclusions . . . . .	70
<b>4</b>	<b>Gust Identification</b>	<b>71</b>
4.1	Identification Theory . . . . .	71
4.1.1	Regularisation Methods . . . . .	75
4.1.2	Identification Using Cubic B-Spline Collocation Method . . . . .	76
4.2	Aeroelastic Models . . . . .	80
4.3	Identification Results for the Simplified Model . . . . .	82

---

4.3.1	Gust Identification Considering Measurement Noise . . . . .	83
4.3.2	Effect of the Location of the Collocation Points . . . . .	88
4.3.3	Gust and Turbulence Event Identification . . . . .	89
4.4	Identification Using Measurements from the FFAST Model . . . . .	91
4.4.1	Identification Model: Modal Reduction . . . . .	92
4.4.2	Identification Model: Realistic Example, Simulating Measured Data Using the Detailed Model and Using the Simplified Model for Iden- tification . . . . .	94
4.5	Conclusion . . . . .	96
<b>5</b>	<b>Generation of Gusts in the Wind Tunnel</b>	<b>98</b>
5.1	Gust Generator Design, Installation and Commissioning . . . . .	99
5.1.1	Vane Design . . . . .	100
5.1.2	Actuation . . . . .	102
5.1.3	Vane Structural Characterisation . . . . .	105
5.1.4	Smoke Test . . . . .	106
5.2	Experimental Setup . . . . .	107
5.2.1	Hot-Wire Sensor . . . . .	109
5.2.2	Test Cases . . . . .	112
5.2.3	Post-Processing . . . . .	113
5.3	Initial Results . . . . .	114
5.3.1	Discrete Gust . . . . .	114
5.3.2	Continuous Gusts . . . . .	115
5.3.3	Flow Uniformity . . . . .	116
5.4	Improvement of the ‘1-cos’ Gust Profile . . . . .	120
5.4.1	Identification of the Transfer Function . . . . .	122
5.4.2	Results of the Parametric Study . . . . .	132
5.5	Conclusions . . . . .	138
<b>6</b>	<b>Model Validation</b>	<b>140</b>
6.1	Wing and Wingtips Design . . . . .	140
6.2	Experimental Setup . . . . .	144

---

6.2.1	Accelerometer . . . . .	144
6.2.2	Displacement Sensor . . . . .	145
6.2.3	Balance . . . . .	150
6.3	Spar and Wing Structural Characterisation . . . . .	152
6.3.1	Impact Hammer Test 3D-Printed Section . . . . .	153
6.3.2	Impact Hammer Test Wing Spar . . . . .	153
6.3.3	Impact Hammer Test of Wing with Different Wingtips . . . . .	155
6.4	Wind Tunnel Tests . . . . .	159
6.4.1	Static Test . . . . .	160
6.4.2	Dynamic Test . . . . .	164
6.5	Numerical Model . . . . .	176
6.5.1	Comparison Between Numerical and Experimental Gust Responses	180
6.6	Conclusion . . . . .	183
<b>7</b>	<b>Conclusions and Future Work</b>	<b>184</b>
7.1	Conclusions . . . . .	184
7.2	Original Contributions . . . . .	186
7.3	Recommendations for Future Work . . . . .	186
<b>A</b>	<b>Development equation of motion for the simplified model</b>	<b>188</b>
A.1	Aeroelastic equation rigid aircraft with elastic wing . . . . .	188
A.2	Aeroelastic equation rigid aircraft with elastic wing and hinged wingtip .	191
A.3	Modification of the orthogonality condition for an engine on the elastic wing	194
A.4	Quantities of interest . . . . .	195
	<b>Bibliography</b>	<b>196</b>

# LIST OF FIGURES

<b>Title</b>	<b>Page No.</b>
1.1 CO <sub>2</sub> emission forecast (directly adapted from [1]) . . . . .	2
1.2 <i>Effects that the location of the primary stiffness direction has on the characteristics of the wing (directly adapted from [2]). . . . .</i>	6
1.3 <i>B777X in different configurations (directly adapted from [3]) . . . . .</i>	7
1.4 <i>A schematic view of an aircraft having folding winglets (directly adapted from [4]). . . . .</i>	8
1.5 <i>A schematic view of the wingtip ‘wash-in’ and ‘wash-out ’ concept due to hinge wingtip (directly adapted from [5]). . . . .</i>	8
1.6 <i>Folding wingin the Bristol wind tunnel (directly adapted from [6]) . . . . .</i>	9
1.7 <i>Wing in the wind tunnel in a free-hinge configuration (directly adapted from [7]). . . . .</i>	10
1.8 <i>AlbatrossOne during flight tests, wingtips free to rotate . . . . .</i>	12
1.9 <i>Tethered flight test of the AlbatrossOne model (directly adapted from [8]).</i>	14
1.10 <i>Discrete-gust approach to design (directly adapted from [9]). . . . .</i>	15
1.11 <i>Spectral-technique: input-output relations for gust response (directly adapted from [9]). . . . .</i>	15
1.12 <i>Force prediction methods (directly adapted from [10]) . . . . .</i>	16
1.13 <i>Schematic of the active grid developed by Makita et al. (directly adapted from [11]). . . . .</i>	18
1.14 <i>View of the modulation valve system (directly adapted from [12]). . . . .</i>	19

1.15	<i>View from upstream of the gust generator apparatus mounted in the wind tunnel (directly adapted from [13]). . . . .</i>	19
1.16	<i>Example of conventional gust generators (a, directly adapted from [14]; b, directly adapted from [15]; c, directly adapted from [16]) . . . . .</i>	20
1.17	<i>Example of unconventional gust generators (a, directly adapted from [17]; b, directly adapted from [18]; c, directly adapted from [19]) . . . . .</i>	21
2.1	<i>Collar's aeroelastic triangle (directly adapted from [20]) . . . . .</i>	27
2.2	<i>Aeroservoelastic pyramid (directly adapted from [20]) . . . . .</i>	28
2.3	<i>Aerodynamic 'strip' on a continuous rectangular wing (directly adapted from [20]) . . . . .</i>	29
2.4	<i>Typical doublet and horseshoe vortex set-up for the DLM (directly adapted from [20]) . . . . .</i>	31
2.5	<i>Gusts with different gust wavelengths . . . . .</i>	32
2.6	<i>Bode diagram of the von Karman approximation of atmospheric turbulence</i>	33
2.7	<i>Model one - aircraft with a straight wing . . . . .</i>	34
2.8	<i>Model two - aircraft with a straight wing and folding wingtip . . . . .</i>	34
2.9	<i>Comparison between model one (continuous line) and the reference model[20] (dashed lines) . . . . .</i>	41
2.10	<i>Comparison between model two with rigid connections (high stiffness) (continuous line) and the reference model [20] (dashed lines) . . . . .</i>	41
2.11	<i>Rigid body responses to a 20 m 1-cos gust . . . . .</i>	42
2.12	<i>Elastic mode responses to a 20 m 1-cos gust . . . . .</i>	42
2.13	<i>Rigid body responses to a 200 m 1-cos gust . . . . .</i>	43
2.14	<i>Elastic mode responses to a 200 m 1-cos gust . . . . .</i>	43
2.15	<i>Gust response for different gust lengths and values of stiffness connection</i>	44
2.16	<i>Gust response for different gust lengths and flare angle (<math>k_\theta = 0</math> Nm/rad)</i>	44
2.17	<i>Gust response for different gust lengths and positions of the wigtip centre of mass (<math>k_\theta = 0</math> Nm/rad) . . . . .</i>	45
2.18	<i>Modified FFAST aeroelastic model . . . . .</i>	46

---

2.19	<i>Lower frequency aeroelastic modes of the FFAST model at 200 m/s and sea level</i>	47
3.1	<i>Trim angles for different values of wingtip stiffness connection: fuselage incidence (<math>\alpha</math>), elevator angle (<math>\eta</math>) and wingtip deflection (<math>\theta</math>)</i>	51
3.2	<i>Quantities of interest in trim for different values of wingtip stiffness connection</i>	52
3.3	<i>Flight configurations considered, worst-cases wingtip rigidly connected to the wing and free to rotate</i>	54
3.4	<i>Shear force and bending moment plotted against each other and the obtained convex hull</i>	54
3.5	<i>Comparison of the shear force-bending moment convex hull obtained with the wingtip rigidly connected to the wing and the wingtip free to rotate</i>	55
3.6	<i>Comparison of the shear force-torsional moment convex hull obtained with the wingtip rigidly connected to the wing and the wingtip free to rotate</i>	55
3.7	<i>Comparison of the bending moment-torsional moment convex hull obtained with the wingtip rigidly connected to the wing and the wingtip free to rotate</i>	56
3.8	<i>Multi-objective optimization results, optimization parameters: wingtip CM position, flare angle and wingtip span</i>	57
3.9	<i>Pareto front on the bending moment and torsional moment plane at the optimal compromise</i>	58
3.10	<i>Shear force-bending moment convex hull for the rigid connection and for optimized configurations</i>	58
3.11	<i>Shear force-torsional moment convex hull for the rigid connection and for optimized configurations</i>	59
3.12	<i>Multi-objective optimization, optimization parameters: wingtip CM position and flare angle</i>	60
3.13	<i>Pareto front on the bending moment and torsional moment plane at the optimal compromise</i>	61
3.14	<i>Shear force-bending moment convex hull for the rigid connection and for optimized configurations</i>	61

---

3.15	<i>Shear force-torsional moment convex hull for the rigid connection and for optimized configurations</i>	62
3.16	<i>Multi-objective optimization, optimization parameters: wingtip CM position with a 30° flare angle</i>	63
3.17	<i>Pareto front on the bending moment and torsional moment plane at the optimal compromise, flare angle 30°</i>	64
3.18	<i>Shear force-bending moment convex hull for the rigid connection and for optimized configurations</i>	64
3.19	<i>Shear force-torsional moment convex hull for the rigid connection and for optimized configurations</i>	65
3.20	<i>Multi-objective optimization, optimization parameters: wingtip CM position with a 20° flare angle</i>	66
3.21	<i>Pareto front on the bending moment and torsional moment plane at the optimal compromise, flare angle 20°</i>	67
3.22	<i>Shear force-bending moment convex hull for the rigid connection and for optimized configurations</i>	67
3.23	<i>Shear force-torsional moment convex hull for the rigid connection and for optimized configurations</i>	68
3.24	<i>Flutter speed at different altitudes, in the reference configuration, in the optimized configuration, in the optimized configuration with smaller flare angle (strategy 1) and in the optimized configuration with stabilizing stiffness connection (strategy 2)</i>	68
3.25	<i>Shear force-bending moment convex hull obtained in the reference configuration, in the optimized configuration, in the optimized configuration with smaller flare angle (strategy 1) and in the optimized configuration with stabilizing stiffness connection (strategy 2)</i>	69
3.26	<i>Shear force-torsional moment convex hull obtained in the reference configuration, in the optimized configuration, in the optimized configuration with smaller flare angle (strategy 1) and in the optimized configuration with stabilizing stiffness connection (strategy 2)</i>	69
4.1	<i>The definition of direct and inverse problems</i>	72
4.2	<i>A cubic B-spline curve constructed by four cubic polynomials</i>	77



---

4.3	<i>Cubic B-spline functions in the interval <math>[0, 1]</math> for the collocation interval <math>h = 1/6</math></i>	78
4.4	<i>Cubic B-spline curves with different values of collocations interval <math>h</math></i>	78
4.5	<i>Gust represented as a summation of cubic B-Splines and the cubic B-Splines involved</i>	79
4.6	<i>Aircraft centre of mass pitch angle gust responses</i>	81
4.7	<i>Wingtip angle gust responses</i>	82
4.8	<i>Gust reconstruction by model inversion considering clean and noisy measurements of the bending mode</i>	83
4.9	<i>GCV of noisy measurement of the bending mode with Tikhonov regularisation</i>	84
4.10	<i>GCV of noisy measurement of the bending mode with TSVD regularisation</i>	84
4.11	<i>GCV of noisy measurement of the bending mode with DSVD regularisation</i>	85
4.12	<i>Gust reconstruction by model inversion considering measurements of the bending mode with 10% measurement noise and three regularisation methods</i>	85
4.13	<i>Gust reconstruction by model inversion considering measurements of the bending mode with 30% measurement noise and TIKH and TSVD regularisation</i>	86
4.14	<i>Residual considering clean measurement and measurement with 10%, 20% and 30% of noise</i>	86
4.15	<i>Gust reconstruction by cubic B-spline function, considering clean measurement and measurement with 10% and 30% noise</i>	87
4.16	<i>Gust response considering the real gust and the identified gusts from noisy measurements</i>	87
4.17	<i>Residual considering measurement of the bending mode</i>	88
4.18	<i>Gust reconstruction considering 73 cubic B-splines</i>	89
4.19	<i>Gust reconstruction considering 79 cubic B-splines</i>	89
4.20	<i>Gust reconstruction considering 99 cubic B-splines</i>	90

---

4.21	<i>Residual for the identification of gust and turbulence event using the measurement of the bending mode</i>	90
4.22	<i>Gust and turbulence event reconstruction considering 230 collocation points using the measurement of the bending mode</i>	91
4.23	<i>Residual considering 4 modes model, 5 modes model and 55 modes model and measurement of the pitch of the aircraft</i>	92
4.24	<i>Gust and turbulence event reconstruction considering 5 modes model, 8 modes model and 55 modes model, measurement of the pitch of the aircraft and 600 collocation points</i>	93
4.25	<i>Error in the gust and turbulence event reconstruction</i>	93
4.26	<i>Pitch angle gust and turbulence event response considering 5, 6, 7, 8 and 55 modes models</i>	94
4.27	<i>Residual considering the <i>simplified</i> model and measurement of the pitch of the aircraft</i>	95
4.28	<i>Gust and turbulence event reconstruction considering the <i>simplified</i> model, the measurement of the pitch of the aircraft and 450 and 600 collocation points</i>	96
4.29	<i>Error in the gust and turbulence event reconstruction</i>	96
5.1	<i>Discrete gust with different gust wavelengths</i>	99
5.2	<i>Swansea University wind tunnel</i>	100
5.3	<i>3D printed section</i>	101
5.4	<i>Vanes during manufacturing and before to be installed</i>	102
5.5	<i>Vane support before installation and installed in the wind tunnel</i>	103
5.6	<i>Motors, gearboxes, and couplings</i>	105
5.7	<i>Drives</i>	106
5.8	<i>Gust generator installed in the wind tunnel</i>	106
5.9	<i>Gust generator installation</i>	107
5.10	<i>Gust generator smoke test</i>	108
5.11	<i>Hot wire anemometer equipment used</i>	110

---

5.12	<i>Hot wire calibration</i> . . . . .	111
5.13	<i>Gust generator in the wind tunnel</i> . . . . .	111
5.14	<i>Bode plot of the filters used</i> . . . . .	113
5.15	<i>Measured gust and filtered gust</i> . . . . .	114
5.16	<i>Discrete gust, evaluation repeatability</i> . . . . .	114
5.17	<i>Discrete gust vane rotations amplitude of 5°, 10°, 15° and 20°, 1 to 7 Hz rotation frequency. Each case was repeated three time and all data are plotted</i> . . . . .	116
5.18	<i>Discrete gust vane rotations amplitude of 5°, 10°, 15° and 20°, 8 to 14 Hz rotation frequency. Each case was repeated three time and all data are plotted</i> . . . . .	117
5.19	<i>Maximum gust peaks as a function of frequency and maximum vane angle of rotation for gusts at 18 m/s</i> . . . . .	117
5.20	<i>Continuous gust for vane rotations amplitude of 5° and 12.5°, at 1 to 5 Hz</i>	118
5.21	<i>Continuous gust for vane rotations amplitude of 5° and 12.5°, at 6 to 10 Hz</i>	118
5.22	<i>Gust uniformity at different horizontal locations (a) and discrete gusts at each location (b)</i> . . . . .	119
5.23	<i>Gust uniformity at different vertical locations (a) and discrete gusts at each location (b)</i> . . . . .	120
5.24	<i>Starting and stopping vortices (directly adapted from [21])</i> . . . . .	121
5.25	<i>The creation of the starting vortex and the resulting circulation around the airfoil</i> . . . . .	121
5.26	<i>Motor rotation and gust measured by the cross hot-wire sensor for the identification of the transfer function</i> . . . . .	123
5.27	<i>Identified transfer function by periodic sinusoidal rotations of the vanes</i> .	123
5.28	<i>Experimental and identified shedding times from continuous sinusoidal vane rotation</i> . . . . .	125
5.29	<i>Measured transfer function, mean transfer function and identified transfer function from impulse tests at 18 m/s</i> . . . . .	126
5.30	<i>Time delay between impulse vane rotation and gust at 10 m/s</i> . . . . .	127

5.31	Time delay between impulse vane rotation and gust at 14 m/s . . . . .	127
5.32	Time delay between impulse vane rotation and gust at 18 m/s . . . . .	128
5.33	Comparison of identified transfer functions at 18 m/s . . . . .	129
5.34	Discrete gust vane rotations with desired AoA 1°, 2° and 3°, and frequency 6 to 10 Hz . . . . .	130
5.35	Discrete gust vane rotations with desired AoA 1°, 2° and 3°, and frequency 11 to 15 Hz . . . . .	130
5.36	Comparison motor rotation found from inverse transfer function and ‘1-cos’	131
5.37	Comparison desired gust profile at 9 Hz, gust obtained from ‘1-cos’ vane rotation and gust obtained from motor rotation obtained from the inverse transfer function . . . . .	131
5.38	Proposed method to parameterize the vane rotation . . . . .	133
5.39	Proposed method, effect of $t_{01}$ on the gust produced . . . . .	134
5.40	Proposed method, effect of $\theta_{GG}(t_2)$ on the gust produced . . . . .	134
5.41	Proposed method, effect of $t_3$ on the gust produced . . . . .	135
5.42	Proposed method to parameterize the discrete gust vane rotation for am- plitude of 5°, 10°, 15° and 20°, and frequencies of 4 to 15 Hz . . . . .	135
5.43	Frequency content of discrete gusts obtained at 18 m/s, frequency of 13 Hz, by ‘1-cos’ vane rotation for amplitude of 5°, 10°, 15° and 20° (color lines) and frequency content of the equivalent exact discrete gusts with the same gust wavelength and maximum amplitude (black lines) . . . . .	136
5.44	Frequency content of discrete gusts obtained at 18 m/s, frequency of 13 Hz, by the proposed method for amplitude of 5°, 10°, 15° and 20° (color lines) and frequency content of the equivalent exact discrete gusts with the same gust wavelength and maximum amplitude (black lines) . . . . .	137
5.45	Discrete gust at 8 Hz from ‘1-cos’ vane rotation and vane amplitude 10°, from the vane rotation calculated from the inverse of the transfer function with a desired gust of 2°, from the proposed method with $A_{GG} = 15^\circ$ and corresponding ideal ‘1-cos’ gusts (black dashed lines) . . . . .	137
5.46	Maximum gust peaks as a function of frequency and maximum vane angle of rotation . . . . .	138
5.47	Negative peak factor using the three methods . . . . .	139

---

6.1	<i>Aluminium spar</i>	141
6.2	<i>3D printed section</i>	141
6.3	<i>Wingtips manufactured</i>	142
6.4	<i>Details of the hinged wingtip with torsional spring</i>	143
6.5	<i>Wingtip threaded bar</i>	143
6.6	<i>Laser triangulation principle (directly adapted from [22])</i>	145
6.7	<i>Static test to measure the effect of the plexiglass on static laser measurements</i>	147
6.8	<i>Static effect of the plexiglass</i>	148
6.9	<i>Error due to the plexiglass before and after corrections</i>	148
6.10	<i>Test setup for the dynamic effect of the plexiglass</i>	149
6.11	<i>Measurement from sensors inside and outside the wind tunnel</i>	150
6.12	<i>Test setup for the identification of the fold angle</i>	151
6.13	<i>Measured vs identified fold angle</i>	152
6.14	<i>Impact hammer test 3D-printed section</i>	153
6.15	<i>3D-printed airfoil section frequency response functions</i>	154
6.16	<i>Spar impact hammer test</i>	154
6.17	<i>Spar frequency response functions</i>	155
6.18	<i>Spar mode shapes</i>	156
6.19	<i>Impact hammer test of the wing with different wingtip</i>	156
6.20	<i>Wing with fixed wingtip frequency response functions</i>	157
6.21	<i>Wing with hinged wingtip and torsional spring frequency response functions</i>	157
6.22	<i>Wing with hinged wingtip frequency response functions</i>	158
6.23	<i>Identification wingtip natural frequency and damping ratio of the wing with hinged wingtip</i>	158
6.24	<i>Wing installed in the wind tunnel</i>	159
6.25	<i>Lift coefficient at different angle of attack and airspeed</i>	160

---

6.26	<i>Lift coefficient at different angle of attack and 18 m/s . . . . .</i>	161
6.27	<i>Rolling moment coefficient at different angle of attack and airspeed . . . . .</i>	162
6.28	<i>Rolling moment coefficient at different lift coefficient and airspeed . . . . .</i>	163
6.29	<i>Wingtip fold angle at different angle of attack and airspeed . . . . .</i>	164
6.30	<i>Typical gust response, each measurement is repeated three times to evaluate repeatability (gust length 9 m) . . . . .</i>	165
6.31	<i>WRBM gust response for the wing with fixed wingtip, hinged wingtip and hinged wingtip with torsional spring and fold angle time history. Small discrete gust amplitude and wing root AoA 2° . . . . .</i>	166
6.32	<i>WRBM gust response for the wing with fixed wingtip, hinged wingtip and hinged wingtip with torsional spring and fold angle time history. Small discrete gust amplitude and wing root AoA 4.4° . . . . .</i>	167
6.33	<i>WRBM gust response for the wing with fixed wingtip, hinged wingtip and hinged wingtip with torsional spring and fold angle time history. Small discrete gust amplitude and wing root AoA 6° . . . . .</i>	168
6.34	<i>WRBM gust response for the wing with fixed wingtip, hinged wingtip and hinged wingtip with torsional spring and fold angle time history. Medium discrete gust amplitude and wing root AoA 2° . . . . .</i>	169
6.35	<i>WRBM gust response for the wing with fixed wingtip, hinged wingtip and hinged wingtip with torsional spring and fold angle time history. Medium discrete gust amplitude and wing root AoA 4.4° . . . . .</i>	170
6.36	<i>WRBM gust response for the wing with fixed wingtip, hinged wingtip and hinged wingtip with torsional spring and fold angle time history. Medium discrete gust amplitude and wing root AoA 6° . . . . .</i>	171
6.37	<i>WRBM gust response for the wing with fixed wingtip, hinged wingtip and hinged wingtip with torsional spring and fold angle time history. Large discrete gust amplitude and wing root AoA 2° . . . . .</i>	172
6.38	<i>WRBM gust response for the wing with fixed wingtip, hinged wingtip and hinged wingtip with torsional spring and fold angle time history. Large discrete gust amplitude and wing root AoA 4.4° . . . . .</i>	173
6.39	<i>WRBM gust response for the wing with fixed wingtip, hinged wingtip and hinged wingtip with torsional spring and fold angle time history. Large discrete gust amplitude and wing root AoA 6° . . . . .</i>	174

---

6.40	<i>WRBM maximum peak for all the cases considered</i>	175
6.41	<i>Convergence of the aerodynamic model of the wing with fixed wingtip</i>	177
6.42	<i>Nastran model</i>	178
6.43	<i>Comparison between numerical and experimental interesting quantities</i>	181
6.44	<i>WRBM maximum peak for all the cases considered</i>	182

# LIST OF TABLES

<b>Title</b>	<b>Page No.</b>
1.1 <i>Summary of existing gust generator installations around the world . . . . .</i>	20
2.1 <i>Aircraft parameters . . . . .</i>	40
2.2 <i>Wingtip parameters . . . . .</i>	40
2.3 <i>Model characteristics . . . . .</i>	45
2.4 <i>Natural frequencies and damping ratios of the FFAST aeroelastic model below 10 Hz at 200 m/s and sea level . . . . .</i>	48
3.1 <i>Civil commercial aircraft parameters . . . . .</i>	50
3.2 <i>Civil commercial aircraft wingtip parameters . . . . .</i>	50
3.3 <i>Civil commercial aircraft engine parameters . . . . .</i>	50
3.4 <i>Parameters of the selected points on the Pareto front . . . . .</i>	57
3.5 <i>Parameters of the selected point on the Pareto front . . . . .</i>	60
3.6 <i>Parameters of the selected point on the Pareto front, flare angle 30° . . . .</i>	62
3.7 <i>Parameters of the optimal point on the Pareto front, flare angle 20° . . . .</i>	65
4.1 <i>Natural frequencies and damping ratios of the simplified model . . . . .</i>	81
4.2 <i>First five natural frequencies and damping ratios of the FFAST aeroelastic model at 200 m/s and sea level . . . . .</i>	93
5.1 <i>Vane design and dimensions . . . . .</i>	101
5.2 <i>Minimum required vane deflection performance . . . . .</i>	103



---

5.3	<i>Parts selected</i>	104
5.4	<i>Inertia and torque requirements of rotating parts in their own reference frames</i>	105
5.5	<i>Identified delay, convection time, and shedding time at 10 m/s, 14 m/s, and 18 m/s identified from continuous sinusoidal vane rotation</i>	124
5.6	<i>Identified delay, convection time, and shedding time at 10 m/s, 14 m/s, and 18 m/s identified from impulse vane rotation</i>	126
5.7	<i>Comparison identified delay at 10 m/s, 14 m/s, and 18 m/s</i>	128
5.8	<i>Selected parameters</i>	132
6.1	<i>Weight components</i>	144
6.2	<i>Properties of the 3D-printing materials</i>	144
6.3	<i>Specifications of the accelerometers used</i>	145
6.4	<i>Wind tunnel force balance minimum, maximum and resolution of each channel</i>	151
6.5	<i>Spar measured natural frequencies, damping ratios and mode shapes</i>	155
6.6	<i>Measured natural frequencies and damping ratios of the wing with different wingtips</i>	159
6.7	<i>Convergence study on the structural model of the spar</i>	176
6.8	<i>Convergence of the aerodynamic model of the wing with hinged wingtip</i>	178
6.9	<i>Summary Nastran model</i>	178
6.10	<i>First five structural natural frequencies of the spar measured experimentally and calculated from the Nastran model</i>	179
6.11	<i>Structural natural frequencies below 50 Hz of the wing with the different wingtips measured experimentally and calculated from the Nastran models</i>	179



# ABBREVIATIONS

AoA	Angle of Attack
ARA	Aircraft Research Association
CM	Centre of mass
CTA	Constant Temperature Anemometer
DLM	Doublet Lattice Method
DSVD	Damped Singular Value Decomposition
EAS	Equivalent Air Speed
EASA	European Aviation Safety Agency
EU28	European Union
EFTA	European Free Trade Association
FEM	Finite Element
FFT	Fast-Fourier transformation
FRF	Frequency Response Function
FWT	Folding Wing Tip
GA	Genetic Algorithm
GCV	Generalized Cross-Validation
GLA	Gust Load Alleviation
GG	Gust generator
LDA	Laser-Doppler Anemometer
LIDAR	Light Detection and Ranging
NASA	National Aeronautics and Space Administration
NPF	Negative Peak Factor
PIV	Particle-Imaging Velocimetry
RMS	Root mean square
$std(\bullet)$	Standard deviation of $\bullet$
SAH	Semi Aeroelastic Hinge
SFC	Specific Fuel Consumption
SVD	Singular Value Decomposition
TIKH	Tikhonov
TSVD	Truncated Singular Value Decomposition
WA	Wing aerodynamic

<i>WE</i>	Wing elastic
<i>WM</i>	Wing mass
WRAoA	Wing Root Angle of Attack
WRBM	Wing root out-of-plane bending moment

# NOMENCLATURE

$a$	Lower interval
$A$	Amount of bending present along the wingspan
$A_{GG}$	Maximum vane deflection
$AR$	Aing aspect ratio
$\mathbf{A}$	Structural inertia matrix
$a_w$	Sectional wing lift curve slope
$a_T$	Tailplane curve slope (defined with respect to incidence)
$a_E$	Tailplane curve slope (defined with respect to elevator angle)
$b$	Upper interval
$B$	Amount twist present along the wingspan
$B_g$	Gearbox backlash
$B_{GG}$	Vane rotation unknown
$B_i(t)$	Cubic polynomial function
$B_m$	Motor backlash
$B_{tot}$	Motor coupled with gearbox backlash
$\mathbf{B}$	Structural damping matrix
$c$	Chord
$c_i$	Parameters of the cubic B-spline basis
$c_{laser}$	Laser coefficient
$C_L$	Lift coefficient
$C_l$	Rolling moment coefficient
$C_D$	Drag coefficient
$C_{Di}$	Lift-induced drag
$C_L$	Lift coefficient
$C_{GG}$	Vane rotation unknown
$\mathbf{C}$	Structural stiffness matrix
$C_{M_{0W}}$	Zero lift pitching moment coefficient
$d_{laser}$	Measured distance by the laser
$d_{vs}$	Distance between the vane trailing edge and sensor
$d_1$	Laser vertical measurement
$d_2$	Laser vertical measurement

---

$dy$	Infinitesimal wing span length
$\mathbf{D}$	Aerodynamic damping matrix
$e$	Wing span efficiency
$\mathbf{E}$	Aerodynamic stiffness matrix
$f(t)$	Force input function
$f_i$	Filter factors
$\mathbf{f}$	Force vector
$\mathbf{f}_{aero}$	Fourier transform of the generalised aeroelastic force
$F_x$	Balance force in $x$ direction
$F_y$	Balance force in $y$ direction
$F_z$	Balance force in $z$ direction
$g$	Gravity force field
$h$	Uniform interval
$H$	Gust gradient
$\hat{H}$	Frequency response function
$\mathbf{H}$	Transformation matrix with Toeplitz structure
$H(s)$	Transfer function
$I_i$	Inertia $i$ -th component
$I_y$	Aircraft pitching moment
$l_g$	Gust length
$k$	Reduced frequency
$k(x, t)$	Kernel function
$\mathbf{K}$	Structural stiffness matrix
$k_{e0}$	Wing root displacement
$k_b$	Wing bending stiffness
$k_t$	Wing torsional stiffness
$k_\epsilon$	Downwash
$k_\theta$	Wingtip stiffness connection
$K$	Transfer function gain factor
$L$	Lift force
$L_T$	Scale of turbulence
$l_A$	Distance aerodynamic axis-elastic axis
$l_E$	Distance elastic axis-mass axis
$l_g$	Gust length
$l_T$	Distance aircraft centre of mass-tailplane aerodynamic centre
$l_W$	Distance aircraft centre of mass-aerodynamic axis
$l_{WM}$	Distance aircraft centre of mass-mass axis
$\mathbf{L}$	Regularisation matrix
$\mathbf{M}$	Structural inertia matrix
$M_i$	Wing root bending moment
$M_{WRBM}$	Wing root out-of-plane bending moment
$M_{wr}$	Wing root bending moment

$M_x$	Balance moment in $x$ direction
$M_y$	Balance moment in $y$ direction
$M_z$	Balance moment in $z$ direction
$M_{0W}$	Zero lift pitching moment
$M_\infty$	Mach number
$m$	Aircraft mass
$m_b$	Bending modal mass
$m_t$	Torsional modal mass
$m_M$	Engine mass
$m_{wt}$	Wingtip mass
$n_{crit}$	Number of critical cases
$n_{GG}$	Negative Peak Factor
$p$	Transfer function pole
$\mathbf{q}$	Generalised coordinates
$q_\infty$	dynamic pressure
$\mathbf{Q}_{hh}(k, M_\infty)$	Generalized aerodynamic forces matrices related to the generalized coordinates
$\mathbf{Q}_{hx}(k, M_\infty)$	Generalized aerodynamic forces matrices related to the control surfaces
$\mathbf{q}_{hg}(k, M_\infty)$	Generalized aerodynamic forces matrices related to gust
$r$	Residual
$r_g$	Gearbox ratio
$s$	Semi-span elastic wing
$s_1$	First contribution to the semi-span
$s_2$	Second contribution to the semi-span
$s_3$	Wingtip span
$S$	Aerodynamic surface
$S(t)$	Cubic spline function
$S_i$	Wing root shear force
$S_{wr}$	Wing root shear force
$t$	Time
$t_{conv}$	Convection time
$t_s$	Shedding time
$t_{ss}$	Sinusoidal excitation shedding time
$t_{vs}^i$	Identified second order polynomial equation of the shedding time
$t_{01}$	Vane rotation unknown
$t_{02}$	Vane rotation unknown
$t_1$	Vane rotation unknown
$t_2$	Vane rotation unknown
$t_3$	Vane rotation unknown
$T$	Kinetic energy
$T_i$	Wing root torsional moment
$T_{max}$	Motor minimum required torque
$T_{wr}$	Wing root torsional moment

---

$t^*$	Time leg wing aerodynamic centre-tailplane aerodynamic centre
$U$	Potential energy
$U_{max}$	Maximum gust velocities
$\mathbf{U}$	Matrix with orthogonal columns
$U_{hw}$	Horizontal airspeed measured by the cross hot-wire sensor
$V_{laser}$	Measured voltage by the laser
$V_{hw}$	Vertical airspeed measured by the cross hot-wire sensor
$V$	Unperturbed air speed
$\mathbf{V}$	Matrix with orthogonal columns
$w_g$	Gust velocity
$w_{g0}$	Peak of the gust velocity
$x_M$	Engine chordwise position
$w_{ref}$	Reference gust velocity
$\tilde{\mathbf{w}}_g$	Identified gust
$y(t)$	Measured response
$y(x)$	Real-valued function
$y_M$	Engine spanwise position
$\hat{y}(t)$	Noisy measured response
$\mathbf{y}$	Physical displacement
$z$	Vertical displacement
$z_{tf}$	Transfer function zero
$\alpha$	Aircraft pitch angle
$\alpha_0$	Incidence for zero wing lift
$\alpha_{min}$	Minimum gust value
$\alpha_{max}$	Maximum gust value
$\Gamma_x$	Wingtip centre of mass chordwise position
$\Gamma_y$	Wingtip centre of mass spanwise position
$\gamma$	Hinge angle
$\gamma_{e0}$	Wing root twist deformation
$\boldsymbol{\delta}$	Control surfaces vector
$\Delta$	Increment
$\eta$	Elevator angle
$\xi$	Modal displacement
$\theta$	Wingtip rotation
$\theta_{GG}$	Vane deflection
$\lambda$	Regularisation parameter
$\Pi$	Fitness function
$\rho$	Air density
$\sigma$	Gust severity root mean square
$\sigma_w$	Component of the gust velocity
$\sigma^*$	Singular value
$\boldsymbol{\Sigma}$	Diagonal matrix



$\tau_T$	Ratio between the scale of turbulence and the orizontal velocity
$\tau$	Increment
$\tau_f$	Time delay
$\tau_{tf}$	Transfer function delay
$\Phi_v$	Atmospheric turbulence
$\Phi_w$	Spectrum gust velocity
$\Phi_x$	Spectrum gust severity
$\Phi_\eta$	Power spectral density of the white noise
$\Phi$	Modal matrix
$\Psi$	Matrix collecting the cubic polynomial functions
$\omega$	Excitation frequency
$\omega_c$	Width rejected band
$\omega_0$	Central rejected frequency
$\Omega$	Spatial frequency

### Subscripts

0	Zero incidence
$AC$	Aerodynamic axis
$AC_{wt}$	Wingtip aerodynamic centre
$b$	Bending
$C$	Centre of mass
$F$	Fuselage
$g$	Gravitational field
$T$	Tailplane
$TE$	Tip trailing edge
$T_g$	Gust on the tailplane
$t$	Torsion
$W$	Wing
$W_i$	Initial weight
$W_f$	Final weight
$WA$	Wing aerodynamic axis
$W_g$	Gust on the wing
$wt$	Wingtip
$\Gamma$	Wingtip centre of mass
$\eta$	Elevator

### Superscripts

$\dot{()}$	differentiation with respect to time
$()^+$	Moore–Penrose generalized inverse matrix

### Symbol

$d$	Infinitesimal increment in $y$
$\delta$	Virtual increment



# Chapter 1

---

## INTRODUCTION

---

### 1.1 Motivation

---

Since the Wright brothers' first flight in 1903, the aerospace industries have been constantly growing and modernizing. In the last century, remarkable progress in aircraft design and flight operations has been achieved, making a revolution in transporting people and goods. The aviation industry is considered to have the fastest growth in the transport sector [23]. Pre-COVID-19 pandemic the number of global aviation passengers was predicted to double by the year 2037 [24]. This will increase air traffic and hence higher pollution rates. The primary pollutant emitted by aircraft engines in operations is carbon dioxide (CO<sub>2</sub>). Figure 1.1 show the CO<sub>2</sub> emission forecast up to the year 2040. The CO<sub>2</sub> emissions of all flights departing from the European Union (EU28) and the European Free Trade Association (EFTA) increased from 88 to 171 million tonnes (+95%) between 1990 and 2016. Between 2005 and 2014, the efficiency gain was insufficient to counterbalance the increase in CO<sub>2</sub> emitted due to the growth in the number of flights, aircraft size, and flown distance. Future CO<sub>2</sub> emissions under the base traffic forecast and advanced technology scenario are expected to increase [1]. This translates to the need for more efficient and sustainable aircraft.

The Breguet formula expresses the performance of an aircraft in terms of maximum achievable range as a function the aerodynamic, structural and engine design parameters

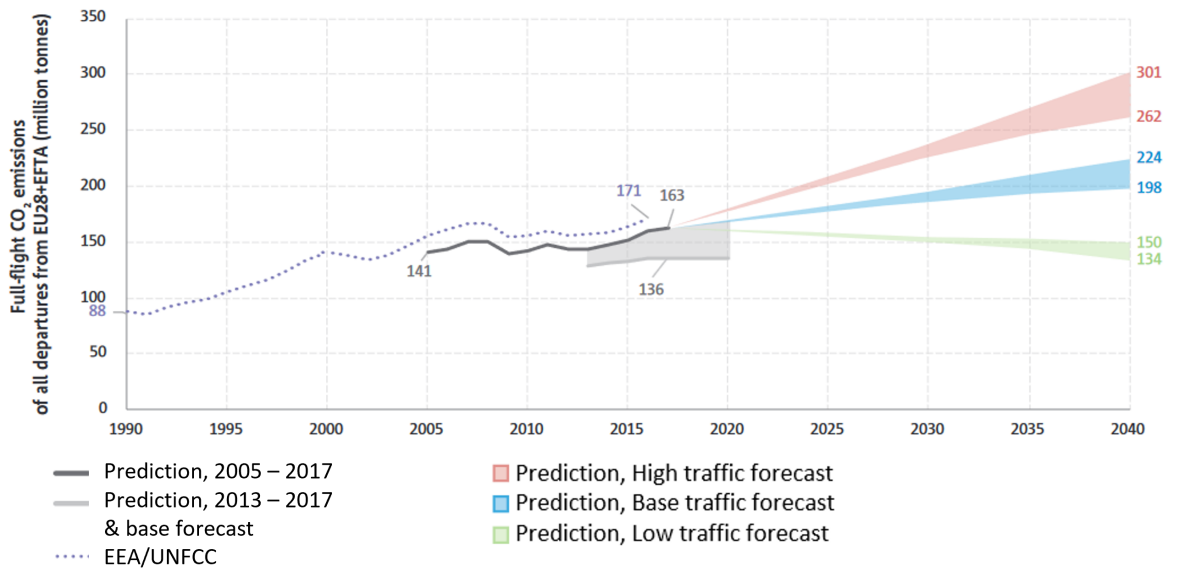


FIGURE 1.1: CO<sub>2</sub> emission forecast (directly adapted from [1])

as

$$R_{AC} = \frac{V}{g} \frac{1}{SFC} \frac{C_L}{C_D} \ln \frac{W_i}{W_f} \quad (1.1)$$

where  $V$  is the flight speed,  $g$  is the gravitational field,  $SFC$  is the specific fuel consumption,  $C_L$  and  $C_D$  are the lift and drag coefficients and  $W_i$  and  $W_f$  are the initial and final weights respectively. This relation suggests that to improve the aircraft range the designers can:

- maximise the cruise speed,
- improve the engine efficiency,
- improve the aerodynamic efficiency by maximising the lift/drag ratio,
- minimise the structural weight, thus minimising the final weight.

Although improvements in structural weight and aerodynamics can be made in isolation, they have to be considered together to obtain the most significant benefit due to their strong interaction. A considerable contribution, usually 30%–40% of the overall drag, is lift-induced drag. For a planar wing with an elliptical lift distribution, the lift-induced drag can be estimated as

$$C_{Di} = \frac{C_L^2}{\pi e AR} \quad (1.2)$$

where  $e$  is the wing span efficiency and  $AR$  is the wing aspect ratio (defined as  $AR = b^2/S$ , where  $b$  is the wing span and  $S$  is the surface area). Equation (1.2) shows how the wing

geometry influences the induced drag. The lift-induced drag is due to the tip vortices created by the pressure difference on the lower and upper wing surfaces, and it can be reduced by increasing the wingspan.

This thesis focuses on numerical and experimental studies of an aeroelastic wing with hinged wingtips. This new concept allows the improvement of aerodynamic performance while alleviating the structural loads, saving structural weight and, consequently, fuel consumption. No considerations are provided regarding engines and their efficiency.

---

## 1.2 State of the Art

---

During flight, aircraft are expected to encounter atmospheric turbulence events with different levels of severity. Turbulence events not only reduce the comfort of the passengers but also produce additional loads in the airframe and in the case of severe turbulence events, the structure could be subjected to fatigue damage [25]. Turbulence can be considered as the air movement through which the aircraft passes where the component of the air velocity normal to the flight path will change the effective incidence of the aerodynamic surface, the aerodynamic forces will change, and consequently, the dynamic response of the aircraft will also change [20]. The dynamic loads are significant and aircraft designers must ensure that the airworthiness requirement is met, i.e. the aircraft is able to withstand vertical and lateral discrete gusts and turbulence.

Atmospheric gusts and turbulence increase airframe loads and significantly affect aircraft ride quality and comfort. Until the early 1930s, airframes were designed to support flight manoeuvre load conditions alone. The flexible, dynamic structural response was incorporated in the mid-1950s. Over the past few decades, the fidelity and accuracy of the models have improved, flight control systems have become more critical in the analysis, and the methods and techniques codified in terms of airworthiness standards. Gust loads are among the most critical cases an aircraft can encounter, so mitigating the loads enables the design of a lighter structure, consequently reducing production and fuel consumption costs. Furthermore, the fatigue life of the structure is also increased by the alleviation of the loads. To optimise the wing load distribution, academic and aircraft manufacturer communities have proposed different strategies [26, 27]. Load alleviation strategies are divided into two categories, active and passive load alleviation. Active load alleviation systems use information from sensors to drive the position of control surfaces to reduce the loads. Passive load alleviation techniques are based on the capability of

the structure to deform, limiting the loads when certain types of perturbation, such as wind gusts, occur.

In the rest of this section, a literature review is provided showing the main active and passive load alleviation approaches explored with a particular emphasis on hinged wingtips, the techniques developed to recover from in-flight data gusts and turbulence events, and the approach followed to validate numerical models experimentally.

### 1.2.1 Active Load Alleviation

Passive load alleviation devices have been developed and applied more recently within the aeronautical industry than active approaches. Traditional aircraft designed using aluminium alloys, fixed-wing geometries, a more conservative design approach, and standard wing structural elements (primarily spars with transverse ribs) have led to quite stiff aircraft structures unable to exploit the flexible effects characterising the passive load alleviation strategies. Active Gust Load Alleviation (GLA) is not a new topic, for example in 1974 investigations were performed on the Lockheed C-5A fatigue issues leading to the development of the ‘Active Lift Distribution Control System’ [28]. Initially, GLA was implemented either to fix a developing problem or to provide enhancements to existing aircraft. Over the past few decades, the fidelity and accuracy of the models has improved, flight control systems have become more critical in the analysis, and the methods and techniques have been codified in terms of airworthiness standards [25, 27]. Over the years, two main strategies have been considered for the design of active GLA. The first strategy is based on a feedback controller using motion measurements of some aircraft points (primarily using accelerometers); the second approach uses a direct measure of the turbulence and the use of a feedforward system to counteract it. These two strategies can be combined together. Rynaski et al. [29] suggests a dual feedforward-feedback arrangement, where the feedback using the smaller surfaces increases the natural frequencies and damping ratio of the structural modes, while the feedforward using the primary control surfaces alleviates the rigid body modes of the aircraft. In the last decades, many GLA systems have been implemented on numerous aircraft, such as the Lockheed C-5A/L-1011-500, Boeing B-1 and Airbus A320/A330/A340/A380/A350, although very little information is available in the public domain. An accurate survey on the main milestones of the development of active GLA systems is provided by Regan and Jutte [27].

Recently various works have shown that the Doppler LIDAR (Light Detection and Ranging) wind speed sensor is a mature, reliable, and compact technology for in-flight measurement systems, able to give information about the airspeed at different distances from

the sensor [30, 31] and can be used for active GLA [32–35].

Aeroelastic modelling for gust response is a relatively mature technology and is a crucial element during the design of new aircraft. The structure of recent flexible and lighter-weight aircraft has become more elastic, and the separation between flexible and rigid body modes has been reduced. Therefore flutter suppression, gust load alleviation, and flying qualities need to be treated simultaneously [27].

## 1.2.2 Passive Load Alleviation

Passive load alleviation strategies are of considerable interest since they do not need sensors and actuators that introduce weight, require power, and risk failure. However, passive approaches are based on fluid-structure interaction effects, therefore the performance may not be satisfactory for all the points of the flight envelope.

### **Aeroelastic tailoring**

Aeroelastic tailoring can be defined as “the incorporation of directional stiffness into an aircraft structural design to control aeroelastic deformation, static or dynamic, in such a fashion as to affect the aerodynamic and structural performance of that aircraft in a beneficial way” [36]. The objectives associated with aeroelastic tailoring include, but are not limited to, weight minimisation, increasing flutter or divergence speed, reducing stress, increasing lift, reducing drag and avoiding skin buckling.

The design concepts of aeroelastic tailoring are not at all new. In 1949 Munk et al. [37] oriented the wood’s fibers of the blades of a fixed-pitch propeller in such a way that they twist elastically and favorably as the thrust changes. Almost 20 years later, the idea to passively control the wing incidence due to flexural distortion was again proposed by General Dynamics as part of a program to improve transonic performance [36]. Indeed, the use of advanced composite material was proposed to provide the best wing ‘shape’ (primarily twist distribution) at both cruise and a design maneuver condition. The authors exploit the anisotropy of composite material to create coupling between bending and torsion deformation. At this time, the name ‘aeroelastic tailoring’ was coined [36]. Figure 1.2 summarises possible aeroelastic benefits of laminate tailoring. The wing ‘primary stiffness’ direction “refers to the points where the structure exhibits the most resistance to bending deformation” [36]. This location can be tailored using stiffeners, ribs, or skin to move the axis fore or aft of the conventional elastic axis changing the wing’s bending and torsional stiffness and the degree of coupling between the two. The structural reference axis is the conventional wing structure elastic axis. The wing will have bend twist coupling when the primary stiffness axis is not coincident with the

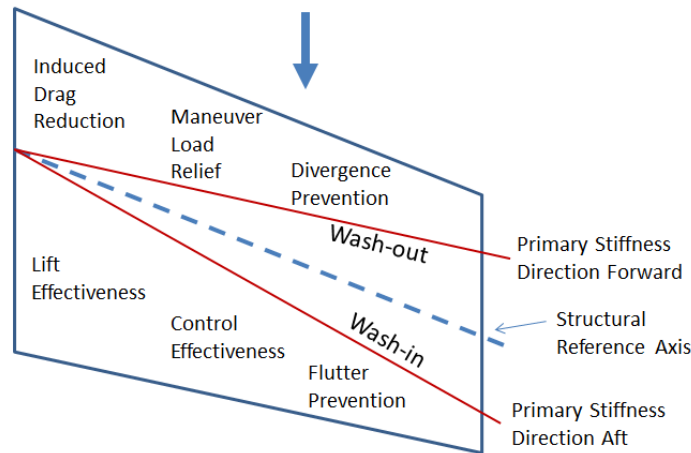


FIGURE 1.2: *Effects that the location of the primary stiffness direction has on the characteristics of the wing (directly adapted from [2]).*

structural reference axis. The ‘wash-out’ appears when the primary stiffness direction is moved forward of the structural reference axis, so the bending twist coupling causes the wing to have leading-edge down characteristics. The ‘wash-in’ appears when the primary stiffness direction is moved aft of the structural reference axis, so the bending-twist coupling causes the wing to have leading edge-up characteristics. Moving the primary stiffness axis in either direction produces desirable changes in wing performance, but the two directions involve trade-offs with each other [2, 38]. Over the years, researchers have spent a great effort on the topic of aircraft aeroelastic tailoring. It has been used with different objectives such as: weight minimisation, flutter control, divergence, stress, roll reversal, control effectiveness, lift, drag, skin buckling, and fatigue [2].

### 1.2.3 Hinged Wingtip

While GLA plays a crucial role, great efforts have been made to find techniques that reduce aerodynamic drag. A simple technique to reduce lift-induced drag is to increase the wingspan. However, such a design solution has some limitations related to the maximum aircraft dimensions allowed at airports and also to the increase in bending moments along the wing. A possible solution to the first problem is to use a folding wing that can be employed on the ground. An example of this technique is the latest version of the Boeing B777X, which, through the use of wingtips, the wingspan will be 7 meters longer than that of the original B777. Figure 1.3a shows a Boeing B777X on the ground with wingtip folded up, and Figure 1.3b shows the same model during fly with the additional wingtip in a horizontal position. The folding wingtip capability will be used only on the ground during taxi to and from the gates allowing the aircraft to





(a) B777X on the ground

(b) B777X flying

FIGURE 1.3: B777X in different configurations (directly adapted from [3])

fit within the airport gate. Over the years folding wingtips have been used on a number of aircraft [39]. The first known use of a hinged wing for GLA was on the Rey R.1 aircraft which made its first flight in 1949. The introduction of the hinged wings gave a reduction of 60% in the stresses resulting from gust loads [40]. Each wing of the Rey R.1 is divided in two sections connected by rubber disk. The torsion of the rubber provides the ‘spring action’ [41]. In the 1970s, the XB-70 Valkyrie, a large supersonic strategic bomber, was developed. This design used folding wingtips that could pivot downwards to control the lift-to-drag ratio at both low subsonic and supersonic speeds [39]. In 1999 Allen [4] introduced the concept of combining the benefits of a foldable winglet for maximizing the wingspan of the aircraft during cruise operation while reducing wing bending moments during extreme flight manoeuvres. The foldable winglet is joined to the aircraft wing via a hinge, and an actuator is mounted on the aircraft wing and attached to the foldable winglet. In cruise, the winglet can be rotated from a vertical position to a fully extended position wherein the winglet becomes an extension of the wing. When the wing is subjected to severe loads, the loads overcome the action of the actuator and pivot the winglet to the vertical position. Figure 1.4 shows a schematic view of an aircraft having folding winglets in vertical and horizontal positions. Pitt [5] considered a straight wing of a modern aircraft and examined the capabilities of using a hinge to produce aeroelastic tailoring. The author showed that the effect of moving the wing fold line at a relative angle to the bend direction is similar to the pitch-bending coupling of helicopter blades. Figure 1.5 shows a straight wing with a schematic view of the wingtip wash-in and wash-out concept with different hinge sweep. In the case of a straight hinge, the wing bending does not change the tip angle of attack. A positive hinge line sweep is clockwise, looking down on the wing from leading edge to trailing edge. For a positive hinge line sweep, the angle of attack is reduced at the tip of an upward bending wash-out. In a classical wing without the hinge, the upward bending generally corresponds to lift increasing on the wing. Thus, the positive hinge sweep acted as a

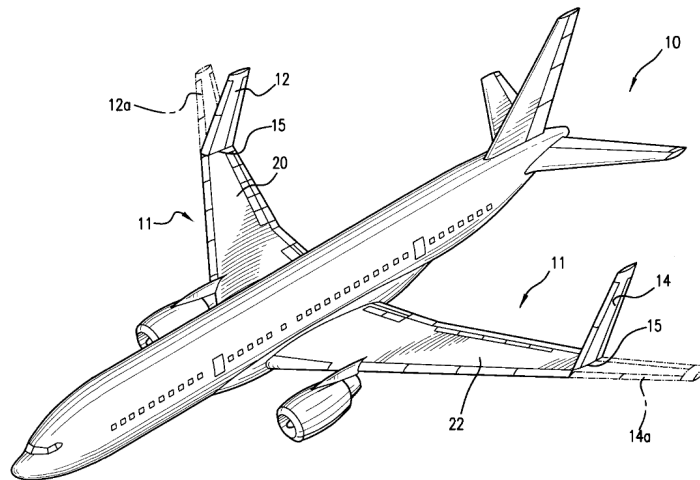


FIGURE 1.4: A schematic view of an aircraft having folding winglets (directly adapted from [4]).

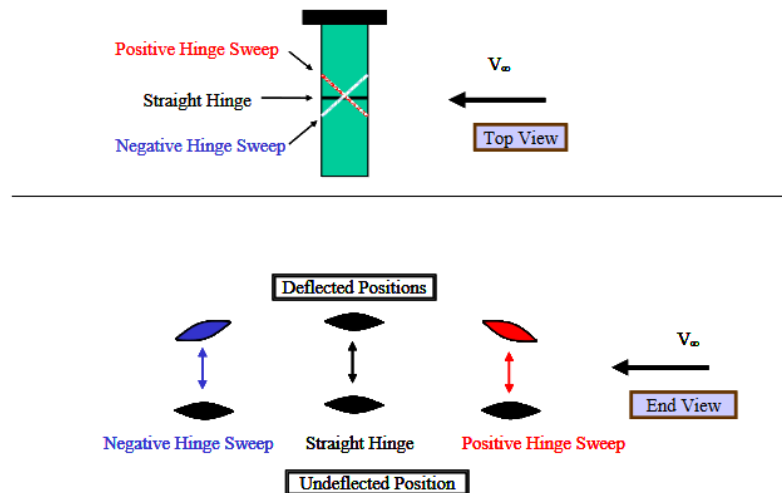


FIGURE 1.5: A schematic view of the wingtip ‘wash-in’ and ‘wash-out’ concept due to hinge wingtip (directly adapted from [5]).

static load relief mechanism in that as the lift increased, the local twist angle decreased, subsequently reducing the lift. A negative swept hinge line resulted in wash-in with bending. Pattinson et al. [42] showed the potential of a folding wingtip to alleviate the wing loads by coupling a flexible multi-body dynamics solver with a computational fluid dynamics coupled structural model. Wilson et al. [40] defined the flare angle as the angle between the longitudinal axis of the aircraft and the hinge rotation axis. They showed that for short-range aircraft, a zero stiffness flared hinge reduces gust and manoeuvre loads. The use of a zero stiffness hinge could cause flutter which can be stabilized via tip masses, the choice of hinge location and hinge flare angle. The choice of hinge flare and hinge location has a small effect on the bending moment at the wing root. Similarly Castrichini et al. [43] investigated the effects of using a folding wingtip as a

load alleviation device considering a numerical aeroelastic model of a typical commercial jet aircraft. In this work, they investigated the effect of hinge stiffness, damping, hinge orientation and wingtip mass on the static loads, gusts loads and flutter behaviour. For low hinge spring stiffness and wingtip mass, an increase in the hinge angle with respect to the free stream direction allowed improved load alleviation capability. They showed that in the case of a  $25^\circ$  hinge a low wingtip mass is beneficial for the flutter speed, while a zero stiffness hinge with a high wingtip mass decreases the flutter speed. Castrichini et al. [44, 45] investigated the effect of a passive nonlinear hinge spring to connect the folding wingtip to the main wing. They showed that significant load alleviation was possible when the system has a low overall stiffness around the trim equilibrium point for a large enough range of deflection angles. Moreover, they showed that through proper design of the wingtip device, it is possible to increase the wing aspect ratio with a small increase, or even reduction, of the gust loads experienced by the aircraft. Valente et al. [46] compared a high fidelity method for aeroelastic analysis with respect to the traditional linear Doublet Lattice Method (DLM) in the case of a wing with a Folding Wing Tip (FWT). Both linear and non-linear trim and gust response analysis confirmed the capability of the FWT to alleviate bending moment and torque. The loads calculated by the highly detailed method showed higher load alleviation performance with respect to the one predicted by the DLM. Cheung et al. [6] performed a series of low-speed wind tunnel tests using a flared-hinged folding wingtip device. Figure 1.6 shows the wing in the wind tunnel and the gust generator. They considered both steady

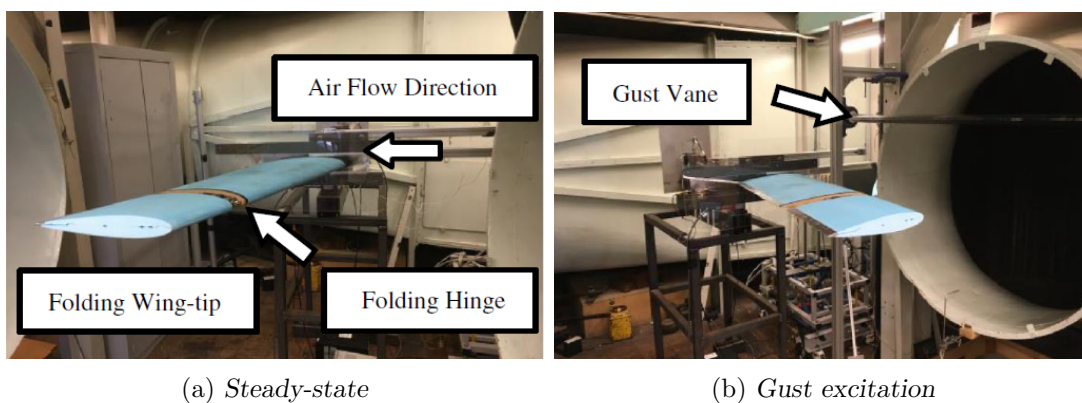


FIGURE 1.6: Folding wing in the Bristol wind tunnel (directly adapted from [6])

and dynamic aerodynamic conditions, in conjunction with variations in the stiffness of the folding hinge. The steady aerodynamic tests for a stiff-hinge and a free-hinge demonstrated that the folding wingtip is statically aerodynamically stable regardless of hinge stiffness and measurements compared with aeroelastic predictions gave similar trends. Numerical results generated by the MSC/NASTRAN aeroelastic models showed similar trends to the experimental data in terms of gust load alleviation performance

with respect to changes in hinge spring stiffness for different hinge angles. Moreover, the achieved reduction from the wind tunnel measurements is higher than the predicted. Cheung et al. [7, 47] added an aerodynamic surface into the wingtip to control the folding action. Figure 1.7 shows the wing in the wind tunnel in a free-hinge configuration. In

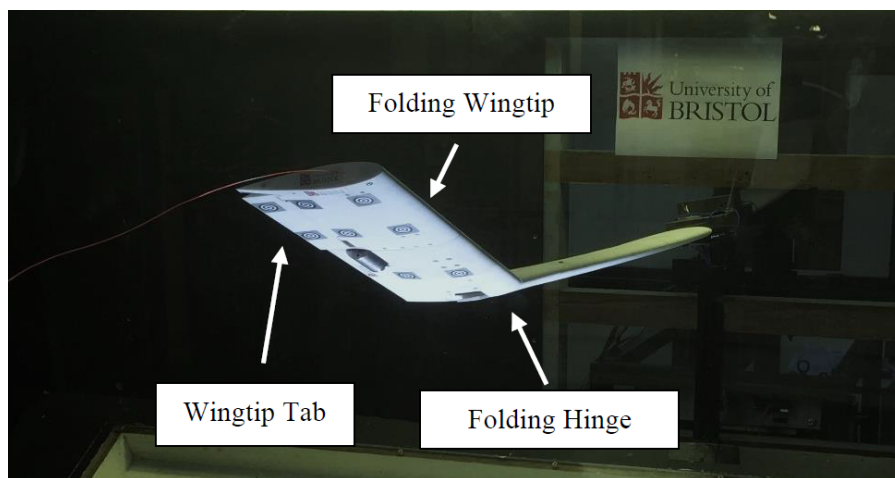


FIGURE 1.7: Wing in the wind tunnel in a free-hinge configuration (directly adapted from [7]).

a series of steady aerodynamic tests, they demonstrated that this device is capable of maintaining the orientation of the wingtip over a range of wind tunnel velocities and angles of attack. Moreover, they showed that actuating the secondary aerodynamic surface could improve the load alleviation capability already achieved by the folding wingtip alone. Castrichini et al. [48] showed that regardless of the 25% increment in span, a free-hinge aircraft has the same handling qualities and dynamic response of the baseline model with no wingtip extension. The authors suggested that the FWT could be used both as a load alleviation device and to alleviate the roll-damping increment induced by the longer span. Moreover, this increases the aileron authority with the consequent weight-saving respect to the fixed-hinge aircraft that required a bigger aileron size. Ajaj [49] confirmed that the introduction of the FWT has a minor influence on the handling qualities regardless of the flare angle, fold angle, and wingtip size to the case of no extension. The main effects are on the phugoid mode improving the damping due to the increased drag at large fold angles, and the time constant for the spiral mode significantly reduces, making this mode more stable. Healy et al. [50] experimentally validated the use of FWT to significantly improve the roll performance of an aircraft with FWT when compared to a fixed configuration of the same span. During the roll, the improved roll performance is achieved by unloading the wingtip reducing the developed aerodynamic roll damping, thus increasing the maximum roll rate of the aircraft. In addition, they showed that the FWT reduces the time required to reach the steady-state roll rate and increases the peak angular acceleration of a wing.

Two experimental and one numerical works considered the nonlinear effects of hinged wingtips. Firstly, based on the numerical and experimental evidence that hinged wingtips can undergo large rotations, Healy et al. [51] explored, with wind tunnel tests, the effects of the geometrical nonlinearities introduced due to the large deformation of the wingtip. They found that changing the root angle of attack of the model can vary the flutter speed by over 25%. Secondly, Healy et al. [52] considered the dynamic behaviour of a wing at velocities beyond the flutter boundary. They showed that after the flutter boundary, a stable limit cycle oscillation predominately bounded by geometric nonlinearities appears.

The authors also showed the effects of a wingtip tab, introduced in a previous work [7], can significantly alter the stability boundary of the system suggesting the use of a wingtip tab in flight to extend the stability boundary of the aircraft. Thirdly, Conti et al. [53] investigated the effects of geometric nonlinearities on the quasi-steady aeroelastic response of an aircraft with FWT. They showed that in the case of a high angle of attack, the wingtip response could vary significantly when geometric nonlinearities are accounted for; however, a negligible impact was observed on the main airframe structure. Moreover, nonzero sideslip affects the effective flare angle leading to an asymmetric stiffness between the left and right hinge.

The effects of the bending stiffness and tailoring of the main wing, the impact of the hinge release instant on the final GLA of the hinged wingtip is considered in [54]. In that work, the authors found that the linear model overpredicts the flutter speed by more than 40%, and a change in the flutter mechanism is found at different hinge conditions. Contrary to conventional wings, wash-in tailoring increases flutter speed. Moreover, the authors showed no clear relationship between the GLA and the structural properties of the wing, while a notable effect of the hinge release timing on the GLA was found. In the case of statically unloaded conditions ( $\alpha = 0$ ), in terms of GLA, releasing the hinge before the gust hits the wing is equivalent to a free hinge. In contrast, the later it is released, the worse the GLA becomes, reaching the condition of increasing the peak loads when it is released close to the peak load. In the case of statically loaded conditions ( $\alpha = 5$ ), if the hinge is released before it hits the wing, the dynamic effects of the wingtip due to the change in the configuration, compensates the gust load and reduces the peak load by more than 90%. The authors underline the importance of detecting the gust and reacting on time, and considering the wing oscillation during the release of the wingtip that can be detrimental to the fatigue life of the structure.

### **Semi aeroelastic hinge concept**

In 2017 Wilson et al. [40] proposed the Semi Aeroelastic Hinge (SAH) concept; the wingtip is kept in a horizontal position during flight to maximise the aerodynamic performance by using a dedicated locking mechanism. When a trigger event is detected, the

wingtip is actively released, and it acts as a passive load alleviation system driven only by aerodynamic and inertia forces. When the load event is finished, an actuator returns the wingtip to its original configuration. This concept could allow a substantial increment of the wing-span and a weight-saving opportunity. Castrichini et al. [55] showed that the capability of the SAH concept is strongly affected by the timing between the hinge released and the load event. They found that the release time of the wingtip is a crucial parameter for load alleviation. Indeed, they observed a worsening or an improvement of the loads alleviation effects by varying the hinge release delay. An early release of the wingtip is required to obtain the same load alleviation performance as a pure floating hinge aircraft. A series of patents from Airbus followed [56–58].

In recent years, Airbus developed AlbatrossOne, a basic proof of concept demonstrator for the Semi Aeroelastic Hinge technology. The wing was approximately 1:14 scale of a generic short range aircraft. It was geometrically scaled to represent a future full scale aircraft, although, it was not dynamically scaled for either handling qualities and/or aeroelasticity in terms of mass and stiffness properties. Figure 1.8 shows AlbatrossOne during flight tests in the free hinge configuration, before take-off in Figure 1.8a and during flight in Figure 1.8b. The main objectives were to:



(a) *AlbatrossOne on the ground (directly adapted from [59]).*



(b) *AlbatrossOne during flight (directly adapted from [60]).*

FIGURE 1.8: *AlbatrossOne during flight tests, wingtips free to rotate*

- qualitatively demonstrate the semi aeroelastic hinge concept,
- validate the near-linear variation of the symmetric and anti-symmetric wing tip flapping mode frequencies with airspeed,
- validate the static and dynamic stability of the free wing tip,
- validate the increase of the free wing tip fold angle with aircraft angle of attack,
- validate the reduction of the wing loads when the wing tip is free to fold,
- validate the near instant reduction in wing loads when the hinge is released, the consequent aircraft pitch-up response and the elevator compensation,
- demonstrate the possibility of recovering the wingtip to its planar position using an actuator,
- demonstrate there is no contact between the wingtips and the ground when the aircraft lands with freely hinged wingtips,
- demonstrate the reduction in roll damping when the wing tips are free to fold.

The wing has five wing tip configurations: a 2.6 m wing span with no wingtips, a 3.2 m wing span with fixed wingtips, a 3.2 m wing span with the wingtips free to rotate, a 3.7 m wing span with fixed wingtips, a 3.7 m wing span with the wingtips free to rotate. Flight testing showed that the wingtips were statically and dynamically stable throughout the flight. The wing load alleviation effect from the free wingtips was confirmed through different flights [60]. Healy et al. [8] described a novel flight test method for a UAV constrained by a tether, resulting in steady, controlled, elliptical flight paths. Figure 1.9 shows AlbatrossOne in a tethered flight test. The authors applied this technique to the AlbatrosONE and characterised the effect of sideslip on the equilibrium position of free-floating hinged wingtips. This innovative approach allowed the boundaries of the flight envelope to be determined safely to verify the stability boundary of such a device.

### 1.2.4 In Flight Gust Identification

A better knowledge of the actual gusts and turbulence to which the aircraft is subjected could improve different aeronautical practice (e.g. design of gust load alleviation system, analysis of accidents or estimation of the loads on the structure). In recent years with the development of lighter and more efficient aircraft, the effort to develop new active or

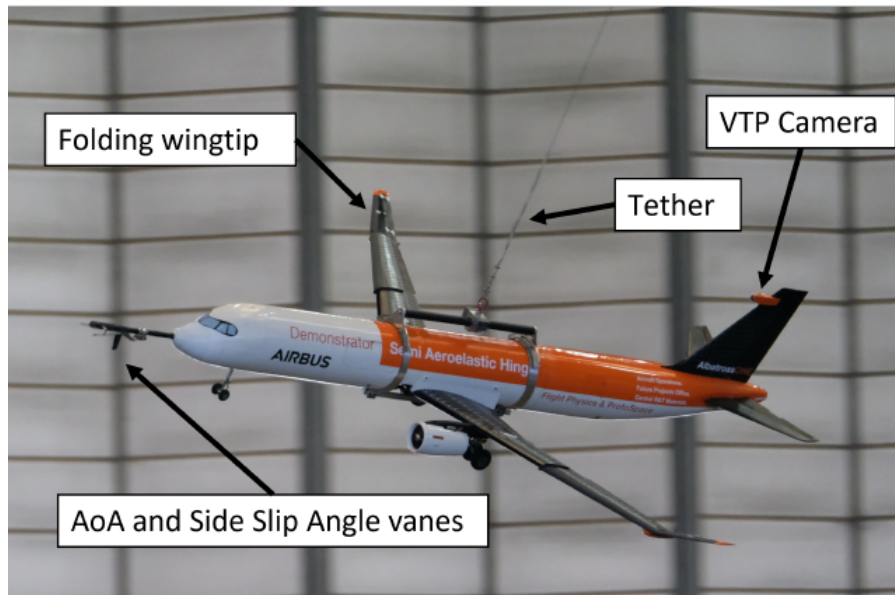


FIGURE 1.9: Tethered flight test of the AlbatrossOne model (directly adapted from [8]).

passive GLA systems has increased [27]. A large database of real gusts and turbulence events to which aircraft are subjected could lead to a more efficient design of the GLA system. Moreover, aircraft are equipped with a digital flight data recorder, a device used to record specific aircraft performance parameters, which is designed to survive under extreme conditions that can result from an accident. In the analysis of flight incidents, gust and turbulence events are of primary importance in the estimation of limit loads [10]. Nowadays, the interest of the aerospace industry in digital twins is growing [61–63]. A possible benefit of a digital twin for aircraft is the possibility to calculate the loads on the airframe. To have a reliable calculation of the loads, it is necessary to measure the gusts and the turbulence events. A better estimation of the airframe loads is a major benefit for aircraft operators. Indeed, knowing the loads at any location of the structure during the flight, or soon after the flight, can avoid unnecessary or expensive inspection of the structure and the inspections could be limited to specific parts of the aircraft [10, 64].

The earliest approach for the study of gust velocity profiles is known as the discrete-gust approach and dates back to the 40s and 50s. It is based on the analysis of peak vertical accelerations  $\Delta n$  directly measured by the aircraft flying in gusts. These accelerations were assumed to originate from a series of isolated discrete gusts and were used to derive gust parameters as the distance parallel to the aeroplane's flight path for the gust to reach its peak velocity  $H$  (called gradient distances) and the maximum gust velocities  $U_{max}$  [9, 65]. The resulting gusts were then used in the design phase of a new aircraft. This process was known as the 'discrete-gust approach' and is shown in Figure 1.10. This



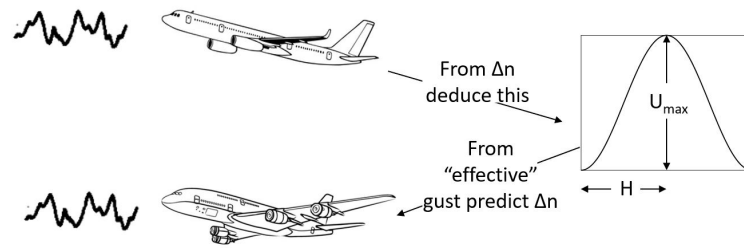


FIGURE 1.10: *Discrete-gust approach to design (directly adapted from [9]).*

approach was not able to return the real air turbulence, but was sufficient to evaluate normal accelerations on future aircraft designs [66].

In the 60s and 70s, further progress was made on developing spectral techniques to design aircraft subject to gust encounters [67]. These techniques were based on two main assumptions: the time histories of gust velocities obtained from aircraft may be converted to space fixed ‘temporarily frozen’ histories and the scale of the turbulence is larger compared to the airplane dimensions. These assumptions imply that the gusts are random in the flight direction only but are considered uniform in the spanwise direction. The

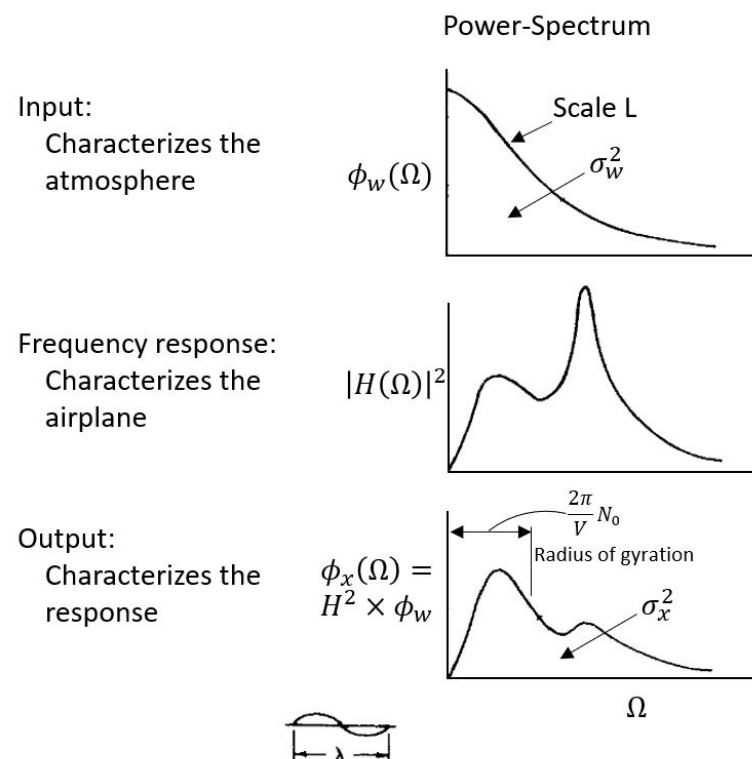
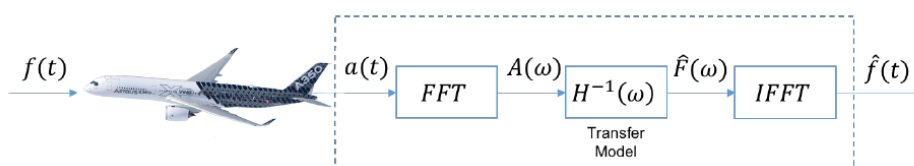


FIGURE 1.11: *Spectral-technique: input-output relations for gust response (directly adapted from [9]).*

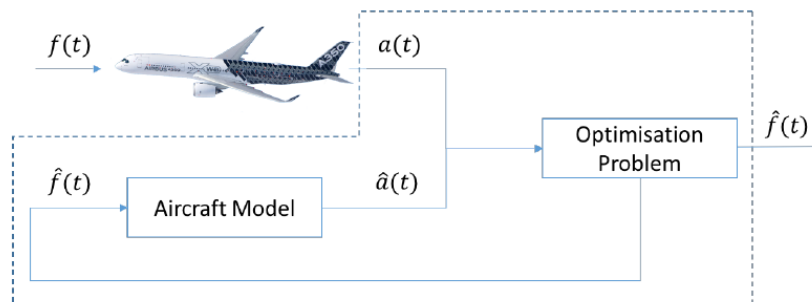
procedure involved the selection of a spectrum for gust velocity input  $\Phi_w$ , a scale value

$L$ , a RMS value  $\sigma_x$  and gust severity value  $\sigma_w$ . Then, through the frequency response function  $\hat{H}$ , two basic structural parameters are found,  $A$  and  $N_0$ .  $A$  is the proportionality constant relating the RMS value of the chosen output parameter of concern,  $\sigma_x$  is the RMS value of gust severity, or  $\sigma_x = A\sigma_w$ .  $N_0$  denotes the number of times per second the output response crosses the mean ‘1-g’ load level value of  $x$  with a positive slope. However, the complexity in the definition of the frequency response functions  $\hat{H}$ , due to intricacy of  $\hat{H}$ , was a limitation for this technique [9].

In 1999, in the context of space and missile systems, a Monte-Carlo flight gust loads analysis approach was proposed [67]. The procedure uses forcing functions that were derived by extracting the short-duration, turbulent components of measured wind profiles. However, the method was limited applicability with a restriction to gust wavelengths greater than 500 ft (152 m). In 2009, a method consisting of a model-based approach with an observer for a non-linear aircraft model and a disturbance model for the estimation of gusts and structural loads was proposed [68]. This method uses on-board measured data and parameters available on commercial aircraft making the estimation of manoeuvre-induced structural loads easier. The only unknowns remain the gust velocities which were determined through a non-linear parameter optimisation that computed the gain matrix of the observer model. Recently, a neural network technique for wind gust identification using flight data recordings was used [69]. In the last 80 years, different techniques for gust loads identification have been studied, but mainly two approaches have been considered, i.e. the direct method and the optimisation method [70]. Figure 1.12 shows the two approaches. In the direct methods, the excitation  $f(t)$  is calculated directly from the



(a) Direct method



(b) Optimisation method

FIGURE 1.12: Force prediction methods (directly adapted from [10])

measured responses  $y(t)$  by evaluating the inverse model (Figure 1.12a). In structural dynamics the process of calculating the excitation force from the measured response is called an inverse problem. The optimisation methods, instead, use directly the model in an optimisation framework where the input is tuned until the model responses match the measured responses (Figure 1.12b)[10].

### 1.2.5 Wind Tunnel Testing of Gust Load Alleviation

The unsteady nature of a gust and strong coupling between the resulting aerodynamic loads and structural deformations make the modelling process quite complex. Analysing the performance of a GLA system through flight tests has some drawbacks. Indeed to evaluate the system performance, it is difficult to find the proper turbulence conditions or extreme gusts because, by definition, extreme gusts are very rare. The artificial generation of atmospheric turbulence and gusts is a complex task, and a possible approach could be flying in the wake of an aircraft. The phenomenon of encountering wakes has some peculiarities to the gust and turbulence encountered and can be considered a problem on its own [71, 72]. The measurement of gust disturbance acting during flight tests is a challenging task. Due to the impossibility of controlling the variables of interest, it is difficult to replicate the same test without the GLA system and with different control strategies. Experiments are possible with full-scale aircraft and models. Although flight tests of full-scale aircraft are necessary to test control systems, wind tunnel tests are an interesting alternative to validate numerical models. Testing models in the wind tunnel offer the possibility to perform the test in a controlled environment, to generate the disturbance almost arbitrarily and to guarantee the repeatability of the test. Wind tunnel tests are less risky and cheaper than flight tests, and are possible even during the design process of the aircraft [73].

#### Generation of gusts in the wind tunnel

The experimental validation of active or passive control technologies on scaled aeroelastic models is a challenging task [74, 75] and requires specific equipment in the wind tunnel. Active and passive grids are commonly used in wind tunnels to generate turbulence. In 1991 Makita et al. [11], after a series of investigations, proposed a new type of active turbulence generator able to produce homogeneous, and quasi-isotropic turbulence with a high turbulence Reynolds number. The majority of active grids follow the general design proposed by Makita et al. [76]. They consist of grid bars with attached ‘agitator wings,’ rotated by stepper motors located outside the wind tunnel. Figure 1.13 shows a schematic of the original active grid developed by Makita et al.. Active grids had a significant impact on the experimental study of turbulence in wind (or water) tunnels

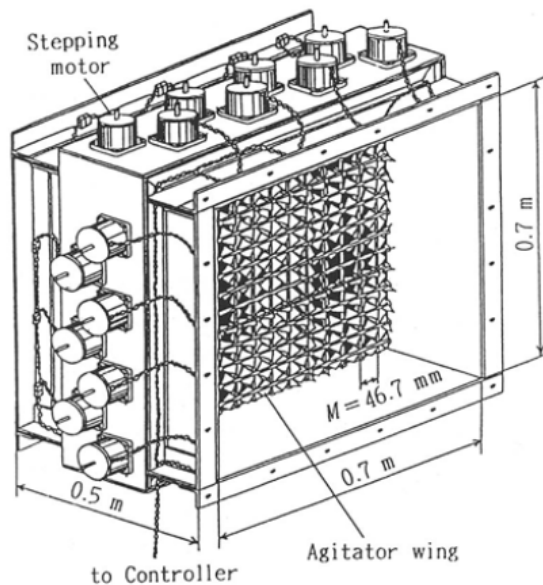


FIGURE 1.13: Schematic of the active grid developed by Makita et al. (directly adapted from [11]).

[76]. Active grids are not used for aeroelastic testing because they cannot generate discrete large amplitude gusts.

The first documented attempt to produce gust in the wind tunnel was in 1966 at the National Aeronautics and Space Administration's (NASA) Langley Research Center by Richard et al. [12]. The aim of the project was to produce gusts up to 50 Hz with an amplitude of 10 ft/s (3.05 m/s). Various types of vanes and setup were considered. Due to their limitations in amplitude or frequency to create discrete gusts and the inability to separate transverse and longitudinal gust components, they decided to inject air to induce pure longitudinal oscillations in a wind tunnel stream. The air was stored in a 56.6 m<sup>3</sup> tank at 793 kPa, and electrovalves were used to modulate the air supplied to the four injectors. Figure 1.14 shows the modulation system and the ball valves used. One-dimensional and two-dimensional gusts were produced. They showed the ability of the air injection technique to generate longitudinal gusts in the wind tunnel. In 1969 Buell et al. [13] proposed cascade oscillation vanes to produce longitudinal gusts. In contrast with the previous designs, this concept allows large Reynolds numbers and turbulence scales appropriate for large structures. Buell et al. considered various arrangements of vanes. Figure 1.15 shows a view of the installed vanes from the upstream direction. Velocity measurements downstream from the vanes demonstrated that gusts in either the longitudinal or the lateral directions can be generated.

In the past 50 years, different configurations have been considered driven by experimental

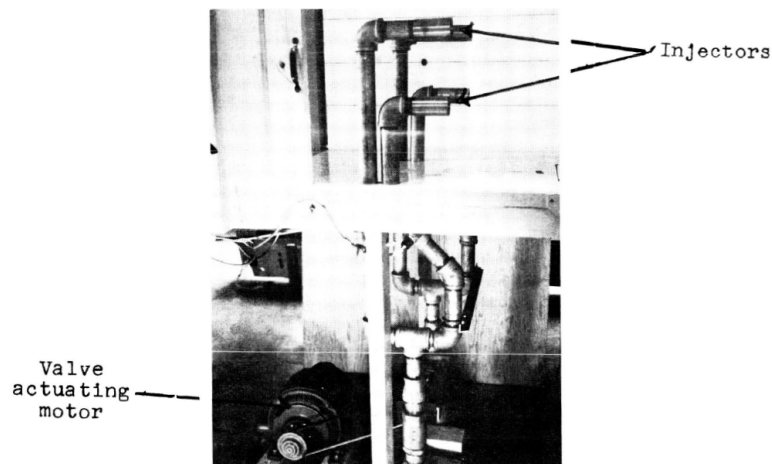


FIGURE 1.14: View of the modulation valve system (directly adapted from [12]).

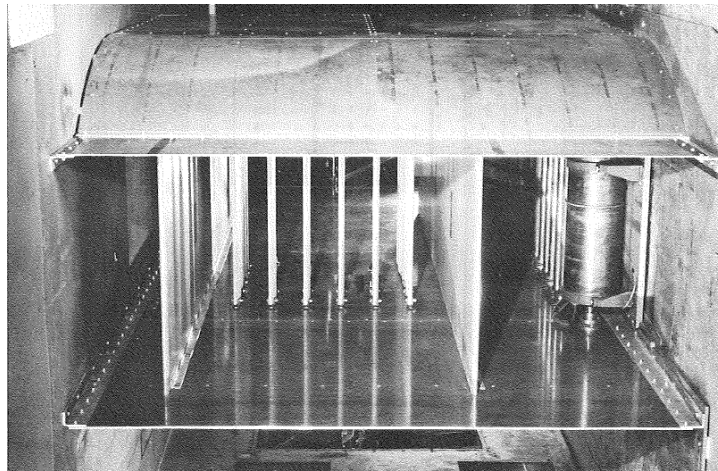


FIGURE 1.15: View from upstream of the gust generator apparatus mounted in the wind tunnel (directly adapted from [13]).

requirements and the available wind tunnel facilities [15]. Table 1.1 reports a summary of the existing gust generators installed around the world. Most gust generators are based on one or multiple pitching airfoils [13–16, 19, 77–85]; however, alternative solutions exist. Figures 1.16 and 1.17 show conventional and unconventional gust generators installed in different wind tunnels. In 1981 Reed et al. [17] built a gust generator for the Transonic Dynamic Tunnel using small pitching surfaces mounted on the sidewall of the tunnel. The vanes did not span the entire test section width. The vane trailing vortices induce a vertical velocity component across the model suspended in the center by cables. Figure 1.17a shows the gust generator and the B-52 model suspended by cables. To reduce the mechanical complexity and increase the controllability and reliability of a gust generator Tang et al. [18] used a four vanes with a rotating slotted cylinder at the trailing edge. Results showed the ability of this technique to produce controllable harmonic gusts requiring very low torque. However, this technique’s maximum gust angle is lower than

Research Institute/University	Year	Top speed	Wind tunnel cross section
NASA (USA) [12]	1966	30.5 m/s	Rectangular 0.6 m $\times$ 0.9 m
NASA (USA) [13]	1969	76.2 m/s	Rectangular 2.13 m $\times$ 3.05 m
MIT (USA) [86]	1974	37 m/s	Elliptical 2.13 m $\times$ 3.32 m
Duke University (USA) [18]	1996	25m/s	Rectangular 0.7 m $\times$ 0.53 m
Virginia Tech (USA) [77]	2004	15 m/s	Square 2.15 m $\times$ 2.15 m
TSAGI (Russia) [78]	2005	30 m/s	Elliptical 4.0 m $\times$ 2.33 m
TSAGI (Russia)[78]	2005	120 m/s	Circular 7 m diameter
University of Maryland (USA) [87]	2008	N/A	N/A
Politecnico di Milano (Italy) [79]	2008	30 m/s	Rectangular 1.0 m $\times$ 1.5 m
University of Colorado (USA) [88]	2009	20 m/s	Square 0.34 m $\times$ 0.34 m
DLR (Germany) [16]	2010	Mach 0.75	Square 1.0 m $\times$ 1.0 m
ONERA (France) [80]	2011	Mach 0.73	Rectangular 0.76 m $\times$ 0.8 m
Cranfield University (England) [81]	2015	14.5 m/s	Elliptical 1.52 m $\times$ 1.14 m
ARA (England) [19]	2015	Mach 0.85	Rectangular 2.74 m $\times$ 2.44 m
Politecnico di Milano (Italy) [14]	2016	55 m/s	Rectangular 4.0 m $\times$ 3.84 m
University of Bristol (Uk) [82]	2017	60 m/s	Octagonal max. width 2.1 m, max. height 1.5 m
Delft University (Netherland)[15]	2017	35 m/s	Square 2.85 m $\times$ 2.85 m
University of Maryland (USA) [83]	2019	25 m/s	Square 0.9 m $\times$ 0.9 m
Michigan State University (USA) [84]	2021	10 m/s	Square 0.61 m $\times$ 0.61 m
Mitsui engineering (Japan) [85]	N/A	20 m/s	N/A

TABLE 1.1: Summary of existing gust generator installations around the world

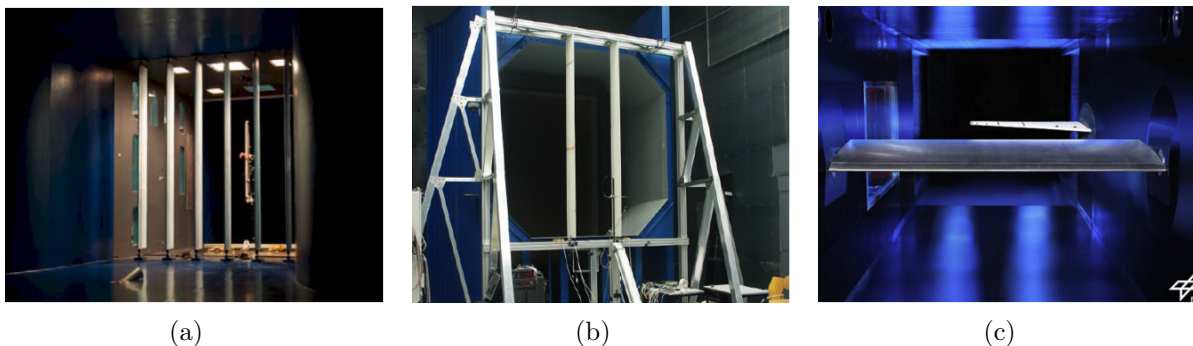


FIGURE 1.16: Example of conventional gust generators (a, directly adapted from [14]; b, directly adapted from [15]; c, directly adapted from [16])

that obtained with pitching vanes. Figure 1.17b shows a sketch of the gust generator with four vanes/rotating cylinders. To study the behavior of small-scale micro aerial vehicles and small birds Roadman et al. [88] used an active grid to generate continuous turbulence following the Makita style [11]. This design cannot produce ‘1-cos’ gusts as prescribed by the certification authorities [26]. Allen et al. [19] built a gust generator at the Aircraft Research Association (ARA) to operate under transonic flow conditions, within a large wind tunnel section, by blowing air jets mounted on two fixed profiles. Figure 1.17c shows an aircraft model and the gust generator installed in the wind tunnel.

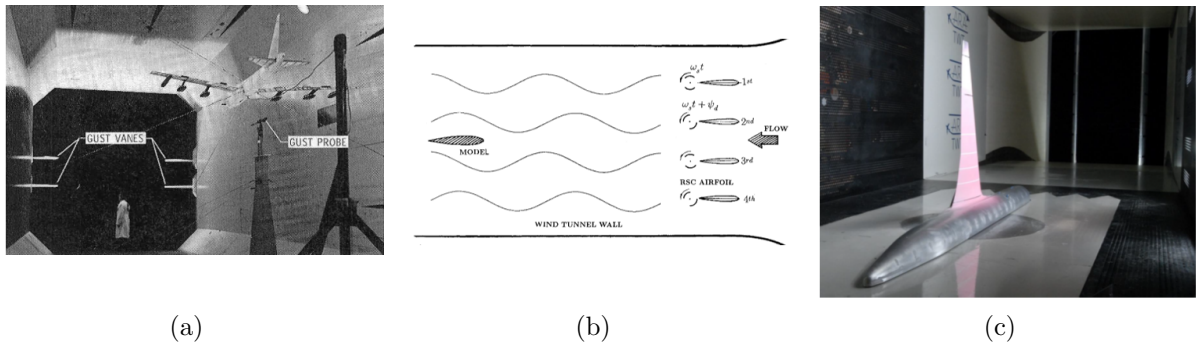


FIGURE 1.17: Example of unconventional gust generators (a, directly adapted from [17]; b, directly adapted from [18]; c, directly adapted from [19])

---

## 1.3 Thesis Outline

---

This thesis work deals with aeroelastic modelling, identification and experimental validation of aeroelastic systems. The application considered is the hinged wingtip for gust load alleviation.

**Chapter 1** provides the motivation and the general background in active, passive and hinged wingtip for load alleviation, in-flight gust identification, and wind tunnel testing of gust load alleviation system. The remainder of the chapter provides the main body of the thesis showing the novel and original findings from the research activity.

**Chapter 2** describes techniques to define aeroelastic models with different levels of accuracy. Moreover, two models of an aircraft with hinged wingtips are presented. The first model uses the lowest number of degrees of freedom to model a symmetric rigid aircraft with an elastic wing and rigid hinged wingtip. The second model is a detailed model representative of a civil, commercial aircraft. These two models will be used in the thesis.

**Chapter 3** focuses on the problem of worst-case gust prediction and multi-objective optimisation for the worst-case gust prediction. The simplified model introduced in Chapter 2 is used considering dimensions and weight distribution of the detailed model of Chapter 2. Moreover, techniques to overcome the flutter speed reduction due to the hinged wingtip are considered.

**Chapter 4** combines the simplified model and the detailed model described in Chapter 2 for the problem of gust identification. The models were both used to generate in-flight gust response data and as a model for the inverse problem. Classical regularisation methods showed the inability to identify the gust in the presence of noisy data. A robust technique for aircraft gust identification based on cubic B-splines was proposed.

**Chapter 5** focuses on creating continuous and discrete gusts in the Swansea University wind tunnel. The gust generator's design, installation, commissioning and characterisation are reported. To improve the creation of discrete gusts, two techniques were considered. Firstly, the identification of a transfer function to calculate the required vane rotation was performed. Secondly, a parametric study on vane rotation shown that a more complicated vane rotation function made it possible to obtain improved discrete gusts.

**Chapter 6** presents the design, structural characterisation and wind tunnel tests of a wing able to accommodate a fixed wingtip and two hinged wingtips. Static wind tunnel tests shown the ability of a hinged wingtip to reduce gust loads. Aeroelastic models of the wing with different wingtips were defined, and structural validations were performed. Experimental gust response measurements were used to validate the numerical models.

**Chapter 7** gives the conclusions of the work performed in this thesis and provides recommendations for future studies.

---

## 1.4 Aims and Research Outcome

---

The major aims and novel scientific contributions from this study are:

- The simplified modelling of an aircraft with an elastic wing and hinged wingtips for the worst-case gust prediction and multi-objective optimisation.



- The development of a robust technique for aircraft gust identification considering simulated in-flight data from a detailed model and gust identification based on a simplified model.
- Design and characterisation of a gust generator for the Swansea University wind tunnel. Furthermore, the study of techniques to improve the creation of discrete gust.
- Design, static and dynamic wind tunnel testing of a wing able to accommodate a fixed wingtip and hinged wingtips. The creation of aeroelastic models representative of the manufactured wing with the different wingtips. Validation of the aeroelastic models through comparison of the experimental and simulated gust response time history.

### 1.4.1 Research Outcome

The following is the research outputs of the work performed as part of this thesis in terms of journal publications, conference presentations and research posters:

#### Journal Publications

- **D. Balatti**, H.H. Khodaparast, M.I. Friswell, & M. Manolesos (2022). Improving wind tunnel ‘1-cos’ gust profiles. *Journal of Aircraft*, DOI: 10.2514/1.C036772. In press (2022).
- **D. Balatti**, H.H. Khodaparast, M.I. Friswell, M. Manolesos, & M.R. Amoozgar, The effect of folding wingtips on the worst-case gust loads of a simplified aircraft model, January 2021, *Proceedings of the Institution of Mechanical Engineers Part G Journal of Aerospace Engineering*, DOI: 10.1177/09544100211010915
- **D. Balatti**, H.H. Khodaparast, M.I. Friswell, M. Manolesos, & A. Castrichini, Aircraft turbulence and gust identification using simulated in-flight data, May 2021, *Aerospace Science and Technology* 115(3):106805, DOI: 10.1016/j.ast.2021.106805

#### Journal Publication in preparation

- **D. Balatti**, H.H. Khodaparast, M.I. Friswell, M. Manolesos, & A. Castrichini, Improving gust load alleviation performance of hinge wingtip using validated aeroelastic models.

## Conference Proceedings

- **D. Balatti**, H.H. Khodaparast, M.I. Friswell, & M. Manolesos (2022). Aeroelastic model validation through wind tunnel testing of a wing with hinged wingtip. *International Forum on Aeroelasticity and Structural Dynamics (IFASD)*, Madrid (Spain)
- **D. Balatti**, H.H. Khodaparast, M.I. Friswell, & M. Manolesos (2022). Improving wind tunnel ‘1-cos’ gust profiles. *AIAA SCITECH 2022 Forum* (p. 2485).
- **D. Balatti**, M. Manolesos, H.H. Khodaparast, & M.I. Friswell (2021). Generating a ‘1-cos’ gust profiles in a wind tunnel. *Online Symposium on Aeroelasticity, Fluid-Structure Interaction, and Vibrations* (p. 158).
- **D. Balatti**, H.H. Khodaparast, M.I. Friswell, M. Manolesos, & M.R. Amoozgar (2020). The effect of folding wingtips on the flight dynamics of an aircraft with elastic wing. *11th International Conference on Structural Dynamics* (pp. 631-639). European Association for Structural Dynamics.

## Conference Presentations

- **D. Balatti**, C. Turner, M. Manolesos, H.H. Khodaparast, & M.I. Friswell (2021). Design and characterisation of a gust generator for aeroelastic wind tunnel testing. *UK Fluids conference*, 8-10 September 2021.
- **D. Balatti**, H.H. Khodaparast, M.I. Friswell, M. Manolesos, & M.R. Amoozgar (2019) Gust Load Estimation for a Simplified Aeroelastic Wing Model with Movable Wingtip. *Airbus DiPaRT Symposium*, 26-28 November 2019, Bristol.
- H.H. Khodaparast, **D. Balatti**, & M.I. Friswell (2019). Aircraft gusts loads predictions using in flight measurement data. *The Real World’s Counterpart: Digital Twins - The present and the future*, London Royal Aeronautical Society, 8 October 2019.

## Poster

- **D. Balatti**, H.H. Khodaparast, M. Manolesos, & M.I. Friswell (2021). Experimental and numerical studies of aeroelastic hinged wingtips. *The Annual Zienkiewicz Centre for Computational Engineering (ZCCE) Postgraduate Workshop*, Swansea University, United Kingdom, 18 January, 2021.

- 
- **D. Balatti**, H.H. Khodaparast, M. Manolesos, & M.I. Friswell, (2020). Development of active and passive wing gust load alleviation system considering non-linearity and uncertainty in the model. *The Annual Zienkiewicz Centre for Computational Engineering (ZCCE) Postgraduate Workshop*, Swansea University, United Kingdom, 13-14 January, 2020.
  - **D. Balatti**, H.H. Khodaparast, M. Manolesos, & M.I. Friswell (2020). Development of active and passive wing gust load alleviation system considering non-linearity and uncertainty in the model. *Quarterly DigiTwin meeting*, Bristol University, United Kingdom, 8-9 January, 2020.

# Chapter 2

---

## AEROELASTIC MODELLING OF AN AIRCRAFT

In this Chapter, techniques to define aeroelastic models with different levels of fidelity are presented. Two models of an aircraft with hinged wingtips are presented: a simplified model and a detailed model. The simplified model is a numerical model developed in Matlab. It has the lowest number of degrees of freedom, consisting of a rigid fuselage, elastic wing, and rigid wingtip. The detailed model is a Nastran model composed of a few thousand elements. Both models are defined to study the problem of gust response. The simplified model is used in Chapters 3 and 4, while the detailed model is used in Chapter 4.

---

### 2.1 Introduction to Aeroelasticity

---

Aeroelasticity is the science that investigates the mutual interaction between aerodynamic, elastic, and inertia forces and how this affects the static and dynamic aircraft structural response [89]. Figure 2.1 shows a schematic representation of the classical Collar aeroelastic triangle. It shows how the interaction between the major disciplines of structural dynamics, stability and control, and static aeroelasticity result from the interaction of two of the three types of force. However, dynamic aeroelasticity, such as a

manoeuvre or a gust, occurs when all three forces interact. Aeroelastic effects have had

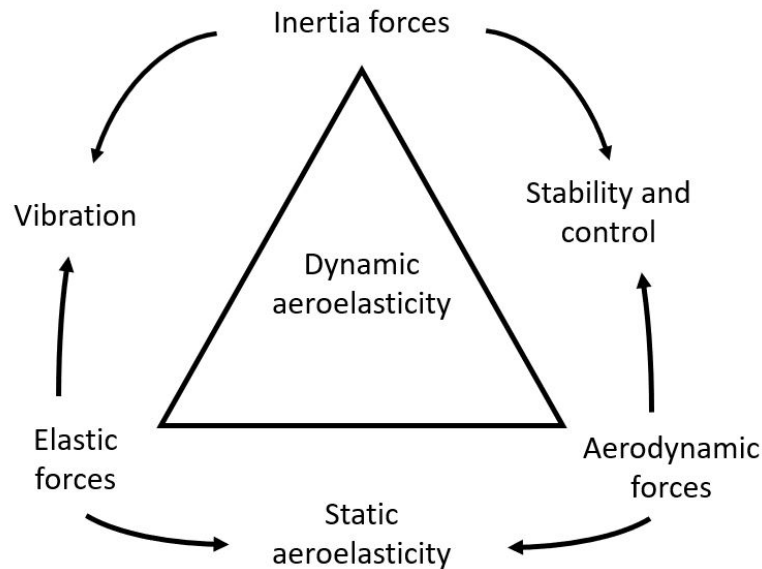


FIGURE 2.1: Collar's aeroelastic triangle (directly adapted from [20])

a significant impact on aircraft design since before the first controlled powered flight of the Wright Brothers. Since aeroelastic phenomena can be destructive (e.g. flutter and divergence), engineers had designed heavier structures to ensure the structural integrity [20]. The classic Collar aeroelastic triangle can be extended to a pyramid when a control system is included in the problem. The science that studies these phenomena is called aeroservoelasticity. Figure 2.2 shows the aeroservoelastic pyramid. In modern commercial aircraft design, flight control systems are employed for different purposes, such as improving handling qualities and stability, flight performance, ride quality, reducing loads (gust and/or manoeuvre), and improving service life.

The model sophistication depends on the type of aircraft configuration, the type of dynamic simulation of interest, the flight envelope of the aircraft, and finally the stage in the design process. Flutter is the phenomenon that requires the most careful and accurate aerodynamic modelling. Depending on the analysis of interest and on the stage of the design, models with different levels of accuracy can be developed. Aeroelastic models can be categorised into simplified and detailed models. During the preliminary design of an aircraft, when the information available is limited, a simplified model can be used to extract information on handling qualities, stability, and flight performance. Moreover, for an elastic aircraft, the starting point for the design and analysis of an active controller is a numerical model of the aeroelastic system. Model reduction techniques are necessary when working with a detailed model; an alternative is to use a simplified model directly. Although there are some possibilities of designing adaptive controllers without

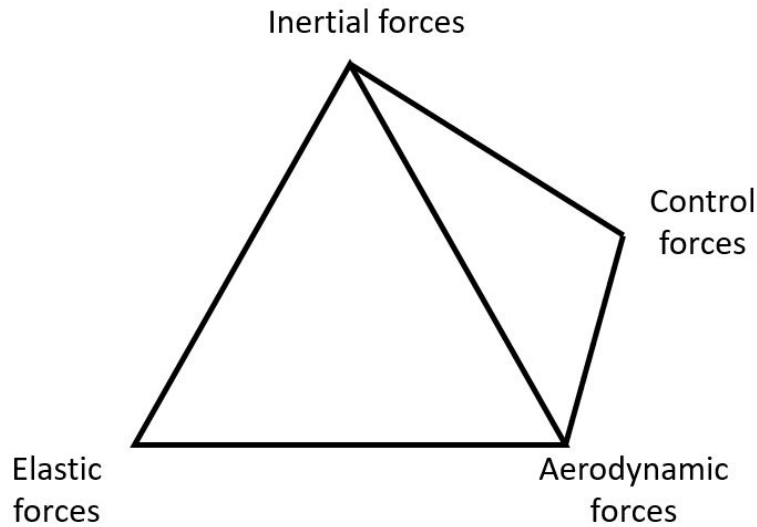


FIGURE 2.2: *Aeroservoelastic pyramid (directly adapted from [20])*

previous knowledge of the system, some knowledge can be beneficial in the tuning and numerical validation phase. Regarding the simplified models, the d'Alembert principle, the Lagrange formulation, and Finite Element (FE) models can be used to calculate the structural properties. Unsteady two-dimensional strip theory and the DLM are typically used as an aerodynamic model. For the detailed model, a classical approach to develop a structural model is the 'stick' representation, in which each major component is treated as an assembly of sticks placed along the reference axes. The aerodynamic models used in the aeroelastic calculations are essential to ensure a correct estimation of the deformations and loads. Different manufacturers tend to adopt different practices in detail, though there will be similar core features. Typically two-dimensional unsteady strip theory or three-dimensional unsteady panel methods are used, combined with the output of steady computational fluid dynamics and wind tunnel studies [20].

### 2.1.1 General Form of the Aeroelastic Equations

As mentioned in the previous section, aeroelasticity studies the mutual interaction between aerodynamic, elastic, and inertial forces. Indeed, aeroelastic models are obtained combining structural and aerodynamic models. Independently from the technique used, the definition of the structural model yields an equation of the form

$$\mathbf{M}\ddot{\mathbf{q}}(t) + \mathbf{C}\dot{\mathbf{q}}(t) + \mathbf{K}\mathbf{q}(t) = \mathbf{f}(t) \quad (2.1)$$

where  $\mathbf{M}$ ,  $\mathbf{C}$  and  $\mathbf{K}$  are the structural inertia, damping and stiffness matrices, and  $\mathbf{q}(t)$  and  $\mathbf{f}(t)$  are the vectors of the physical or generalised coordinates and forces. The

definition of the numerical model of an aeroelastic system requires the computation of unsteady aerodynamic forces and impacts the nature of the equation obtained.

### Aerodynamic model: strip theory

In two-dimensional strip theory, the lift coefficient on each chordwise strip of the wing is proportional to the angle of incidence  $\alpha(y)$  at a distance  $y$  and it is assumed that the lift on each strip does not influence another. Figure 2.3 shows a strip of a wing at distance  $y$ , having chord  $c$  and width  $dy$ . The lift produced by the strip is

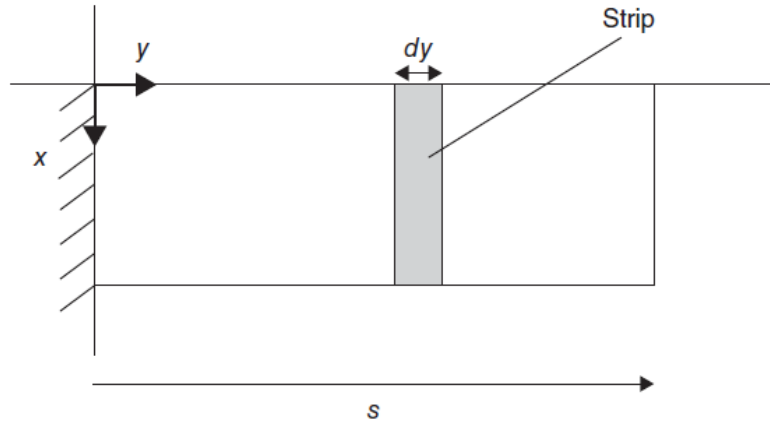


FIGURE 2.3: Aerodynamic ‘strip’ on a continuous rectangular wing (directly adapted from [20])

$$dL = \frac{1}{2} \rho V^2 dy c a_w \alpha(y) \quad (2.2)$$

where  $a_w$  is the lift curve slope. The total lift produced by a single wing of span  $S$  is obtained by integrating the effect of all the strips, so that

$$L = \int_0^S dL \quad (2.3)$$

In the case of a tapered wing,  $c$  in Eq.(2.2) can be modified into  $c(y)$  to consider the actual chord length at each spanwise coordinate. The assumption of independence of each strip from its position can be removed to ensure that the lift is zero at the tip due to the trailing tip vortex. In Eq.(2.2) the lift curve slope  $a_w$  can be replaced with  $a_w(y)$ .  $a_w(y)$  can be defined as a quadratic or sinusoidal function of the spanwise coordinate with the constraint that  $a_w(S) = 0$  [90]. The change in the angle of incidence can be due to a vertical motion, change in the trim, or a gust. Coupling Eq.(2.3) with a structural model allow the classical second-order form of the aeroelastic equation to be obtainable, namely

$$\mathbf{A}\ddot{\mathbf{q}} + (\rho V \mathbf{B} + \mathbf{D})\dot{\mathbf{q}} + (\rho V^2 \mathbf{C} + \mathbf{E})\mathbf{q} = \mathbf{f} \quad (2.4)$$

where  $\mathbf{A}$ ,  $\mathbf{D}$  and  $\mathbf{E}$  are the structural inertia, damping and stiffness matrices,  $\mathbf{B}$  and  $\mathbf{C}$  are the aerodynamic damping and stiffness matrices,  $\mathbf{q}$  is the vector of generalised coordinates, and the force vector  $\mathbf{f}$  on the right-hand side of the equation can have contributions due to trim, lift at zero incidence, gravitational field, and gust on the aerodynamic surfaces. Equation (2.4) can be used for stability analysis and time or frequency domain simulation. Aerodynamic strip theory was used by several authors [91–95] for the implementation of aeroelastic loads.

### Aerodynamic model: panel methods

The panel method is a numerical approximation method that can be used to calculate the forces acting on an object in a flow. Horseshoe vortices are used to calculate the lift variation along the chordwise and spanwise. The most common three-dimensional unsteady panel approach is the DLM. The DLM is a linear potential unsteady aerodynamic theory for thin lifting bodies. It is based on the assumptions of inviscid, attached, irrotational, and perfect isentropic flow. As a consequence, nonlinear aerodynamic effects such as flow separations, shocks, boundary layers, turbulence as well as aerodynamic drag are not accounted for. At 1/4 chord of each panel acceleration potential doublets are used to calculate the aerodynamic forces resulting from the unsteady motion. The doublets lead to the calculation of complex Aerodynamic Influence Coefficients that relate the lift acting along the doublet line to the displacement of each panel [96, 97]. The steady forces corresponding to the steady flow are calculated using the steady Vortex Lattice method [97, 98]. Figure 2.4 shows a typical panel set-up with both vortices and doublets.

Aerodynamic models based on the DLM [96] or three dimensional unsteady panel methods [99, 100] lead to the formulation of the equations of motion in the frequency domain. In modal coordinates the aeroelastic equations can be expressed as

$$(-\omega^2\tilde{\mathbf{M}} + i\omega\tilde{\mathbf{C}} + \tilde{\mathbf{K}})\boldsymbol{\xi} = \mathbf{Q}_e + \mathbf{f}_{aero} \quad (2.5)$$

where  $\tilde{\mathbf{M}}$ ,  $\tilde{\mathbf{C}}$ , and  $\tilde{\mathbf{K}}$  are the modal mass, damping and stiffness matrices,  $\boldsymbol{\xi}$  the modal displacement,  $\mathbf{Q}_e$  is the Fourier transform of the non-aerodynamic external generalised forces, and  $\mathbf{f}_{aero}$  is the Fourier transform of the generalised aeroelastic force. The formulation in modal coordinates introduces a truncation error due to the neglected modes.

The same modal basis is used for the formulation of the unsteady aerodynamic forces, defined in the frequency domain as

$$\mathbf{f}_{aero} = q_\infty[\mathbf{Q}_{hh}(k, M_\infty)\boldsymbol{\xi} + \mathbf{Q}_{hx}(k, M_\infty)\boldsymbol{\delta} + \mathbf{q}_{hg}(k, M_\infty)w_g] \quad (2.6)$$



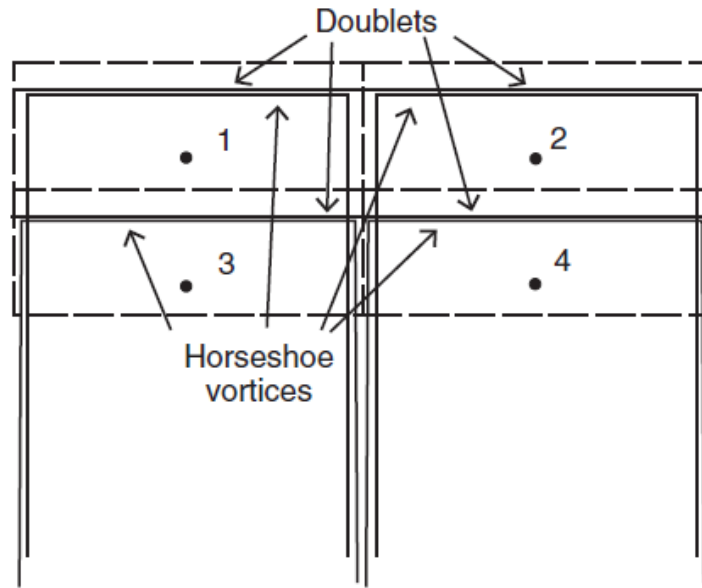


FIGURE 2.4: Typical doublet and horseshoe vortex set-up for the DLM (directly adapted from [20])

where  $\mathbf{Q}_{hh}(k, M_\infty)$ ,  $\mathbf{Q}_{hx}(k, M_\infty)$ , and  $\mathbf{q}_{hg}(k, M_\infty)$  are respectively the generalized aerodynamic forces matrices related to the Fourier transform of the generalized coordinates  $\boldsymbol{\xi}$ , control surfaces vector  $\boldsymbol{\delta}$  and gust shape  $w_g$ ,  $q_\infty$  is the dynamic pressure,  $k$  is the reduced frequency and  $M_\infty$  is the Mach number. The non-rational frequency domain formulation of Eq. (2.5) is a typical representation of the dynamics of an aeroelastic system. However, it is not the most convenient form for introducing nonlinearities in the system and for designing a control system.

Several methods were developed to convert the aerodynamic forces into the time domain, therefore enabling the formulation of the aeroelastic equations in the time domain [101–106]. These techniques approximate the transcendental dependency of the aerodynamic matrices with the reduced frequency  $k$  using a polynomial formulation. This approach leads to the transformation from an integral-differential to a purely differential set of equations.

### 2.1.2 Gust Model

Atmospheric disturbance models are categorized into two idealized categories: discrete gusts and continuous turbulence [26]. Due to its shape, a discrete gust is typically called

a ‘1 - cosine’ gust. The profile is defined as

$$w_g(t) = \begin{cases} \frac{w_{g0}}{2} \left[ 1 - \cos\left(2\pi\frac{V}{l_g}t\right) \right] & \text{for } 0 \leq t \leq \frac{l_g}{V} \\ 0 & \text{for } t > \frac{l_g}{V} \end{cases} \quad (2.7)$$

where  $w_{g0}$  is the maximum gust velocity and  $l_g$  is the gust wavelength. According to the European Aviation Safety Agency (EASA) regulation [26] for the case of civil, commercial aircraft, gust wavelengths are varied between 18 m to 214 m, and the gust velocity is calculated as

$$w_{g0} = w_{ref} \left( \frac{H}{106.14} \right)^{1.6} \quad (2.8)$$

where the gust gradient  $H$  is half the gust wavelength  $l_g$  and the reference gust velocity  $w_{ref}$  reduces linearly from 17.07 m/s Equivalent Air Speed (EAS) at sea level to 13.41 m/s EAS at 4572 m, and then again to 6.36 m/s EAS at 18288 m. Figure 2.5 shows gusts at different wavelengths at sea level for an airspeed of 200 m/s.

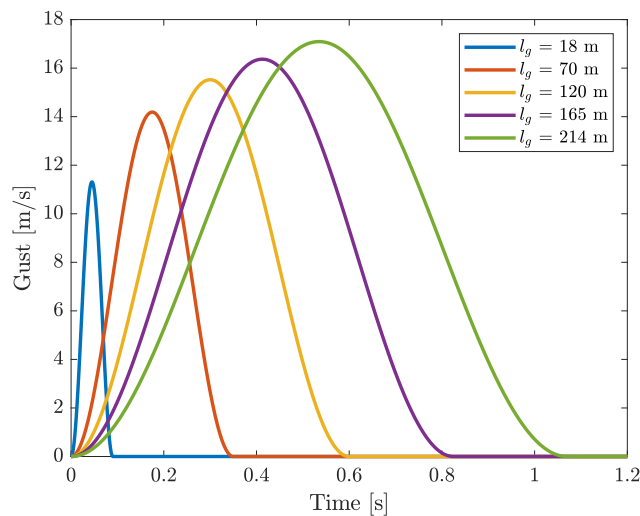


FIGURE 2.5: Gusts with different gust wavelengths

According, to the EASA regulations [26], the power spectral density of atmospheric turbulence is described by the von Karman spectra as

$$\Phi_v(\Omega) = \frac{L_T}{\pi} \frac{1 + \frac{8}{3}(1.339\Omega L_T)^2}{[1 + (1.339\Omega L_T)^2]^{11/6}} \quad (2.9)$$

where  $\Omega$  is the spatial frequency,  $L_T$  is the scale of turbulence (commonly assumed to be 2500 ft). According to Hoblit [25] the turbulence velocity time history is obtained as the output of a shape filter with the input given by a stationary Gaussian ‘white-noise’

time history. The transfer function that approximates the von Karman shape is

$$G(s) = \frac{\sigma_w}{\sqrt{\Phi_\eta}} \frac{\sqrt{\tau_T}}{\pi} \frac{(1 + 2.187\tau_T s)(1 + 0.1833\tau_T s)(1 + 0.021\tau_T s)}{(1 + 1.339\tau_T s)(1 + 1.118\tau_T s)(1 + 0.1277\tau_T s)(1 + 0.0146\tau_T s)} \quad (2.10)$$

where  $\Phi_\eta$  is the power spectral density of the white noise,  $\tau_T$  is the ratio between  $L_T$  and the horizontal velocity of the aircraft and  $\sigma_w$  is the component of the gust velocity. Figure 2.6 shows the Bode diagram of the approximation of the von Karman turbulence model. The atmospheric turbulence is obtained in the time-domain as the output of the state-space form of the transfer function Eq.(2.10) whose input is white noise.

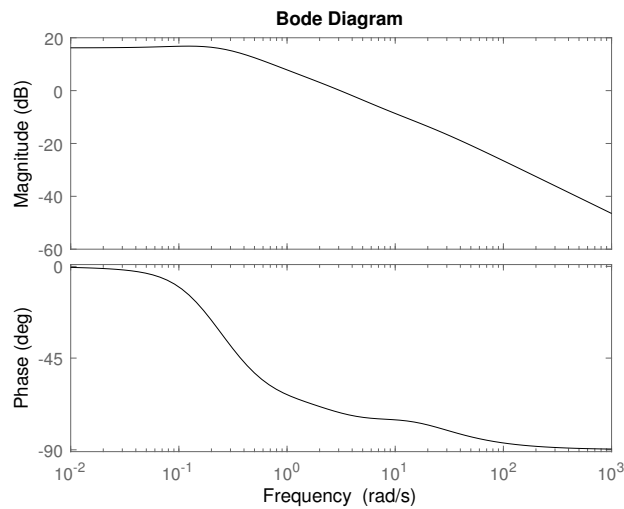


FIGURE 2.6: Bode diagram of the von Karman approximation of atmospheric turbulence

---

## 2.2 Simplified Aeroelastic Models

---

In this section a simplified aeroelastic model of the aircraft with a straight wing is presented (model one) and subsequently the wingtip is introduced (model two). Figure 2.7 shows model one and Figure 2.8 shows model two.

The structural and aerodynamic models were selected to obtain a model with the least number of degrees of freedom without losing the main effects. The only deformable parts of the model are the wing, in bending and in torsion, and the wingtip. These two elastic modes were considered because, typically, they are the modes at lower frequencies which are excited by the gusts [20]. Additional degrees of freedom could have secondary effects in the study of the gust load alleviation. The aerodynamic model is based on

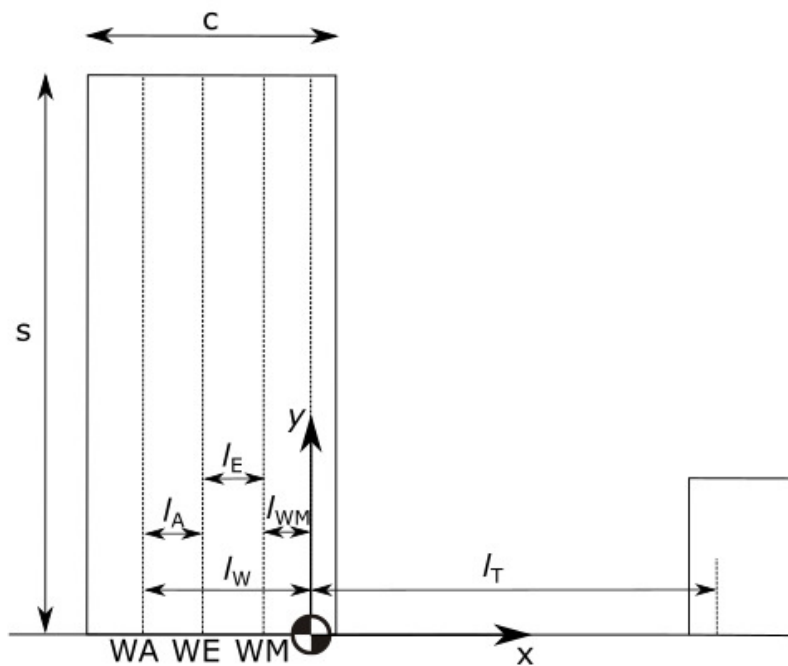


FIGURE 2.7: Model one - aircraft with a straight wing

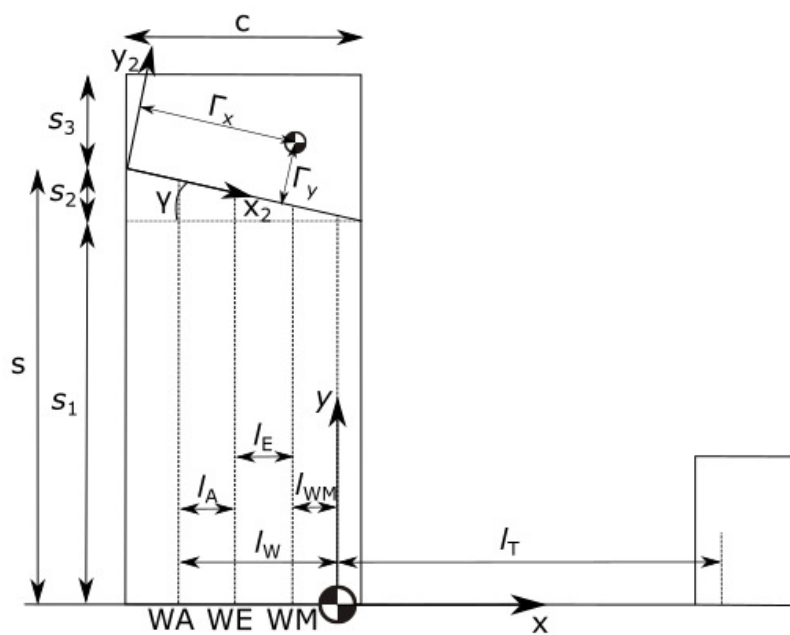


FIGURE 2.8: Model two - aircraft with a straight wing and folding wingtip

strip theory. Although the panel method could provide more accurate results it would lead to further aerodynamic degrees of freedom [105]. In the two aeroelastic models, the following degrees of freedom are considered: displacement  $z_c$  (downwards) and pitch  $\alpha$  (nose up) at the centre of mass on the inertial axis and the torsional  $q_t$  (nose up) and the bending  $q_b$  (downwards) modes of the wing on the elastic axis of the wing [20]. The wingtip's span is assumed to be 20% of the half span and there is a relative angle ( $\gamma$ ) between the hinge axis and the free stream velocity. The two aeroelastic models of the symmetric aircraft were obtained through the Lagrange formulation.

### 2.2.1 Structural and Aerodynamic model of an Aircraft With a Straight Wing (Model One)

The simplified flexible aircraft consists of a uniform, untapered, unswept flexible wing of chord  $c$  and semi-span  $s$ , plus a rigid fuselage and tailplane, as shown in Figure 2.7. The wing is assumed to have a uniform mass distribution and the wing mass axis (WM) lies at distance  $l_{WM}$  ahead of the aircraft centre of mass.

The mass and pitch moment of inertia of the aircraft fuselage is represented by discretization into three 'lumps' of mass  $m_F$ ,  $m_C$  and  $m_T$ . These discrete masses are located, respectively, at the front fuselage (at a distance of  $l_F$  forward of the CM), at the whole aircraft CM and at the tailplane aerodynamic centre (at a distance of  $l_T$  aft of the CM). The wing elastic axis (WE) is assumed to lie at a distance of  $l_E$  ahead of the WM axis. The wing aerodynamic axis (WA) is at the wing quarter chord and is at a distance of  $l_W$  ahead of the centre of mass and at a distance of  $l_A$  ahead of the elastic axis. In order to minimize any coupling between the rigid body modes and the flexible mode equations, the mean axis reference frame was used [20]. The wing is modelled using Euler–Bernoulli beam theory, so a quadratic shape function is used for the bending mode and a linear shape function for the torsion mode.

The displacement  $z_{WA}(y, t)$  (downwards positive) of the wing aerodynamic axis is

$$\begin{aligned} z_{WA}(y, t) = & z_c(t) - l_W \alpha(t) + \left[ k_{e0} \left( 1 + A \left( \frac{y}{s} \right)^2 \right) - l_A \gamma_{e0} \right] q_b(t) \\ & + \left[ k_{e0} - l_A \gamma_{e0} \left( 1 + B \left( \frac{y}{s} \right) \right) \right] q_t(t) \end{aligned} \quad (2.11)$$

where  $A$  and  $B$  are constants defining the amount of bending and twist present along the wingspan and  $k_{e0}$  and  $\gamma_{e0}$  are constants defining the wing root displacement and twist deformation. The displacement  $z_T(t)$  (downwards positive) of the tailplane aerodynamic

centre is

$$z_T(t) = z_c(t) + l_T\alpha(t) \quad (2.12)$$

The aerodynamic terms due to the wing and the tailplane have to be determined. To this end, the tailplane is considered as rigid, while the wing contribution involves integration using a strip  $dy$  because of the flexibility. The lift of a strip  $dy$  at the position  $y$  along the wingspan is

$$dL = \frac{1}{2}\rho V^2 c dy a_w \left[ \alpha - \alpha_0 + \gamma_{e0} \left( 1 + B \left( \frac{y}{s} \right) \right) q_t + k_{e0} \left( 1 + A \left( \frac{y}{s} \right)^2 \right) \frac{\dot{q}_b}{V} + \frac{\dot{z}_c}{V} \right] \quad (2.13)$$

where  $\alpha_0$  is the incidence for zero wing lift and  $a_w$  is the sectional wing lift curve slope. There is also a zero lift pitching moment for the wing

$$M_{0W} = \frac{1}{2}\rho V^2 S_W c C_{M_{0W}} \quad (2.14)$$

The tailplane lift considering the contribution of the downwash  $k_\epsilon$ , the effective incidence due to the nose up pitch rate and the increment of lift due to a rigid vertical displacement, is

$$L_T = \frac{1}{2}\rho V^2 S_T \left\{ a_T \left[ k_\epsilon \alpha_0 + (1 - k_\epsilon) \alpha + \frac{\dot{\alpha} l_T}{V} + \frac{\dot{z}_c}{V} \right] + a_E \eta \right\} \quad (2.15)$$

where  $a_E$  is the tailplane curve slope defined with respect to the elevator angle and  $\eta$  is the elevator angle and was included to provide trim.

The effect of the vertical gust on the aerodynamics is a change of angle of attack. Thus on the elastic wing, the increment of lift on a strip  $dy$ , located at distance  $y$  from the root, is given by

$$dL_{W_g} = \frac{1}{2}\rho V^2 c dy a_w \frac{w_g}{V} \quad (2.16)$$

while on the tailplane the gust will act with a delay given by the ratio between the distance between the wing aerodynamic centre and the tailplane aerodynamic centre and the free stream velocity ( $t^* = \frac{l_W + l_T}{V}$ ). Hence

$$L_{T_g} = \frac{1}{2}\rho V^2 S_T a_T \frac{w_g(t - t^*)}{V} \quad (2.17)$$

The kinetic energy due to the rigid motion and the dynamic motion is

$$T = \frac{1}{2}m\dot{z}_c^2 + \frac{1}{2}I_y\dot{\alpha}^2 + \frac{1}{2}m_b\dot{q}_b^2 + \frac{1}{2}m_t\dot{q}_t^2 \quad (2.18)$$

where  $m$  is the total mass of the aircraft,  $I_y$  is the aircraft pitching moment at the centre of mass, and  $m_b$  and  $m_t$  are respectively the bending and torsional modal masses. The

elastic potential energy corresponds to the strain energy in bending and torsion, such that

$$U = \frac{1}{2}k_b q_b^2 + \frac{1}{2}k_t q_t^2 \quad (2.19)$$

Finally, the virtual work done by lift forces and moment and the gravitational field force is

$$\delta W_E = \int_0^s -dL\delta z_{WA} - L_T\delta z_T + \int_0^s -dL_{W_g}\delta z_{WA} - L_{T_g}\delta z_T + M_{0W}\delta\alpha + mg\delta z_c \quad (2.20)$$

Appendix A.1 shows all the steps required to obtain the aeroelastic equation exploiting the Lagrange formulation. The full aeroelastic equation in the classical second-order form is obtained as

$$\mathbf{A} \begin{Bmatrix} \ddot{q}_b \\ \ddot{q}_t \\ \ddot{\alpha} \\ \ddot{z}_c \end{Bmatrix} + \left( \rho V \mathbf{B} + \mathbf{D} \right) \begin{Bmatrix} \dot{q}_b \\ \dot{q}_t \\ \dot{\alpha} \\ \dot{z}_c \end{Bmatrix} + \left( \rho V^2 \mathbf{C} + \mathbf{E} \right) \begin{Bmatrix} q_b \\ q_t \\ \alpha \\ z_c \end{Bmatrix} = \mathbf{f}_\eta \eta + \mathbf{f}_0 + \mathbf{f}_g + \mathbf{f}_{W_g} w_g \quad (2.21)$$

$$+ \mathbf{f}_{T_g} w_g(t - t^*)$$

where  $\mathbf{A}$ ,  $\mathbf{D}$  and  $\mathbf{E}$  are the structural inertia, damping and stiffness matrices,  $\mathbf{B}$  and  $\mathbf{C}$  are the aerodynamic damping and stiffness matrices and the force vector  $\mathbf{f}$  on the right hand side of the equation has contributions due to the elevator ( $\mathbf{f}_\eta$ ), zero incidence ( $\mathbf{f}_0$ ), gravitational field ( $\mathbf{f}_g$ ), gust on the wing ( $\mathbf{f}_{W_g}$ ) and gust on the tailplane ( $\mathbf{f}_{T_g}$ ). The validation of this model is not reported because Model Two was obtained by Model One, and in Section 2.3, the validation of Model Two is performed.

## 2.2.2 Structural and Aerodynamic Model of an Aircraft With a Straight Wing and Folding Wingtip (Model Two)

As mentioned above the difference between the two models is the presence of the movable wingtip. The model of the aircraft with the folding wingtip can be obtained from the equations of model one considering the additional contributions from the wingtip and taking into account that the elastic wing is composed of two contributions from wingspan  $s_1$  and wingspan  $s_2$ , as shown in Figure 2.8. It is worth noting that in the region of  $s_2$  the chord is not constant, but is a function of the flare angle  $\gamma$ , of the elastic wingspan  $s$  and of the span position  $y$ . The geometric relation is

$$c(y) = \frac{s - y}{\tan(\gamma)} \quad (2.22)$$

The wingtip is considered as a rigid body of mass  $m_{wt}$  with the centre of mass at  $\mathbf{\Gamma} = (\Gamma_x, \Gamma_y)$  defined in a reference coordinate system with the origin at the leading edge of the elastic wing tip and with the  $x$ -axis parallel to the hinge axis, as shown in Figure 2.8.  $\theta$  is the degree of freedom related to the wingtip rotation and it is defined such that a positive angle variation produces a downwards displacement.

Considering small rotation of the wingtip and assuming the aerodynamic centre of the wingtip is at the quarter chord and halfway along its span its vertical displacement is

$$z_{AC_{wt}} = \left[ k_{e0} (1 + A) - l_A \gamma_{e0} \right] q_b + \left[ k_{e0} - l_A \gamma_{e0} (1 + B) \right] q_t + z_c - l_w \alpha + \frac{s_3}{2} \theta \quad (2.23)$$

The wingtip centre of mass is at position  $\mathbf{\Gamma} = (\Gamma_x, \Gamma_y)$  measured with respect to coordinate system  $x_2, y_2$  in model two (see Figure 2.8). The origin of this reference system is where the wing leading edge and the hinge axis meet. Hence, the  $x_2$  axis in this local coordinate is parallel to the hinge axis as shown in Figure 2.8. The vertical displacement of the wingtip centre of mass is

$$z_{\Gamma} = k_{e0} (1 + A) q_b - \left( x_f - \frac{\Gamma_x}{\cos(\gamma)} \right) \gamma_{e0} (1 + B) q_t - \left( l_W + \frac{c}{4} - \frac{\Gamma_x}{\cos(\gamma)} \right) \alpha + z_c + \Gamma_y \theta \quad (2.24)$$

where  $x_f$  is the longitudinal position of the elastic axis measured from the wing leading edge. The wingtip lift is given by

$$L_{wt} = \frac{1}{2} \rho V^2 S_{wt} a_w \left[ k_{e0} (1 + A) \frac{\dot{q}_b}{V} + \gamma_{e0} (1 + B) q_t + \alpha - \alpha_0 + \frac{\dot{z}_c}{V} + \theta \sin(\gamma) + \frac{S_3}{2} \frac{\dot{\theta}}{V} + \frac{w_g}{V} \right] \quad (2.25)$$

where the contribution  $\theta \sin(\gamma)$  is the component of the rotation around the hinge perpendicular to the free air-stream.

The kinetic energy due to the rigid and dynamic motion of the wingtip is

$$T_{wt} = \frac{1}{2} m_{wt} \dot{z}_{\Gamma}^2 \quad (2.26)$$

which give a negligible contribution to the total inertia. The potential energy corresponding to the strain energy of the spring at the hinge between the elastic wing and



the wingtip is

$$U_{wt} = \frac{1}{2}k_\theta\theta^2 \quad (2.27)$$

The total work done by the external force of the wingtip is

$$\delta W_{wt} = -L_{wt}\delta z_{AC_{wt}} + m_{wt}g\delta z_\Gamma \quad (2.28)$$

Appendix A.2 shows the additional contributions due to the hinged wingtip required to obtain the aeroelastic equation exploiting the Lagrange formulation. The full aeroelastic equation in the classical second-order form is obtained as

$$\mathbf{A} \begin{Bmatrix} \ddot{q}_b \\ \ddot{q}_t \\ \ddot{\alpha} \\ \ddot{z}_c \\ \ddot{\theta} \end{Bmatrix} + \left( \rho V \mathbf{B} + \mathbf{D} \right) \begin{Bmatrix} \dot{q}_b \\ \dot{q}_t \\ \dot{\alpha} \\ \dot{z}_c \\ \dot{\theta} \end{Bmatrix} + \left( \rho V^2 \mathbf{C} + \mathbf{E} \right) \begin{Bmatrix} q_b \\ q_t \\ \alpha \\ z_c \\ \theta \end{Bmatrix} = \mathbf{f}_\eta \eta + \mathbf{f}_0 + \mathbf{f}_g + \mathbf{f}_{W_g} w_g \quad (2.29)$$

$$+ \mathbf{f}_{T_g} w_g(t - t^*)$$

In contrast to the previous case, Eq.(2.21), an extra degree of freedom related to the wingtip rotation was introduced.

In the following analysis, Eqs. (2.21) and (2.29) were solved using a 5<sup>th</sup> order Runge-Kutta method with a 4<sup>th</sup> order time step selection [107].

---

## 2.3 Validation

---

To analyse the models, a numerical example found in the literature for the gust analysis of a flexible aircraft is considered [20]. The airplane and wingtip main parameters are reported in Tables 2.1 and 2.2. All the analysis considers an equivalent airspeed of 150 m/s. The coefficients  $A$ ,  $B$ ,  $\gamma_{e0}$ ,  $k_{e0}$ , the bending and the torsion modal masses were obtained through a minimization process exploiting the orthogonality condition between the elastic modes and the rigid modes (for the detail see Appendix C of Wright and Cooper [20]). The bending and torsional modal stiffnesses are determined to obtain the respective modal frequencies [20]. Due to the linearity of the model, the analysis did not consider the static contribution due to the initial trim in order to analyse only the dynamic response to the gust. For the model validation, discrete gusts are considered,

with a maximum gust velocity of 5 m/s and a gust wavelength in the range of 20 to 200 m.

Half span	7.5 m	Chord	2 m	$a_W$	4.5 –
Total mass	5000 kg	$l_W$	0.6 m	$a_T$	3.2 –
$m_F$	750 kg	$l_T$	7 m	$a_E$	1.5 –
$m_T$	750 kg	$l_A$	0.25 m	$k_\epsilon$	0.35 –
$m_W$	1500 kg	$l_E$	0.25 m	$\alpha_0$	-0.03 rad
Wing inertia	1330 kg m <sup>2</sup>	$l_{WM}$	0.1 m	$C_{M_{0W}}$	-0.03 –
Aircraft inertia	72000 kg m <sup>2</sup>	$l_F$	6.8 m		

TABLE 2.1: Aircraft parameters

Mass	150 kg
Span	1.5 m
$\gamma$	20°
$\Gamma_x$	0.94 m
$\Gamma_y$	0.70 m

TABLE 2.2: Wingtip parameters

### 2.3.1 Comparison of Different Models

To validate the developed numerical model, the gust response of an elastic aircraft is obtained and compared with those reported by Wright et al. [20] for the gust response of an elastic aircraft (reference model). The reference model has three degrees of freedoms, the vertical displacement and the pitch angle of the aircraft centre of gravity and the torsional mode of the wing. To enable a proper comparison, the natural frequencies of the elastic modes not considered in the reference model were set to a high value and the torsional frequency is the same as the reference model. Therefore in both models, the torsional mode frequency is set at 8.5 Hz, the bending mode at 56 Hz and the flapping mode at 61 Hz in model two.

The gust response in terms of vertical displacement of the trailing edge of the tip of the wing ( $z_{TE}$ ), angle of incidence ( $\alpha$ ) and vertical displacement of the center of gravity ( $z_c$ ) are simulated for gusts with different wavelengths. Figures 2.9 and 2.10 compare the results of model one and model two, respectively, with the reference model (black dashed lines). The results show that the models give similar results.

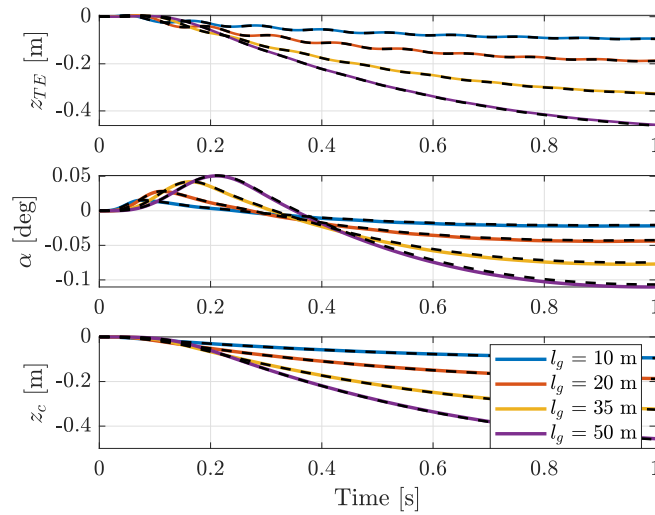


FIGURE 2.9: Comparison between model one (continuous line) and the reference model [20] (dashed lines)

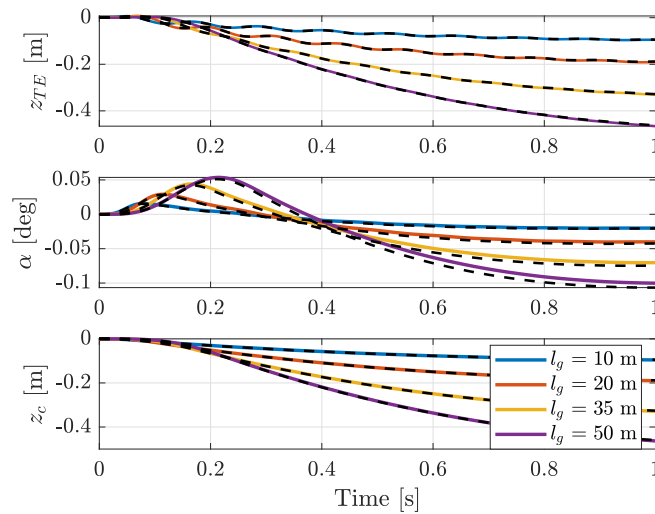


FIGURE 2.10: Comparison between model two with rigid connections (high stiffness) (continuous line) and the reference model [20] (dashed lines)

### 2.3.2 Model Two Gust Response

This section presents the dynamic response of model two for different gust lengths and for various wingtip parameters. The modal stiffness was set in order to obtain the frequency of the bending mode at 5 Hz and the frequency of the torsional mode at 8.5 Hz when a high value of the wingtip stiffness connection is considered.

Figures 2.11, 2.12, 2.13 and 2.14 show the gust responses for low and high values of the stiffness connections between the wing and the wingtip. These two extreme cases represent the cases when the wingtip is free to rotate at the hinge ( $k_\theta = 0$  Nm/rad) and

the wingtip is rigidly attached to the wing ( $k_\theta = 10^8$  Nm/rad). When the wingtip is free to rotate at the hinge, the heave mode is less excited and the pitch mode is more excited with respect to the case when the wingtip is rigidly attached to the wing. It is also possible to see that the zero stiffness connection reduces the torsional and bending mode responses.

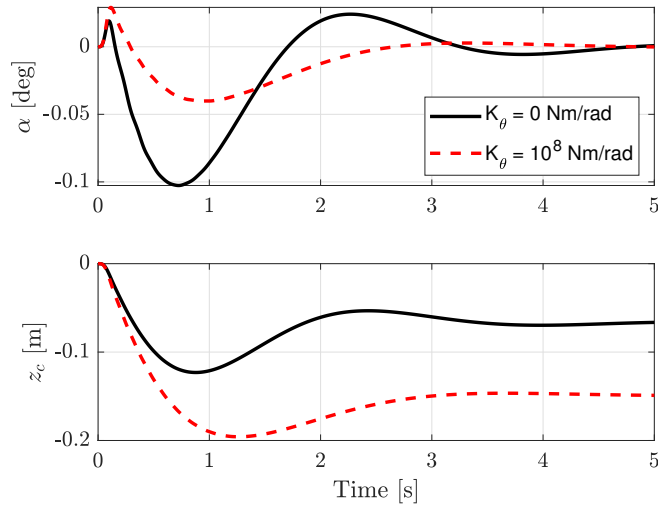


FIGURE 2.11: Rigid body responses to a 20 m 1-cos gust

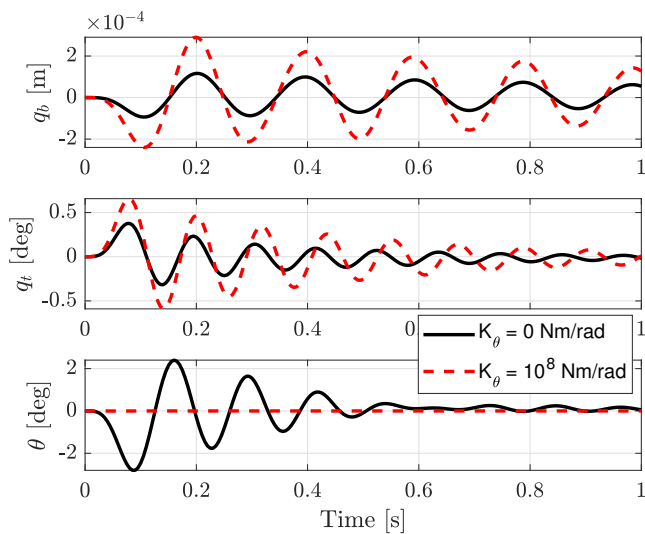


FIGURE 2.12: Elastic mode responses to a 20 m 1-cos gust

Figures 2.15, 2.16 and 2.17 show the maximum and minimum values of the wing bending and torsional modes responses for values of the gust length between 20 m to 200 m. Figure 2.15 considers different cases of the wingtip stiffness connection, Figure 2.16 considers different cases of the flare angle ( $\gamma$ ) and Figure 2.17 considers different positions, along the chordwise direction, of the wingtip centre of mass ( $\Gamma_x$ ).

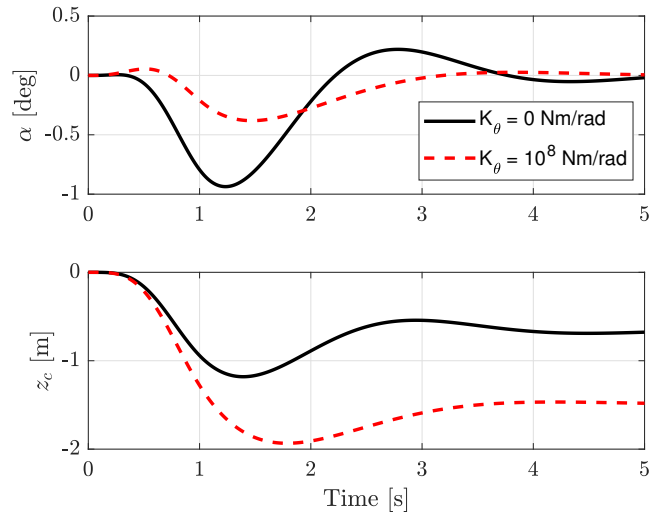


FIGURE 2.13: Rigid body responses to a 200 m 1-cos gust

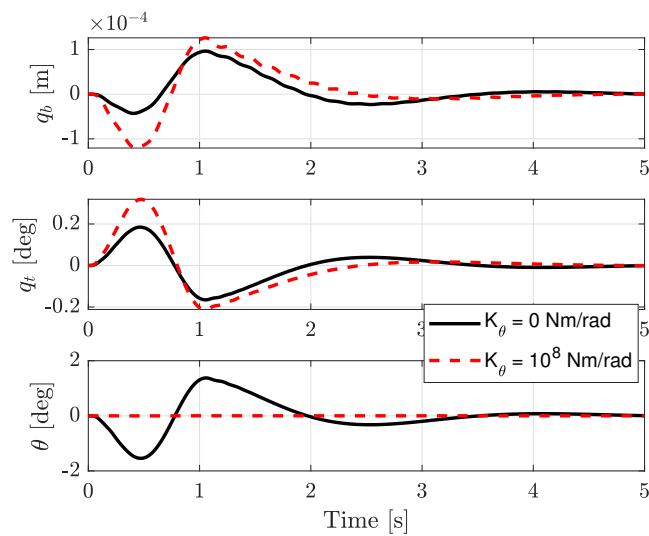


FIGURE 2.14: Elastic mode responses to a 200 m 1-cos gust

The hinge with zero torsional stiffness and the introduction of a larger flare angle are able to reduce the wing bending and the wing torsional mode response for all gust lengths. Furthermore for gusts at high frequency, if the centre of mass position is towards the trailing edge of the wingtip the torsional mode has larger positive and negative peaks, but for gusts at low frequency the torsional mode response has smaller peaks.

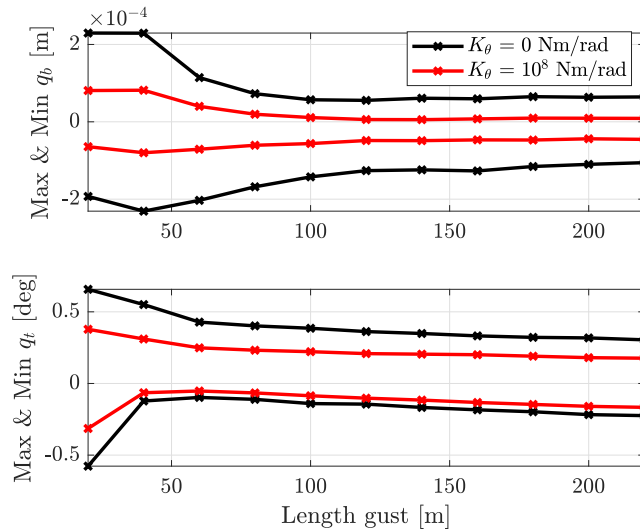
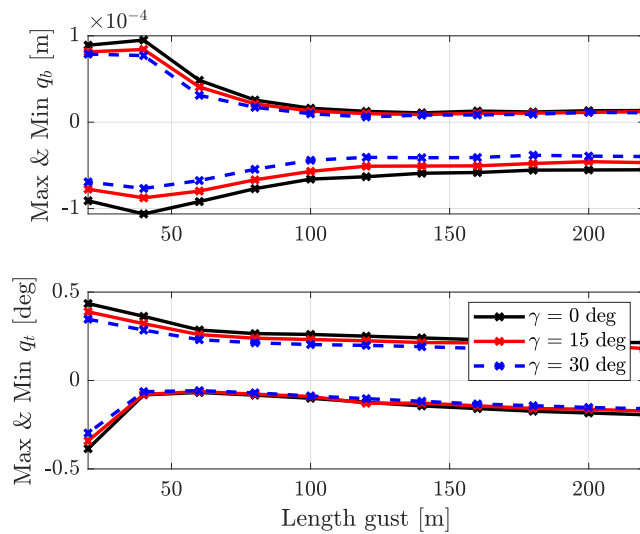


FIGURE 2.15: Gust response for different gust lengths and values of stiffness connection

FIGURE 2.16: Gust response for different gust lengths and flare angle ( $k_\theta = 0 \text{ Nm/rad}$ )

---

## 2.4 Detailed Aeroelastic Model

---

This section provides an overview of the detailed aeroelastic model representative of an aircraft with hinged wingtips. This model was developed in Nastran and used in previous works [43–45, 48, 53, 55, 108]. The main objective was to investigate the effect of hinged wingtips for load alleviation. The model is a modified version of the FFAST (Future Fast Aeroelastic Simulation Technologies) aeroelastic model of a representative civil jet aircraft [109]. The structure was modelled using a ‘stick’ model, by using ‘CBAR’

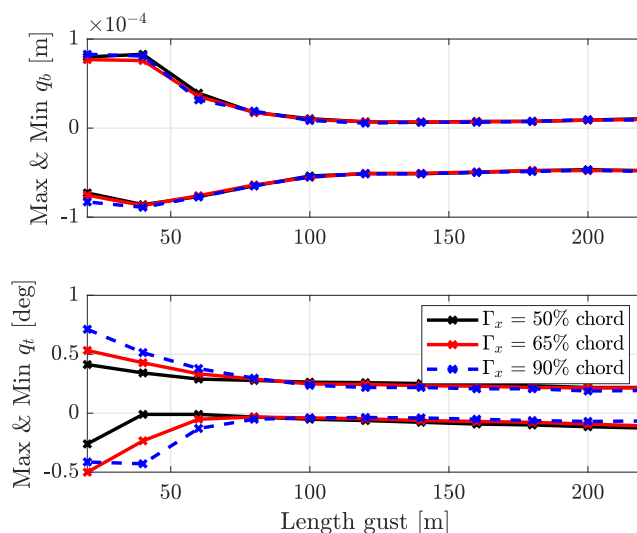


FIGURE 2.17: Gust response for different gust lengths and positions of the wigtip centre of mass ( $k_\theta = 0 \text{ Nm/rad}$ )

Span [m]	57.88
Length [m]	63.91
Weight [kg]	$187929 \cdot 10^5$

TABLE 2.3: Model characteristics

and ‘RBE2’ elements and non-structural distributed masses (defined through material density) by using ‘CONM2’ elements. The model also includes engine pylons and masses. Each half-span wing has at 80% span a hinge connected to the wingtips giving an increase in span of 25% compared to the baseline. The hinge flare angle is  $25^\circ$ . The hinge was modelled by constraining two coincident nodes, one on the main wing and one on the wingtip, to have the same displacement and rotation except for the rotation on the predefined hinge axis by using the ‘RJOIN’ element. Hinge torsional stiffness and damping are modelled using the ‘CBUSH’ element. In the case of the hinge free to rotate, a small torsional stiffness value is required to avoid numerical singularities [110]. Table 2.3 reports the weight and the dimensions.

The Doublet Lattice Method is used for the aerodynamic model [111]. Due to the small angle of attack or side slip assumption, the aerodynamic forces do not change their direction as a function of the actual deformation of the structure and wingtip deflection. The aerodynamic forces are defined with respect to the local normal direction of each panel by modifying the modulus, but not the orientation, of each aerodynamic force as a function of the local deformation. This is one drawback of the aerodynamic model used and has a significant effect when there are high deformations, such as high wingtip rotation. However, the results showed that the wingtip deflections are in general quite

limited [44, 45]. Figure 2.18 shows the aeroelastic model used for the analyses. The model

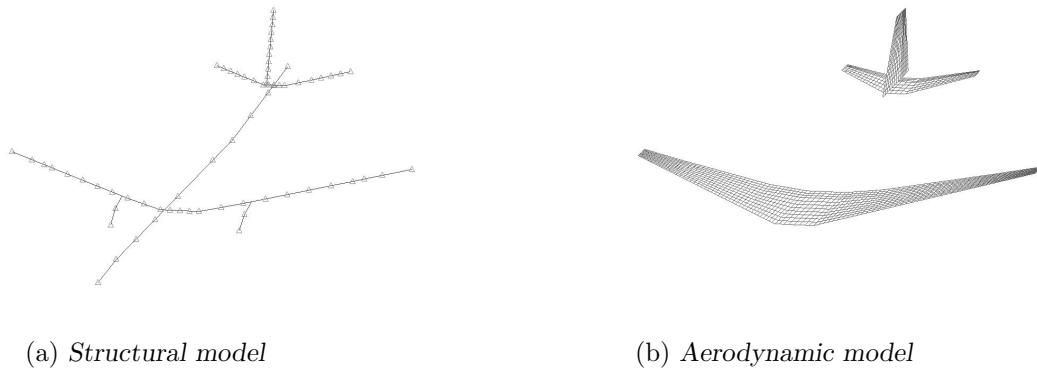


FIGURE 2.18: *Modified FFAST aeroelastic model*

is composed of a few thousand elements but exploiting modal reduction and considering only the modes with a frequency below 40 Hz it is possible to reduce the order of the model to 55 modes.

All the rigid body motions are constrained except for the aircraft heave and pitch. Table 2.4 shows the natural frequencies, damping ratios and mode shapes below 10 Hz of the aeroelastic model at 200 m/s and sea level. Figure 2.19 shows the mode shapes described in Table 2.4.

---

## 2.5 Conclusions

---

Two simplified aeroelastic models representing a symmetric aircraft were developed and a detailed model was introduced. The first simplified model consists of two rigid body modes and the torsional and bending modes of a straight wing. The second simplified model was developed by including an additional degree of freedom due to wingtip rotation in the first model. The simplified model with a hinged wingtip was validated against an existing model's gust responses in the literature for the case in which the wingtip is rigidly connected to the wing (high rotational stiffness value), and the results show good agreement. The gust response analysis considering different stiffness connections of the folding wing shown that if the wingtip is free to rotate at the hinge it is possible to reduce the bending and torsional deflection and consequently reduce the moment transmitted from the wing to the fuselage.



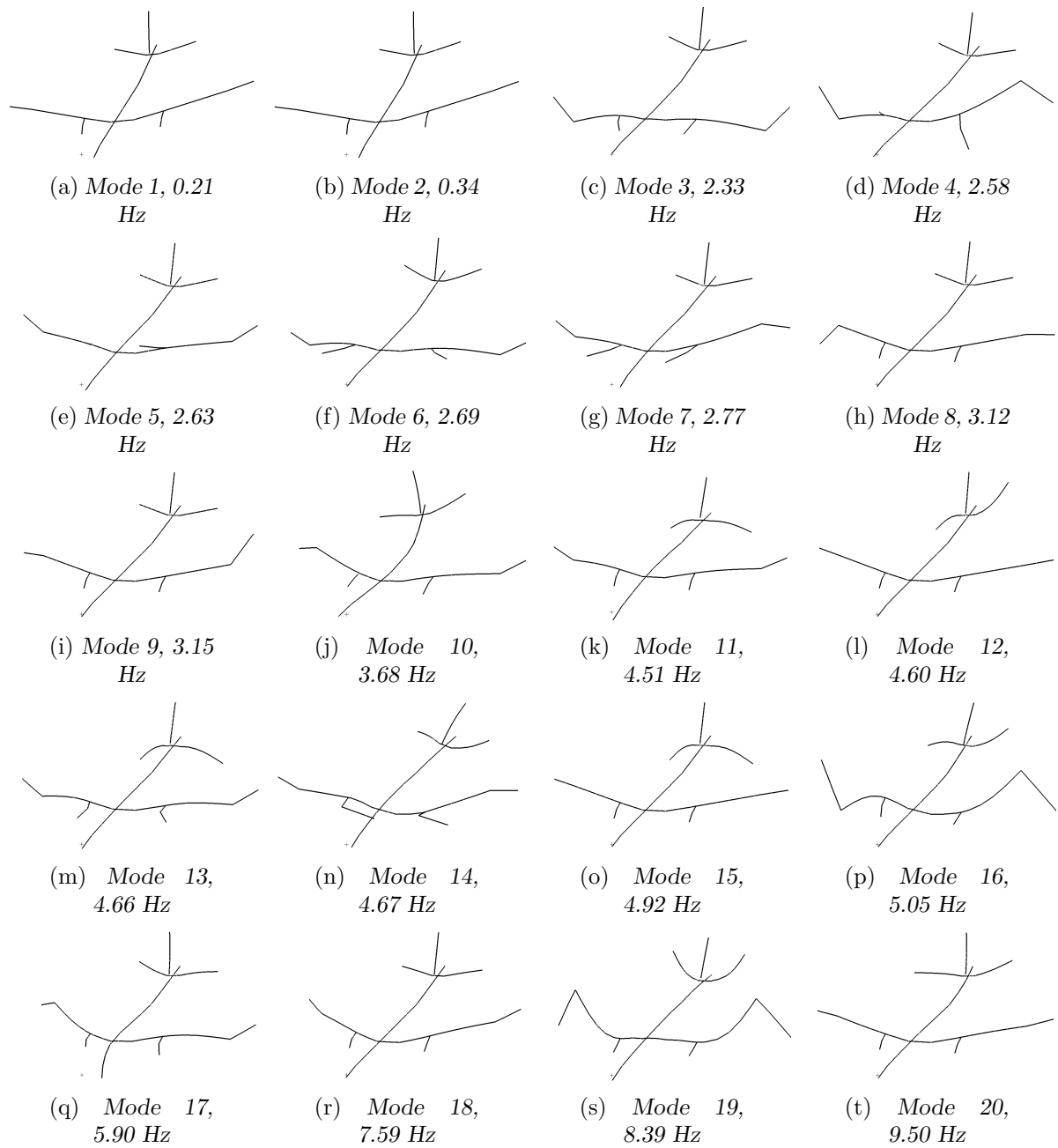


FIGURE 2.19: Lower frequency aeroelastic modes of the FFAST model at 200 m/s and sea level

Mode	Frequency [Hz]	Damping ratio [%]	Mode shape
1	0.21	15	Rigid body mode
2	0.34	56	Rigid body mode
3	2.33	8	Sym. 1 <sup>st</sup> wing bending & wingtip
4	2.58	2	Anti-sym. 1 <sup>st</sup> wing bending
5	2.63	0.3	Anti-sym. 1 <sup>st</sup> wing torsion
6	2.69	2	Anti-sym. torsional and wing bending and fuselage
7	2.77	0.5	Anti-sym. wing bending and wingtip and wing torsion
8	3.12	81	Sym. wingtip
9	3.15	81	Anti-sym. wingtip
10	3.68	3	Fuselage bending
11	4.51	6	Sym. tailplane bending
12	4.60	26	Anti-sym. tailplane bending
13	4.66	0.2	Sym. wing bending and tailplane bending
14	4.67	0.04	Fuselage bending, wing bending and tailplane bending
15	4.92	20	Sym. tailplane bending
16	5.05	5	Anti-sym. 2 <sup>nd</sup> wing bending, tailplane bending and wingtip
17	5.90	0.2	Fuselage bending, wing bending and tailplane bending
18	7.59	0.04	Sym. 1 <sup>st</sup> wing in-plane bending
19	8.39	3	Sym. 2 <sup>nd</sup> wing bending, tailplane bending and wingtip
20	9.50	1	Anti-sym. tailplane in-plane bending

TABLE 2.4: Natural frequencies and damping ratios of the FFAST aeroelastic model below 10 Hz at 200 m/s and sea level

# Chapter 3

## MULTI-OBJECTIVE OPTIMISATION FOR THE WORST-CASE GUST PREDICTION

Unsteady loads represent an important aspect through the design of an aircraft and have an impact on the detailed structural design. They determine the extreme stress levels estimate fatigue damage and damage tolerance for a specific design. Dynamic gust loads are among the most extreme loads an aircraft is subjected to. In this Chapter, the simplified model introduced in Section 2.2, considering the dimensions and weight distribution of a civil, commercial aircraft, is firstly used for the problem of the worst-case gust prediction. Secondly, multi-objective optimizations are performed to find the wingtips parameters to reduce the gust loads. Different possible solutions to overcome the reduction in the flutter due to the hinged wingtip are considered.

### 3.1 Civil Commercial Aircraft Case

In this Chapter, the model introduced in Section 2.2 is applied considering dimensions and total weight similar to the one of the detailed model of Section 2.4. The weights distribution, the dimensions and the main parameters are reported in Tables 3.1 and 3.2. To have a more realistic model, the effect of engine mass is considered in this model. The engine is modelled as lumped mass  $m_M$  located at the longitudinal distance  $x_M$  from the elastic axis (positive aft) and  $y_M$  from the symmetric axis as reported in Table 3.3. The coefficients  $A$ ,  $B$ ,  $\gamma_{e0}$ ,  $k_{e0}$ , and the bending and the torsional modal masses were obtained through a modified minimization process in order to consider the effects of the engine (see Appendix A.3). The bending and torsional modal stiffnesses are determined so as to obtain a bending modal frequency of 2.5 Hz and a torsion modal frequency of 4.5 Hz.

Half span	32.5 m	Chord	4 m	$a_W$	4.5
Total mass	187429 kg	$l_W$	0.8 m	$a_T$	3.2
$m_F$	28114 kg	$l_T$	30.9 m	$a_E$	1.5
$m_T$	28114 kg	$l_A$	0.32 m	$k_\epsilon$	0.35
$m_W$	56229 kg	$l_E$	0.32 m	$\alpha_0$	-0.03 rad
Wing inertia	12083 kg m <sup>2</sup>	$l_{WM}$	0.16 m	$C_{M_{0W}}$	-0.03
Aircraft inertia	12425757 kg m <sup>2</sup>	$l_F$	30.58 m		

TABLE 3.1: Civil commercial aircraft parameters

Mass	500 kg
Span	6.5 m
$\gamma$	30°
$\Gamma_x$	4.1 m
$\Gamma_y$	1.7 m

TABLE 3.2: Civil commercial aircraft wingtip parameters

Mass	1680 kg
x position from EA	0.0 m
y position from fuselage	9.344 m

TABLE 3.3: Civil commercial aircraft engine parameters

### 3.1.1 Quantities of Interest

The objective of a gust load alleviation system is the reduction of the stresses acting on the airframe. Since the most critical point for an aircraft is the connection between the wing and the fuselage, the wing root bending moment, the torsional moment and the shear force are taken as interesting quantities. The intensity of these forces and moments can be recovered from the aerodynamic, inertia and gravitational field force distribution acting on the wing and on the wingtip (see Appendix A.4).

### 3.1.2 Static Trim Solution

From the equation of motion of the full aircraft, Eq. (2.29), it is possible to calculate the static deformation of the aircraft. The degrees of freedom that have to be calculated are the bending and torsional modes of the wing, the deflection of the wingtip, the pitch of the complete aircraft and the deflection of the elevator. Although the vertical displacement of the centre of gravity of the aircraft is a degree of freedom of the system, its value is imposed a priori and will affect the air density. The deflection of the elevator was introduced as an unknown of the trim calculation in order to enforce the vertical balance of forces.

Figures 3.1 and 3.2 show the trim configuration for different values of the stiffness on the folding hinge in terms of pitch angle of the aircraft ( $\alpha$ ), elevator angle ( $\eta$ ), wingtip deflection ( $\theta$ ) and the interesting quantities at 200 m/s at sea level. For high values

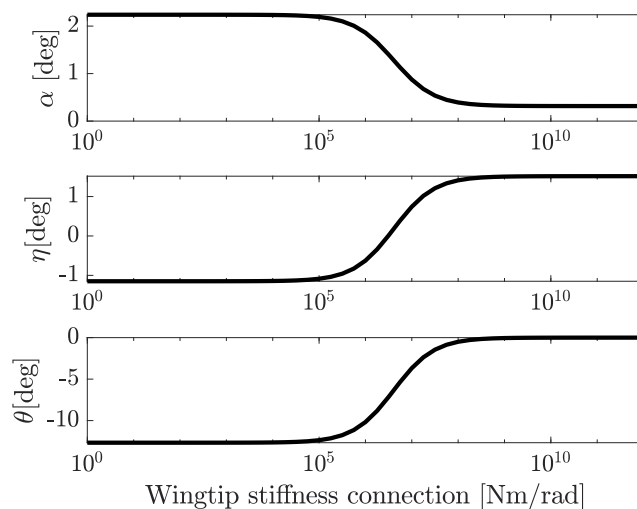


FIGURE 3.1: Trim angles for different values of wingtip stiffness connection: fuselage incidence ( $\alpha$ ), elevator angle ( $\eta$ ) and wingtip deflection ( $\theta$ )

of the stiffness connection, which represents the wingtip rigidly connected to the elastic

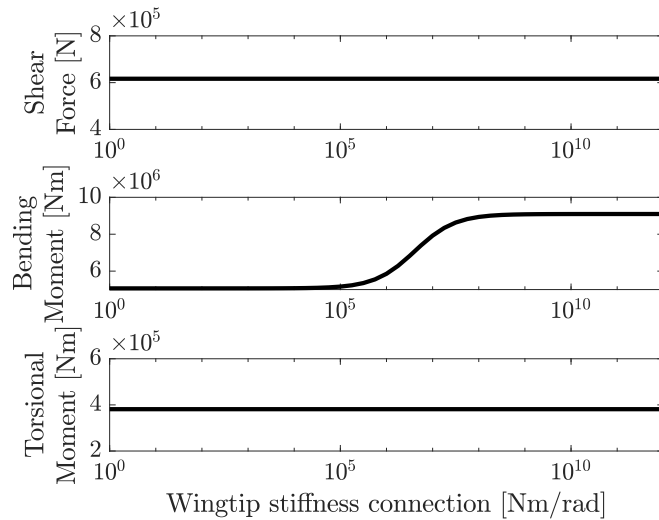


FIGURE 3.2: Quantities of interest in trim for different values of wingtip stiffness connection

wing, the wingtip is not rotating. For lower values of the stiffness connection, the wingtip rotates in the opposite direction to gravity and consequently produces a lower lift. The vertical equilibrium is respected through an increase of the pitch of the aircraft. For different trim configurations, the elevator deflection is imposed to keep the tailplane lift constant. In order to ensure that for different trim configurations the tailplane generates the same lift and the elevator deflection changes accordingly. The shear force is not varying for different values of the stiffness connection because the total lift generated by the wing and weight of the wing are constant. The distance of the aerodynamic centre from the elastic axis is constant therefore a different lift distribution has no effect on the torsional moment but it modifies the bending moment, indeed the increment of the stiffness connection produces a greater lift on the wingtip and therefore the bending moment increases.

---

## 3.2 Multi-Objective Optimization

---

Previous studies shown the importance of the flare angle and wingtip weight [43, 112]. In this work, several optimizations are performed to obtain the optimal position of the wingtip centre of mass (CM), the flare angle and the wingtip span. The MATLAB genetic algorithm (GA) Toolbox is used for optimization because of its reliability in finding global optimal solutions even in cases where the objective functions have several

local maxima and minima. In this work, parallel computing inside the GA is used to speed up the optimization process. It is worth noting that the genetic algorithms require lower and upper bounds on the design variables and they are stochastic search algorithms that can give different results on repeating the optimization [113].

In the optimization process different optimization functions, able to minimize all the interesting quantities, were considered. In this work, the optimization is performed in terms of wing root internal loads, but in the real case, the objective is the wing weight reduction which leads to the reduction in the fuel burn. To estimate the wing weight or the fuel burn a detailed model of a specific aircraft is required and the results of the optimizations will be model dependent. To overcome this problem, it was decided to perform multi-objective optimization [113, 114].

In the following sections, the results of four different multi-objective optimizations considering the whole flight envelope are reported, and in each case different parameters are considered. In all the multi-objective optimizations it was considered the hinge connection between the wing and wingtip without any spring. The objective of the optimization is to find the optimal position of the wingtip CM, flare angle and wingtip span (first section), the optimal position of the wingtip CM and flare angle (second section), the optimal position of the wingtip CM fixing the flare angle at  $30^\circ$  (third section) and the optimal position of the wingtip CM fixing the flare angle at  $20^\circ$  (fourth section). After the optimizations, different techniques to increase the flutter speed will be presented.

### 3.2.1 Optimization: Set-Up

In the following subsections, a number of optimizations are performed for the whole flight envelope and the entire gusts frequency range. A set of 104 flight configurations was defined, as shown in Figure 3.3. For each flight configuration, the response to 15 different gusts with gust lengths in the range of 18 m to 214 m was considered, making a total of 1560 different gust responses to be evaluated.

Before performing the optimizations, two extreme cases were analysed, the wingtip rigidly connected to the wing and the wingtip free to rotate at the hinge. In each analysis, the gust response in terms of shear force, bending moment and torsional moment time histories were calculated for all the 1560 cases, including the static loads. The shear force and bending moment were plotted against each other. In the case of the wingtip free to rotate, Figure 3.4 shows the shear force and bending moment time history plotted against each other and the obtained convex hull. Figure 3.5 shows the convex hull in the cases of the wingtip rigidly connected to the wing and the wingtip free to rotate in

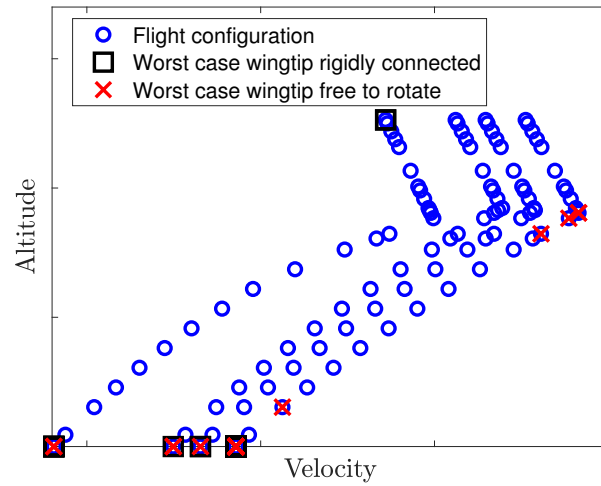


FIGURE 3.3: *Flight configurations considered, worst-cases wingtip rigidly connected to the wing and free to rotate*

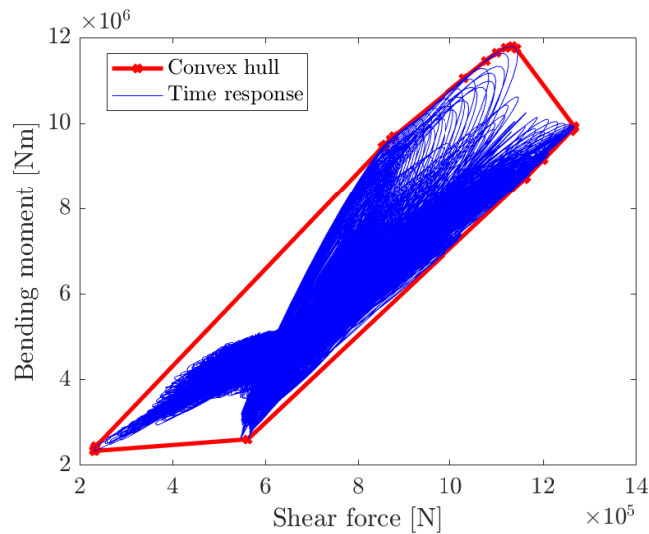


FIGURE 3.4: *Shear force and bending moment plotted against each other and the obtained convex hull*

the hinge. The same procedure was repeated, considering the shear force against the torsional moment and the bending moment against the torsional moment. Figures 3.6 and 3.7 show the results. Figure 3.3 shows the flight configurations associated with the point on the convex hulls for both extreme cases.

The case of null stiffness connection between the wing and the wingtip was considered as a reference configuration for the optimization processes. The flight configuration and the gust length related to each point in both the convex hulls of the reference configuration were considered as critical cases for the following analyses.



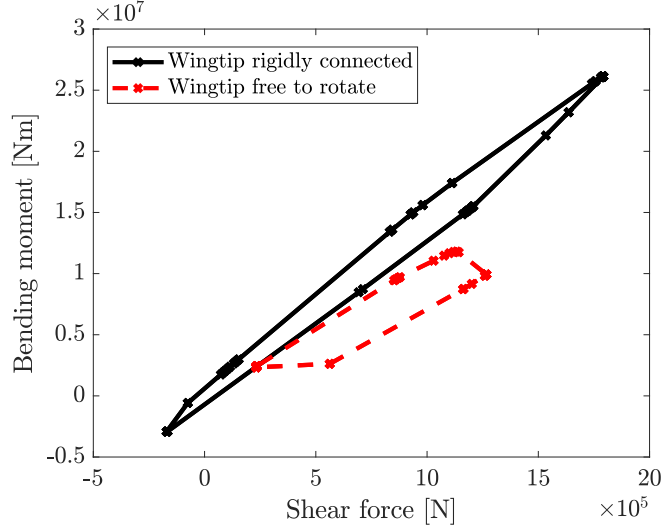


FIGURE 3.5: Comparison of the shear force-bending moment convex hull obtained with the wingtip rigidly connected to the wing and the wingtip free to rotate

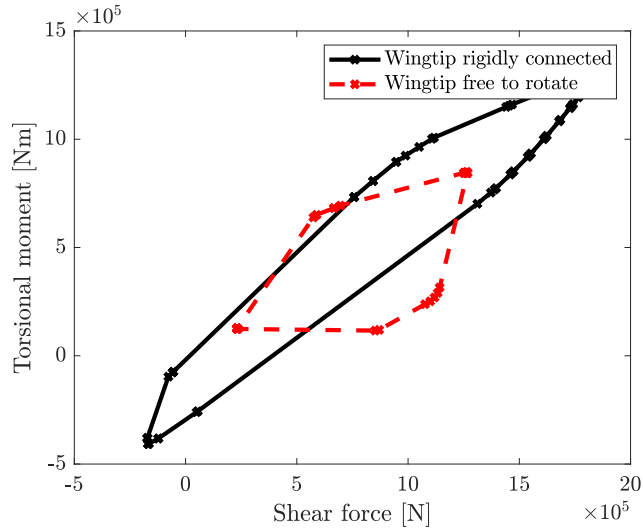


FIGURE 3.6: Comparison of the shear force-torsional moment convex hull obtained with the wingtip rigidly connected to the wing and the wingtip free to rotate

The following fitness functions were considered for the multi-objective optimization:

$$\begin{cases} \Pi_1 = \max(\max(\text{abs}(M_{wr_i}(t)))) \\ \Pi_2 = \max(\max(\text{abs}(T_{wr_i}(t)))) \\ \Pi_3 = \max(\max(\text{abs}(S_{wr_i}(t)))) \end{cases} \quad i = 1 : n_{crit} \quad (3.1)$$

where  $n_{crit}$  is the number of critical cases and  $M_i$ ,  $T_i$  and  $S_i$  are the bending moment, torsional moment and shear force time history response for the  $i^{th}$  critical case. For each configuration, every fitness function represents the maximum between all the absolute

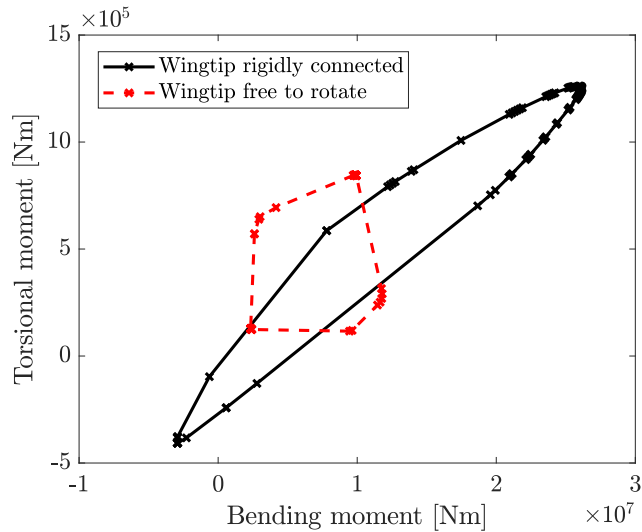


FIGURE 3.7: Comparison of the bending moment-torsional moment convex hull obtained with the wingtip rigidly connected to the wing and the wingtip free to rotate

maximum peaks of a specific quantity of interest. In the next sections, the results of multi objective optimization for different parametrization will be presented.

### 3.2.2 A. Optimal Parameters: Wingtip CM Position, Flare Angle and Wingtip Span

In this section, multi-objective optimization was performed considering the coordinates of wingtip CM position, the flare angle and the wingtip span as optimal parameters. The lower and upper bounds of the flare angle are  $0^\circ$  and  $45^\circ$ , the wingtip CM position is constrained to lie in any position inside the current wingtip and the wingtip span to be within the wing span.. In each iteration, the wingtip weight was calculated considering as unit span weight of 100 kg/m and the elastic wing weight is corrected to have the total wing weight constant. The model developed does not consider the aerodynamic stall, so, a constraint on the maximum angle of attack was introduced. The upper bound of fuselage angle of attack is considered as  $7^\circ$  and it ensures that the optimizer does not converge on high value of wingtip span that needs high angle of attack to ensure equilibrium. Figure 3.8 shows the results. Figure 3.8a shows the fitness function values corresponding to the Pareto points and the fitness function values related to the minimum bending moment, torsional moment and shear force. Moreover, the fitness function points were interpolated by a surface, and by rotating the figure it is possible to obtain a better view of its structure, as shown in Figures 3.8b, 3.8c and 3.8d. The results shows a wide range of variation for all the interesting quantities.

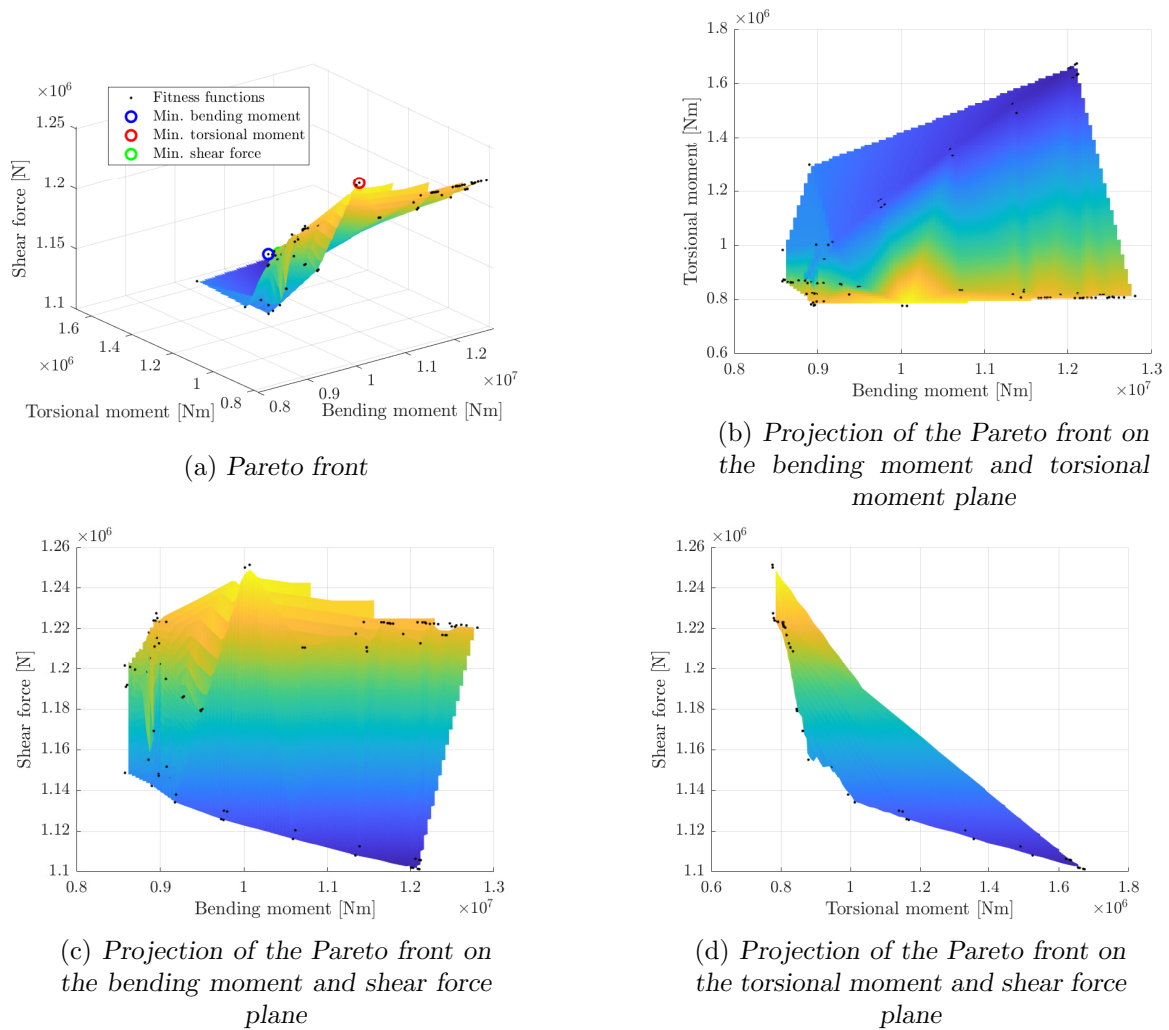


FIGURE 3.8: Multi-objective optimization results, optimization parameters: wingtip CM position, flare angle and wingtip span

Figure 3.9 shows the fitness function points of Figure 3.8b. In Figure 3.9, four fitness function values were considered and the corresponding parameters are reported in Table 3.4.

	Flare angle	Spanwise CM position	Chordwise CM position	Wingtip span
A	44.2°	1.19 m	0.18 m	5.95 m
B	44.2°	1.22 m	0.55 m	6.02 m
C	44.2°	1.98 m	1.49 m	5.95 m
D	44.2°	3.38 m	3.07 m	6.42 m

TABLE 3.4: Parameters of the selected points on the Pareto front

In the configuration selected the flare angle is always 44.2°, the spanwise position of the CM is between 1.19 m and 3.38 m (corresponding to the 20% and 53% of the total

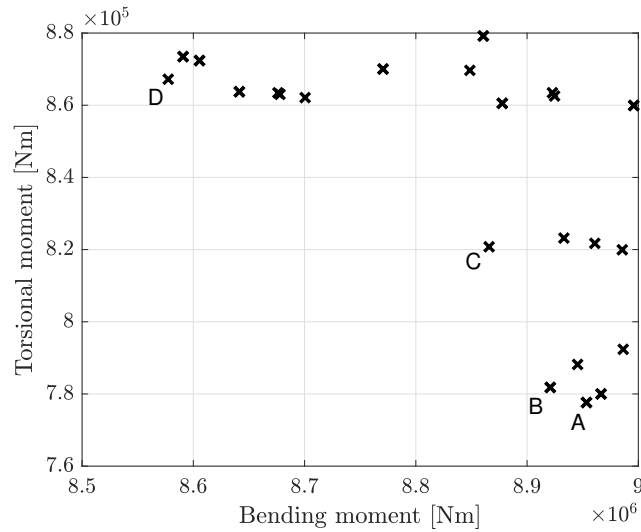


FIGURE 3.9: Pareto front on the bending moment and torsional moment plane at the optimal compromise

wingtip span) and the chordwise position of the CM is between 0.18 m and 3.38 m (corresponding to the 5% and the 85% of the chord) and the wingtip span is between 5.95 m and 6.42 m (corresponding to the 18% and the 20% of the total wingspan). Figures 3.10 and 3.11 show the convex hull in the case of wingtip rigidly connected and the optimized configurations tested on the whole flight envelope. As in the previous cases, the configurations selected can reduce all the quantities of interest with respect to the case of wingtip rigidly connected to the wing. The maximum peak of the bending moment is reduced by 62%-63%, the maximum peak of the torsional moment is reduced by 31%-38% and the maximum peak of the shear force is reduced by 31%-33%.

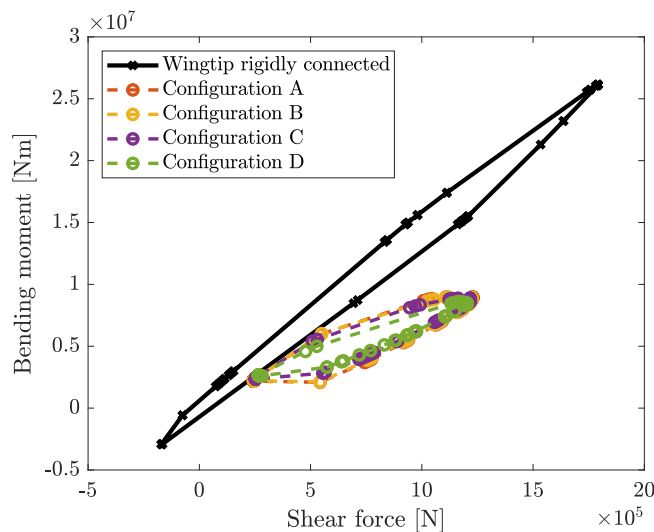


FIGURE 3.10: Shear force-bending moment convex hull for the rigid connection and for optimized configurations

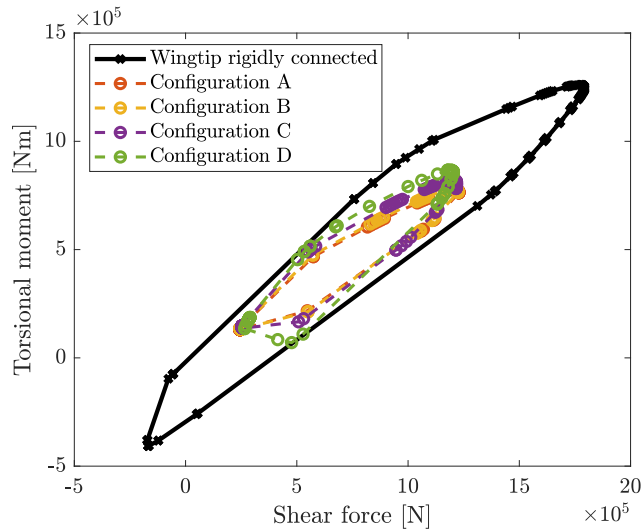


FIGURE 3.11: Shear force-torsional moment convex hull for the rigid connection and for optimized configurations

### 3.2.3 B. Optimal Parameters: Wingtip CM Position and Flare Angle

The optimization parameters considered in this case are the wingtip CM position and flare angle. The lower and upper bounds of the flare angle are  $0^\circ$  and  $45^\circ$  and the CM is constrained to lie in any position inside the wingtip. Figure 3.12 shows the results. Figure 3.12a shows the fitness function values corresponding to the Pareto points, the interpolated surface and the fitness function values related to the minimum bending moment, torsional moment and shear force. Figure 3.12a shows the Pareto front and Figures 3.12b, 3.12c and 3.12d show Figure 3.12a from different views. Figure 3.12 shows a wide range of variation in the bending moment and torsional moment. Moreover, the Pareto front shows a corner representative of an optimal compromise between the bending moment and the torsional moment. Figures 3.12c and 3.12d show a small variation in the shear force.

Figure 3.13 shows the fitness function points of Figure 3.12b in the proximity of the corner of the Pareto points. In Figure 3.13, six fitness function values were selected and the corresponding parameters are reported in Table 3.5. In all of the configurations the optimal flare angle is  $45^\circ$ , the optimal spanwise position of the CM is between 1.34 m and 1.42 m (corresponding to the 21% and 22% of wingtip span) and the optimal chordwise position of the CM is between 0.33 m and 0.42 m (corresponding to the 8.25% and 10.5% of chord).

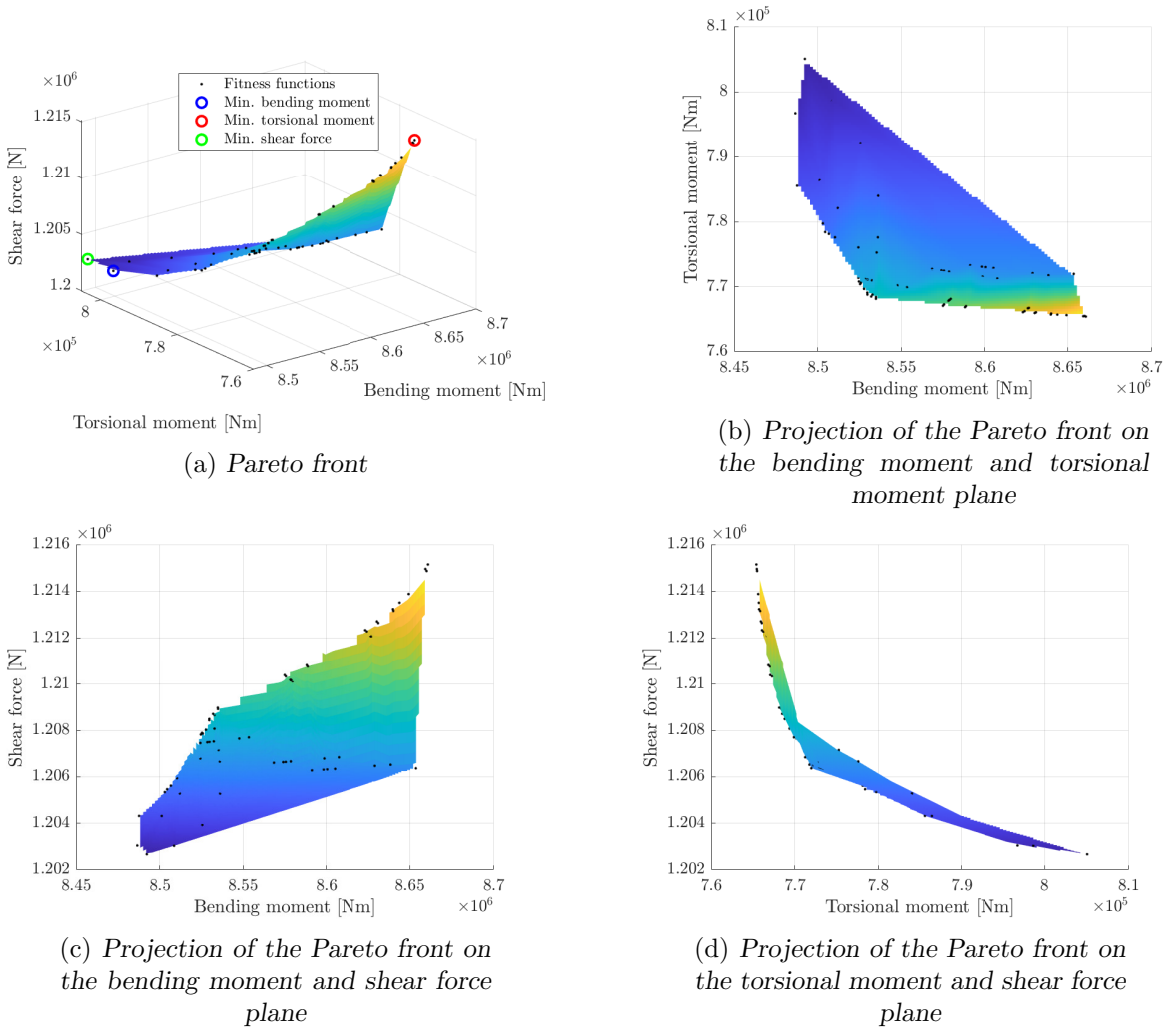


FIGURE 3.12: Multi-objective optimization, optimization parameters: wingtip CM position and flare angle

	Flare angle	Spanwise CM position	Chordwise CM position
A	45°	1.34 m	0.33 m
B	45°	1.36 m	0.33 m
C	45°	1.38 m	0.33 m
D	45°	1.42 m	0.35 m
E	45°	1.42 m	0.39 m
F	45°	1.42 m	0.42 m

TABLE 3.5: Parameters of the selected point on the Pareto front

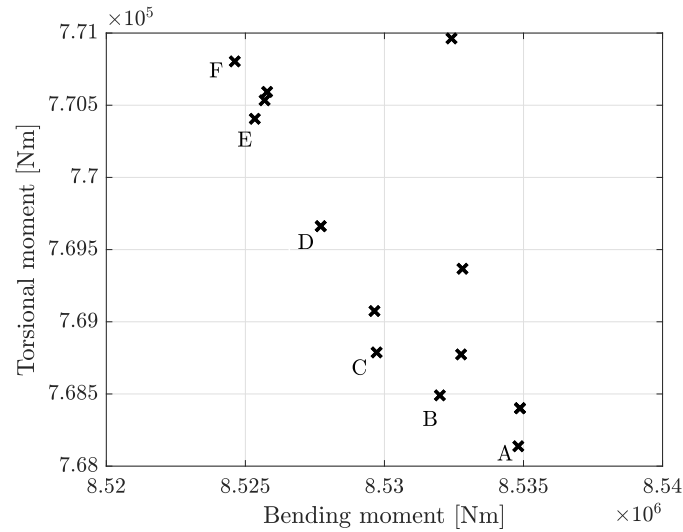


FIGURE 3.13: Pareto front on the bending moment and torsional moment plane at the optimal compromise

Figures 3.14 and 3.15 show the convex hull in the case of wingtip rigidly connected and the optimized configurations tested on the whole flight envelope. The configurations selected can reduce all the quantities of interest with respect to the case of wingtip rigidly connected to the wing. The higher reduction is on the bending moment, where the reduction of the maximum peak is 67%, the maximum peak of the torsional moment is reduced by 39% and the maximum peak of the shear force is reduced by 33%.

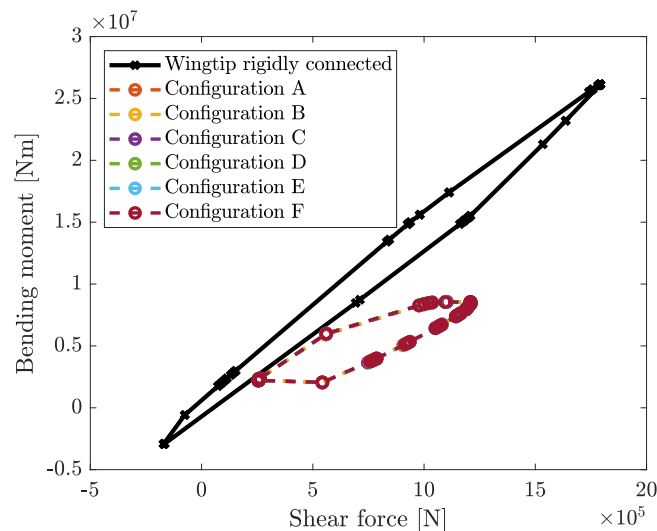


FIGURE 3.14: Shear force-bending moment convex hull for the rigid connection and for optimized configurations

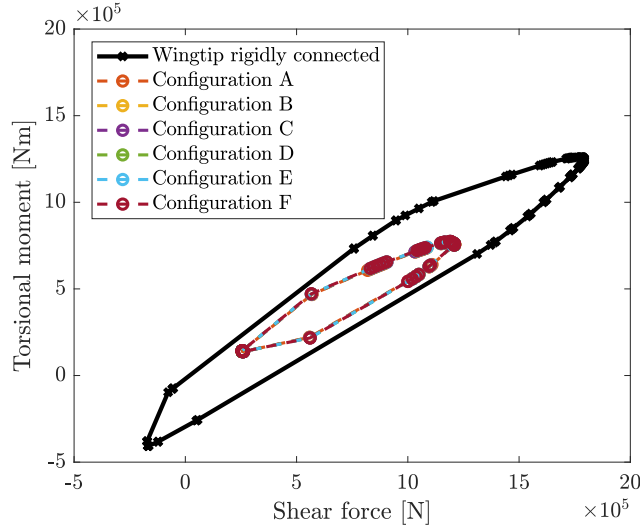


FIGURE 3.15: Shear force-torsional moment convex hull for the rigid connection and for optimized configurations

### 3.2.4 C. Optimal Parameters: CM Positions with Flare Angle Fixed at $30^\circ$

The multi-objective optimization was repeated considering the  $x$  and  $y$  coordinates of the wingtip CM position as optimal parameter. To limit the flare angle, in this case, it is limited to  $30^\circ$ . The wingtip CM is constrained to lie in any position inside the wingtip. Figure 3.16 shows the results. Figure 3.16a shows the fitness function values corresponding to the Pareto points, the interpolated surface and the fitness function values related to the minimum bending moment, torsional moment and shear force. Figures 3.16b, 3.16c and 3.16d show Figure 3.16a from different views. Comparing Figures 3.16c and 3.16d with Figures 3.12c and 3.12d, one can observe higher variation in the shear force. In Figure 3.16b the Pareto front has a corner representative of the optimal compromise between bending moment and torsional moment.

Figure 3.17 shows the fitness function points of Figure 3.16b. In Figure 3.17, four fitness function values were considered and the corresponding parameters are reported in Table 3.6. Configuration A is the configuration that minimizes the torsional moment

	Spanwise CM position	Chordwise CM position
A	0.001	3.99
B	1.48	0.00
C	2.46	1.11
D	6.420	3.57

TABLE 3.6: Parameters of the selected point on the Pareto front, flare angle  $30^\circ$



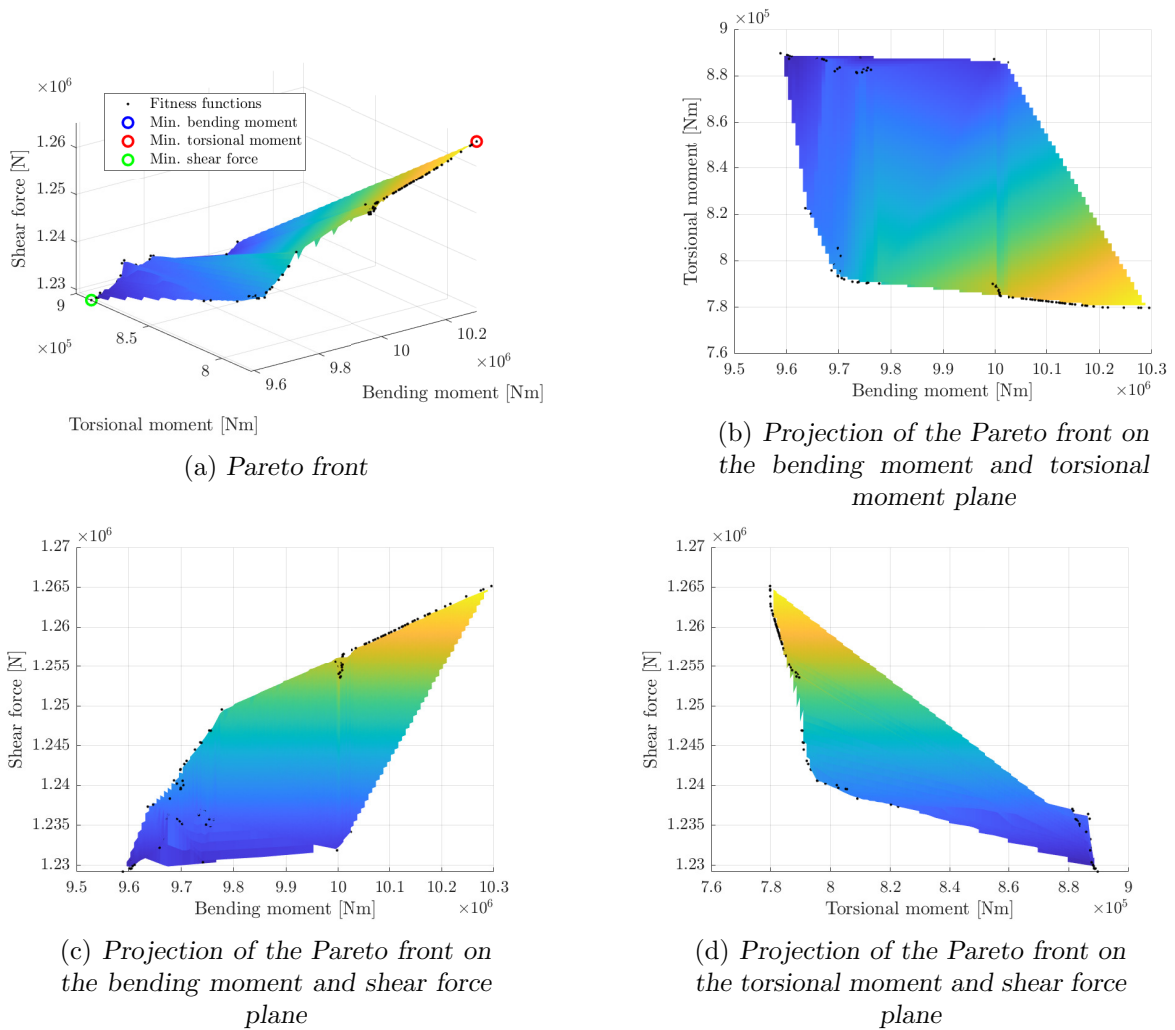


FIGURE 3.16: Multi-objective optimization, optimization parameters: wingtip CM position with a  $30^\circ$  flare angle

and configuration D minimizes the bending moment. Configurations B and C represent a compromise between the torsional moment and the bending moment. In the configuration selected the spanwise and the chordwise position of the CM covers a wide range of variation. Figures 3.18 and 3.19 show the convex hull in the case of wingtip rigidly connected and the optimal configurations tested on the whole flight envelope. As in the previous cases, the configurations selected can reduce all the quantities of interest with respect to the case of wingtip rigidly connected to the wing. From configuration A to D the maximum peak of the bending moment reduced and the maximum peak of the torsional moment increased. The maximum peak of the bending moment is reduced by 61% in configuration A and 63% in configuration D. The maximum peak of the torsional moment is reduced by 28% in configuration D and 38% in configuration A. The maximum peak of the shear force is reduced by 29% in configuration A and 31% in configuration

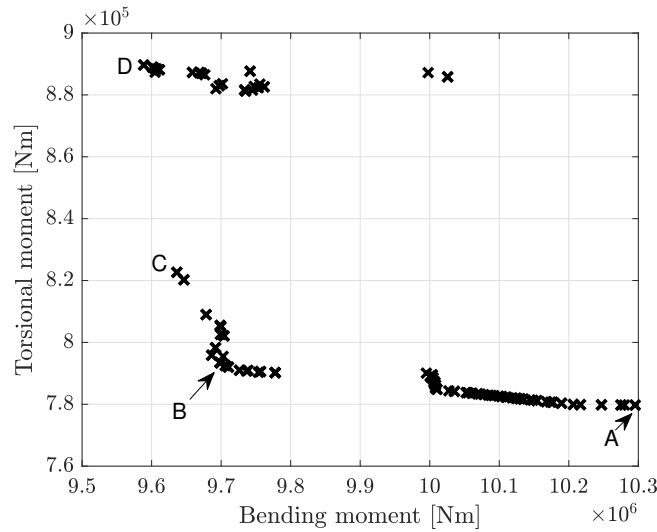


FIGURE 3.17: Pareto front on the bending moment and torsional moment plane at the optimal compromise, flare angle  $30^\circ$

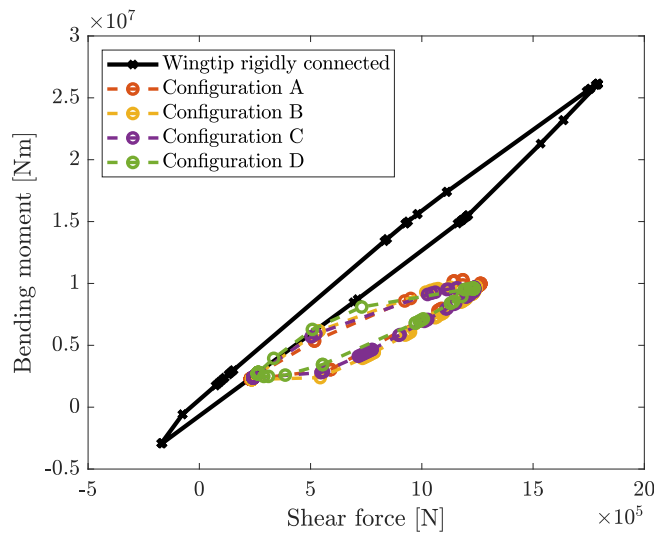


FIGURE 3.18: Shear force-bending moment convex hull for the rigid connection and for optimized configurations

D.

### 3.2.5 D. Optimal Parameters: CM Positions with Flare Angle Fixed at $20^\circ$

The multi-objective optimization was repeated considering the coordinate of wingtip CM position as optimal parameters and assuming flare angle is fixed at  $20^\circ$ . The wingtip CM is constrained to lie in any position inside the wingtip. The results are reported as in previous cases. Figure 3.20 shows the Pareto front and Figures 3.20b, 3.20c and

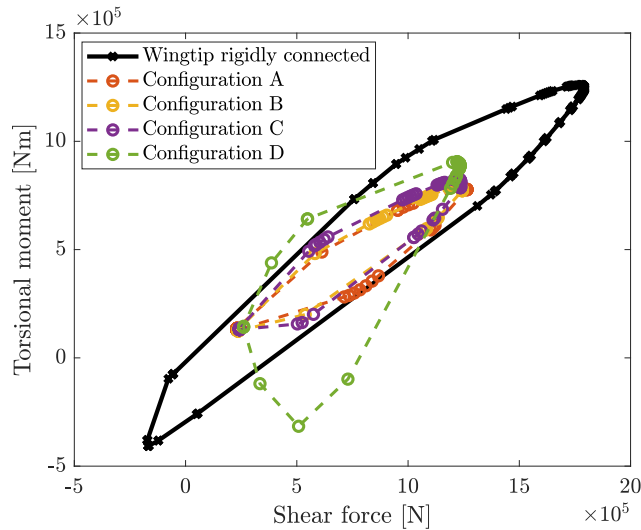


FIGURE 3.19: *Shear force-torsional moment convex hull for the rigid connection and for optimized configurations*

3.20d show Figure 3.20a from different views. The results in Figure 3.20b shows a corner representative of the optimal compromise between bending moment and torsional moment.

Figure 3.21 shows the fitness function points of Figure 3.20b. In Figure 3.21 six fitness function values were considered and the corresponding parameters are reported in Table 3.7. In the optimal configuration the spanwise position of the CM is between 0.37 m and

	Spanwise CM position	Chordwise CM position
A	0.45 m	3.94 m
B	0.40 m	3.94 m
C	0.37 m	3.94 m
D	1.03 m	0.02 m
E	1.48 m	0.02 m
F	1.75 m	0.02 m

TABLE 3.7: *Parameters of the optimal point on the Pareto front, flare angle 20°*

1.75 m (corresponding to the 6% and 27% of the total wingtip span) and the chordwise position of the CM is 3.94 m for the first three configurations (corresponding to the profile trailing edge) and 0.02 m for the last three configurations (corresponding to the profile leading edge). Figures 3.22 and 3.23 show the convex hull in the case of wingtip rigidly connected and the optimized configurations tested on the whole flight envelope. As in the previous cases, the configurations selected can reduce all the quantities of interest with respect to the case of wingtip rigidly connected to the wing. The maximum peak of the bending moment is reduced by at least 59%, the maximum peak of the torsional

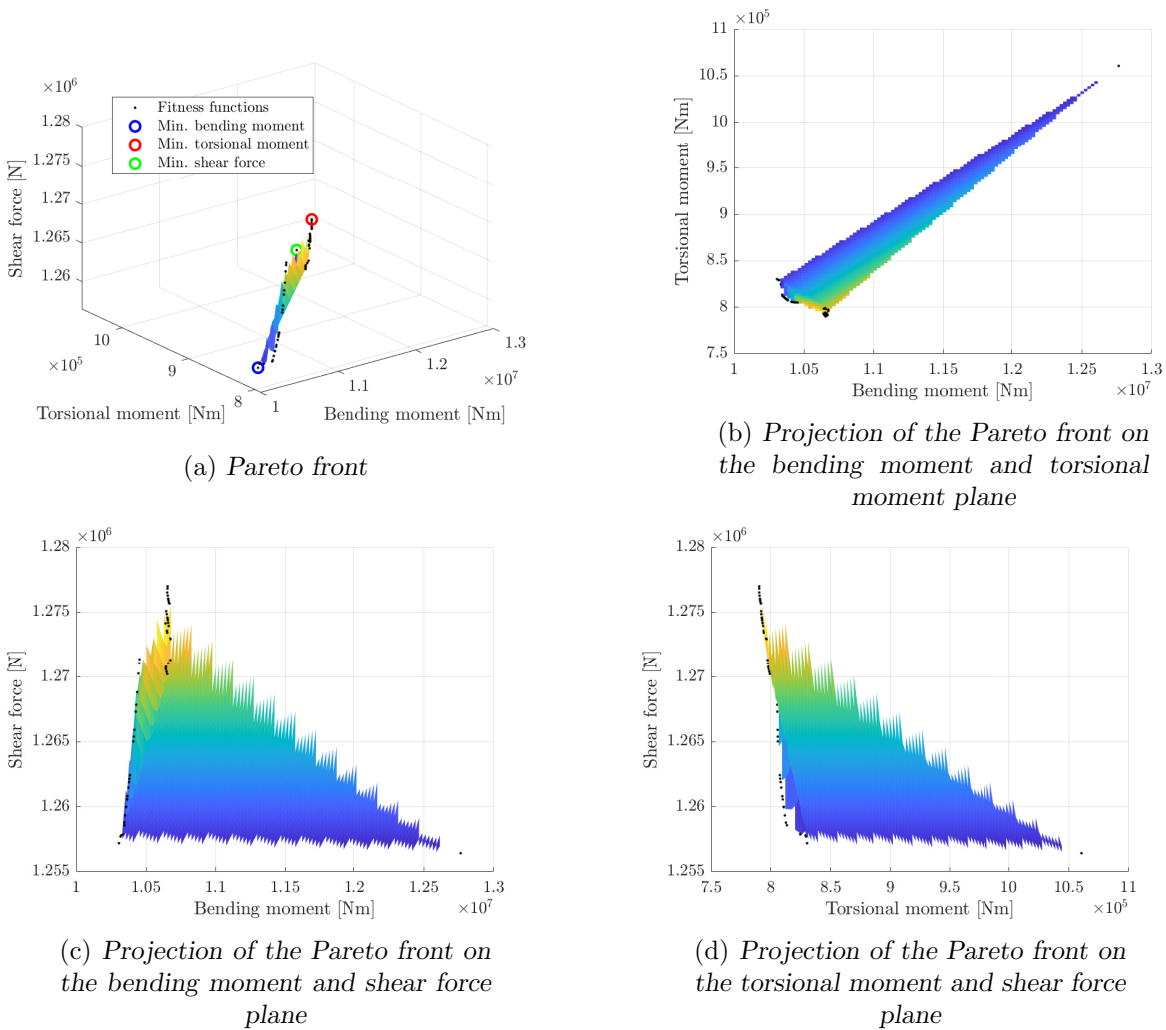


FIGURE 3.20: Multi-objective optimization, optimization parameters: wingtip CM position with a  $20^\circ$  flare angle

moment is reduced by at least 35% and the maximum peak of the shear force is reduced by at least 29%.

### 3.2.6 Flutter Speed

After performing the optimizations, an important aspect is to ensure that the aircraft will never suffer aeroelastic instability. In the optimization process before calculating the gust response, an eigenvalue analysis is performed to verify the stability of the model. The regulation [26] required to ensure for each altitude a minimum flutter speed greater than 115% of the maximum airspeed. It was considered the optimal configuration of minimum bending moment (wingtip CM spanwise position 6.43 m and chordwise position 3.57 m) obtained in Section 3.2.4. Figure 3.24 shows the flutter speed for various

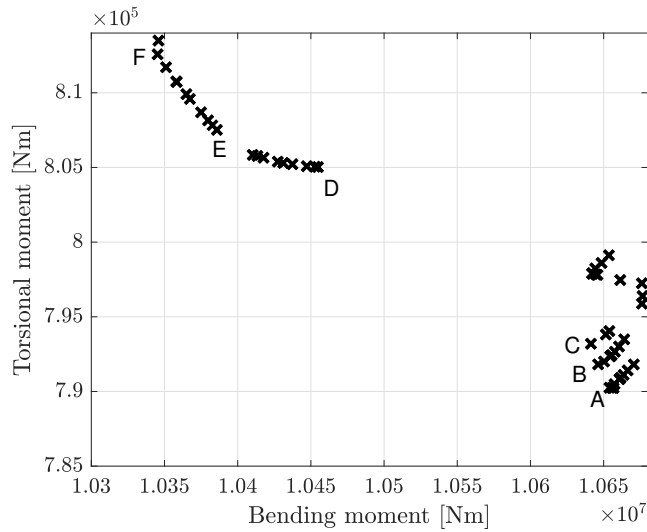


FIGURE 3.21: Pareto front on the bending moment and torsional moment plane at the optimal compromise, flare angle  $20^\circ$

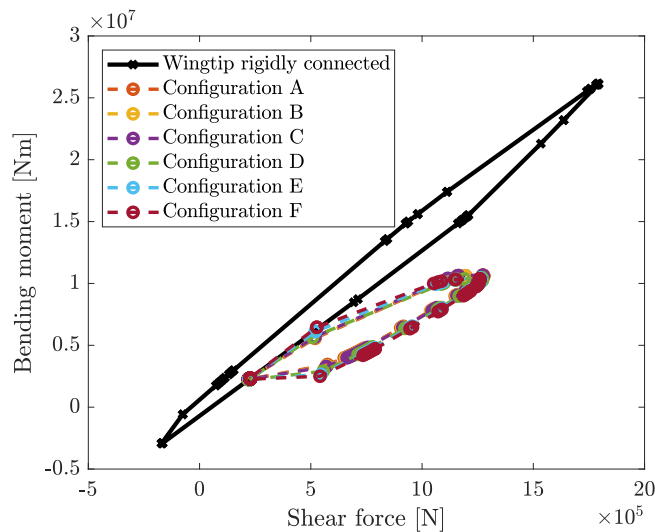


FIGURE 3.22: Shear force-bending moment convex hull for the rigid connection and for optimized configurations

altitude. At low altitude the flutter speed is lower than the limit. In the literature there are different techniques to increase the flutter speed of a wing, such as changing the stiffness parameters or adding a balancing mass [20, 89]. This work followed a different approach and considered the possibility to slightly change the parameters of the wingtip. In particular, it was considered to change the flare angle or to introduce in the hinge connection an inerter, a damper or a spring. The results shown that the introduction of the inerter and the damper are not able to increase the flutter speed but the introduction of a relatively small value of stiffness ( $k_\theta = 2.4 \cdot 10^5$  Nm/rad) as well as the reduction of the flare angle (1.7% reduction) are able to increase the flutter speed as shown in

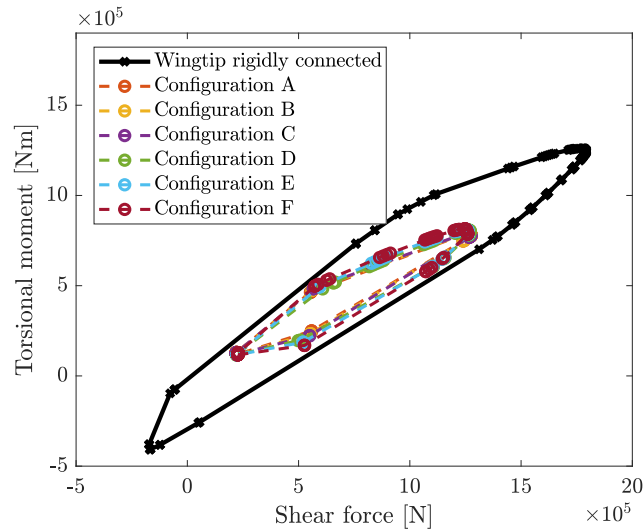


FIGURE 3.23: Shear force-torsional moment convex hull for the rigid connection and for optimized configurations

Figure 3.24, without compromising the capability for gust load alleviation. The smaller value able to sufficiently increase the flutter speed was selected for the stiffness and flare angle selection. Figures 3.25 and 3.26 show the convex hull of respectively the shear force and bending moment and the shear force and torsional moment for the reference configuration, for the optimized configuration, for the optimized configuration with the reduction of the flare angle (strategy 1) and for the optimized configuration with the introduction of the stiffness on the hinge (strategy 2).

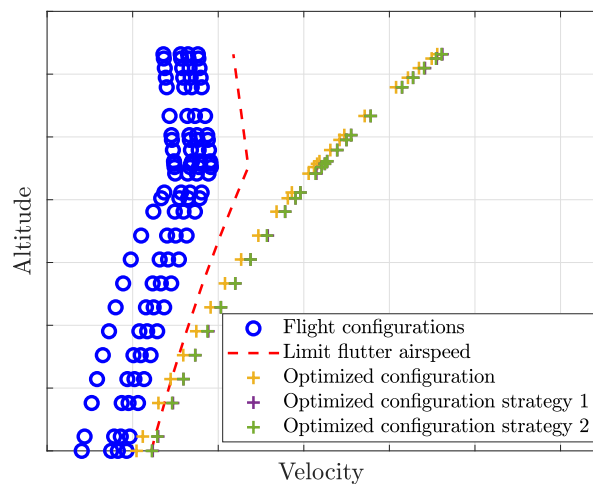


FIGURE 3.24: Flutter speed at different altitudes, in the reference configuration, in the optimized configuration, in the optimized configuration with smaller flare angle (strategy 1) and in the optimized configuration with stabilizing stiffness connection (strategy 2)

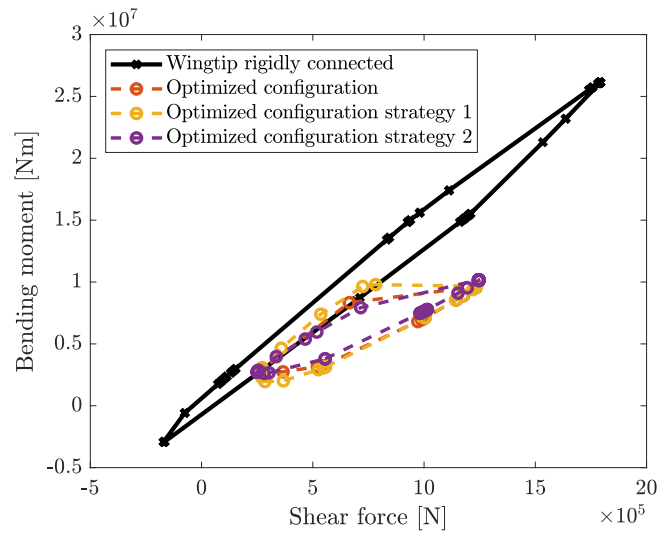


FIGURE 3.25: Shear force-bending moment convex hull obtained in the reference configuration, in the optimized configuration, in the optimized configuration with smaller flare angle (strategy 1) and in the optimized configuration with stabilizing stiffness connection (strategy 2)

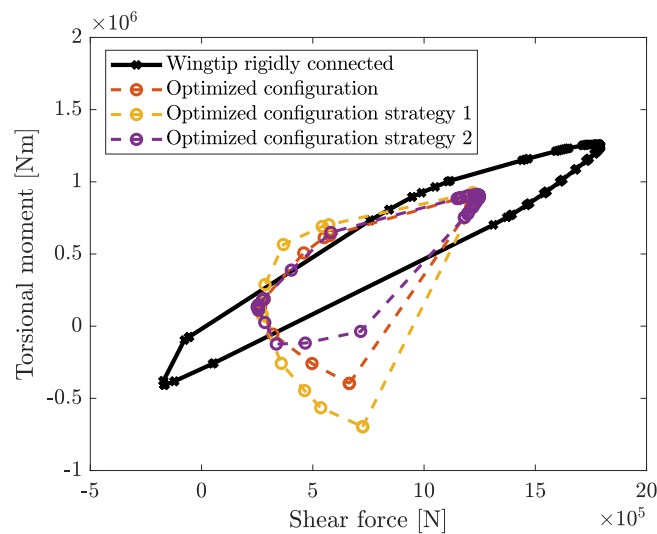


FIGURE 3.26: Shear force-torsional moment convex hull obtained in the reference configuration, in the optimized configuration, in the optimized configuration with smaller flare angle (strategy 1) and in the optimized configuration with stabilizing stiffness connection (strategy 2)

---

### 3.3 Conclusions

---

The simplified model considers a civil commercial aircraft's dimensions and weight distribution. The gust response for the whole flight envelope was considered and in the frequency range prescribed by the airworthiness regulations. Different multi-objective optimizations were performed to explore the possible combinations of the flare angle, wingtip span and position of the wingtip centre of mass. The results show a wide range of suitable combinations, so when a detailed model is available, it is possible to select the most suitable configuration. The different possible solutions were shown to overcome the reduction in the flutter speed through the use of a spring in the connection between the wing and the wingtip and through the reduction of the flare angle. These solutions result in a small deterioration in the ability to relieve gust loads. The optimizations shown that the choice of the wingtip span, the centre of mass and the flare angle are interconnected. Further investigations are needed in order to better understand the effect of the degrees of freedom not considered.



# Chapter 4

---

## GUST IDENTIFICATION

Analysing the effect of aeroelastic modelling with different levels of fidelity is one of the aims of this PhD thesis. This aim can be achieved by considering different strategies. In this Chapter, an inverse problem is considered. Defining the gusts of interest in designing GLA systems is crucial in determining the final GLA. However, the direct measurement of gusts and turbulence events is difficult, if not impossible, and so an indirect measure is necessary. This Chapter demonstrates a robust technique for aircraft gust identification based on cubic B-splines. To enable the performance of the identification methods to be assessed, the aeroelastic equations of motion are used not only as a model for gust identification but also to create simulated data. The aeroelastic models introduced in Chapter 2, representative of a civil jet aircraft with folding wingtips, were considered. These two models, with different levels of fidelity, allow the measured data to be simulated with the detailed model and the gust to be identified with the simplified model to determine the effects of modelling error.

---

### 4.1 Identification Theory

---

The direct measurement of many properties of real-world systems is not possible and this information can be deduced from other quantities which may be measured directly [115]. In general, an inverse problem consists of either reconstructing forcing signals acting on

a system whose internal characteristics are known, or determining the characteristics of a system driven by controlled or known exciting signals. Figure 4.1 shows the difference between direct and inverse problems. In the direct problem, the input, as well as the system, are known, so it is possible to calculate the output (see Figure 4.1a). In the inverse problem, the input or the dynamics of the system is unknown and can be estimated by exploiting the known output (see Figure 4.1b). Many problems in science and

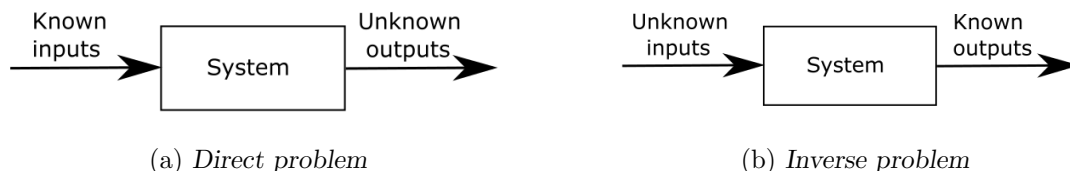


FIGURE 4.1: *The definition of direct and inverse problems*

engineering have the form of a Fredholm integral equation of the first kind [115]. This class of problems are typically ill-posed or strongly ill-conditioned after discretization. The generic form of the Fredholm integral equation can be written as

$$y(x) = \int_a^b k(x, t) f(t) dt \quad a \leq x, t \leq b \quad (4.1)$$

Eq.(4.1) links the unknown function  $f(t)$ ,  $w_g(t)$  in the aeroelasticity application, over the interval  $[a, b]$  to the given kernel function  $k(x, t)$  and real-valued function  $y(x)$ . The kernel function  $k(x, t)$  represents the mathematical characteristics of the system and  $y(x)$  is the observed data. The inverse problem takes the form of a deconvolution problem where the kernel function satisfies  $k(t, x) = h(t - x)$ . The transfer function  $h(t)$  is the impulse response function and represents the response to a unit impulse force. For linear time-invariant systems, assuming zero initial conditions of displacement and velocity, i.e.,  $y(0) = 0$  and  $\dot{y}(0) = 0$ , the time-domain convolution integral between the impulse response function  $h(t)$  and the exciting gust  $w_g(t)$  is written as

$$y(t) = \int_0^t h(t - \tau) w_g(\tau) d\tau \quad (4.2)$$

where  $\tau$  is the time delayed operation satisfying  $t \geq \tau$  and the kernel function  $h(t - \tau)$  is a convolution-type kernel.

Many inverse problems of science and engineering have the form of a Fredholm integral equation of the first kind which is commonly ill-posed. Different regularisation techniques were widely used for the numerical solution of this ill-posed problem, such as truncated singular value decomposition, Tikhonov regularisation, basis function expansion and collocation methods [116, 117]. The Fredholm integral equation was solved by

expansion methods using different techniques, for example the Coifman wavelet method [118], the Rationalized Haar wavelet method [119], the Sinc-collocation method [120] and collocation methods based on cubic B-spline [121]. Regularisation techniques applied to force identification are mainly divided into two categories, namely frequency-domain and time-domain methods. Frequency-domain methods are based on fast-Fourier transformation (FFT) and it was widely developed for stationary and pseudo-stationary conditions. However, these methods give poor results for nonstationary and transient responses [122]. On the other hand, time-domain methods show great promise for the study of transient and impulsive phenomena. Methods based on artificial neural networks [123], wavelet decomposition [124], Chebyshev polynomials [125] and cubic B-spline [126] were used for impact force identification. In force identification, the basis functions used to regularise the problem could also be ill-posed. The inverse problem of force identification can become well-posed if the selected number of basis functions can accurately approximate the impact force [126]. In numerical solution of integral equations, more basis functions give better results. However in force identification, more basis functions could introduce oscillations in the solution [127]. Moreover, it is important to select proper basis functions that can reasonably represent the characteristic of the desired solution. Cubic B-splines were used in a Newton form to reconstruct the impact force by solving two linear systems of equations [121] and as an efficient regularization method combined with the generalized cross-validation criteria to identify impact forces [126].

Traditional research in force identification is based on deterministic assumptions. However, uncertainties are inevitable in practice due to material property variation, measurement imperfections, or other factors. Uncertainties can lead to a deterioration of the identification accuracy. The implementation of high-precision identification methods on stochastic structures with distributed dynamic loads is still an unsolved problem [128]. Researchers considered dynamic loads with a defined probability density function [129], dynamic loads in the context of the probability theory [130] and unknown-but-bounded uncertainty in the structural system [128, 131].

Chapter 2 described methods to calculate the aeroelastic equation. Regardless of the approach used for the modelling, the aeroelastic problem can be formulated in terms of the physical displacement  $\mathbf{y}$  or modal coordinates  $\mathbf{q}$  using the relation

$$\mathbf{y} = \Phi \mathbf{q} \tag{4.3}$$

where  $\Phi$  is the modal matrix. The aeroelastic equation of motion representative of an aircraft subjected to gust can be expressed as

$$\mathbf{A}\ddot{\mathbf{q}} + (\rho V \mathbf{B} + \mathbf{D})\dot{\mathbf{q}} + (\rho V^2 \mathbf{C} + \mathbf{E})\mathbf{q} = \mathbf{f}_g w_g(t) \quad (4.4)$$

Eq.(4.4) can be expressed in the frequency domain, as

$$[-\omega^2 \mathbf{A} + j\omega(\rho V \mathbf{B} + \mathbf{D}) + (\rho V^2 \mathbf{C} + \mathbf{E})]\mathbf{q}(\omega) = \mathbf{f}_g w_g(\omega) \quad (4.5)$$

where  $\omega = 2\pi f$  is the frequency of interest. Eq.(4.5) can be used to calculate the transfer functions between the gust  $w_g(\omega)$  and the degrees of freedoms  $\mathbf{q}(\omega)$ .

In the aeroelastic problem, the kernel function  $h(t - \tau)$  is calculated in the frequency domain as the transfer function between the gust  $w_g(\omega)$  and the measurement of interest  $y(\omega)$  by means of Eq.(4.5) and is converted to time domain using the inverse Fourier transformation. The observed data  $y(t)$  can represent any response (e.g. displacement, velocity, acceleration, deformation, etc.) at an arbitrary point of the system. In practical applications, Eq.(4.2) is discretized over the interval  $[0, t]$ . Considering  $n$  sample points uniformly distributed over the time integral  $[0, t]$ , a set of  $n$  discrete linear equations can be obtained. For convenience Eq.(4.2) can be written in matrix-vector form as

$$\mathbf{y} = \mathbf{H}\mathbf{w}_g \quad (4.6)$$

where  $\mathbf{y}$  and  $\mathbf{w}_g$  are  $n \times 1$  vectors composed of discrete values of the response  $y(t)$  and excitation gust  $w_g(t)$ , respectively.  $\mathbf{H}$  is an  $n \times n$  transfer matrix with Toeplitz structure composed of discrete values of the impulse response function  $h(t)$  as

$$\mathbf{H} = \begin{bmatrix} h(t_1) & 0 & \dots & 0 & 0 \\ h(t_2) & h(t_1) & \dots & 0 & 0 \\ \vdots & \vdots & \ddots & \vdots & \vdots \\ h(t_{n-1}) & h(t_{n-2}) & \dots & h(t_1) & 0 \\ h(t_n) & h(t_{n-1}) & \dots & h(t_2) & h(t_1) \end{bmatrix} \Delta t \quad (4.7)$$

A possible strategy to determine  $\mathbf{w}_g$  when  $\mathbf{H}$  is known and is non-singular and  $\mathbf{y}$  is measured is to solve directly Eq.(4.6), to give

$$\tilde{\mathbf{w}}_g = \mathbf{H}^{-1}\mathbf{y} \quad (4.8)$$

where  $\tilde{\mathbf{w}}_g$  is the identified gust. However, this method is very sensitive to the inversion of the transfer matrix due to its large condition number. Inverse problems are typically

ill-posed problems, and thus small disturbances in the measured  $\mathbf{y}$  may result in a large error in the identified  $\tilde{\mathbf{w}}_g$ .

### 4.1.1 Regularisation Methods

This section presents a brief overview of the regularisation methods used in this Chapter, and more information can be found in [117, 132, 133]. The linear system of equations

$$\mathbf{H}\mathbf{w}_g = \mathbf{y} \quad (4.9)$$

is ill-posed if the singular values of  $\mathbf{H}$  decay gradually to zero and the ratio between the largest and the smallest nonzero singular values is large [117]. When the matrix  $\mathbf{H}$  is ill-conditioned, the problem of Eq.(4.9) is ill-posed in the sense that a small perturbation of  $\mathbf{y}$  or  $\mathbf{H}$  may lead to a large perturbation of the solution. Although different types of direct and iterative regularisation methods exist [117], this work considers three direct regularisation methods: Tikhonov regularisation, Truncated Singular Value Decomposition (TSVD) and Damped Singular Value Decomposition (DSVD).

The general version of Tikhonov's method takes the form

$$\min\{\|\mathbf{H}\mathbf{w}_g - \mathbf{y}\|_2^2 + \lambda\|\mathbf{L}\mathbf{w}_g\|_2^2\} \quad (4.10)$$

where  $\lambda$  is the regularisation parameter defined as a positive constant chosen to control the norm of the solution vector and  $\mathbf{L}$  can represent the first or second derivative operator but is often the identity matrix [133].

The TSVD and DSVD methods are based on the Singular Value Decomposition (SVD). In linear algebra the SVD of  $\mathbf{H}$  is a decomposition of the form

$$\mathbf{H} = \mathbf{U}\mathbf{\Sigma}\mathbf{V}^T \quad (4.11)$$

where  $\mathbf{U} = (\mathbf{u}_1, \dots, \mathbf{u}_n)$  and  $\mathbf{V} = (\mathbf{v}_1, \dots, \mathbf{v}_n)$  are matrices with orthonormal columns, and  $\mathbf{\Sigma} = \text{diag}(\sigma_1^*, \dots, \sigma_n^*)$  where  $\sigma_i^*$  are the singular values of  $\mathbf{H}$  sorted in non-increasing order such that

$$\sigma_1^* \geq \dots \geq \sigma_n^* \geq 0 \quad (4.12)$$

The TSVD defines a new well-posed problem, related to the ill-posed problem of Eq.(4.9) and has a solution which is less sensitive to perturbations. The method approximates the matrix  $\mathbf{H}$  with a lower rank matrix  $\mathbf{H}_k$ . The matrix  $\mathbf{H}_k$  is defined as the rank- $k$

matrix

$$\mathbf{H}_k = \mathbf{U}\mathbf{\Sigma}_k\mathbf{V}^T, \quad \mathbf{\Sigma}_k = \text{diag}(\sigma_1^*, \dots, \sigma_k^*, 0, \dots, 0) \quad (4.13)$$

where  $k < n$  [117, 132].

In the DSVD instead of neglecting  $n - k$  singular values, as in TSVD, a smoother cut-off is used by means of filter factors  $f_i$  defined as

$$f_i = \frac{\sigma_i^*}{\sigma_i^* + \lambda} \quad (4.14)$$

These filter factors decay more slowly than the Tikhonov filter factors and thus, in a sense, introduce less filtering. The regularisation parameter  $\lambda$  is a positive constant and plays a similar role to the parameter in Eq. (4.10), although gust estimates from Eqs.(4.10) and (4.14) will be slightly different even if the same value of  $\lambda$  is used.

The selection of the regularisation parameter is a balance between the perturbation error and the regularisation error in the regularised solution. In this work the Generalized Cross-Validation (GCV) method is used. The selection of the regularisation parameter is obtained through the minimization of the GCV function defined as

$$G = \frac{\|\mathbf{H}\tilde{\mathbf{w}}_g - \mathbf{y}\|_2^2}{(\text{trace}(\mathbf{I} - \mathbf{H}\mathbf{H}^T))^2} \quad (4.15)$$

where  $\mathbf{H}^T$  is a matrix which produces the regularised solution  $\tilde{\mathbf{w}}_g$  when multiplied by  $\mathbf{y}$ , i.e.  $\tilde{\mathbf{w}}_g = \mathbf{H}^T\mathbf{y}$  [117, 134].

### 4.1.2 Identification Using Cubic B-Spline Collocation Method

Splines are piece-wise polynomials of degree  $k$  and continuity  $C^{k-1}$  [135] and they can be used to solve the Fredholm integral equation of the first kind [126, 136]. Cubic B-splines are piecewise polynomials of degree three with  $C^2$  continuity at the junction points between adjacent segments. In this work, gusts are represented as a summation of cubic B-splines with uniformly distributed knots. Therefore, the problem of gust identification becomes the identification of the weight of each B-spline.

Let  $\Delta : \{a = \tau_0 < \tau_1 < \dots \tau_{m-1} = b\}$  be a uniform partition over the interval  $[a, b]$ , where the uniform interval is  $h = (b - a)/(m - 1)$ , and the abscissas  $\tau_i = a + ih$ ,  $i = 0, 1, \dots, m - 1$  are called knots or collocation points. The cubic spline function  $S(t)$  is introduced under the hypothesis that over each interval  $[\tau_{i-1}, \tau_i]$ ,  $S(t)$  is a polynomial of degree three and the function and its first and second derivatives are all continuous. A typical cubic B-spline function requires five knots and introducing additional point knots

at the beginning  $\tau_{-3} < \tau_{-2} < \tau_{-1} < \tau_0$  and at the end  $\tau_{m-1} < \tau_m < \tau_{m+1} < \tau_{m+2}$  the cubic polynomial  $B_i(t)$  on the  $(m+2)$  interval can be defined in a piece-wise polynomial function form by collocating at the five knots [136]

$$B_i(t) = \frac{1}{6h^3} \begin{cases} (t - \tau_{i-2})^3 & t \in [\tau_{i-2}, \tau_{i-1}] \\ h^3 + 3h^2(t - \tau_{i-1}) + 3h(t - \tau_{i-1})^2 - 3(t - \tau_{i-1})^3t & t \in [\tau_{i-1}, \tau_i] \\ h^3 + 3h^2(\tau_{i+1} - t) + 3h(\tau_{i+1} - t)^2 - 3(\tau_{i+1} - t)^3t & t \in [\tau_i, \tau_{i+1}] \\ 0 & (i = -1, 0, \dots, m-1, m) \\ (\tau_{i+2} - t)^3 & t \in [\tau_{i+1}, \tau_{i+2}] \\ 0 & \text{otherwise} \end{cases} \quad (4.16)$$

where the degree of expansion of the cubic B-spline functions is controlled by the collocation interval  $h$  controls. The transitions between two adjacent cubic polynomial segments is marked by the knots  $[\tau_{i-2}, \tau_{i-1}, \tau_i, \tau_{i+1}, \tau_{i+2}]$ . Figure 4.2 illustrates one cubic B-spline, which is composed of four cubic polynomials. Figure 4.2 also shows that at

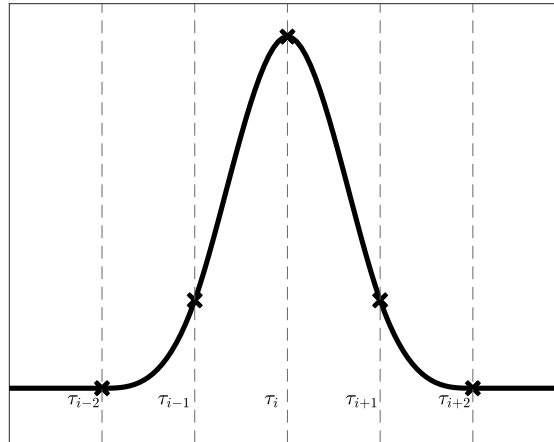


FIGURE 4.2: A cubic B-spline curve constructed by four cubic polynomials

least five knots are required to reconstruct a discrete gust. Figure 4.3 shows translated cubic B-spline functions in the domain  $[0, 1]$  for the collocation interval  $h = 1/6$  with seven uniform spaced knots, and each cubic B-spline function is a translated copy of the previous one. To control the boundary conditions, several additional basis function are required, otherwise the desired solution has a poor accuracy at the extrimity. The number of cubic B-spline functions is equal to the number of control points  $m+2$  over the interval  $[a, b]$ . Cubic B-spline function has a three important propriety:

- Each cubic B-spline function is non negative for all parameter values,

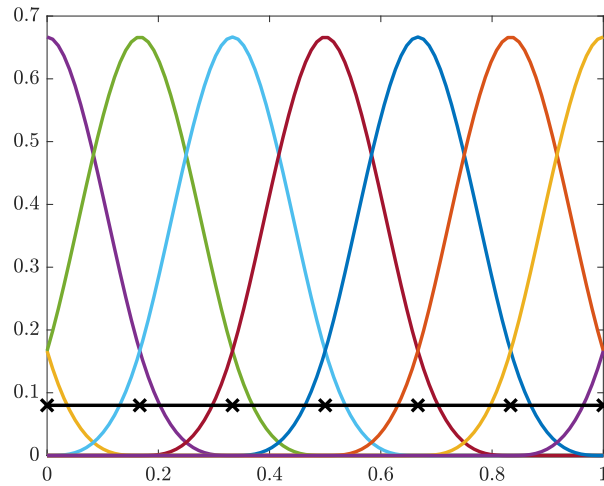


FIGURE 4.3: *Cubic B-spline functions in the interval  $[0, 1]$  for the collocation interval  $h = 1/6$*

- Each cubic B-spline function has only one maximum value.
- The sum of cubic B-spline functions for any parameter value  $t$  within a specified collocation interval is always equal to 1,

$$\sum_{i=-1}^m B_i(t) = 1 \quad \forall t \quad (4.17)$$

Figure 4.4 shows cubic B-spline curves with different values of collocations interval  $h$  from  $1/10$  to  $1/4$ . The shape of the basis function depends on the collocation interval

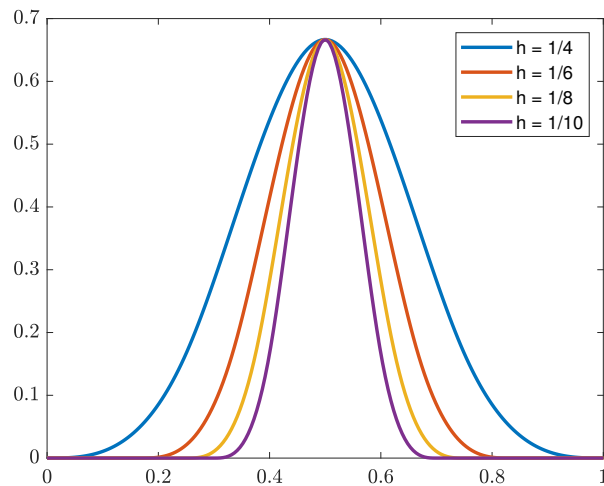


FIGURE 4.4: *Cubic B-spline curves with different values of collocations interval  $h$*

$h$  but does not depend on the specific knot values because B-spline functions are based



on knot differences, as shown in Figure 4.4. Thus, the collocation parameter  $h$ , which controls the mesh size of the cubic B-spline function, can be considered a regularisation parameter.

The cubic B-spline functions  $S(t)$  is constructed as a weighted sum of  $m+2$  cubic B-spline basis functions  $B_i(t)$ , namely

$$S(t) = \sum_{i=-1}^m c_i B_i(t) \quad (4.18)$$

where  $c_i$  are the unknown parameters of the cubic B-spline basis functions  $B_i(t)$ . It is possible to approximate the unknown gust  $\tilde{w}_g(t)$  by the constructed cubic B-spline function of Eq.(4.18) as

$$\tilde{w}_g(t) \approx S(t) = \sum_{i=-1}^m c_i B_i(t) \quad (4.19)$$

Figure 4.5 shows the approximation of a discrete gust as a summation of cubic B-Splines.

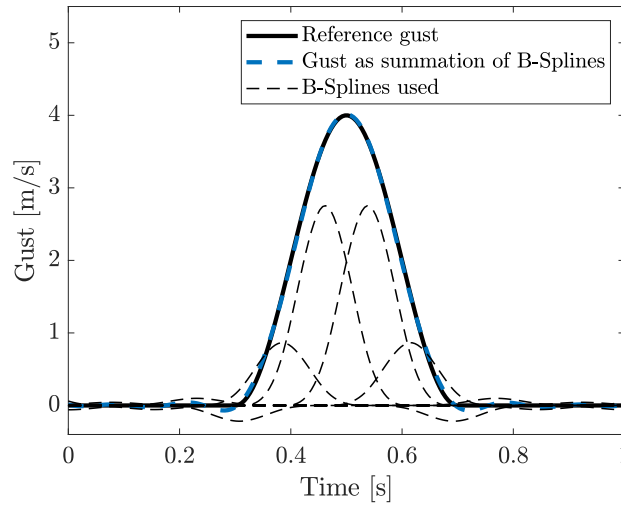


FIGURE 4.5: Gust represented as a summation of cubic B-Splines and the cubic B-Splines involved

Substituting Eq.(4.19) into Eq.(4.2) gives

$$y(t_j) = \sum_{i=-1}^m c_i \int_0^t h(t_j - \tau) B_i(\tau) d\tau \quad j = 1, 2, \dots, n \quad (4.20)$$

By solving Eq.(4.20) it is possible to obtain the coefficients  $c_i$  and then substituting  $c_i$  into Eq.(4.19) the gust  $\tilde{w}_g(t)$  can be estimated.

Let  $\Psi \in R^{n \times (m+2)}$  where the  $(i, j)$  element of  $\Psi$  is  $B_j(t_i)$  be a known matrix consisting of  $m + 2$  cubic B-spline basis vectors, satisfying  $m + 2 \leq n$ . Eq.(4.20) can be discretized in matrix–vector form as

$$\mathbf{y} = (\mathbf{H}\Psi)\mathbf{c} \quad (4.21)$$

Since  $\Psi$  is a sparse matrix whose elements are mainly close to the diagonal, the matrix  $\mathbf{A} = \mathbf{H}\Psi$  is diagonally dominant. The identification problem can be solved by means of the least squares method as

$$\mathbf{c} = \mathbf{A}^+ \mathbf{y} \quad (4.22)$$

where the matrix  $\mathbf{A}^+$  is the Moore–Penrose generalized inverse matrix. Finally, the calculation of the unknown vector  $\tilde{\mathbf{w}}_g$  can be reformulated in matrix vector notation as

$$\tilde{\mathbf{w}}_g = \Psi \mathbf{c} \quad (4.23)$$

The number of collocation points governs the degree of expansion of the cubic B-spline functions employed for to approximate the unknown force. The residual is used to determine the optimal number of collocation points, by minimising

$$r = \|\mathbf{y} - \mathbf{H}\tilde{\mathbf{w}}_g\|_2 \quad (4.24)$$

---

## 4.2 Aeroelastic Models

---

Sections 2.2 and 2.4 describe a simplified and a detailed model. In Section 3.1 the simplified model is applied considering similar dimensions and weights of the detailed model. All the analysis in this chapter will be performed at sea level and 200 m/s. Table 4.1a shows the elastic modes of the simplified aircraft model with no aerodynamic forces present. Table 4.1b shows the frequencies of the aeroelastic model at 200 m/s and sea level. All the modes are oscillatory, except for the modes related to the wingtip deflection which are overdamped (eigenvalues -4.9 and -1680 s<sup>-1</sup>). All the eigenvalues have a negative real part which show the modes are all stable at 200 m/s. The total mass of the simplified model is the same as the FFAST model. The bending natural frequency of the simplified model at 2.50 Hz in Table 4.1a is also close to the wing bending dominant modes of the FFAST model at 2.22 Hz (Table 2.4). The rigid body mode of the wing tip deflection of the simplified model is 0.03 Hz, while the similar mode of the FFAST model is 0.0417 Hz.

Frequency [Hz]	Mode shape
0.03	Wingtip deflection
2.50	Wing bending
4.50	Wing torsional

(a) Structural model

Frequency [Hz]	Damping ratio [-]	Mode shape
2.50	0.01	Wing bending
3.33	0.03	Wing torsional coupled with wingtip

(b) Aeroelastic model at an air velocity of 200 m/s and sea level

TABLE 4.1: Natural frequencies and damping ratios of the simplified model

The modes related to the wingtip deflection and wing bending deflection are the modes that mainly contribute to the gust response as will be shown in the sequel. The extremely simplified version of the FFAST model lacks several details such as coupling between the modes, the effect of swept angle, etc, however, it can reasonably represent the gust response of the detailed FFAST model, as shown in Figures 4.6a, 4.6b, 4.7a and 4.7b.

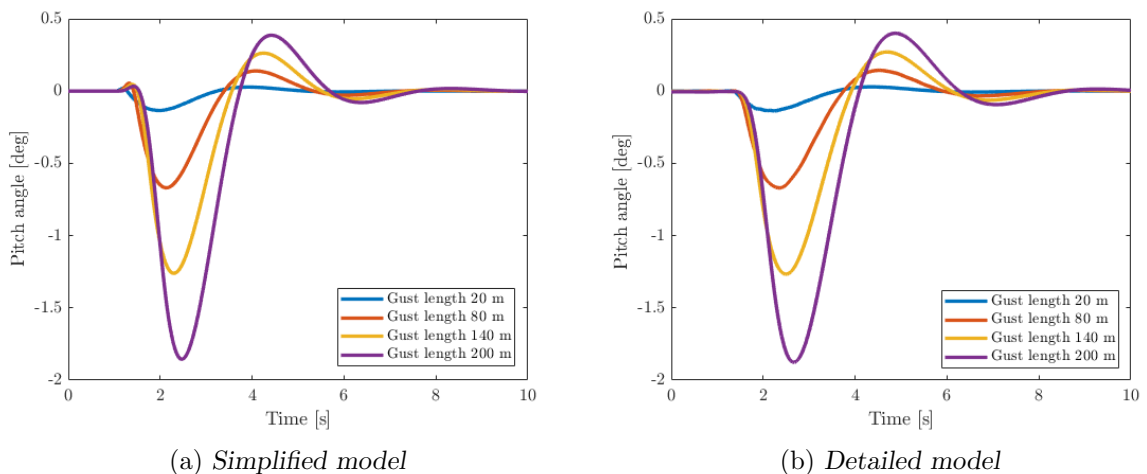
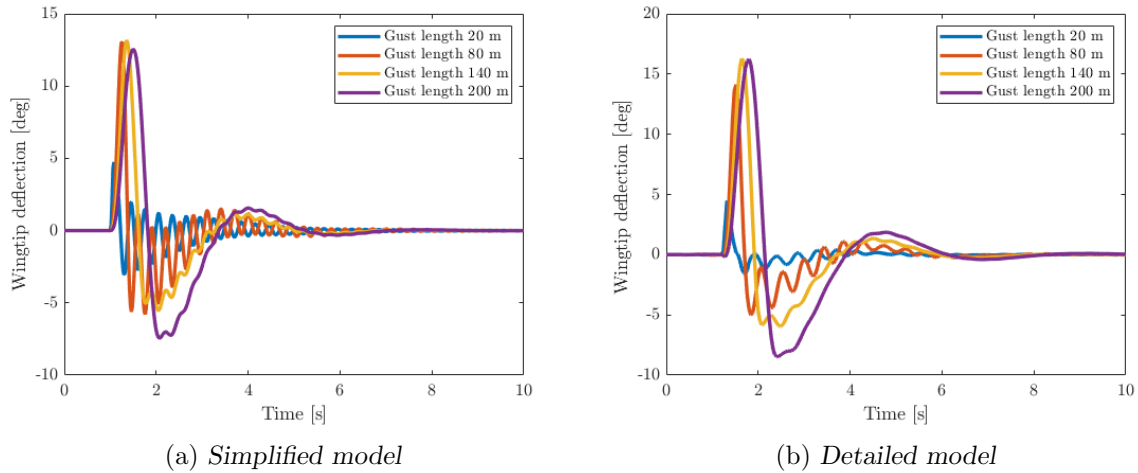


FIGURE 4.6: Aircraft centre of mass pitch angle gust responses

The proposed method used in this Chapter will use flight measured data from a physical structure and utilise them along with the numerical model to identify the gust. In reality, the numerical models are not accurate and often include modelling errors. In this Chapter, one may assume that the ‘measured’ data is simulated using the FFAST model. In section 4.4.2, it is shown that the simulated measured data of the FFAST model may be identified using the simplified model, which highlights the robustness of the identification method to modelling errors.

FIGURE 4.7: *Wingtip angle gust responses*

Figures 4.6a and 4.6b show the aircraft centre of mass pitch angle gust responses for the simplified model and the detailed model, respectively. Figures 4.7a and 4.7b show the wingtip deflection gust responses for the simplified model and the detailed model, respectively. The peak angular deflection of the wingtip is different in the two models because of slight differences in the hinge stiffness. The wingtip deflection was defined such that a positive angle variation produces an upwards displacement.

---

### 4.3 Identification Results for the Simplified Model

---

In this section, the identification results based on the simplified model are presented. The measurement data are simulated by using Eq.(4.4) and the identification is based on the corresponding model in the frequency domain, Eq.(4.5). The response is obtained as a time history of 1000 equally spaced samples representative of 20 seconds. This section analysis compares the results of gust identification based on the regularisation with the one obtained by approximating the gust as a summation of cubic B-spline functions. In addition, for the identification based on cubic B-spline functions, the effects of collocation points location and the ability to identify atmospheric turbulence are investigated. The results assume that the degrees of freedom of the model in modal coordinate may be measured directly (e.g. the bending or the torsional modal coordinate of the wing). In practice, the modal coordinates would be estimated from the physical coordinates using Eq. (4.3). Nevertheless, this is not a limitation of the method and similar results can be obtained using different measurements.

### 4.3.1 Gust Identification Considering Measurement Noise

An important feature of a reliable gust identification technique is the ability to reconstruct the gust in the presence of noisy data, since in the measurement process, measurement noise cannot be avoided. In this work, the noisy measurements data ( $\hat{\mathbf{y}}$ ) are created by summing the measurements and the noise as

$$\hat{\mathbf{y}} = \mathbf{y} + l_{noise} \cdot std(\mathbf{y}) \cdot (2 \cdot rand(n, 1) - 1) \quad (4.25)$$

where the MATLAB script function  $std(\bullet)$  denotes the standard deviation of the vector, the MATLAB script function  $rand(n,1)$  returns an  $n \times 1$  vector containing uniformly distributed random numbers on the interval  $(0, 1)$  and  $l_{noise}$  is the current noise level of the simulated response. In the results 10%, 20% and 30% of measurement noise correspond to  $l_{noise} = 0.1, 0.2$  and  $0.3$ , respectively. Figure 4.8 shows the gust reconstruction considering the model inversion technique of Eq.(4.8) and the measurement of the bending mode in the case of clean data and 10% measurement noise. The reconstruction in the case of

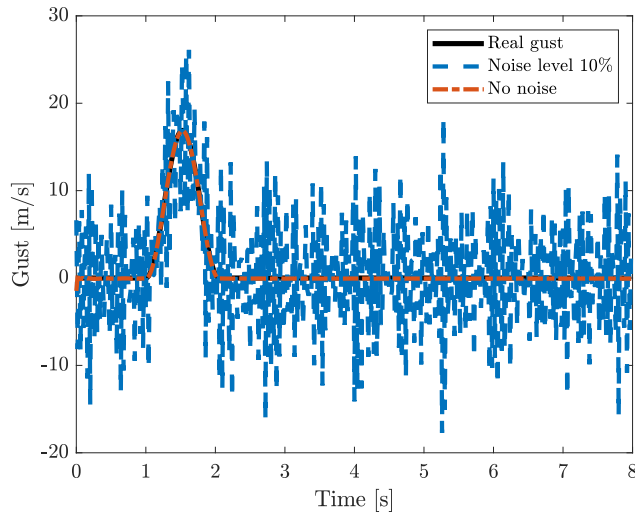


FIGURE 4.8: *Gust reconstruction by model inversion considering clean and noisy measurements of the bending mode*

noisy data has a large error, while the reconstruction from the clean data gives good results. In this case, the order of magnitude of the condition number of the matrix  $\mathbf{H}$  is  $10^{19}$ ; so the problem is ill conditioned and a regularisation method is required. Figures 4.9, 4.10 and 4.11 show the GCV function considering the noisy data, in the case of Tikhonov (TIKH) regularisation, TSVD regularisation and DSVD regularisation, respectively. The GCV function considering clean measurement, in the case of the DSVD and Tikhonov regularisation methods, is a monotonically increasing function and in the case of the TSVD method is a monotonically decreasing function. On the contrary,

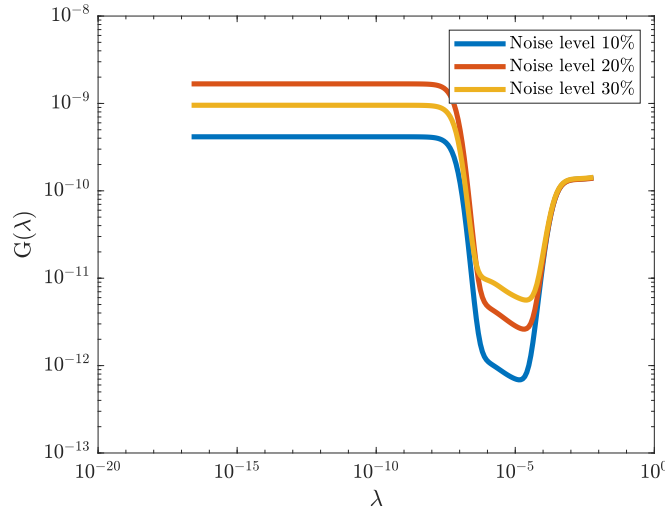


FIGURE 4.9: *GCV of noisy measurement of the bending mode with Tikhonov regularisation*

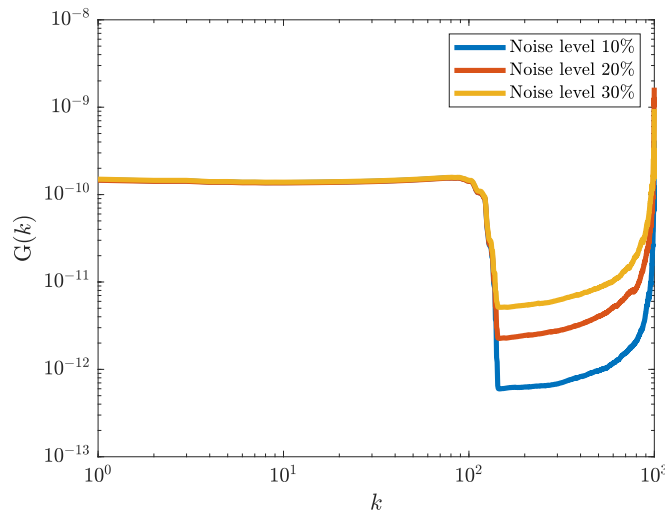


FIGURE 4.10: *GCV of noisy measurement of the bending mode with TSVD regularisation*

in the case of noisy measurement the GCV function has a minimum and the lowest GCV achievable increases with the increase of the noise. Figures 4.12 and 4.13 show the gust reconstruction from the model inversion method considering different regularisation techniques, in the case of 10% and 30% of measurement noise, respectively. The results were obtained by setting the regularisation parameter to the value associated with the minimum GCV. The comparison between the gust identification from noisy data of Figures 4.8 and 4.12 show that the DSVD regularisation method is able to reduce the error in the reconstruction of the gust. Moreover, Tikhonov regularisation and TSVD regularisation can further reduce the reconstruction error.

Figures 4.14 and 4.15 show the results of the gust identification based on cubic B-spline

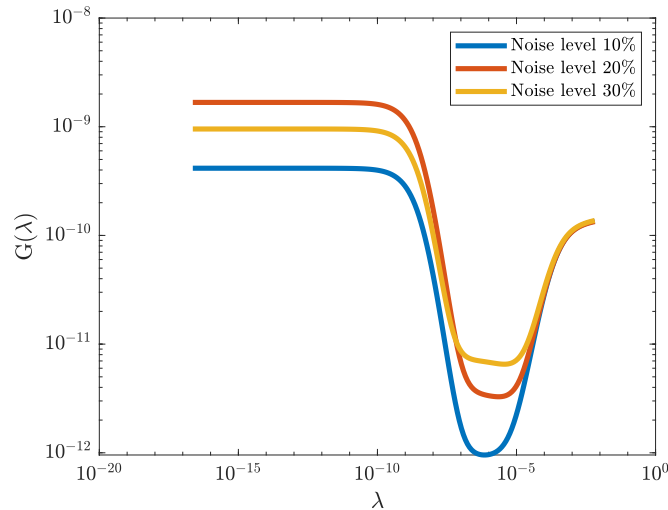


FIGURE 4.11: *GCV of noisy measurement of the bending mode with DSVD regularisation*

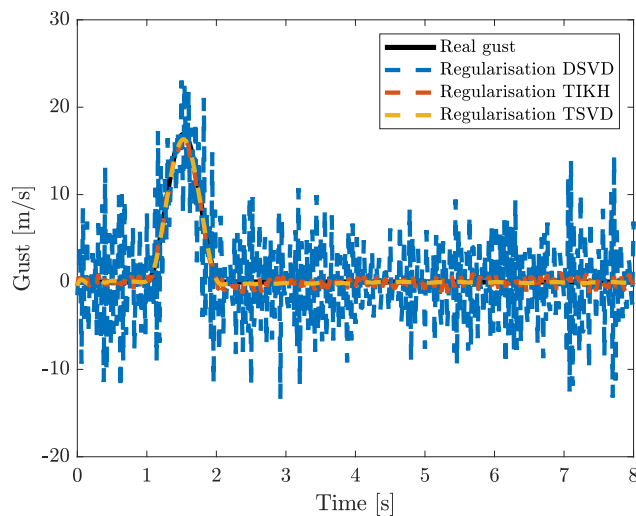


FIGURE 4.12: *Gust reconstruction by model inversion considering measurements of the bending mode with 10% measurement noise and three regularisation methods*

functions. Figures 4.14 shows the residual in the cases of clean and noisy measurement from the bending mode. It shows that for low numbers of cubic B-splines and low noise levels, the noise does not affect the reconstruction of the gust. Moreover, increasing the noise level, the lowest residual value achievable increases. Figure 4.15 shows the gust reconstruction based on cubic B-spline in the case of 10% and 30% of measurement noise. The reconstruction based on 73 collocation points gives good results for both 10% and 30% of measurement noise. The reconstructions for 30% measurement noise in Figure 4.15 confirm the trend of the residual in Figure 4.14. Indeed, the reconstruction based on 200 collocation points is less accurate than the one based on 73 collocation points. Thus, Figure 4.15 shows that the cubic B-spline identification acts as a filter and decreasing the

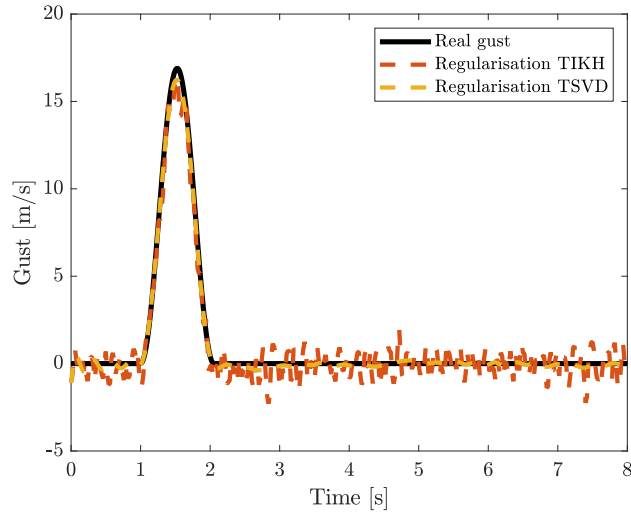


FIGURE 4.13: *Gust reconstruction by model inversion considering measurements of the bending mode with 30% measurement noise and TIKH and TSVD regularisation*

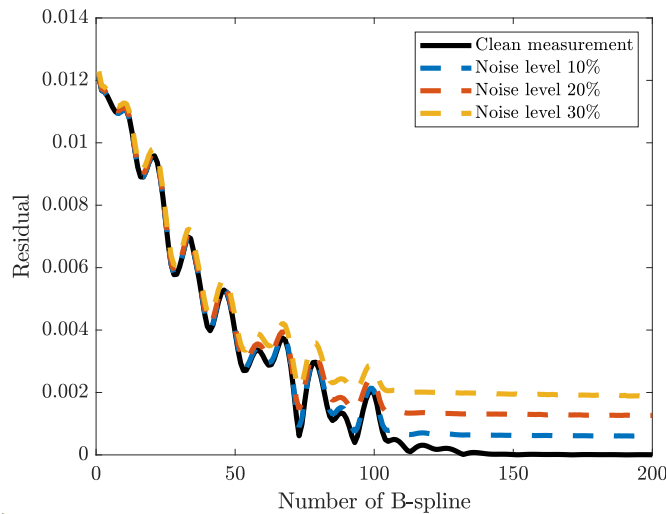


FIGURE 4.14: *Residual considering clean measurement and measurement with 10%, 20% and 30% of noise*

distance between collocation points the identification never converges to a smooth result. These gust identification techniques are also tested using different levels of coloured noise using ‘pinknoise’ command in MATLAB, and similar results were obtained.

Figures 4.12, 4.13 and 4.15 show that the matrix regularisation through TSVD and the approximation of the solution through cubic B-spline functions give similar results. Indeed, in the cubic B-spline method the number of cubic B-splines plays a similar role to the regularisation parameter [126]. The B-spline method was found to perform better than the regularisation methods and therefore the effects of the location of the collocation points will be shown in the next section. Moreover, turbulence identification



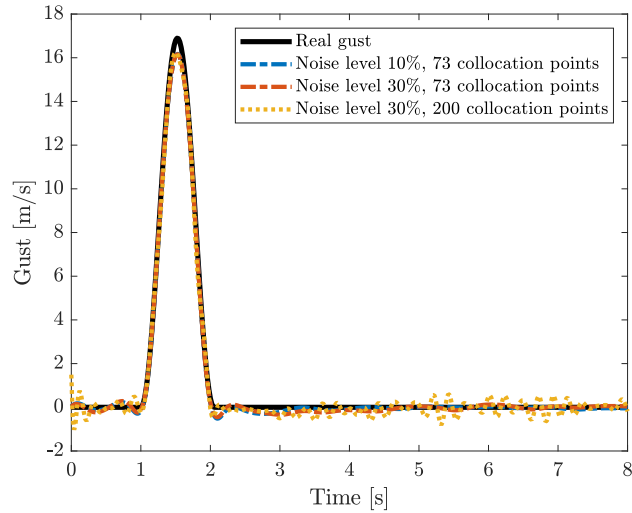


FIGURE 4.15: *Gust reconstruction by cubic B-spline function, considering clean measurement and measurement with 10% and 30% noise*

using cubic B-spline functions will be used for gust identification for the FFAST model. Figure 4.16 compares the gust response obtained from the real gust and the identified gusts calculated using TSVD and cubic B-Spline (73 collocation points), considering 30% measurement noise. The results show that TSVD and cubic B-Splines have similar performance. Although, in the first second of the simulation, the result from TSVD is associated with higher amplitude oscillations when the real gust is zero.

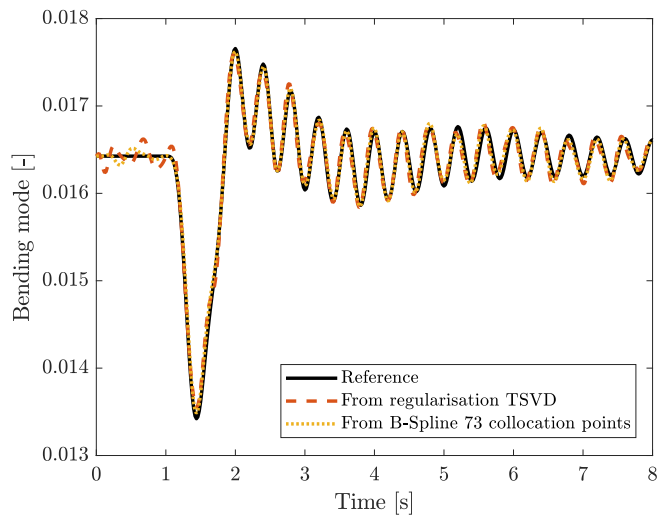


FIGURE 4.16: *Gust response considering the real gust and the identified gusts from noisy measurements*

### 4.3.2 Effect of the Location of the Collocation Points

In the identification through B-spline functions, a fundamental aspect is related to the choice of the number of collocation points. Gusts defined by EASA can have different frequencies and amplitudes and the optimal choice of the number of collocation points for one gust could lead to some error in the identification of a different gust [26]. Figure 4.17 shows the trend of the residual in the interval 1 to 200 cubic B-spline considering as measurement the bending modal coordinate. In the considered interval the residual is not a monotonic decreasing function but has local minima at 73 and 93 cubic B-splines and local maxima at 79 and 99 cubic B-splines. Figures 4.18, 4.19 and 4.20 show the gust reconstruction, the position of the collocation points and the B-splines used for the identification considering 73, 79 and 99 collocation points, respectively. The gust reconstruction based on 73 cubic B-splines has a smaller error with respect to the case of 79 and 99 cubic B-splines. Figure 4.18 shows that the major contribution to the gust reconstruction is given by four B-spline defined in such a way that when the gust is zero they are zero. Instead, Figures 4.19 and 4.20 show a higher number of B-spline that have an effect on the identification of the gust and it produces errors in the reconstruction. The introduction of additional collocation points does not increase the accuracy of the reconstruction because the collocation points are not symmetrically distributed about the gust.

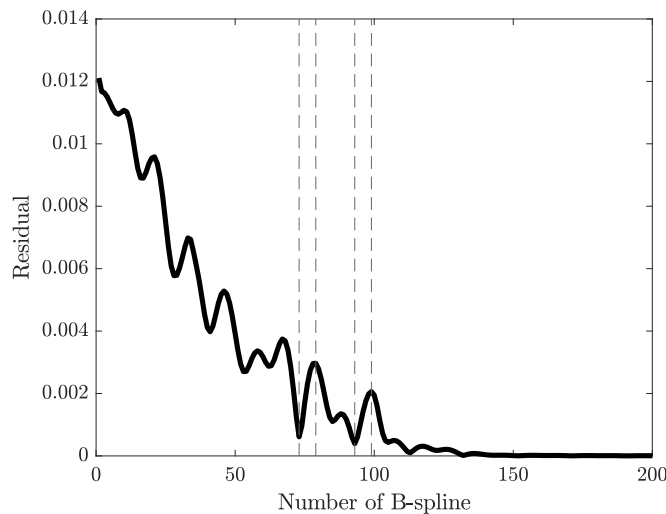
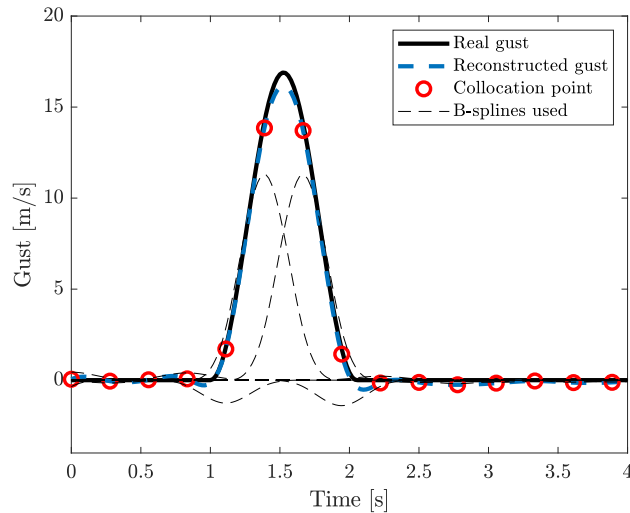
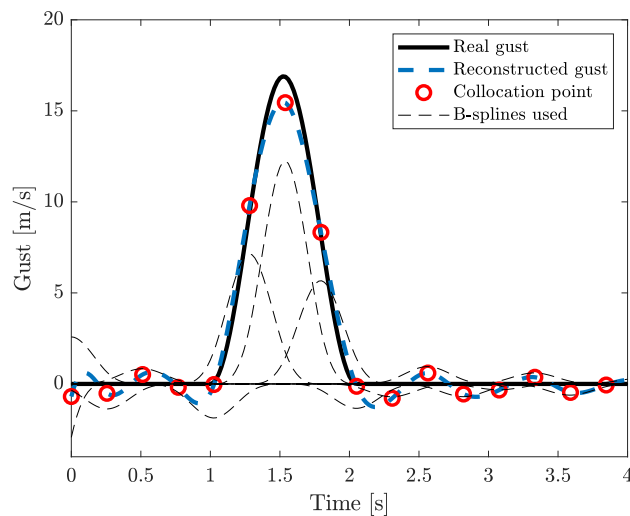


FIGURE 4.17: *Residual considering measurement of the bending mode*

FIGURE 4.18: *Gust reconstruction considering 73 cubic B-splines*FIGURE 4.19: *Gust reconstruction considering 79 cubic B-splines*

### 4.3.3 Gust and Turbulence Event Identification

EASA regulation requires to consider the response of the aircraft to discrete gusts and continuous turbulence event separately [26]. In this section, the identification based on cubic B-spline functions in the case that the gust and the turbulence event are combined together is considered. For all the time histories the turbulence is present and the gust acts after 5 seconds of the simulation. The time-domain response is obtained as a time history of 5000 equally spaced points representative of 40 seconds. The atmospheric turbulence is obtained in the time-domain as the output of the state-space form of the transfer function Eq.(2.10) whose input is band-limited (from 0.01 Hz to 10 Hz) white noise. To increase the stability of the solution in the calculation of the Moore-Penrose

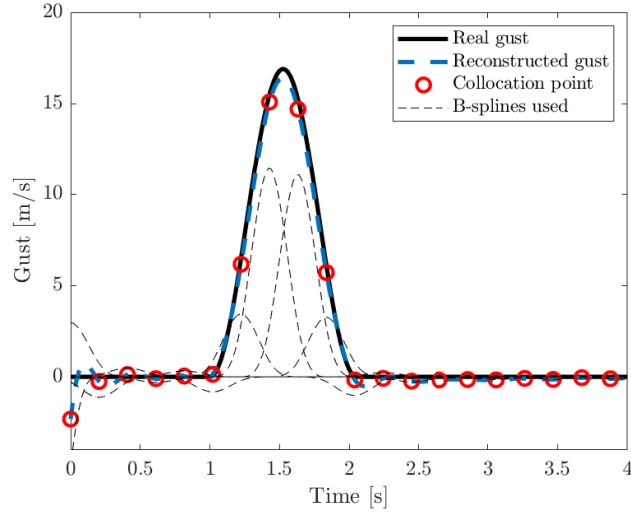


FIGURE 4.20: *Gust reconstruction considering 99 cubic B-splines*

generalized inverse matrix of Eq.(4.22) all values smaller than  $10^{-6}$  were set to zero. Figures 4.21 and 4.22 show the residual and the gust and turbulence event identification considering the measurement of the bending mode. In the case of identification considering 230 collocation points, the error in the reconstruction of the maximum peak is 0.9% and the error in the identification of the turbulence field is in the interval  $\pm 0.25$  m/s.

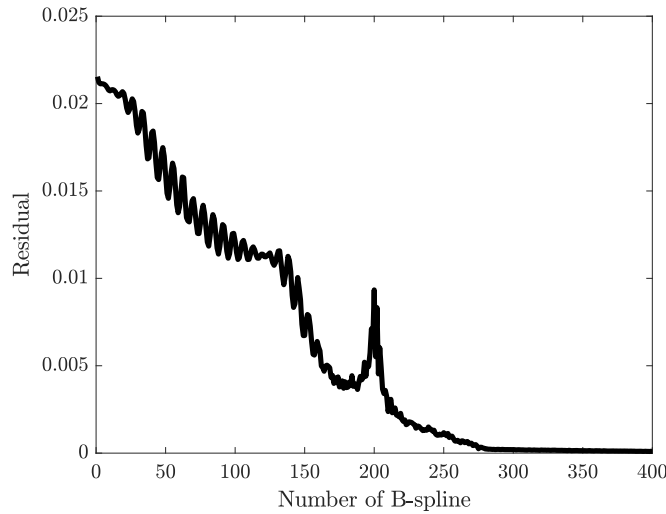


FIGURE 4.21: *Residual for the identification of gust and turbulence event using the measurement of the bending mode*

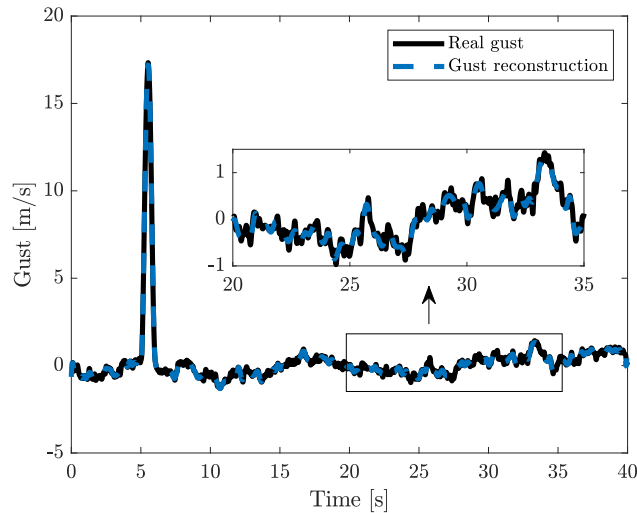


FIGURE 4.22: *Gust and turbulence event reconstruction considering 230 collocation points using the measurement of the bending mode*

---

## 4.4 Identification Using Measurements from the FFAST Model

---

In this section, the results of the identification based on cubic B-spline functions of the FFAST model are presented. The simulation is performed for 100 seconds and is composed of 4000 equally spaced points. In all the cases, the measurement data are generated considering the 55 modes model. The time response from 5 seconds to 100 seconds is considered for identification and the rotation of the centre of gravity of the aircraft in pitch is used as a measurement because this information is typically available on the aircraft. The first 5 seconds of the measurement are not considered for the identification because, due to the complexity of the model and the numerical errors without any gusts, the response of the system is not exactly zero initially. Moreover, for the identification process, the impulse response function assumes zero response and zero first derivative of the response at the initial time. In the B-spline function, it would be possible to introduce controlled end conditions in order to reduce the error at the extremities of the identification [137]. In this work this was not done because it is always possible to change the initial and final time of the identification. In any case controlled end conditions will alleviate but not cancel the identification errors at the extremities. The models used for the identification are based on two approaches; in the first case, the

model is obtained through a modal reduction and in the second case a simplified model is used.

#### 4.4.1 Identification Model: Modal Reduction

The definition of the model through modal coordinates allows us to introduce or exclude modes in the model in order to have different levels of accuracy. The identification is performed considering that the model used for the identification has an increasing number of modes. Figure 4.23 shows the residual when the model used for the identification has the lowest 4 modes, 5 modes and 55 modes. The gust identification based on the 4 modes

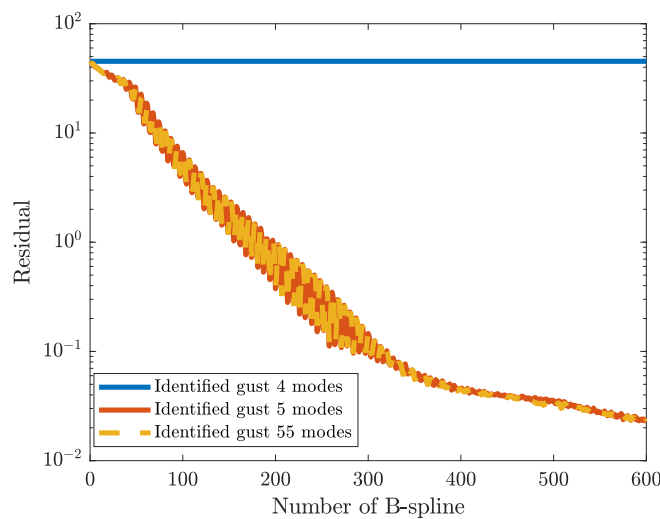


FIGURE 4.23: Residual considering 4 modes model, 5 modes model and 55 modes model and measurement of the pitch of the aircraft

model is not able to converge to the correct result, but the identification based on the 5 modes model gives results similar to the identification based on 55 modes. Table 4.2 shows the first five natural frequencies, damping ratios and mode shapes of the FFAST model at 200 m/s and sea level. The fifth mode is associated with the torsion of the wing. Figure 4.24 shows the identification results considering the 5 modes model, the 8 modes model and the 55 modes model for 600 collocation points.

Figure 4.25 shows the difference between the real gust and the reconstructed gusts of Figure 4.24. As expected, decreasing the accuracy in the model increases the error in the reconstruction. The error in the first seconds of identification is related to the aforementioned problem of the initial conditions and disappears after two seconds of identification. This error can be mitigated by increasing the time of the simulation. Moreover, after the initial condition, the identification error using 55 modes is in the

Mode	Frequency [Hz]	Damping ratio [%]	Mode shape
1	0.21	15	Rigid body mode
2	0.34	56	Rigid body mode
3	2.33	8	Sym. 1 <sup>st</sup> wing bending & wingtip
4	2.58	2	Anti-sym. 1 <sup>st</sup> wing bending
5	2.63	0.3	Anti-sym. 1 <sup>st</sup> wing torsion

TABLE 4.2: First five natural frequencies and damping ratios of the FFAST aeroelastic model at 200 m/s and sea level

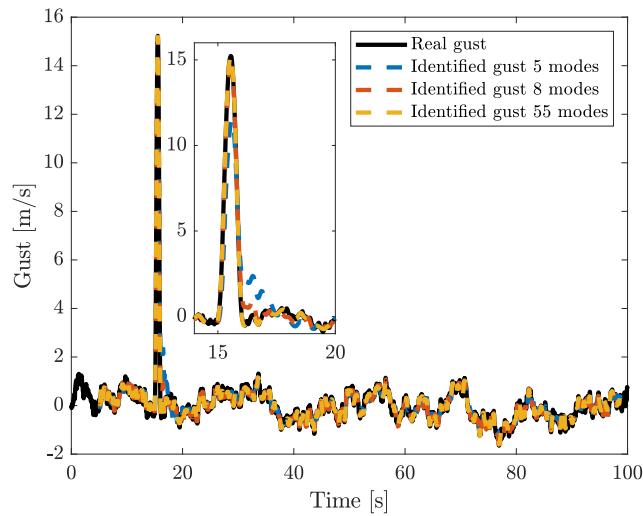


FIGURE 4.24: Gust and turbulence event reconstruction considering 5 modes model, 8 modes model and 55 modes model, measurement of the pitch of the aircraft and 600 collocation points

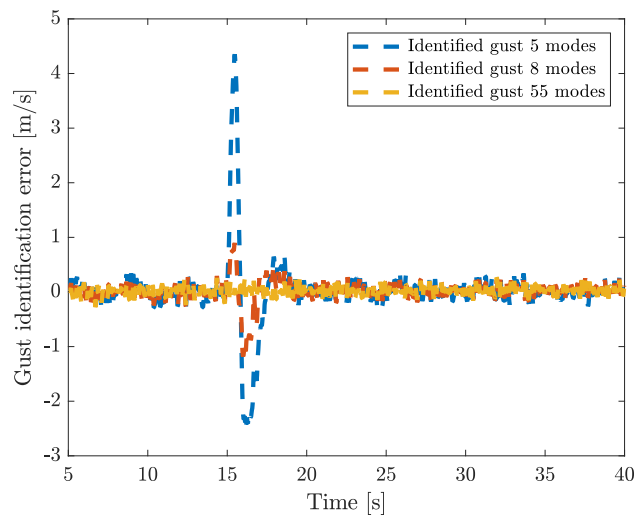


FIGURE 4.25: Error in the gust and turbulence event reconstruction

interval  $\pm 0.2$  m/s and it can be reduced further by increasing the number of B-splines. The identification based on the 5 and 8 modes models has the maximum error during and soon after the peak of the gust where the higher frequency modes are excited. The error in the identification of the peak of the gust is 25% for the 5 modes model and 4% for the 8 modes model. Moreover, Figure 4.25 shows that in the second part of the identification, where the contribution is only from the turbulence event, the three models give similar results.

Figure 4.26 reports the gust and turbulence event response in the frequency domain obtained using the 5, 6, 7, 8 and 55 modes models. The response of the 55 modes model has a higher amplitude at low frequencies and then the amplitude decreases for higher frequencies. The good estimation of the gust and turbulence event with the low order model can be explained considering that they are obtained through a modal reduction, so considering only a subset of the low-frequency modes. Indeed, in Figure 4.26 at low frequency, the response of the reduced order models is similar to that of the complete model.

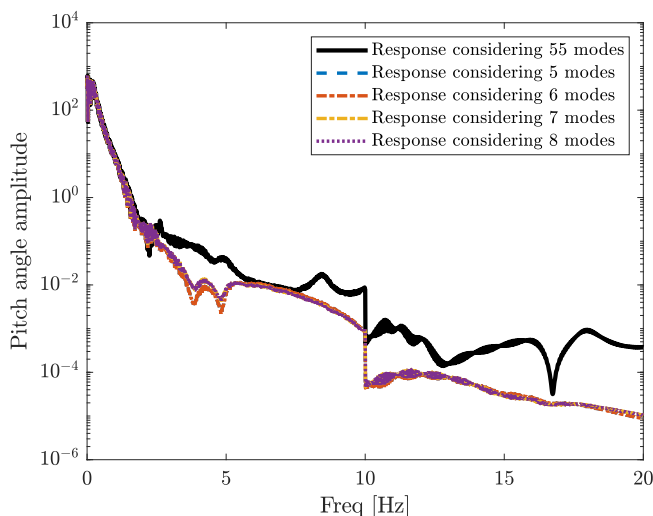


FIGURE 4.26: *Pitch angle gust and turbulence event response considering 5, 6, 7, 8 and 55 modes models*

#### 4.4.2 Identification Model: Realistic Example, Simulating Measured Data Using the Detailed Model and Using the Simplified Model for Identification

In this section, the simplified model is used for identification purposes while the higher fidelity model is utilised to simulate measurement data. Figure 4.27 shows the residual



considering the measurement of the pitch of the aircraft. Figure 4.28 shows the identification based on 450 and 600 collocation points. The comparison between Figures 4.24 and 4.28 show that the identification based on the simplified model gives similar results to the identification based on a reduced order model. It is worth highlighting that the two models were defined using different techniques and the aerodynamic models are different; thus the identification method is robust with respect to modelling errors. Figure 4.29 shows the reconstruction error in the case of identification based on 450 and 600 collocation points. The error in the identification of the peak is 8% in the case of 450 collocation points and 3% in the case of 600 collocation points. The positive and negative peaks of the gust identification error are related to a time delay in the identification of the peak of the gust. Indeed, Figure 4.28 shows in the identification of the peak a time delay of 0.1 seconds in the case of identification considering 450 collocation points and 0.07 seconds in the case of identification considering 600 collocation points. This is due to fact that the simplified model reacts faster than the detailed model. However, the faster reaction of the simplified model does not affect the turbulence event reconstruction that has an error in the interval of  $\pm 0.5$  m/s.

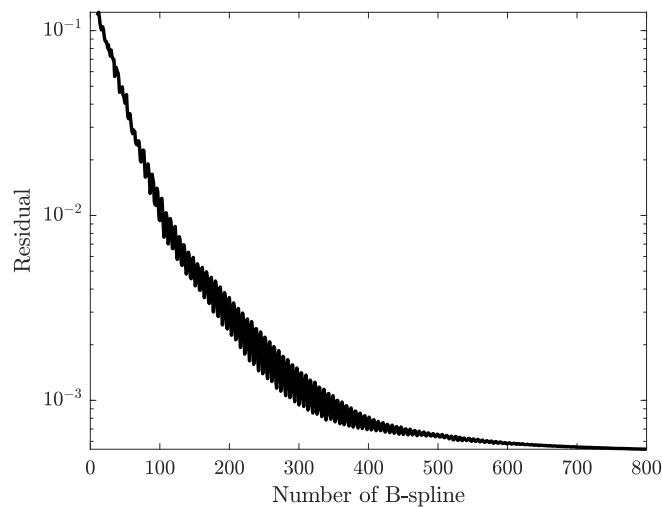


FIGURE 4.27: *Residual considering the simplified model and measurement of the pitch of the aircraft*

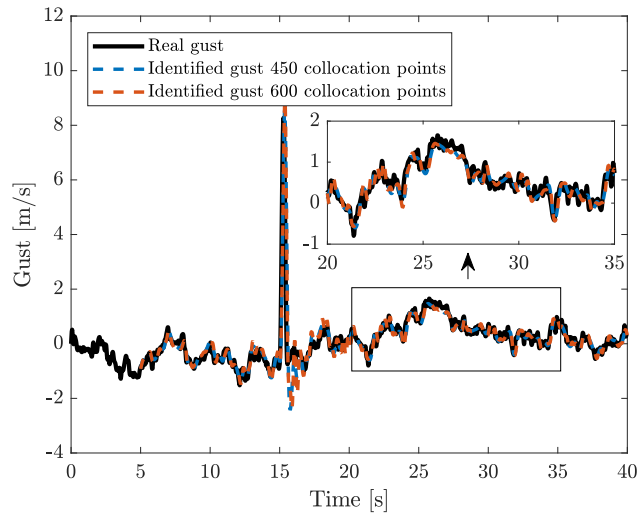


FIGURE 4.28: *Gust and turbulence event reconstruction considering the simplified model, the measurement of the pitch of the aircraft and 450 and 600 collocation points*

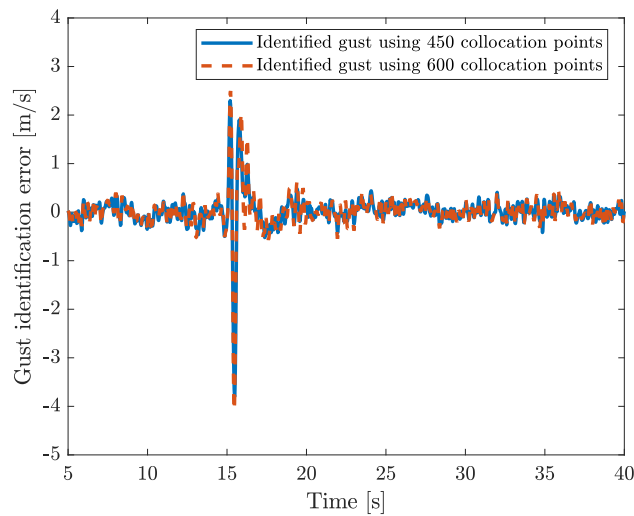


FIGURE 4.29: *Error in the gust and turbulence event reconstruction*

---

## 4.5 Conclusion

---

This Chapter demonstrates a robust technique for aircraft gust identification based on cubic B-splines. Two aeroelastic models were used, a simplified model and a higher fidelity model. Both the models were used to generate data and the identification by cubic B-splines were performed considering reduced-order models of the detailed model and the simplified model. The results shown that it is possible to reconstruct the gust using

models with a small number of degrees of freedom. The identification of the turbulence event gives similar results considering different reduced-order models and, better results can be obtained considering reduced-order models than the simplified model.

# Chapter 5

## GENERATION OF GUSTS IN THE WIND TUNNEL

The validation of active and passive wing gust load alleviation system in the wind tunnel require a Gust Generator (GG). In this Chapter, the design, installation, and commissioning of a GG in the Swansea University wind tunnel are reported. First of all, the desired gusts, as well as the GG design with the component selected, are introduced. Consequently, hot-wire anemometer, vane rotation profile, post-processing technique used are discussed. Discrete and continuous gusts and flow uniformity measurements are presented along with the main reason behind the discrepancy between the desired and the measured ‘1-cos’ gusts. Two innovative techniques to improve the discrete gusts were considered. When a ‘perfect’ ‘1-cos’ gust profile is produced in the wind tunnel, the comparability between data from different facilities and experiments and simulations is significantly improved. In addition, standardization, benchmarking, simulation validation, and reproducibility are improved when a ‘book’ case is correctly reproduced experimentally.

## 5.1 Gust Generator Design, Installation and Commissioning

The aim of the GG is to create gusts according to the CS25 certification from the EASA [26]. In this work, discrete gusts and continuous sinusoidal (harmonic) gust are considered. Figure 5.1a shows gusts at different wavelengths at 200 m/s and sea level according to EASA. Discrete gusts can be seen as a realistic impulse excitation for an aircraft. The duration of the impulse influences the frequency content of the impulse response. Figure 5.1b shows the Fourier transform of the discrete gusts with a maximum amplitude of 20 m/s and gust wavelengths of 40 m and 20 m at an airspeed of 200 m/s, which corresponds to 5 Hz and 10 Hz for 40 and 20 m, respectively. The range of frequency with a flat frequency content is inversely proportional to the duration of the impulse, which in this case, is the gust length. Indeed, a discrete gust with a high gust length mainly excites aircraft's rigid body modes, while a discrete gust with a small gust length excites aircraft's rigid body modes and elastic modes. In the rest of this work, discrete gusts are described in terms of maximum amplitude and frequency, where the frequency is defined as the inverse of the impulse duration.

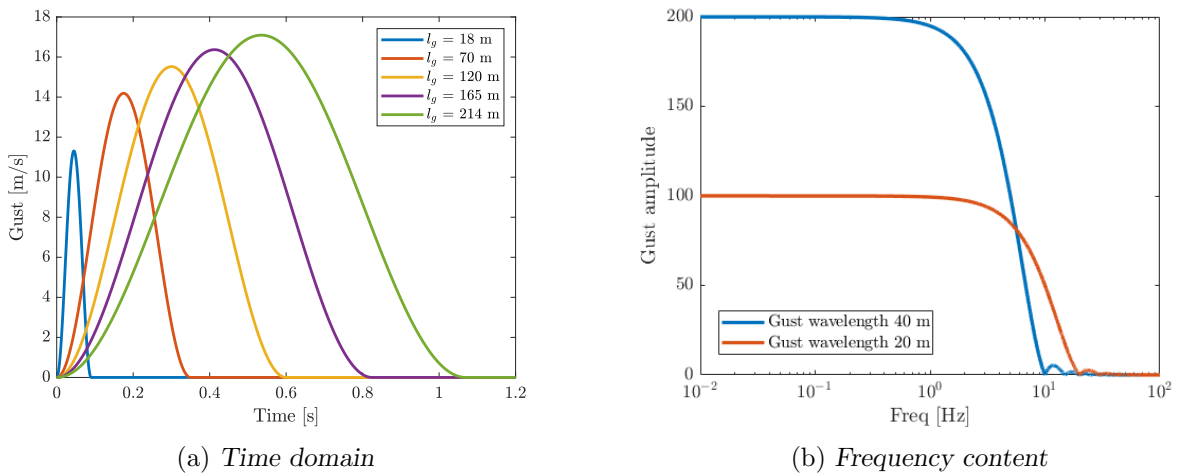
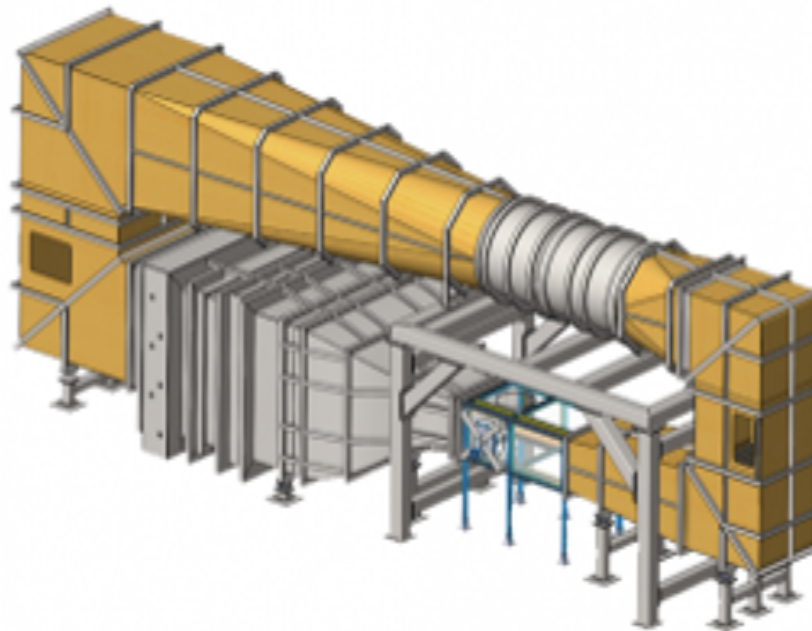


FIGURE 5.1: Discrete gust with different gust wavelengths

Figure 5.2 shows the Swansea University wind tunnel, which is a closed section, closed-circuit system with a test section of 1.5 m by 1 m and a length of 2.36 m. It has temperature control and an airspeed control system that allows working velocities between 10 m/s to 50 m/s.

FIGURE 5.2: *Swansea University wind tunnel*

The GG should be able to produce continuous and discrete gusts with a maximum frequency of 14 Hz and amplitude range from  $5^\circ$  to  $20^\circ$ . The design of the GG, e.g., number of vanes, vane profile, chord and span dimensions, the separation between vanes, and actuation type, were selected based on suggestions given in [14, 82] and engineering judgment. As discussed in [14], increasing the number of vanes could both increase the maximum gust angle and lead to a more uniform gust field in the wind tunnel, but it would increase the blockage in the test section. Moreover, the flow in the test section would be affected by the wakes of the vanes [14]. Vanes with a higher chord dimension could produce gusts with higher intensity, but increasing the chord dimension will increase the inertia and the torque required to rotate the vanes. Reducing the vertical separation between the vanes could produce more significant gusts. However, for future aeroelastic testing of wings subjected to gusts, considering keeping the wing to be tested between the vanes, a small vertical separation would reduce the working height [82]. Considering the Swansea University wind tunnel size, two horizontal vanes were used to cover the entire width of the chamber. The rest of this section will present the vane design, vane actuation, the GG installation, the vane structural characterisation, and the smoke test.

### 5.1.1 Vane Design

A NACA0015 profile with 200 mm chord was chosen to have a symmetric airfoil, limiting the thickness but allowing a spar to fit inside. For manufacturing simplicity, 3D printed

vanes were used. The rigidity of each vane was ensured by a hardened steel shaft to which the 3D printed vanes were bonded at the quarter chord to limit the aerodynamic and structural coupling. Due to the 3D printer size limitations, each vane consists of eight sections. Table 5.1 reports the main vane proprieties. SOLIDWORKS [138] was used to calculate the vane inertia around the axis of rotation. Figure 5.3 shows one 3D

Vane	
Chord	200 mm
Span	1500 mm
Airfoil profile	NACA0015
Vane material	ABS
Density	1.04 g/cm <sup>3</sup>
Young's modulus	2.4 · 10 <sup>9</sup> Pa
Inertia	113.03 · 10 <sup>-4</sup> kg·m <sup>2</sup>
Spar	
Spar diameter	16 mm
Inertia	0.99 · 10 <sup>-4</sup> kg·m <sup>2</sup>
Spar material	Hardened steel
Density	8000 kg/m <sup>3</sup>
Young's modulus	2.00 · 10 <sup>11</sup> Pa

TABLE 5.1: Vane design and dimensions

printed section of the vane. Only some parts of the internal airfoil cross-section were 3D printed to reduce the vane's weight but keeping a high stiffness.



FIGURE 5.3: 3D printed section

Each 3D printed section was bounded to the shaft using PERMABOND TA4204, a 2-part, 1:1 toughened acrylic adhesive. Figures 5.4 and 5.4b show vanes during the assembly process and before the installation.

The vanes are supported on both sides by a 20 mm aluminum plate, and cylinder bearings constrain all the degrees of freedom except for the translation and rotation around the bearing axis. The supporting plates are connected to the wind tunnel aluminum frame.

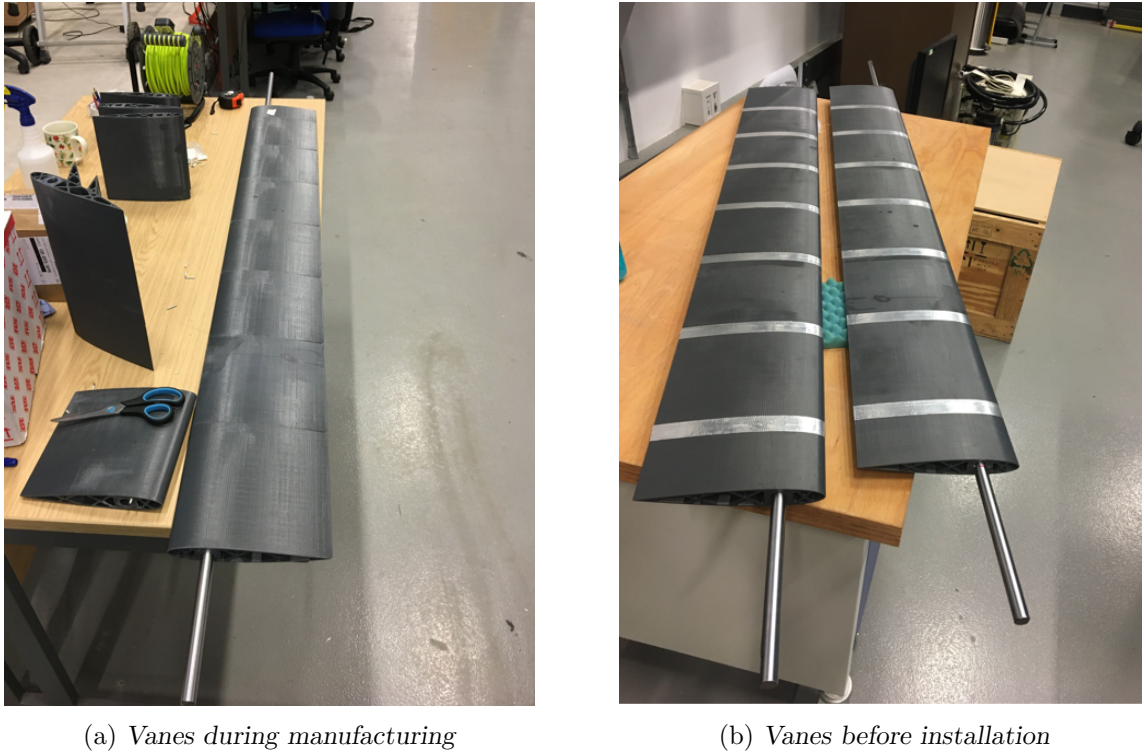


FIGURE 5.4: Vanes during manufacturing and before to be installed

From the Euler Bernoulli beam theory, the first natural frequency of a fixed-fixed beam with homogeneous isotropic linear elastic material is inversely proportional to the square of the length. Therefore, the bearings are at 3 mm from the wind tunnel plexiglass to reduce the first out-of-plane bending frequency. Figure 5.5 shows the vane support plate.

### 5.1.2 Actuation

The gust vanes are actuated using two independent servomotors, which ensures independent motion. The maximum bandwidth of the motion is limited by the maximum torque available from the motor. Servomotors are specified by peak torque and velocity requirements; the first principle can be used to calculate those parameters. The vane deflection  $\theta_{GG}(t)$  is expressed as,

$$\theta_{GG}(t) = \frac{A_{GG}}{2} \left[ 1 - \cos(2\pi ft) \right] \quad (5.1)$$

where  $A_{GG}$  is the maximum deflection of the vanes in degrees and  $f$  is the frequency in Hertz. Differentiating Eq.(5.1) with respect to time provides, the expression for the



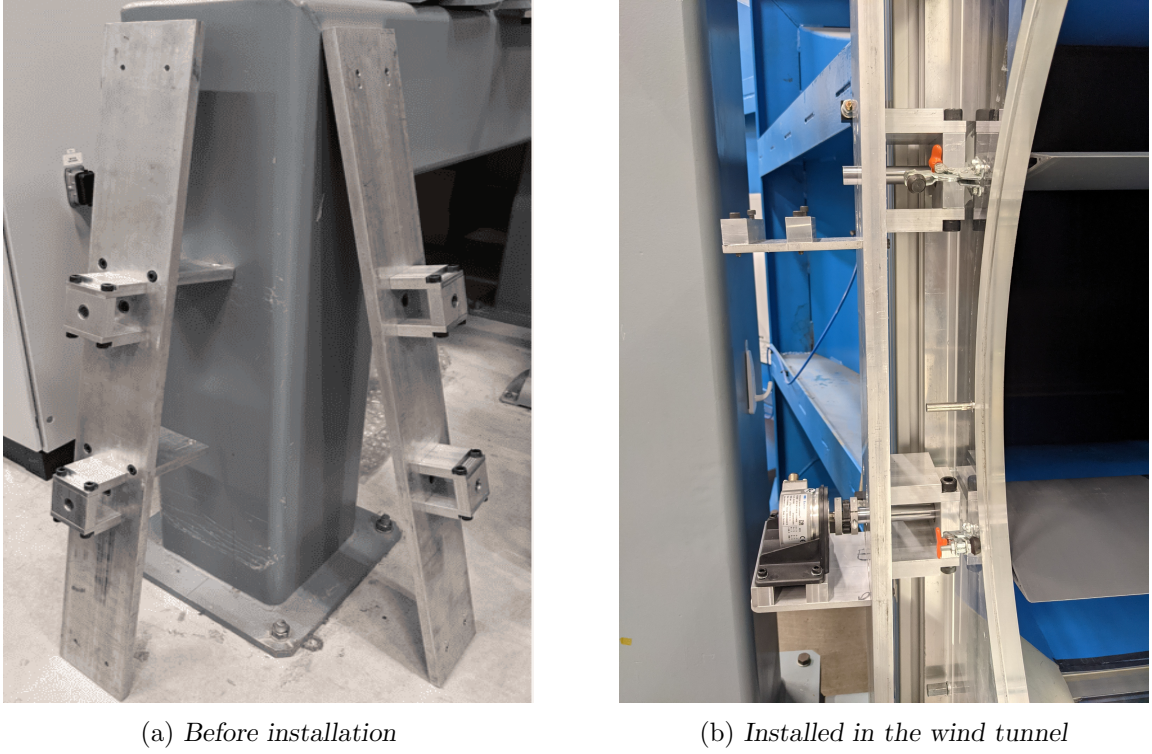


FIGURE 5.5: Vane support before installation and installed in the wind tunnel

rotational velocity,

$$\dot{\theta}_{GG}(t) = A_{GG}\pi f \sin(2\pi ft) \quad (5.2)$$

Differentiating Eq.(5.2) with respect to time, provides the expression for the rotational acceleration,

$$\ddot{\theta}_{GG}(t) = 2A_{GG}(\pi f)^2 \cos(2\pi ft) \quad (5.3)$$

Table 5.2 shows the peak rotational velocity and rotational acceleration values from Eqs.(5.2) and (5.3). The peak torque requirement is based upon the peak acceleration

Amplitude [deg]	Frequency [Hz]	Velocity [rad/s]	Acceleration [deg/s <sup>2</sup> ]
5	30	8.22	15503
10	25	13.71	21532
20	20	21.93	27561

TABLE 5.2: Minimum required vane deflection performance

and the combined rotational inertia of the whole system, including the vane, motor coil, couplings, and any other rotating parts. The minimum required torque  $T_{max}$  for each motor, considering  $n$  components connected to it, can be expressed as,

$$T_{max} = \sum_i^n I_i \ddot{\theta}_{GG_i} \quad (5.4)$$

where  $\ddot{\theta}_{GG_i}$  and  $I_i$  are the peak rotational accelerations and inertia of the  $i$ -th component, respectively. A low backlash gearbox was introduced between the vane and the motor to reduce the required motor torque and increase the motor rotation. Moreover, the gearbox is essential as it decreases the motor error by a factor of the gearing ratio, as

$$B_{tot} = \frac{B_m}{r_g} + B_g \quad (5.5)$$

where  $r_g$  is the gearbox ratio,  $B_{tot}$ ,  $B_m$ , and  $B_g$  are the backlash of the motor coupled with the gearbox, the backlash of the motor, and the backlash of the gearbox, respectively. An iterative process was followed to select the components to ensure the torque requirements. Servomotor and drive were selected to ensure with a safe margin the torque requirements. The gearbox was selected to have the lower backlash possible. Indeed, gearboxes vary in backlash from 15 to 1 arcmin. Up to a ratio of 10:1, single-stage gearboxes can be used, but at higher ratios, two-stage gearboxes must be used, which have significantly more backlash due to extra moving parts, so a 10:1 ratio was chosen. An elastomer coupling was selected to couple the gearbox with the spar allowing a minor misalignment. Table 5.3 summarise the parts selected with the main features. The final torque requirements

Servomotor	Kollmorgen AKM43E-AN9NCA00 Peak torque 15.9 Nm Maximum torque 40 Nm Inertia $2.09 \cdot 10^{-4}$ kg·m <sup>2</sup> Accuracy 10 arcmin
Drive	Kollmorgen AKD-P00306-NBCC-E000
Gearbox	SP+075MF 2 arcmin of backlash Inertia $0.54 \cdot 10^{-4}$ kg·m <sup>2</sup> Torsional rigidity 10 Nm/arcmin
Coupling	EKL-00020BA022 Maximum torque 37.8 Nm Axial misalignment 2 mm Angular misalignment 0.8° Lateral misalignment 0.08 mm Torsional rigidity 1.3 Nm/arcmin Moment of inertia 0.2 kg·cm <sup>2</sup>

TABLE 5.3: *Parts selected*

are summarised in Table 5.4. The peak motor torque requirement is found summing all the torque requirements transformed in the motor reference frame. Considering all the contributions from Table 5.4, the minimum peak torque required from the motor is 10.95 Nm. The selected servomotor has a sufficient peak torque.

Component	Inertia [kg·m <sup>2</sup> ]	Acceleration [rad/s <sup>2</sup> ]	Torque [Nm]	Torque motor reference frame [Nm]
Motor	$2.09 \cdot 10^{-4}$	275610	5.76	5.76
Gearbox	$0.54 \cdot 10^{-4}$	275610	1.49	1.49
Coupling	$0.20 \cdot 10^{-4}$	27561	0.06	0.006
Spar	$0.99 \cdot 10^{-4}$	27561	0.27	0.03
Vane	$113.03 \cdot 10^{-4}$	27561	36.66	3.67

TABLE 5.4: *Inertia and torque requirements of rotating parts in their own reference frames*

Figure 5.6 shows motors, gearboxes, and couplings installed in the wind tunnel.

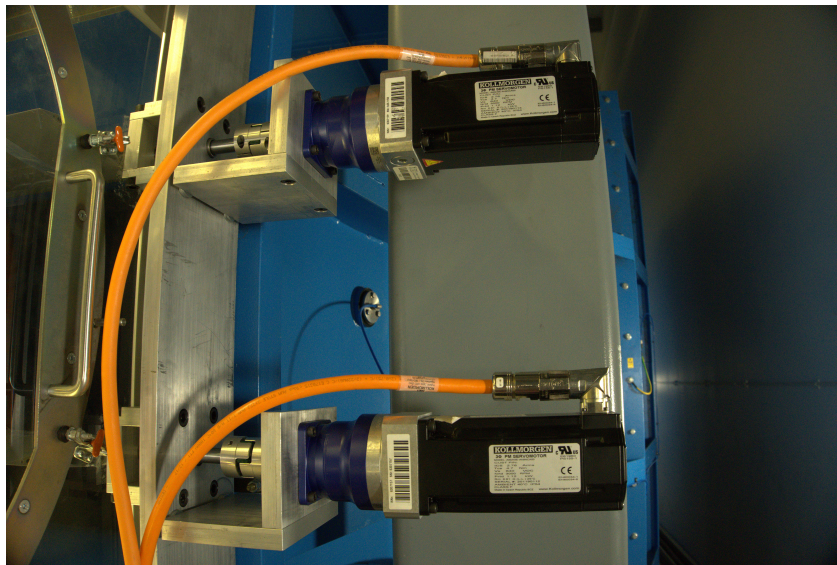
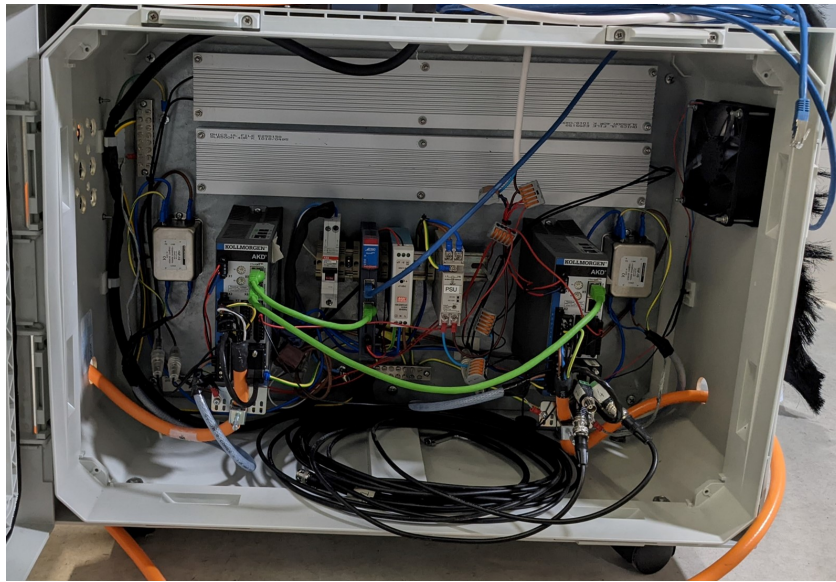
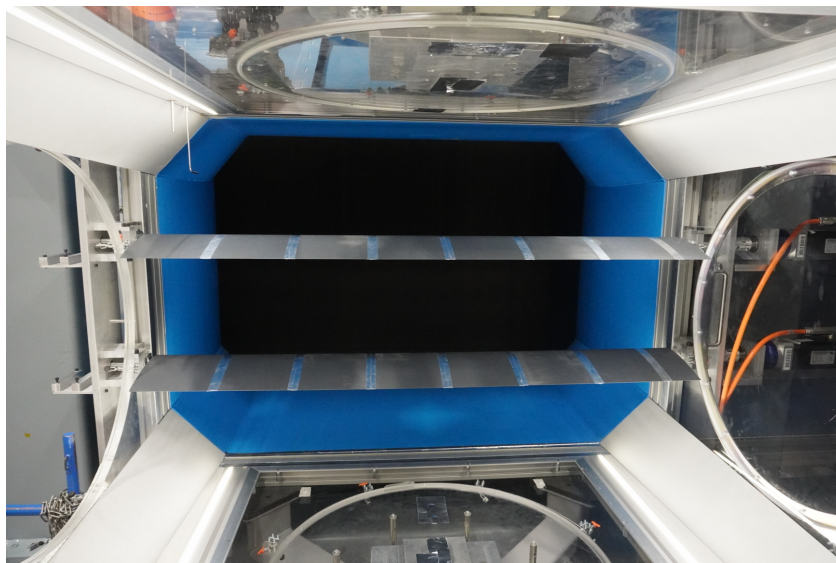
FIGURE 5.6: *Motors, gearboxes, and couplings*

Figure 5.7 shows the drives with the electrical connections used to control the servomotors controlled by a laptop. Figure 5.8 shows the vanes installed in the wind tunnel. The GG was located at the start of the wind tunnel test section to have enough space to fit future models for wing gust experiments. Figure 5.9 shows the vanes during the installation in the wind tunnel.

### 5.1.3 Vane Structural Characterisation

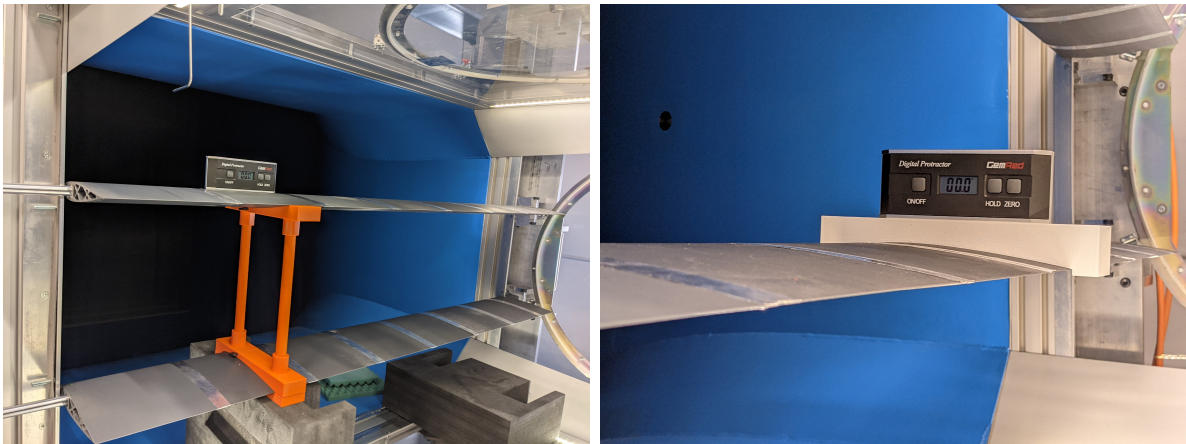
Structural dynamic characterisation was performed to assess the first natural frequency of the vane installed in the wind tunnel. Knowing the first vane natural frequency allows the identification of oscillations in the gust profile that are due to the vane vibration. The first natural frequency was identified by hammer test at 19.7 Hz.

FIGURE 5.7: *Drives*FIGURE 5.8: *Gust generator installed in the wind tunnel*

#### 5.1.4 Smoke Test

The smoke test was performed to visually assess the ability of the GG to produce discrete gusts. The vanes were setup to rotate to produce discrete gusts, and smoke was introduced in the chamber. Figure 5.10 illustrates how the gust is produced by the rotation of the vanes. The steps involved in the creating of the gust are:

- (a) at the initial conditions, vanes are at  $0^\circ$ , and the smoke is undisturbed;
- (b) vanes are rotating downwards, and the smoke is not affected;



(a) Levelling block to ensure the vanes are in the horizontal position

(b) Levelling block to ensure the vanes are at  $0^\circ$  angle of attack

FIGURE 5.9: *Gust generator installation*

- (c) vanes are back to  $0^\circ$ , and the smoke move upwards due to the starting vortices;
- (d) the discrete gust appear at the vanes trailing edge;
- (e) the discrete gust travel downstream, after the gust the smoke is undisturbed;
- (f) the discrete gust travel downstream, after the gust the smoke is undisturbed;
- (g) the discrete gust travel downstream, after the gust the smoke is undisturbed;
- (h) at the final conditions, the smoke is undisturbed;

---

## 5.2 Experimental Setup

---

The measurement of turbulence or airspeed fluctuations in the wind tunnel is carried out using suitable instrumentation like hot-wire anemometers, Laser-Doppler Anemometers (LDA), and with Particle-Imaging Velocimetry (PIV). The instrumentations available at the Swansea University Wind Tunnel and suitable for the characterisation of the GG are the PIV and the hot-wire anemometer. The PIV has a sampling frequency of 15 Hz, which does not ensure a proper airspeed characterisation, so hot-wire anemometer was used. This section shows the experimental setup of the hot-wire sensor, the test cases considered, and the procedure used for the post-processing of the data.

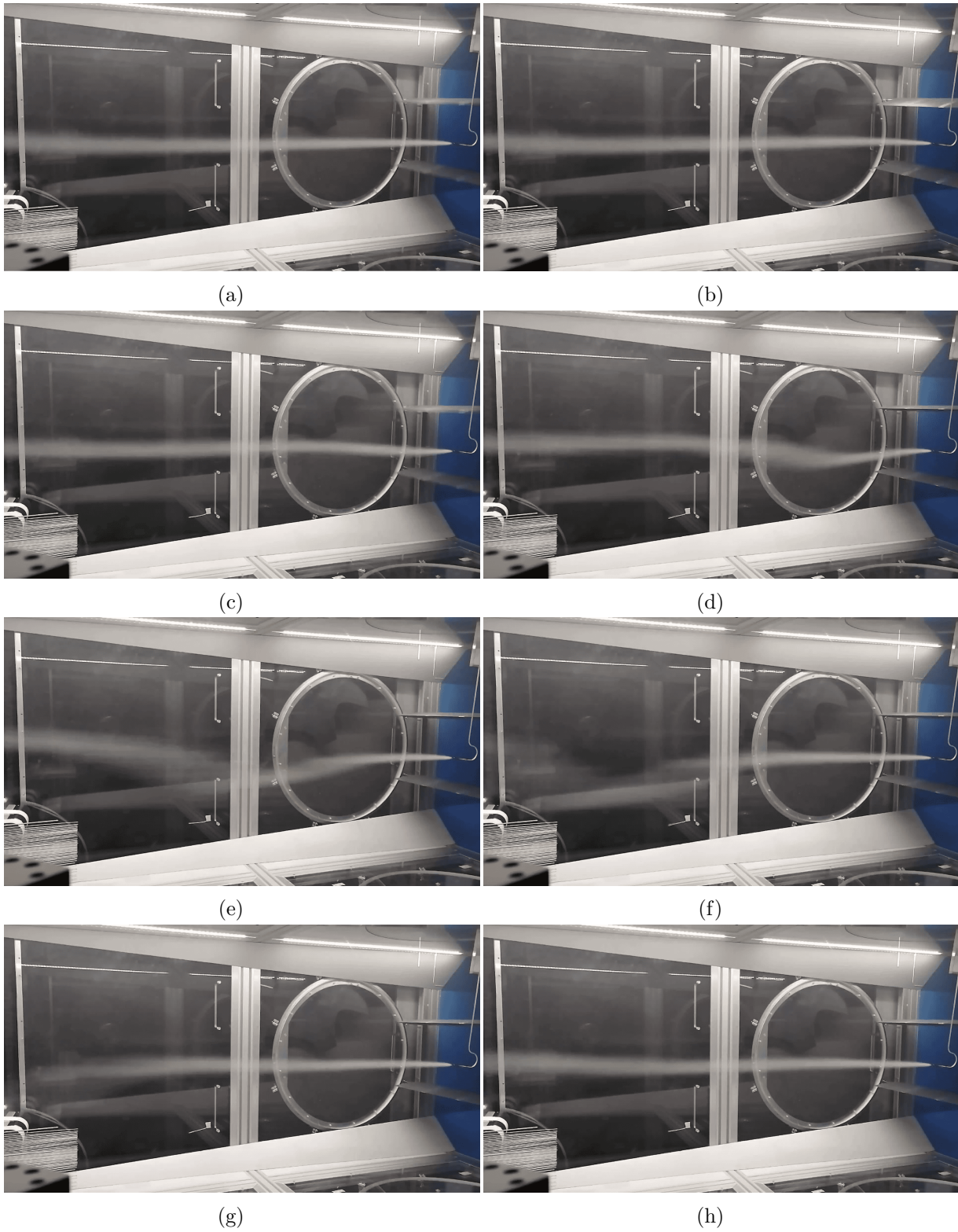


FIGURE 5.10: *Gust generator smoke test*

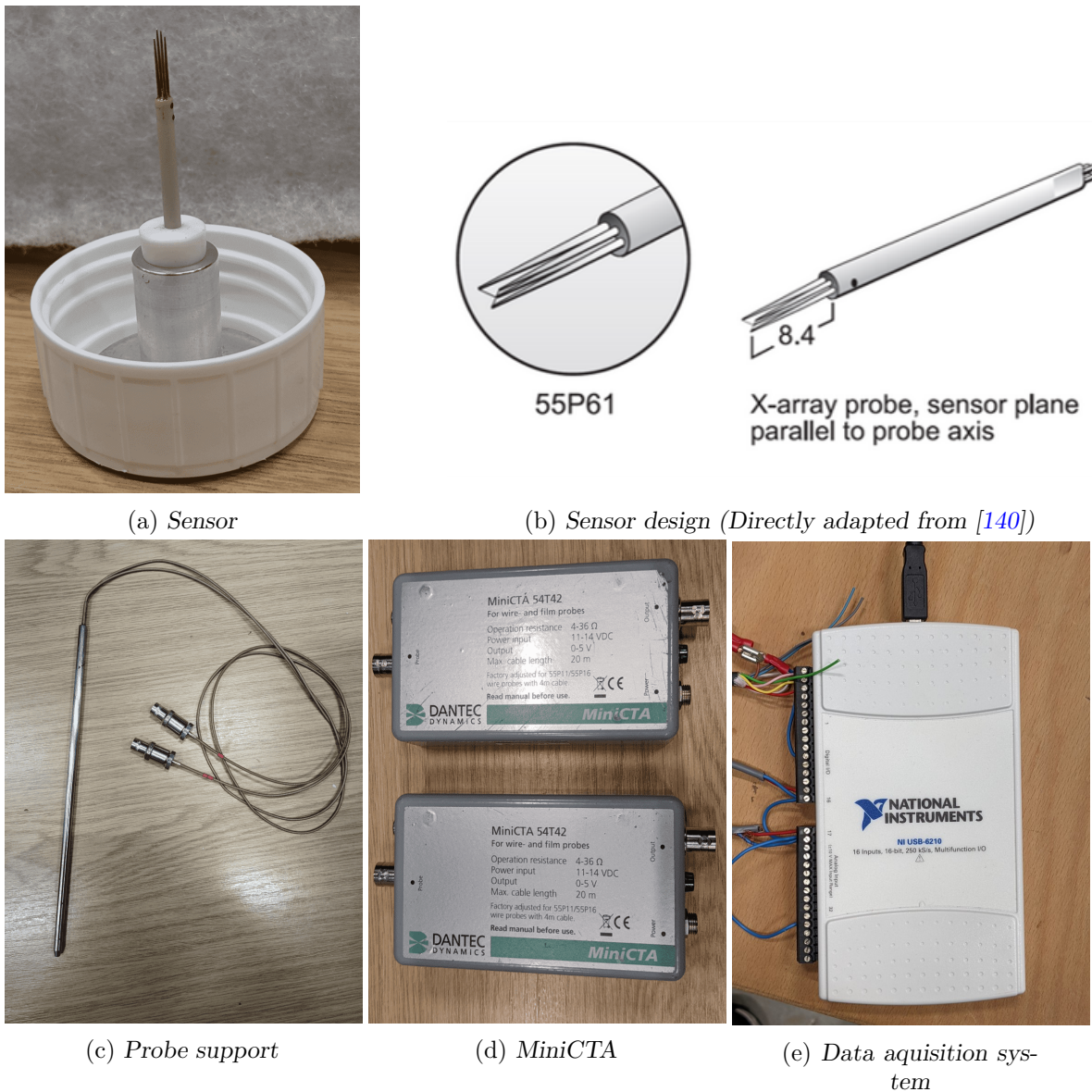
### 5.2.1 Hot-Wire Sensor

The hot-wire anemometer, also called Constant Temperature Anemometer (CTA), is based on convective heat transfer from a heated sensor to the surrounding fluid, where the heat transfer is primarily related to the fluid velocity. Using very fine wire sensors placed in the fluid, coupled with a servo-loop technique, ensures the measurement of velocity fluctuations on a fine-scale and at high frequencies. The advantages of hot-wire sensor over other flow measuring principles are ease of use, the output is an analogue voltage, so no information is lost, very high temporal resolution, and more affordable than LDA or PIV systems [139].

The measuring equipment consist of a probe, probe support, a MiniCTA, an A/D converter, and a computer. Probes are primarily selected on basis of:

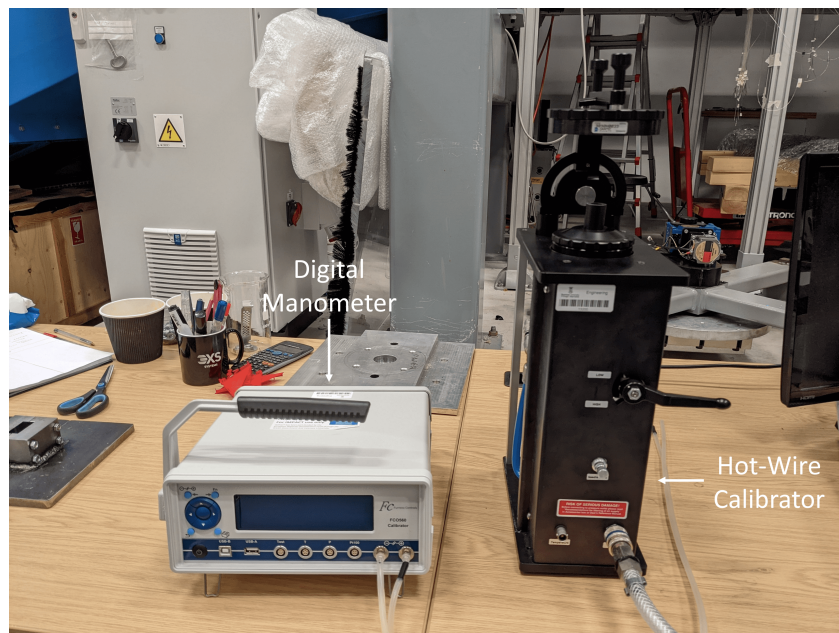
- Fluid medium;
- Expected velocity range;
- Number of velocity components to be measured (one, two or three);
- Quantity to be measured (velocity, wall shear stress etc.);
- Turbulence intensity and fluctuation frequency in the flow;
- Required spatial resolution;
- Temperature variations;
- Available space around the measuring point;
- Contamination risk;

For all the measurements, the straight miniature X wire probe 55P61 was used to measure the horizontal and vertical components of the flow field. The probe has a 5  $\mu\text{m}$  diameter, 1.25 mm long plated tungsten wire sensors, and a 2.3 mm diameter ceramic tube body. The sensors are arranged in X-arrays, where they form an angle of 90° with one another. The dual-sensor probes are designed for use in two-dimensional flows of low turbulence intensity [140]. Figures 5.11a and 5.11b show the cross hot-wire sensor. Figure 5.11c shows the straight, 6 mm diameter, and 235 mm long probe support used. MiniCTA has built-in signal conditioners for high-pass and low-pass filtering and signal amplification and is used to supply power to the sensor. Figure 5.11d shows the two MiniCTA used. To read the analog voltage given as output from the MiniCTA, the National Instruments USB-6210 was used and is shown in Figure 5.11e.

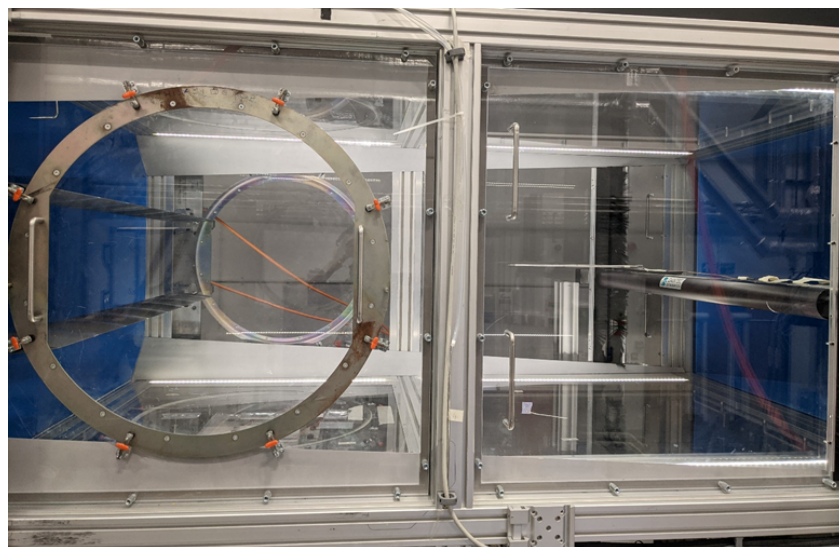
FIGURE 5.11: *Hot wire anemometer equipment used*

Two types of calibrations are required to find the relation between the voltages and airspeed, velocity and directional calibration. In the velocity calibration, the probe is exposed to a set of known velocities at fix angle to determine the coefficients of a fourth-order polynomial equation for each wire probe. Corrections can be used to compensate for the effects of temperature variation. In the directional calibration, the probe is exposed to a set of known velocities at different angles to determine the coefficient of a linear equation for each wire probe. Figure 5.12 shows the equipment used for the calibration. In all the tests, the sampling frequency was kept at 1kHz. The hot-wire anemometer was placed in the center of the cross-section, at the longitudinal distance of 1.234 m from the vane trailing edge (corresponding to 6.2 chords), where future wings



FIGURE 5.12: *Hot wire calibration*

will be set to measure the wing gust response. A 0.3 m stainless steel tube was used as a probe extension to prevent the interference of the probe support on the measurements. The natural frequency of the probe joined with the probe extension was experimentally identified at 25 Hz. Figure 5.13 shows the GG in the wind tunnel with the hot-wire anemometer and the probe extension connected to the traverse.

FIGURE 5.13: *Gust generator in the wind tunnel*

### 5.2.2 Test Cases

A series of wind tunnel tests were performed to assess the ability of the GG to produce single and continuous gusts. In the case of discrete gusts, the shape of the desired gusts are described by Eq. (2.7), so the vane rotation profile  $\theta_{GG}(t)$  was set to follow a similar movement according to

$$\theta_{GG}(t) = \begin{cases} \frac{A_{GG}}{2} \left[ 1 - \cos(2\pi ft) \right] & \text{for } 0 \leq t \leq \frac{1}{f} \\ 0 & \text{for } t > \frac{1}{f} \end{cases} \quad (5.6)$$

where  $A_{GG}$  is the maximum deflection of the vanes in degrees and  $f$  is the frequency in Hertz. An encoder on the motor was used to record the motor rotation to ensure a correct actuation. Due to the high-performance coupling and low backlash gearbox, the vane rotation is expected to follow the motor at the gearbox location. Moving along the vane, the torsion flexibility will introduce a difference between the real and the expected rotation. Nevertheless, at the vane opposite extremity with respect to the motor, the error is expected to be small due to the spar's high torsional stiffness. The free stream velocity ranged from 10 m/s to 26 m/s. This corresponds to a Reynolds numbers in the range of  $2.45 \cdot 10^5$  to  $6.4 \cdot 10^5$  considering the vane chord as characteristic length. In the tests, the vane maximum pitch amplitude ranged from  $5^\circ$  to  $20^\circ$  in  $5^\circ$  increments, while the vane rotation frequency ranged from 1 Hz to 14 Hz. Higher pitching frequencies were avoided to avoid excessive vane vibrations. The maximum reduced frequency is  $k = 0.88$ , where  $k$  is defined as

$$k = \frac{\omega c}{2V_\infty} \quad (5.7)$$

where  $\omega = 2\pi f$ ,  $c$  is the vane chord and  $V_\infty$  is the free stream velocity.

In the case of continuous sinusoidal gusts, the vane rotation profile was set to follow a sinusoidal trajectory, defined as

$$\theta_{GG}(t) = A_{GG} \sin(2\pi ft) \quad (5.8)$$

In this case, the free stream velocity ranged from 10 m/s to 18 m/s, the vane maximum amplitudes are  $5^\circ$  and  $12.5^\circ$ , and the vane rotation frequency varies from 1 Hz to 10 Hz. At the highest rotational speed, the reduced frequency is  $k = 0.63$ . The main objective of this work was to improve the creation of discrete gusts, and so continuous sinusoidal gusts were considered for only a limited set of airspeed and frequency.

### 5.2.3 Post-Processing

The effect of the gust was considered as a temporary change of the angle of attack, calculated as

$$\alpha = \text{atan}\left(\frac{V_{hw}}{U_{hw}}\right) \quad (5.9)$$

where  $V_{hw}$  and  $U_{hw}$  are the vertical and horizontal airspeeds measured by the cross hot-wire sensor. The measured data were filtered using a low-pass filter and a notch filter. The measurement from the hot-wire sensor introduces noise at all frequencies. Therefore, the low-pass filter is required to attenuate the high-frequency noise. The low-pass filter has the transfer function as

$$H(s) = \frac{\omega_0}{s + \omega_0} \quad (5.10)$$

where  $\omega_0 = 2\pi f_0$  and  $f_0$  is the cut-off frequency in Hertz. The low-pass filter is required to attenuate the high-frequency noise measured due to the high sampling ratio. As, the GG will be used to measure the gust response of wings characterized by low aeroelastic frequencies, which would act as a low pass filter, it is expected that higher frequencies will have a negligible impact. The cut-off frequency was set to 20 Hz. Figure 5.14a shows the Bode plot of a low-pass filter with 20 Hz cut-off frequency. A notch filter with a transfer function as

$$H(s) = \frac{s^2 + \omega_0^2}{s^2 + \omega_c s + \omega_0^2} \quad (5.11)$$

where  $\omega_0$  is the central rejected frequency and  $\omega_c$  is the width of the rejected band. The notch filter with a central rejected frequency of 25 Hz and rejected band of 5 Hz was used to reduce the noise due to the probe extension vibrations. Figure 5.14 shows the Bode plot of the notch filter used.

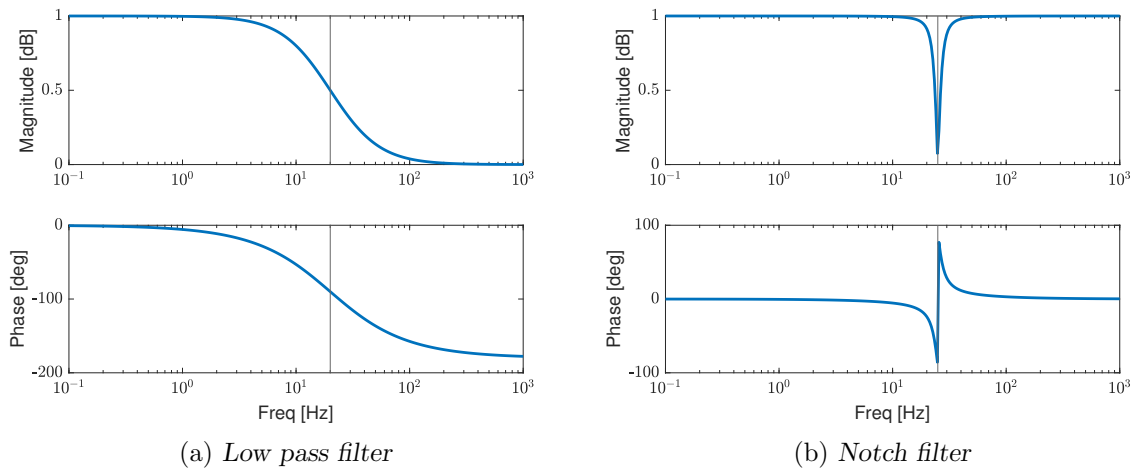


FIGURE 5.14: Bode plot of the filters used

## 5.3 Initial Results

In this section, the results for the discrete gusts and continuous sinusoidal gusts are presented. Figure 5.15 shows the measured gust and the filtered gust. The oscillations at 25 Hz before and after the main peaks and the high-frequency oscillations were filtered out. Indeed, the maximum gust peak is attenuated. Figure 5.16 shows the measured angle of attack repeated three times, measured when the vane rotation amplitude is  $10^\circ$ , the frequency is 8 Hz, and the airspeed is 14 m/s. The maximum standard deviation of the measurements is  $0.14^\circ$ , and it is at the maximum peak.

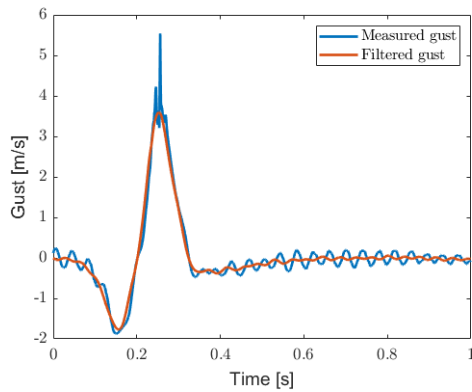


FIGURE 5.15: *Measured gust and filtered gust*

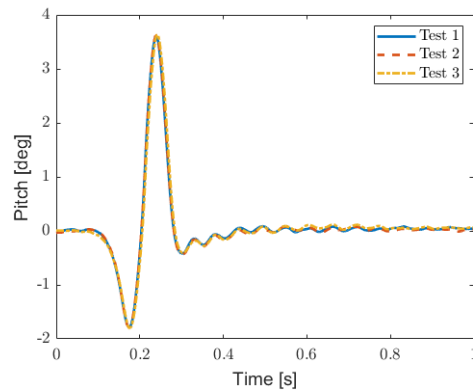


FIGURE 5.16: *Discrete gust, evaluation repeatability*

### 5.3.1 Discrete Gust

Figures 5.17 and 5.18 show the measured flow angles at different airspeeds and pitching amplitude. The results show that with increasing airspeed, the maximum peak reduces while increasing the pitching frequency or increasing the pitch amplitude causes the peak to increase. Figure 5.18 shows that varying the airspeed, or maximum vane rotation amplitude, or gust frequency gives consistent results. Figure 5.17 shows that varying airspeed, and gust frequency gives consistent results only for small ( $5^\circ$  and  $10^\circ$ ) pitch amplitude. For low gust frequency and high maximum vane rotation amplitude, the gust profile is chaotic and inconsistent.

It is likely that the behavior is related to dynamic stall. This phenomenon is significantly affected by the reduced frequency, while the Reynolds number has only a small effect on it [141, 142]. The effect of reduced frequency on the dynamic stall phenomenon is

a well-studied problem; in particular, the dynamic stall angle increases with reduced frequency [141–144]. In the case of reduced frequencies smaller than 0.05, it is possible to consider the flow as steady flow, while for reduced frequencies greater than 0.2, the flow is highly unsteady [144]. The results shown in Figure 5.17 cover a wide range of reduced frequencies. In the literature for a profile NACA0015 at Reynolds number  $3.6 \cdot 10^5$  the static stall angle is at  $13.9^\circ$  [145]. In the case of airspeed 26 m/s and gust frequency 1 Hz, the reduced frequency is 0.024, and the Reynolds number is  $2.45 \cdot 10^5$ , so, it is plausible that at  $15^\circ$  the profile is stalled and at  $20^\circ$  the profile is well beyond the stall condition. At the same gust frequency and lower airspeed, the reduced frequency is increasing, so the effect of the dynamic stall vortex is becoming more important. Indeed, for a gust frequency 1 Hz and maximum vane rotations of  $15^\circ$  and  $20^\circ$  and increasing the airspeed causes the measured gust to become less chaotic. The low repeatability of the measurements affected by the dynamic stall is expected because experimental data shown that the stall behaviour is associated with different separation patterns and is not repeatable [146, 147]. Similar trends are exhibit for gusts with higher frequencies. Based on repeatability and shape of the gust, for the very low value of  $k$ , the GG can always generate gusts for vane rotation amplitude of  $5^\circ$ . For  $k \geq 0.19$ , it can create gusts for vane rotation amplitude of  $10^\circ$  and  $15^\circ$  and for  $k \geq 0.38$ , it can create gusts for vane rotation amplitude of  $20^\circ$ . The results are also in agreement with previous similar work [82].

Figure 5.19 shows the maximum gust peaks as a function of frequency and maximum vane angle of rotation generated using Eq. 5.6 at an airspeed of 18 m/s. At each frequency considered, the trend is again linear in the range of  $5^\circ$  to  $15^\circ$ . For frequencies greater than 9 Hz, the trend is linear in the range  $5^\circ$  to  $20^\circ$ . Similar trends were observed at airspeeds of 10 m/s, 14 m/s, 22 m/s, and 26 m/s.

### 5.3.2 Continuous Gusts

Figures 5.20 and 5.21 shows the pitch angle measurements in the case of the continuous gust. As in the case of the discrete gust, increasing the airspeed, causes the maximum peak to reduce while increasing the pitching frequency of rotation or increasing the maximum vane rotation amplitude causes the peak to increase.

The gusts in Figure 5.18 for gust frequencies greater than 10 Hz show some oscillations at 19.7 Hz, after the main peak, which are due to vibrations of the vanes. This effect is not important in harmonic excitation because the transient response is ignored.

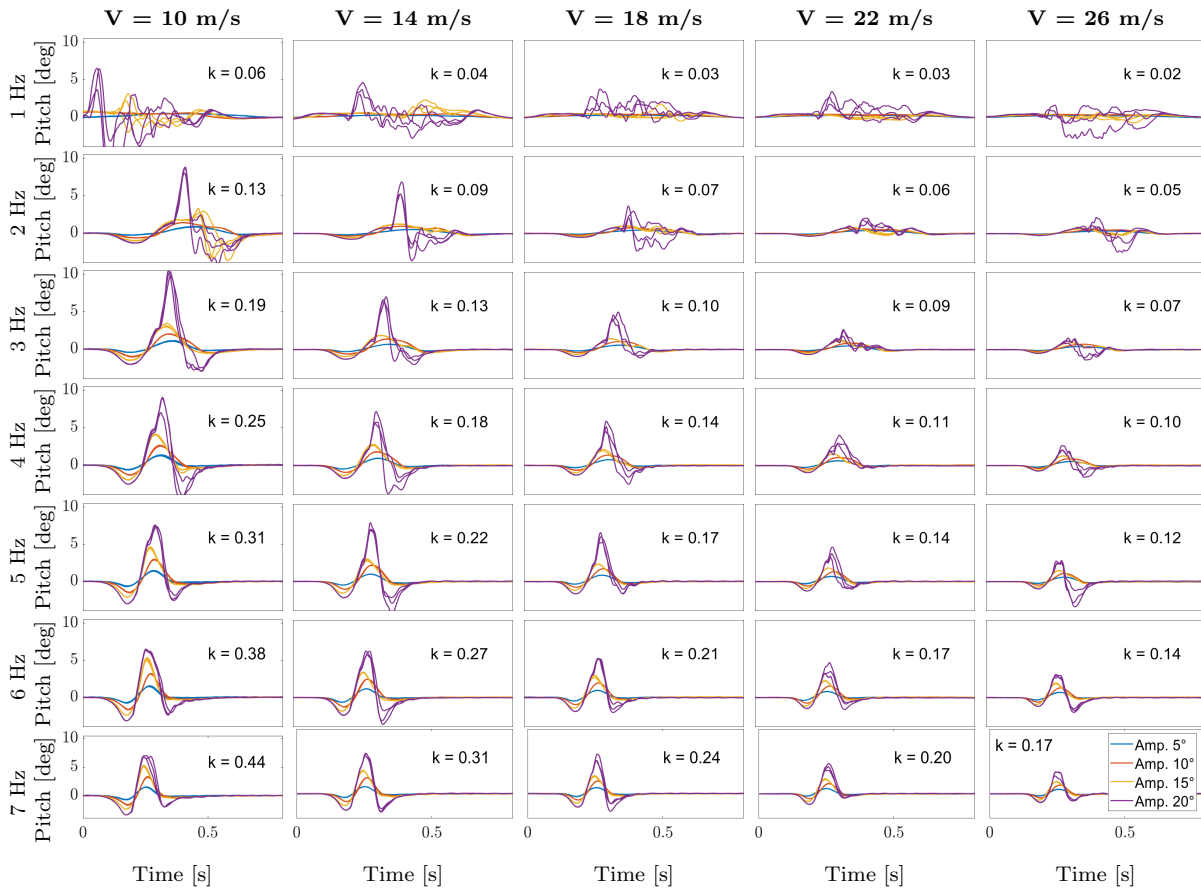


FIGURE 5.17: Discrete gust vane rotations amplitude of  $5^\circ$ ,  $10^\circ$ ,  $15^\circ$  and  $20^\circ$ , 1 to 7 Hz rotation frequency. Each case was repeated three times and all data are plotted

### 5.3.3 Flow Uniformity

Two tests were performed to assess the uniformity of the gust produced by the GG in the wind tunnel cross-section. In both cases, the symmetry of the test chamber is considered. In the first test, the anemometer was moved horizontally (in the vane span direction) in three additional positions with respect to the central position. Each point is 150 mm from the previous one. Figure 5.22a shows the locations considered. Figure 5.22b shows the discrete gusts measured at the four positions, considering an airspeed of 10 m/s,  $10^\circ$  maximum vane rotation, and a gust frequency range of 5 Hz to 10 Hz. The results show a good uniformity of the gust field at all the stations considered. For all the cases considered, the difference between the gusts peaks measured at the central position and the ones measured at positions 2, 3, and 4 are  $0.046^\circ$ ,  $0.003^\circ$ , and  $0.163^\circ$ . The uniformity of the flow ensures that in future aeroelastic tests, the wing will be subjected to a uniform gust along the span.

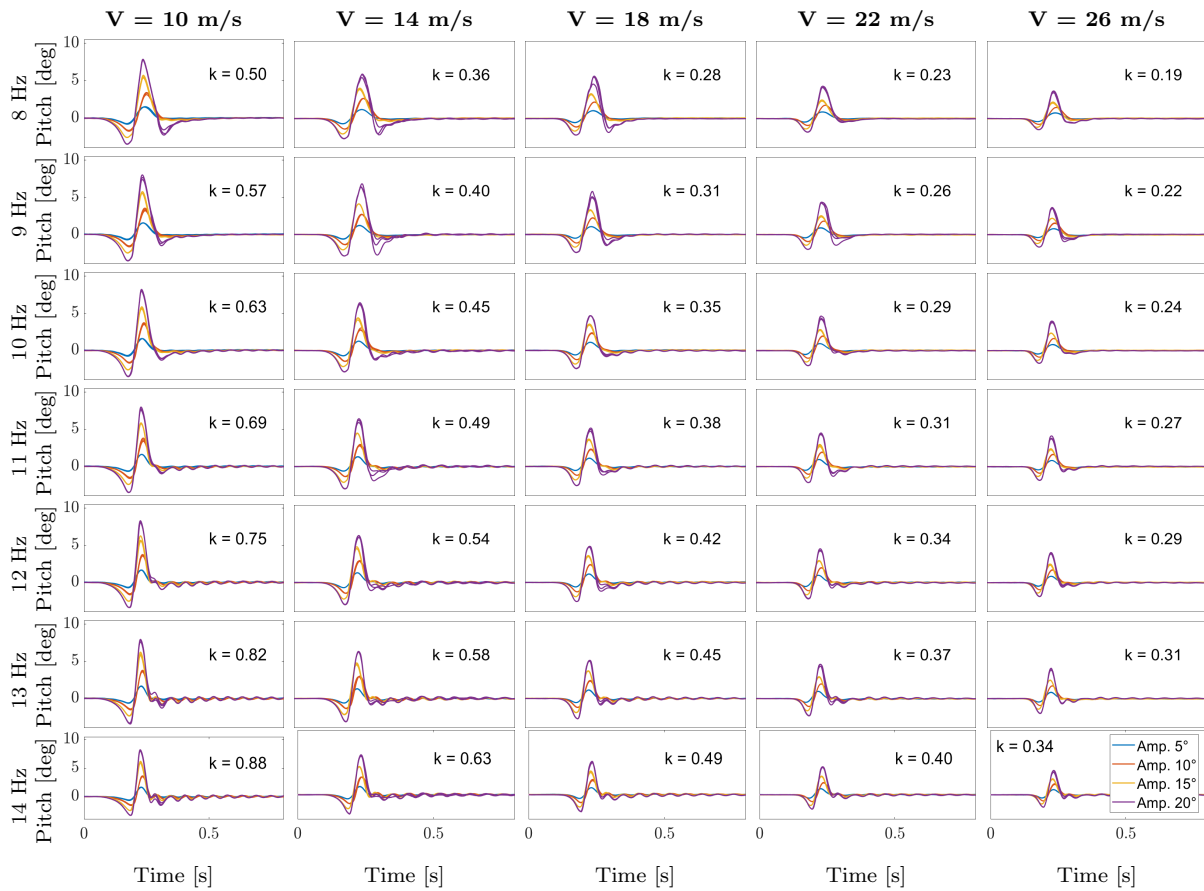


FIGURE 5.18: Discrete gust vane rotations amplitude of  $5^\circ$ ,  $10^\circ$ ,  $15^\circ$  and  $20^\circ$ , 8 to 14 Hz rotation frequency. Each case was repeated three time and all data are plotted

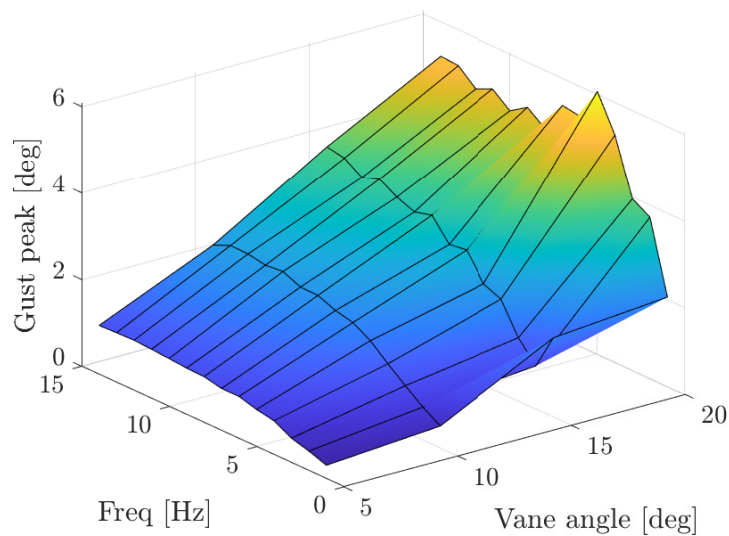


FIGURE 5.19: Maximum gust peaks as a function of frequency and maximum vane angle of rotation for gusts at 18 m/s

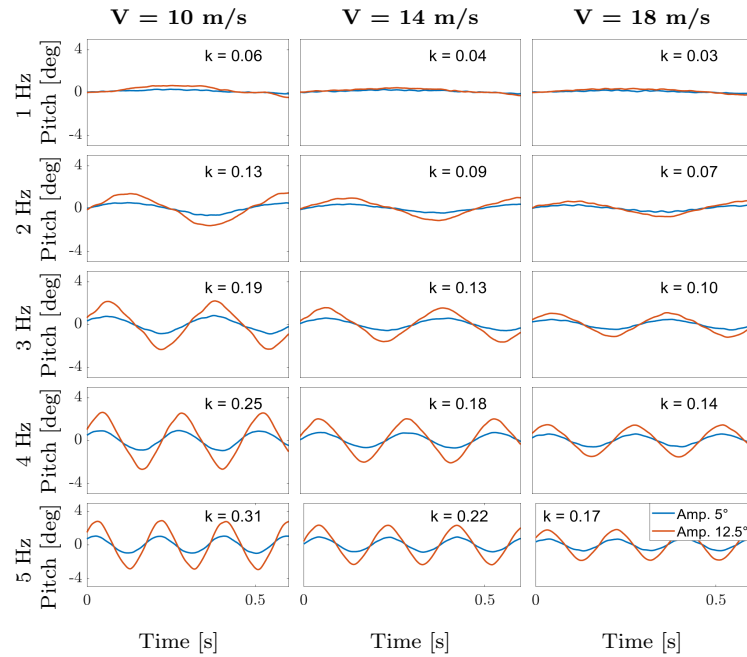


FIGURE 5.20: Continuous gust for vane rotations amplitude of  $5^\circ$  and  $12.5^\circ$ , at 1 to 5 Hz

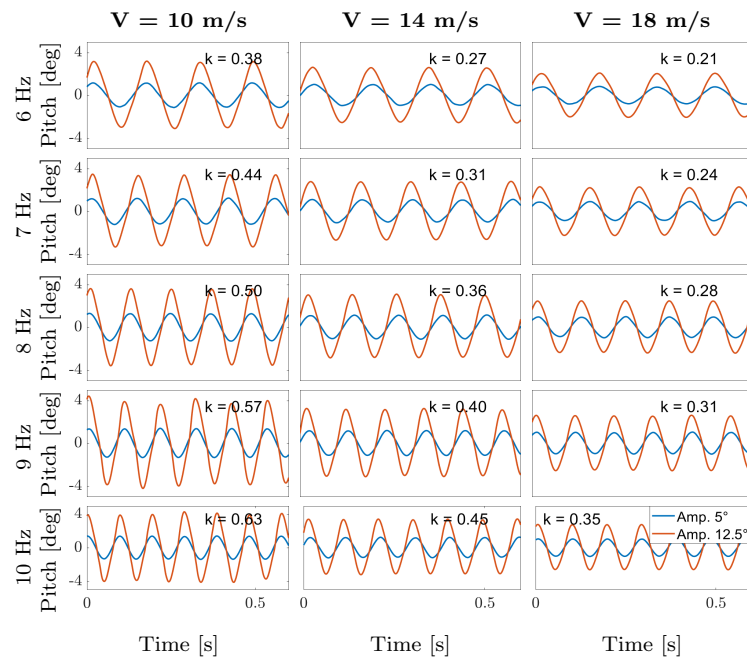


FIGURE 5.21: Continuous gust for vane rotations amplitude of  $5^\circ$  and  $12.5^\circ$ , at 6 to 10 Hz



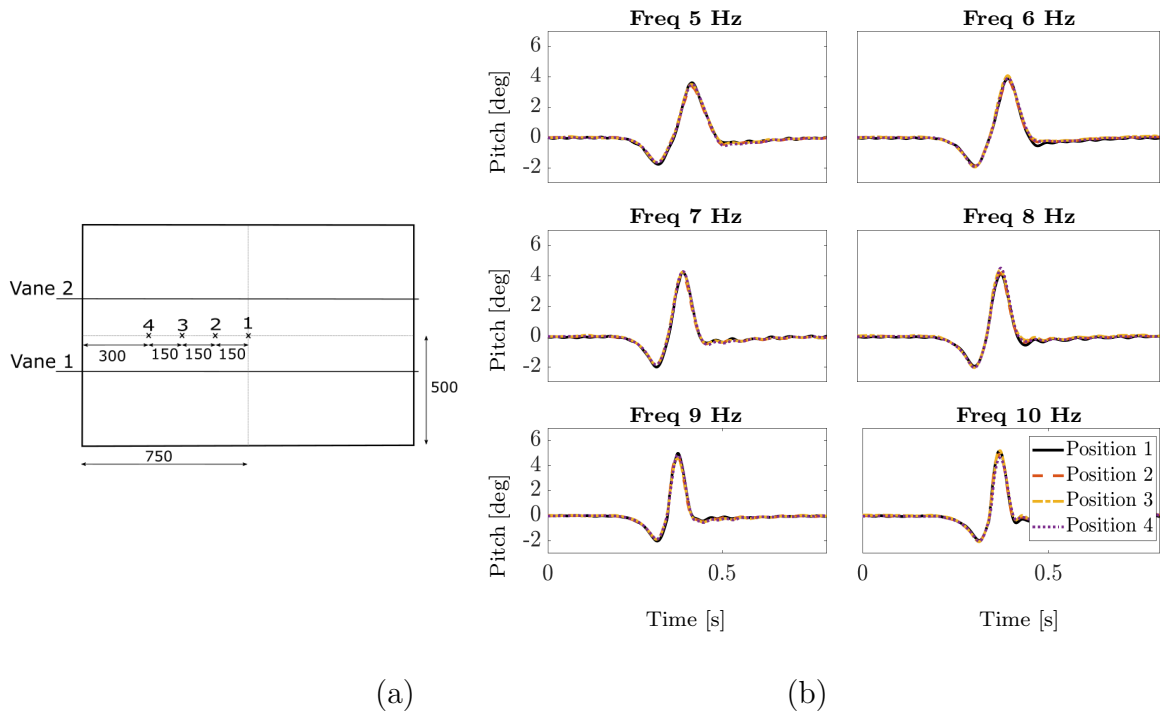


FIGURE 5.22: *Gust uniformity at different horizontal locations (a) and discrete gusts at each location (b)*

In the second test, five points in the vertical direction spaced at an equal distance were considered. Figure 5.23a shows the locations considered. Positions 1 and 2 are between the vanes, position 3 is on the wake of the vane, and positions 4 and 5 are between the vane and the wind tunnel top wall. Figure 5.23b shows the discrete gust measured at the different locations, considering an airspeed of 10 m/s, 10° maximum vane rotation, and gust frequencies in the range from 5 Hz to 10 Hz. The results show a slight difference between the gust measured at position 1 and position 2. At each frequency, the measurements show a similar trend at all the positions considered with the maximum peak reducing from position 1 to position 5. Midway between the two vanes, the gust has its maximum value due to the contribution of both vanes, whereas moving towards a vane, the effect of the farthest vane reduced. Position 3 is in the wake of the vane, and as such it is characterized by high fluctuations before and after the gust.

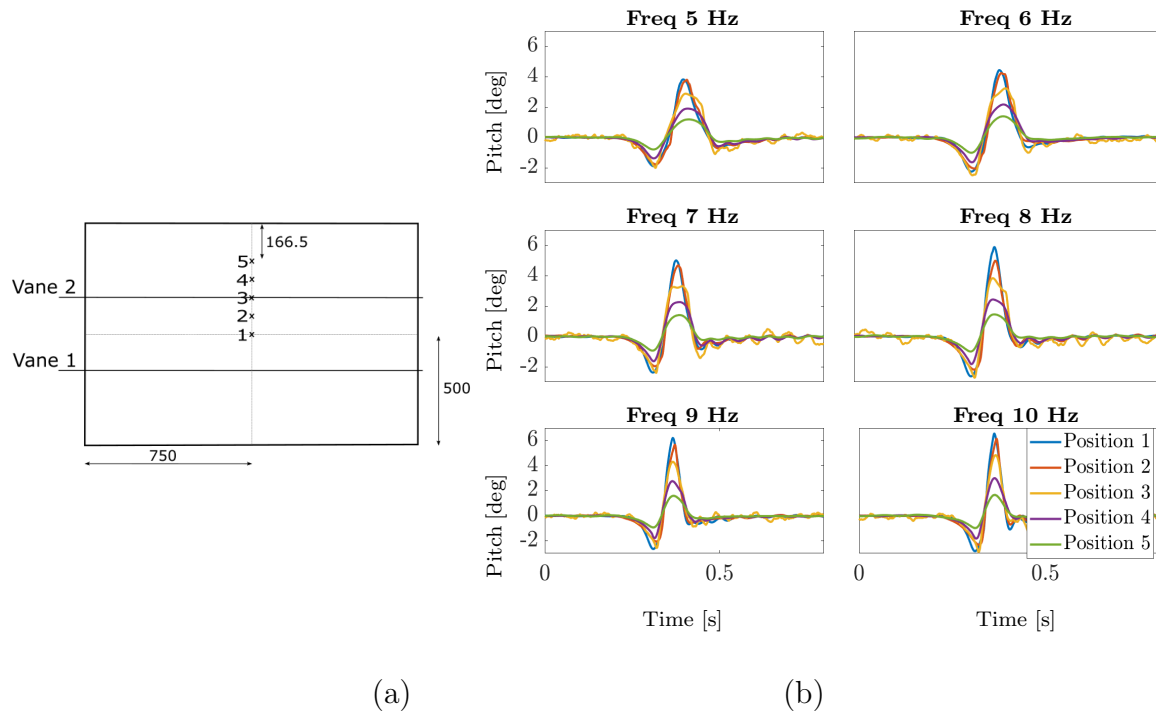


FIGURE 5.23: *Gust uniformity at different vertical locations (a) and discrete gusts at each location (b)*

## 5.4 Improvement of the ‘1-cos’ Gust Profile

The measurements of the discrete gust described in Figures 5.15 to 5.18, 5.22, and 5.23 show a negative peak before and after the positive peak. This behaviour can be observed in the measurements from other gust generator tests [14, 77, 82], but there are no published methods to counter this undesirable effect effectively. The negative peak before the gust is due to the starting vortex that is generated in the wake of the pitching vanes as their angle of attack with respect to the free stream increases [148].

The starting vortex is the vortex which is created downstream of the trailing edge of an airfoil that is impulsively accelerated in a fluid. Figure 5.24 shows experimental measurements of the starting and stopping vortices [21]. Figure 5.25 shows the creation of the starting vortex. The circulation  $\Gamma_1$  around an airfoil at rest (zero airspeeds) is zero. When the airfoil is impulsively accelerated, it generates lift, which corresponds to a nonzero circulation,  $\Gamma_4$  in the Figure 5.25b. Initially, the flow will tend to curl around the trailing edge, having a theoretically infinite velocity. Indeed, experimental

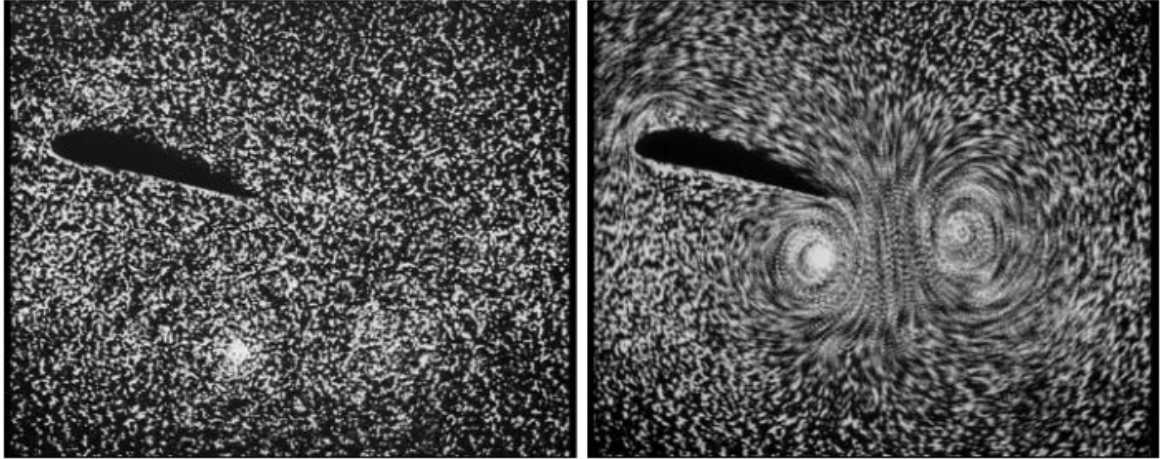


FIGURE 5.24: Starting and stopping vortices (directly adapted from [21])

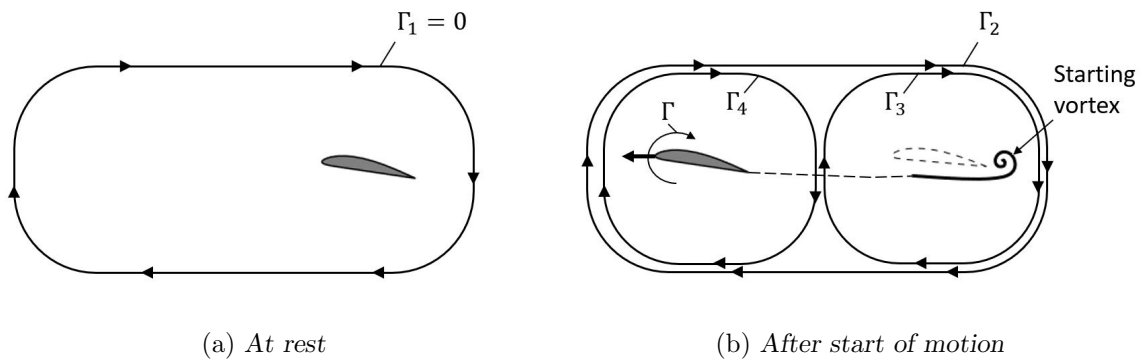


FIGURE 5.25: The creation of the starting vortex and the resulting circulation around the airfoil

flow visualisations show a starting vortex of circulation  $\Gamma_3$  shed from the airfoil trailing edge [148].

According to Kelvin's Theorem, the overall circulation,  $\Gamma_2 = \Gamma_3 + \Gamma_4$  is equal to the total circulation prior to the airfoil movement, or

$$\Gamma_1 = \Gamma_2 = 0 \quad (5.12)$$

Hence, the airfoil and the starting vortex must have equal and opposite circulations. In essence the starting vortex is a result of the change in lift produced by the airfoil.

In the case of the gust generator, a change in lift is produced by the pitching motion of the gust vanes in a constant flow. This change in lift leads to the generation of a starting vortex, responsible for the initial negative peak before the main gust. Similarly, the negative peak after the gust is due to the stopping vortex [149]. In this case, the

stopping of the airfoil pitch down motion leads to a change (reduction) in lift, which is responsible for the generation of the stopping vortex.

To improve the ‘1-cos’ gust, two test campaigns were performed. The first test campaign aimed to identify a transfer function that links the gust time history with the motor rotation and hence to find the motor rotation required to obtain an improved ‘1-cos’ gust. In the second test campaign, a parametric study of the vane rotation was performed. The results of both techniques are shown in the following sections for test campaigns at airspeed of 18 m/s. To quantify the effect of different techniques on the alleviation of the negative peaks, a Negative Peak Factor (NPF)  $n$  was defined as

$$n_{GG} = \left| \frac{\alpha_{min}}{\alpha_{max}} \right| \quad (5.13)$$

where  $\alpha_{min}$  and  $\alpha_{max}$  correspond to the minimum and maximum values of the gust, respectively.

### 5.4.1 Identification of the Transfer Function

The Navier-Stokes equations, which describe the motion of fluids, are notoriously non-linear [150]; nevertheless, as a first approximation, we considered approximating the GG in the wind tunnel as a linear system. The input-output relation for a linear system is described by a transfer function. To experimentally identify the transfer function, the measurements from the cross hot-wire sensor and an encoder on the motor were recorded on the same National Instruments data acquisition system. Two strategies were considered, a series of periodic sinusoidal rotations and impulsive rotation of the vanes.

#### 5.4.1.1 Periodic Sinusoidal Vane Rotation

In the first case, the vane rotation was obtained from Eq.(5.8) for  $A_{GG} = 10$  and values of  $f$  from 1 Hz to 10 Hz in 1 Hz increments. Figure 5.26 shows the motor rotation for  $A_{GG} = 10$  and the measured angle of attack at 18 m/s. For each continuous sinusoidal rotation, it is possible to calculate the input-output relation in terms of amplitude and phase. To identify the transfer function, an optimisation process based on a genetic algorithm was used. Figure 5.27 shows the experimental points obtained and the identified transfer function at 18 m/s. The amplitude of experimental points suggest a behavior as a first-order system with a zero at a lower frequency with respect to the pole. The phase experimental points suggest a pure delay.

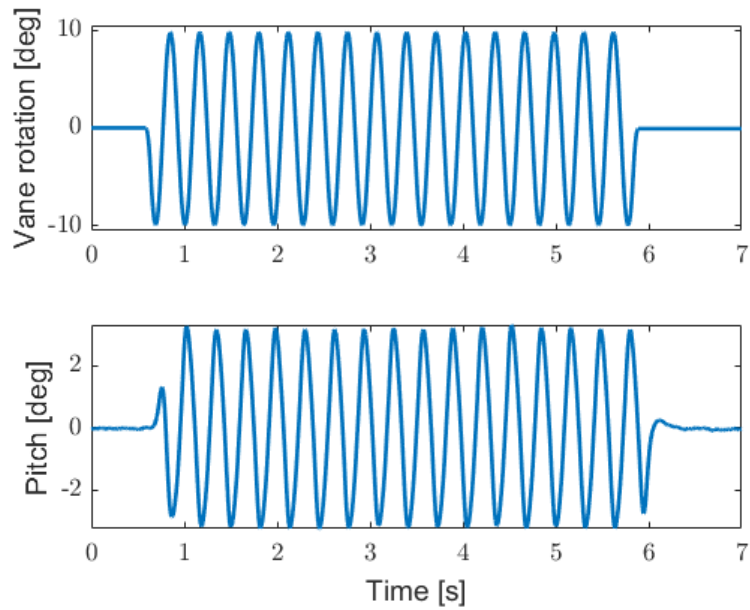


FIGURE 5.26: Motor rotation and gust measured by the cross hot-wire sensor for the identification of the transfer function

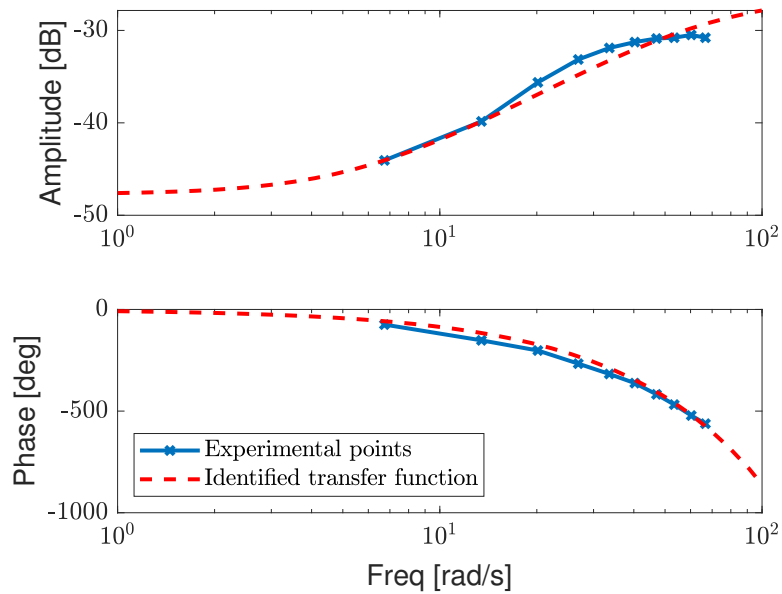


FIGURE 5.27: Identified transfer function by periodic sinusoidal rotations of the vanes

The amplitude of the experimental points suggests a behavior as a first-order system with a zero at a lower frequency with respect to the pole. The phase of the experimental points suggests a pure delay. Although the identification of the transfer function should consider amplitude and phase together, in this work, amplitude and phase identification was performed separately. This strategy was followed because the objective of this work was to find a simplified input-output relation based on the experimental results, while future works will consider more sophisticated identification strategies.

The procedure was repeated at 10 m/s and 14 m/s. The results found have similar trends as the one in Figure 5.27. For each airspeed, a first-order transfer function of the type

$$H_1(s) = K \frac{s + z_{tf}}{s + p} \quad (5.14)$$

was identified from the experimental points of the amplitude.  $K$ ,  $z_{tf}$ , and  $p$  are the gain factor, zero, and pole of the transfer function, respectively. For each airspeed, from the experimental points of the phase, it was identified a pure delay transfer function of the type

$$H_2(s) = e^{-\tau_{tf}s} \quad (5.15)$$

where  $\tau_{tf}$  is the delay of the transfer function. Table 5.5 shows  $K$ ,  $z_{tf}$ ,  $p$ , and  $\tau_{tf}$ . The

Airspeed [m/s]	$K$ [-]	$z_{tf}$ [rad/s]	$p$ [rad/s]	Identified delay $\tau_{tf}$ [s]	Convection time $t_{conv}$ [s]	Shedding time $t_s$ [s]
10	0.0535	0.0001	30.67	0.157	0.123	0.034
14	0.0470	0.00003	39.33	0.123	0.088	0.035
18	0.0495	5.81	69.9	0.105	0.068	0.037

TABLE 5.5: Identified delay, convection time, and shedding time at 10 m/s, 14 m/s, and 18 m/s identified from continuous sinusoidal vane rotation

identified delay,  $\tau_{tf}$ , represents the time between an ideal impulse vane rotation and the measured gust. Further to the transfer function parameters, Table 5.5 also shows the convection time,  $t_{conv}$ , and the shedding time,  $t_s$ . The convection time is defined as

$$t_{conv} = \frac{d_{vs}}{V_\infty} \quad (5.16)$$

where  $d_{vs}$  is the longitudinal distance between the vane trailing edge and the sensor location. The shedding time is defined here as

$$t_s = \tau_{tf} - t_{conv} \quad (5.17)$$

In the airspeed range considered, the shedding time is practically constant. Further to the shedding time for an ideal gust impulse, the shedding time for realistic vane rotations is considered next. At each airspeed and frequency of the vane continuous sinusoidal rotation the sinusoidal excitation shedding time  $t_{ss}$ , was calculated as

$$t_{ss} = \tau_f - t_{conv} \quad (5.18)$$

where  $\tau_f$  is the time delay between the sinusoidal vane rotation and the measured gust, as measured in the experiments. Figure 5.28 shows the sinusoidal excitation shedding time at 10 m/s, 14 m/s, and 18 m/s, and the identified shedding time as a function of the vane frequency sinusoidal rotation. The sinusoidal excitation shedding time shows a similar trend for all airspeeds, decreasing with increasing vane rotation. A second-order polynomial equation,  $t_{vs}^i$ , was fitted to the experimental data to identify the shedding time  $t_s$  as a function of the frequency of the vane rotation  $f$  as

$$t_{vs}^i = 0.0002f^2 - 0.0063f + 0.07 \quad (5.19)$$

It is noted that for the highest vane rotation frequency, the mean shedding time is 0.031 s, very close to the relevant identified value for the ideal gust.

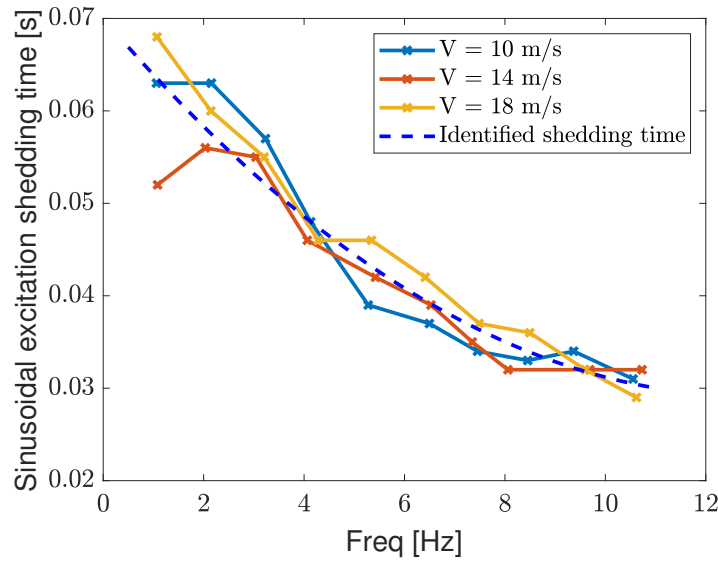


FIGURE 5.28: *Experimental and identified shedding times from continuous sinusoidal vane rotation*

### 5.4.1.2 Impulsive Vane Rotation

In the second case, a series of impulse rotations were considered by using Eq. (5.6) at  $A = 5^\circ$ , for increasing values of  $f$  and airspeed of 10 m/s, 14 m/s, and 18 m/s. From each vane rotation and gust time history, a transfer function was calculated and the mean of all the calculated transfer functions was used to identify the transfer function. As in the case of continuous sinusoidal vane rotation, the amplitude of the transfer function suggests a first-order system while the phase suggests a pure delay. The coefficients of the transfer functions  $H_1(s)$  and  $H_2(s)$ , see Eqs. 5.14 and 5.15, were identified. Figure 5.29 shows the experimental points, the average transfer function and the identified transfer function at 18 m/s. Table 5.6 shows for each airspeed the transfer function parameters

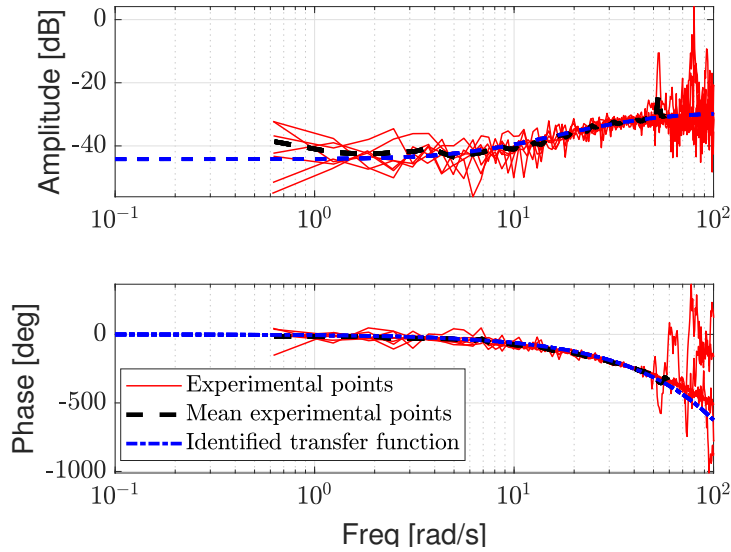


FIGURE 5.29: Measured transfer function, mean transfer function and identified transfer function from impulse tests at 18 m/s

along with convection time, and shedding time identified from the measurements. The

Airspeed [m/s]	$K$ [-]	$z_{tf}$ [rad/s]	$p$ [rad/s]	Identified delay $\tau_{tf}$ [s]	Convection time $t_{conv}$ [s]	Shedding time $t_s$ [s]
10	0.0461	2.18	23.85	0.159	0.123	0.036
14	0.0503	4.77	45.16	0.127	0.088	0.039
18	0.0370	6.76	42.55	0.109	0.068	0.041

TABLE 5.6: Identified delay, convection time, and shedding time at 10 m/s, 14 m/s, and 18 m/s identified from impulse vane rotation

identified delays in Tables 5.5 and 5.6 have a maximum difference of 0.004 s, which is considered negligible since the sampling frequency was 1 kHz.



To calculate the time delay between the vane rotation and the gust, the Matlab function ‘finddelay’ was used [151]. It calculates and then normalises the cross-correlation between each pair of signals at all possible lags. Figures 5.30, 5.31 and 5.32 show the identified time delay between the vane rotation and the gust.

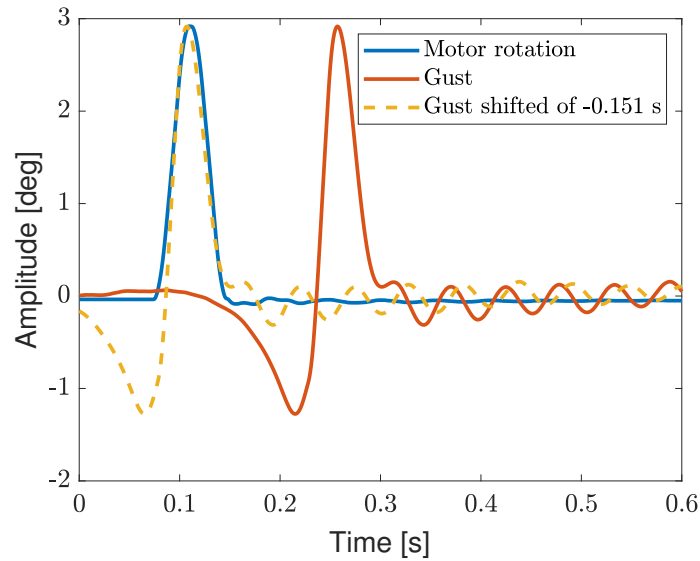


FIGURE 5.30: Time delay between impulse vane rotation and gust at 10 m/s

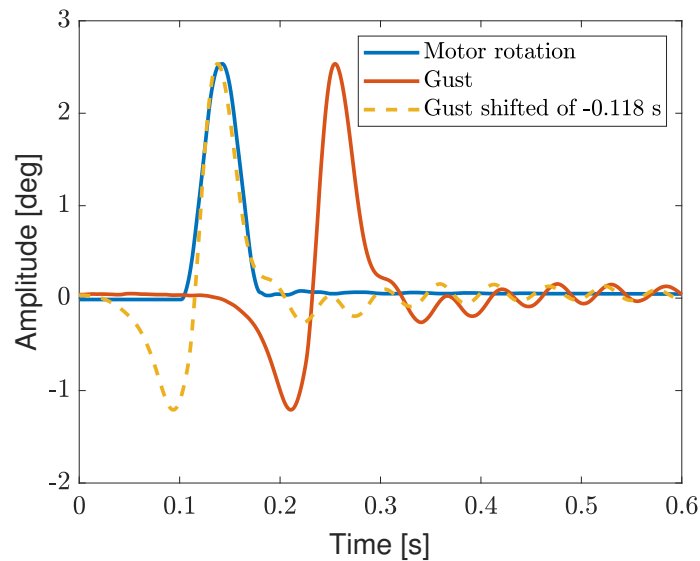


FIGURE 5.31: Time delay between impulse vane rotation and gust at 14 m/s

Table 5.7 shows the comparison between the identified time delay reported in Tables 5.5 and 5.5 and the calculated delay between the impulse vane rotation and the gust. The time required from an ideal impulse vane rotation to create a gust is the identified delay.

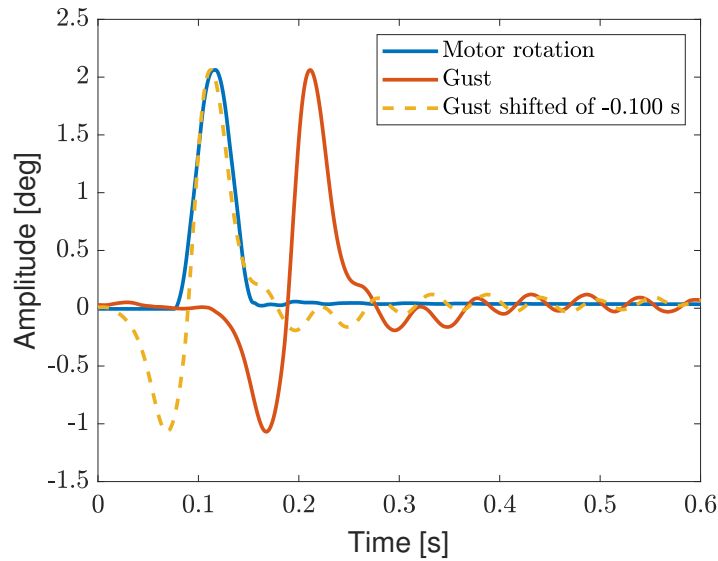


FIGURE 5.32: Time delay between impulse vane rotation and gust at 18 m/s

Table 5.7 shows the difference between the ideal and the realistic impulse vane rotation. Considering the identified delay from the sinusoidal vane rotation as a reference, at 10 m/s, the realistic impulse vane rotation requires 6 ms more than the ideal case to create the gust, and at 14 m/s and 18 m/s, the realistic impulse vane rotation requires 5 ms more than the ideal case to create the gust.

Airspeed [m/s]	Identified delay sinusoidal rotation	Identified delay impulse rotation	Delay between vane rotation and gust
10	0.157	0.159	0.151
14	0.123	0.127	0.118
18	0.105	0.109	0.100

TABLE 5.7: Comparison identified delay at 10 m/s, 14 m/s, and 18 m/s

### 5.4.1.3 Results of the Identified Transfer Functions

Figure 5.33 shows the identified transfer functions at 18 m/s in the two cases considered, and they have a similar trend.

In the frequencies of interest, the amplitude of the transfer function increases with the frequency, as observed from Figures 5.17 to 5.23. The phase increases with the frequency in accordance with the Theodorsen function [20]. Figure 5.1b shows that discrete ‘1-cos’ gusts are characterized by significant low-frequency components and so a good characterisation of the low frequency response is required. Although the identified transfer

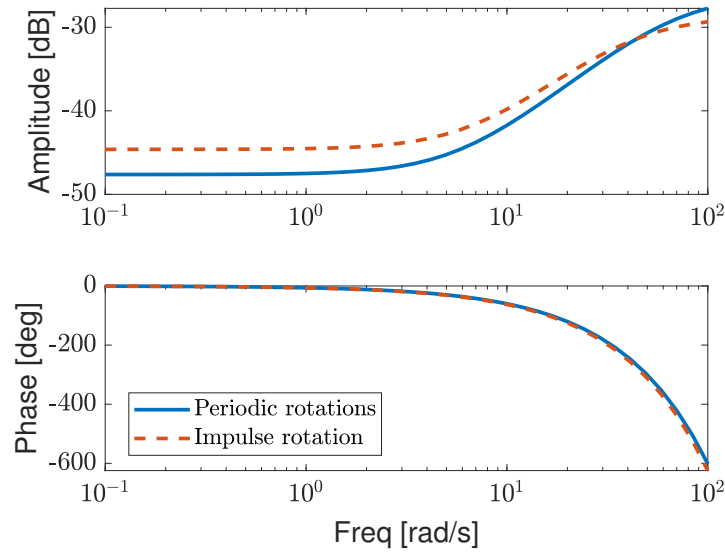


FIGURE 5.33: Comparison of identified transfer functions at 18 m/s

functions have analogous trends both in terms of amplitude and phase, the continuous sinusoidal rotations do not provide a good characterisation of the low frequency range because gust at low frequencies are associated with low amplitude. Indeed, the gust generator cannot produce continuous gusts for frequencies lower than 1 Hz. At the same time, higher amplitude, low-frequency content is provided in the case of impulse rotation of the vane. In hence it was decided only to consider the transfer function obtained by impulse vane rotation at 18 m/s for the remaining of this work.

To calculate the vane rotation required to obtain a ‘1-cos’ gust as in Eq. (2.7) and in Figure 5.1a the desired gust and the vane rotation was considered in the frequency domain. The vane rotation amplitude and the phase content were considered separately. The amplitude was calculated at each frequency by multiplying the inverse of the amplitude of  $H_1(j\omega)$  by the corresponding amplitude of the desired gust. The phase was calculated at each frequency by multiplying the inverse of  $H_2(j\omega)$  by the corresponding phase of the desired gust. The generated vane rotation was applied at the gust generator vanes.

Figures 5.34 and 5.35 show the results obtained in the case of desired maximum amplitudes of  $1^\circ$ ,  $2^\circ$ , and  $3^\circ$  and gust frequencies between 6 to 15 Hz and the desired gust. The results show an attenuation of the negative peaks. However, compared to the desired gust, it is noted that deviations from the ideal ‘1-cos’ persist.

A direct comparison between the gusts obtained considering vane rotations from Eq. (5.6), and the inverse of the transfer function is possible only when the same vane pitch amplitude produces similar gusts. Indeed, Eq. (5.6) does not contain any previous knowledge of the expected maximum gust amplitude. In the following, a comparison

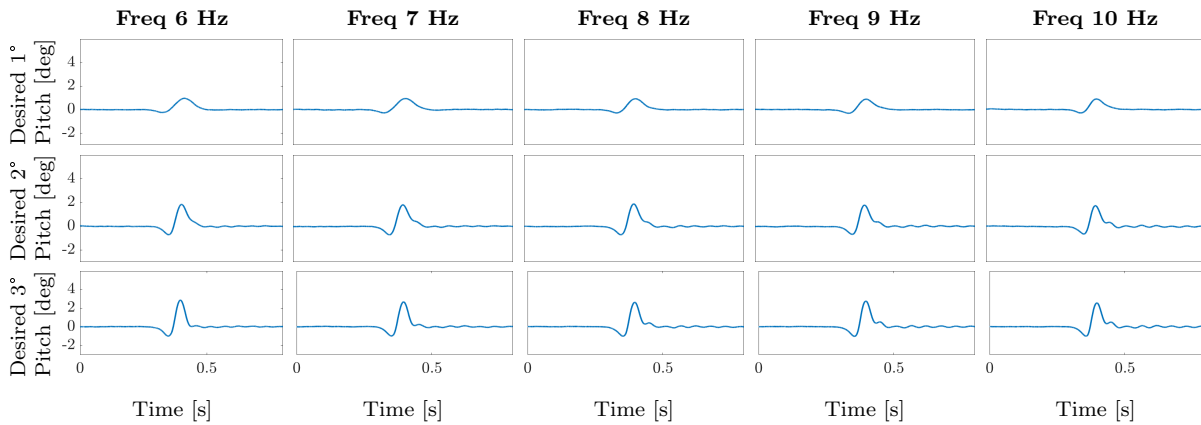


FIGURE 5.34: Discrete gust vane rotations with desired AoA  $1^\circ$ ,  $2^\circ$  and  $3^\circ$ , and frequency 6 to 10 Hz

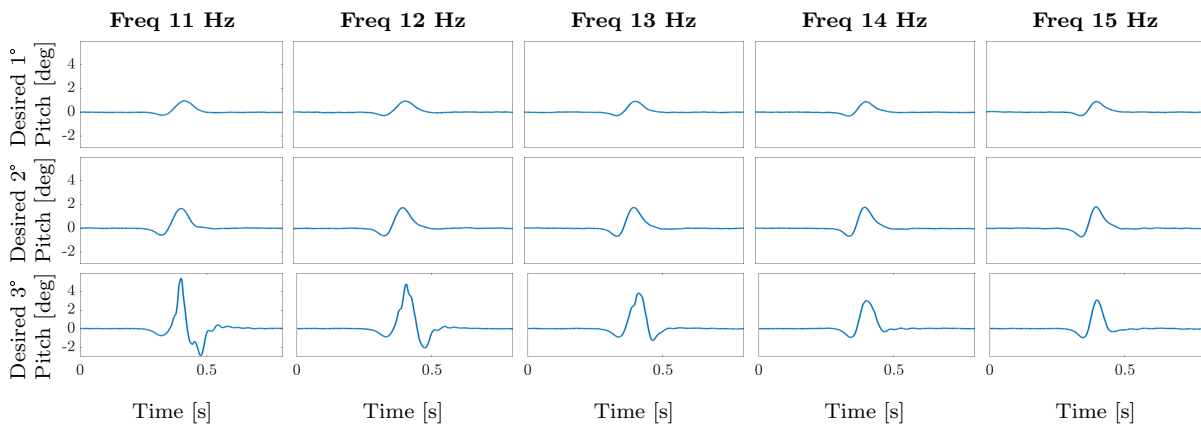


FIGURE 5.35: Discrete gust vane rotations with desired AoA  $1^\circ$ ,  $2^\circ$  and  $3^\circ$ , and frequency 11 to 15 Hz

is given between similar gusts obtained by ‘1-cos’ vane rotation and by the inverse of  $H_1(s)$  and  $H_2(s)$ . The comparison aims to compare similar gusts obtained with different strategies, although the two strategies followed two different aims. Indeed, in the first case, the vane rotation was imposed without any knowledge of the desired gust, while in the second case, the vane rotation was calculated to obtain the desired gust. As an example, the case with a gust of maximum amplitude of  $\sim 3^\circ$  at 9 Hz is considered. In order to achieve such a gust, a ‘1-cos’ vane rotation of  $15^\circ$  at the same frequency is required. The motor rotation found by the inverse of  $H_1(s)$  and  $H_2(s)$  for a desired discrete gust with a maximum amplitude of  $3^\circ$  is shown in Fig. 5.36. Figure 5.37 shows the desired discrete gust with a maximum amplitude of  $3^\circ$  and frequency of 9 Hz, the gust

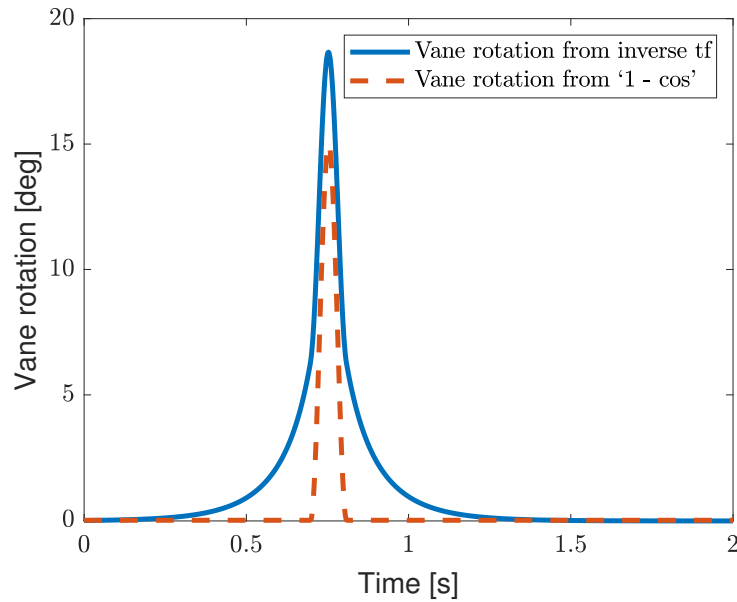


FIGURE 5.36: Comparison motor rotation found from inverse transfer function and ‘1-cos’

produced by a ‘1-cos’ vane rotation of amplitude  $15^\circ$  and the gust produced using the vane rotation found using the inverse of the transfer function identified. The proposed

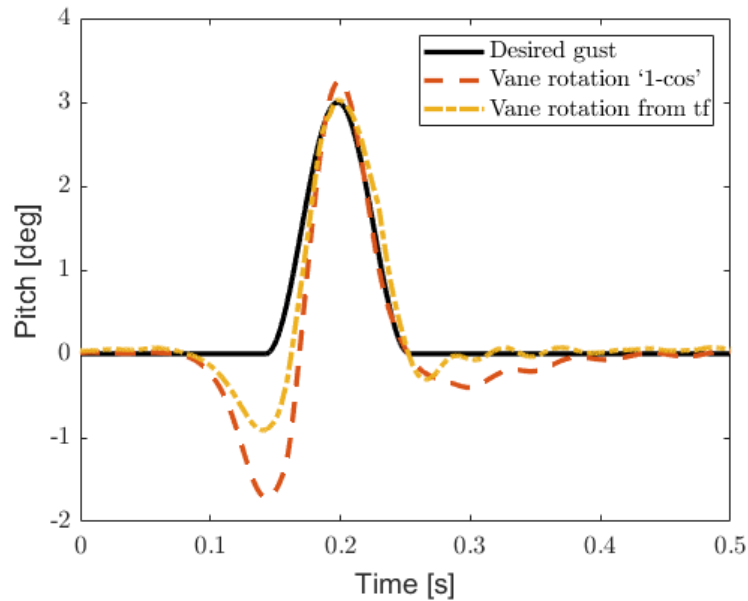


FIGURE 5.37: Comparison desired gust profile at 9 Hz, gust obtained from ‘1-cos’ vane rotation and gust obtained from motor rotation obtained from the inverse transfer function

method allows the attenuation of both the negative peaks with direct control of the gust amplitude. The measured gusts have a similar maximum peak intensity. When the transfer function approach is used, the maximum pitch is close, but not identical, to the desired one. In both cases, an iterative process is required to obtain the desired

amplitude. Nevertheless, the variability in the test conditions would make it very difficult to get exactly the same gust as the desired. Due to the time limitation in accessing the wind tunnel, the iterative process was not performed. The NPF for the gust produced by ‘1-cos’ vane rotation is 0.53, while the NPF for the gust produced using the inverse of the transfer function is 0.30.

### 5.4.2 Results of the Parametric Study

The vane rotation defined in Eq. (5.6) has a zero slope at  $t = 0$ , and for  $t > 0$  the slope increases and decreases rapidly before the vanes attain their maximum value (due to  $\frac{d}{dt}(1 - \cos(t)) = \sin(t)$ ). In the same way, at  $t = 0.5/f$  and at  $t = 1/f$  the slope is zero and between these points the slope decreases and increases quickly. As previously discussed, the negative peaks in the discrete gusts are due to the starting and the stopping vortices and their intensity is related to the rate of change of lift, or equivalently the angle of attack. Considering Eq. (5.6) as a reference, a parametric study was performed on the definition of the vane rotation to attenuate these vortices. The parametric study performed at 18 m/s shown a reduction of both negative peaks when Eq. (5.6) is combined with a growing exponential curve for  $t < 0.5/f$  and a decaying exponential curve for  $t > 0.5/f$ . It was shown that defining the vane rotation as

$$\theta_{GG}(t) = \begin{cases} \exp(B_{GG}t) - 1 & \text{for } 0 \leq t < t_1 \\ \frac{A_{GG}}{2} \left[ 1 - \cos(2\pi f(t - t_01)) \right] & \text{for } t_1 \leq t \leq t_2 \\ \exp(C_{GG}(t - t_02)) & \text{for } t > t_2 \end{cases} \quad (5.20)$$

can reduce the NPF and produce accurate discrete gusts. To determine the seven unknowns of Eq. (5.20) ( $A_{GG}, B_{GG}, C_{GG}, t_01, t_02, t_1, t_2$ ) the parameters of Table 5.8 were used for four values of  $A_{GG}$ . The values of Table 5.8 were selected as a conclusion of the parametric study. The values of  $t_1$  and  $t_2$  can be found considering  $\theta_{GG}(t_1) = 0.9A_{GG}$  in

	$A_{GG} = 5^\circ$	$A_{GG} = 10^\circ$	$A_{GG} = 15^\circ$	$A_{GG} = 20^\circ$
$t_{01}$	0.15 s	0.20 s	0.25 s	0.30 s
$t_3$	$t_{01} + 4/f$	$t_{01} + 4/f$	$t_{01} + 4/f$	$t_{01} + 4/f$
$\theta_{GG}(t_1)$	$0.9A_{GG}$	$0.9A_{GG}$	$0.9A_{GG}$	$0.9A_{GG}$
$\theta_{GG}(t_2)$	$0.5A_{GG}$	$0.5A_{GG}$	$0.5A_{GG}$	$0.5A_{GG}$
$\theta_{GG}(t_3)$	$0.003^\circ$	$0.003^\circ$	$0.003^\circ$	$0.003^\circ$

TABLE 5.8: Selected parameters

the first half of the cosine period and  $\theta_{GG}(t_2) = 0.5A_{GG}$  in the second half of the cosine period. From  $\theta_{GG}(t_1) = 0.9A_{GG}$ ,  $t_1$  can be found. Imposing the continuity at  $\theta_{GG}(t_1)$  the

coefficient  $B_{GG}$  can be found. Imposing the continuity at  $\theta_{GG}(t_2)$  and the point  $\theta_{GG}(t_3)$  the coefficients  $C_{GG}$  and  $t_{02}$  can be found. Figure 5.38 shows the vane rotation in the case of Eq. (5.6) where an offset of  $t_{01}$  was added to the cosine function and in the case of Eq. (5.20) where the three constraint points used are shown.

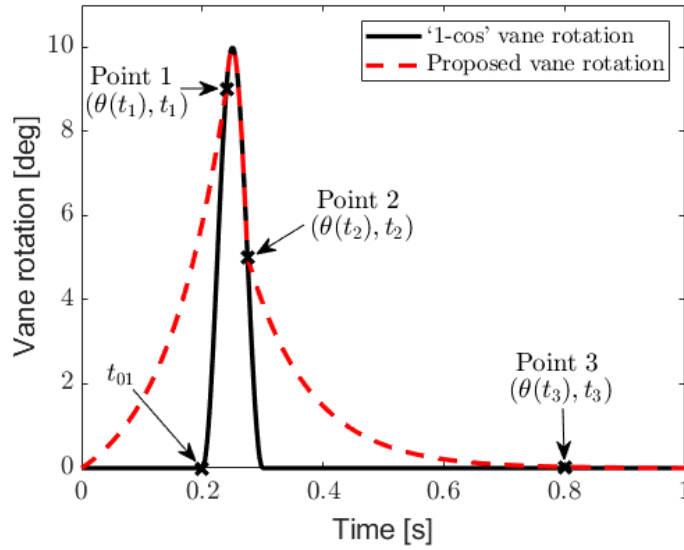


FIGURE 5.38: Proposed method to parameterize the vane rotation

The effect of the parameters shown in Table 5.8 on the identified gust profile is worth investigating. Figures 5.39, 5.40 and 5.41 show the effect of  $t_{01}$ ,  $\theta_{GG}(t_2)$  and  $t_3$  on the gust produced. The selection of  $t_{01}$  affects the behavior of the first part of the gust because it controls the starting vortex. Indeed, a small value of  $t_{01}$  creates a negative peak before the gust similar to that of the ‘1-cos’ vane rotation while a high value of  $t_{01}$  creates a positive peak. The selection of  $t_{01}$  has an impact on the maximum peak of the gust produced; a faster vane rotation creates a gust with a higher maximum peak. Experiments suggest the use of a value of  $t_{01}$  proportional to the maximum vane rotation amplitude.  $\theta_{GG}(t_2)$  and  $t_3$  control the second part of the gust, the negative peak due to the stopping vortex, and the hump in the last part of the gust. A small value of  $\theta_{GG}(t_2)$  produces a negative peak after the gust and delays the creation of the hump.  $\theta_{GG}(t_2)$  affects the maximum peak of the gust produced; a small value of  $\theta_{GG}(t_2)$  creates a gust with a higher maximum peak.  $\theta_{GG}(t_2)$  was kept constant for all the cases considered. A small value of  $t_3$  produces a negative peak after the gust and reduces the amplitude of the hump.  $t_3$  has a negligible effect on the maximum gust peak.  $\theta_{GG}(t_1)$  was kept constant because the effect of the starting vortex is controlled by  $t_{01}$ .  $\theta_{GG}(t_3)$  was kept at  $0.003^\circ$  which practically is equivalent to zero.

Figure 5.42 shows the gusts measured when Eq. (5.20) is used considering different maximum vane rotations  $A_{GG}$ . The reduced frequencies  $k$  are in the range of 0.14 to

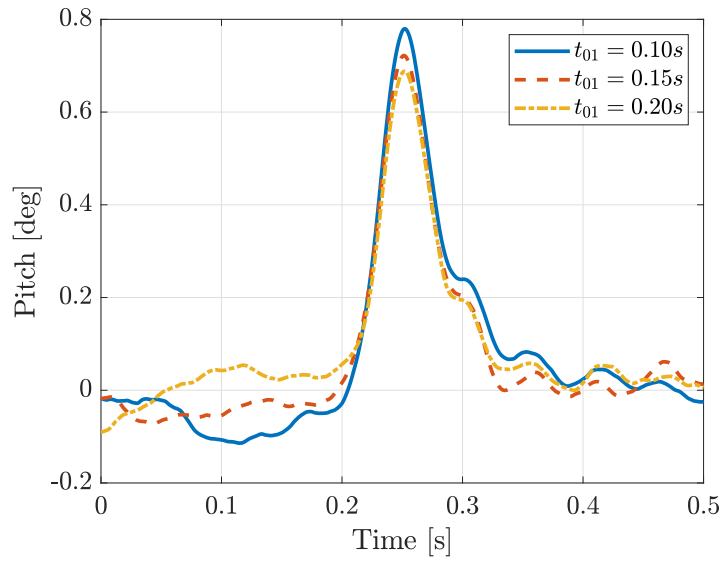


FIGURE 5.39: Proposed method, effect of  $t_{01}$  on the gust produced

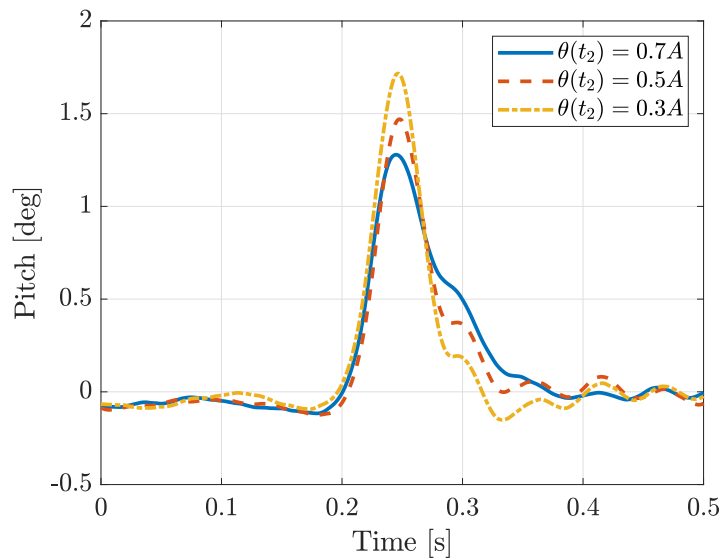


FIGURE 5.40: Proposed method, effect of  $\theta_{GG}(t_2)$  on the gust produced

0.52. Based on the shape of the gust, the proposed method can create discrete gust for all values of  $k$  for vane rotation amplitudes of  $5^\circ$ ,  $10^\circ$  and  $15^\circ$ , while for  $k \geq 0.28$  it can create discrete gust for vane rotation amplitude of  $20^\circ$ . For maximum vane rotations of  $5^\circ$ ,  $10^\circ$  and  $15^\circ$ , the results show a general reduction of the negative peaks. For high gust frequency, the results show that after the main peak, some oscillations due to the vane vibrations appear.

The reduction of the negative peaks improves the frequency content of the gust. Indeed, Figures 5.43 and 5.44 show the frequency content of the measured discrete gusts at 18



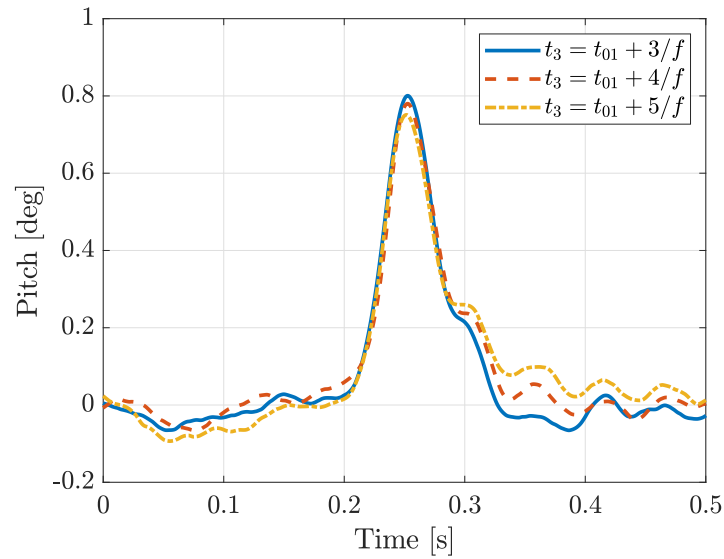


FIGURE 5.41: Proposed method, effect of  $t_3$  on the gust produced

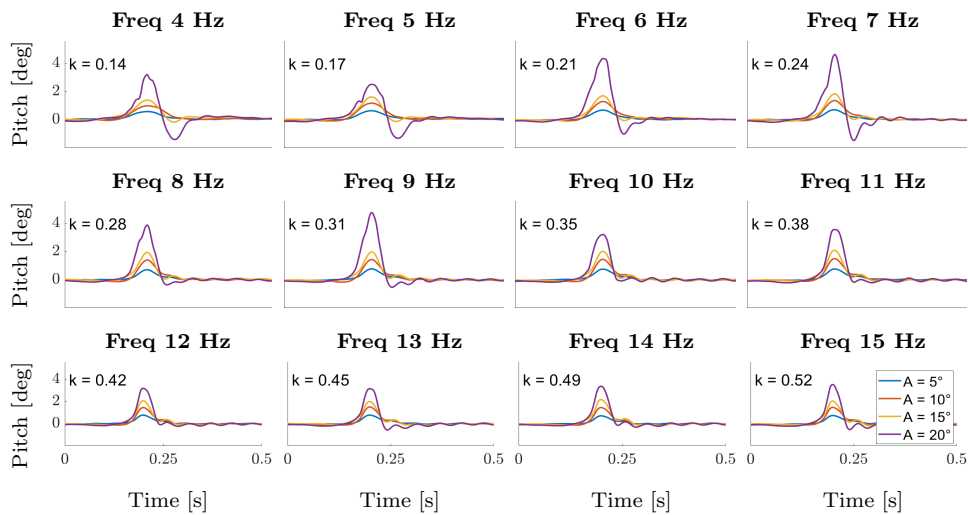


FIGURE 5.42: Proposed method to parameterize the discrete gust vane rotation for amplitude of  $5^\circ$ ,  $10^\circ$ ,  $15^\circ$  and  $20^\circ$ , and frequencies of 4 to 15 Hz

m/s, frequency of 13 Hz, vane rotation for the amplitude of  $5^\circ$ ,  $10^\circ$ ,  $15^\circ$  and  $20^\circ$  in the case of ‘1-cos’ vane rotation and the proposed method, respectively. Figures 5.43 and 5.44 also show the frequency content of discrete gusts with the same gust wavelength and maximum amplitude. The proposed method is able to produce discrete gusts with a more constant low-frequency content with respect to gusts produced by ‘1-cos’ vane rotation.

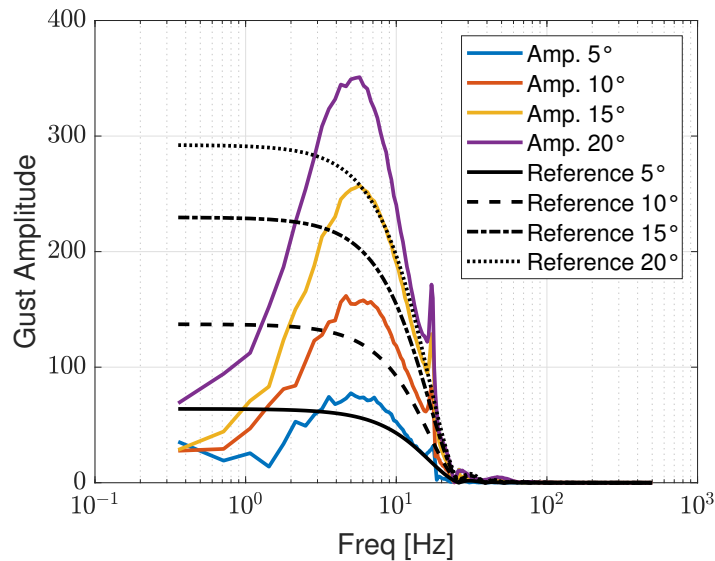


FIGURE 5.43: Frequency content of discrete gusts obtained at 18 m/s, frequency of 13 Hz, by ‘1-cos’ vane rotation for amplitude of  $5^\circ$ ,  $10^\circ$ ,  $15^\circ$  and  $20^\circ$  (color lines) and frequency content of the equivalent exact discrete gusts with the same gust wavelength and maximum amplitude (black lines)

A comparison between gusts produced by different vane rotations is provided here. Figure 5.45 shows the comparison between discrete gusts at 8 Hz generated by ‘1-cos’ vane rotation and vane amplitude of  $10^\circ$ , from the vane rotation calculated from the inverse of the transfer function with the desired gust of  $2^\circ$  and the proposed method with  $A = 15^\circ$ . Figure 5.45 also shows the corresponding ideal ‘1-cos’ gusts. In the three cases considered, the mean square error is 0.16 in the case of the gust obtained by ‘1-cos’ vane rotation, 0.029 for the gust obtained by the vane rotation from the inverse of the transfer function, and 0.0063 for the gust obtained by the vane rotation from the proposed method.

Figure 5.46 shows the maximum gust peaks as a function of frequency and maximum vane angle of rotation found using Eq. (5.20). At each frequency considered, the trend is linear in the range of  $5^\circ$  to  $15^\circ$ . In the linear region, Figure 5.46 can be used to calculate the maximum vane angle of rotation required to obtain the desired discrete gust. The proposed method results in gusts with lower amplitude compared with the maximum peak obtained by ‘1-cos’ vane rotation (see Figure 5.19) for the same rotation angle

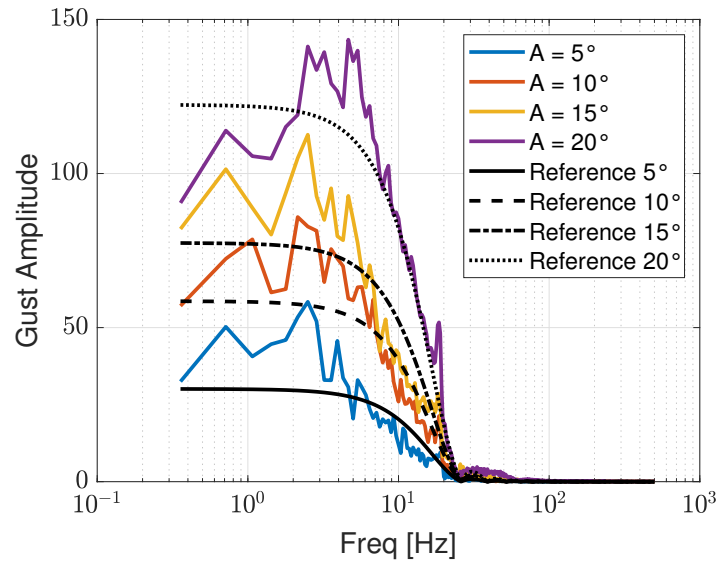


FIGURE 5.44: Frequency content of discrete gusts obtained at 18 m/s, frequency of 13 Hz, by the proposed method for amplitude of 5°, 10°, 15° and 20° (color lines) and frequency content of the equivalent exact discrete gusts with the same gust wavelength and maximum amplitude (black lines)

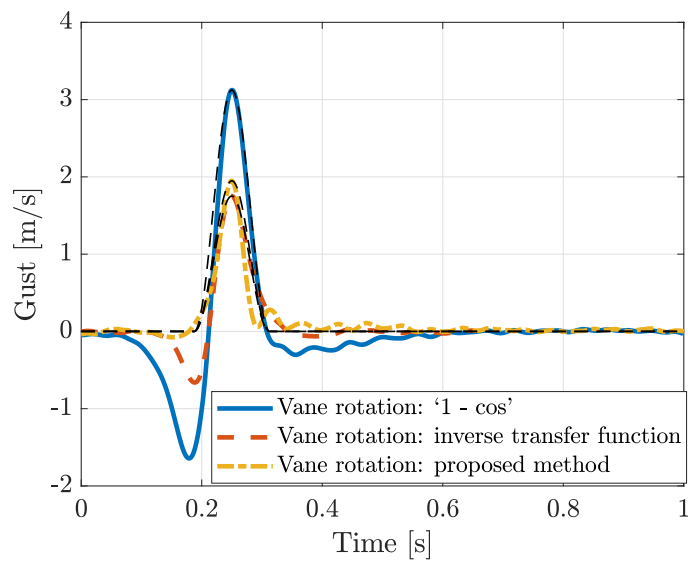


FIGURE 5.45: Discrete gust at 8 Hz from '1-cos' vane rotation and vane amplitude 10°, from the vane rotation calculated from the inverse of the transfer function with a desired gust of 2°, from the proposed method with  $A_{GG} = 15^\circ$  and corresponding ideal '1-cos' gusts (black dashed lines)

and frequency. Indeed, Figures 5.39, 5.40 and 5.41 show the effect of the introduced parameters in attenuating the maximum gust peak.

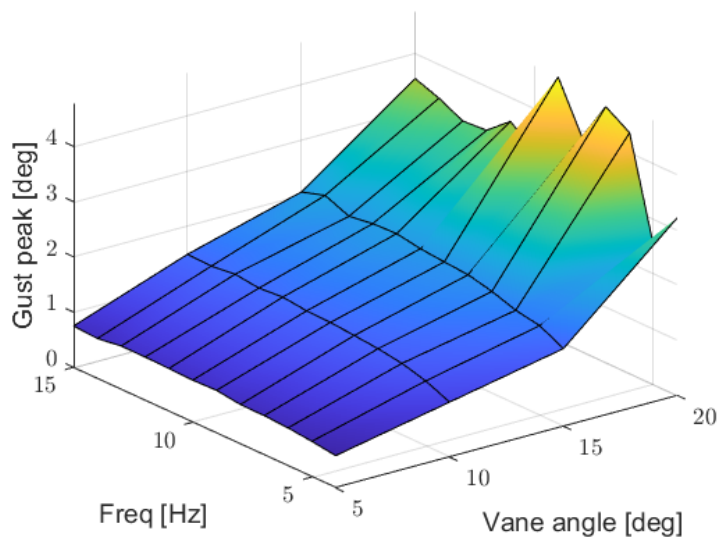


FIGURE 5.46: *Maximum gust peaks as a function of frequency and maximum vane angle of rotation*

The three methods used to generate gusts are compared in terms of NPF. Figure 5.47 shows the NPF for discrete gust in the frequency range of 6 Hz to 14 Hz, in the case of ‘1-cos’ vane rotations, vane rotations from the inverse transfer functions and vane rotations from the proposed method. In the case of ‘1-cos’ vane rotations the mean NPF is 0.51 with its minimum for a vane rotation amplitude of  $20^\circ$  and a frequency 6 Hz due to the high amplitude of the positive peak. For gusts obtained from the vane rotations calculated from the inverse transfer functions, the mean NPF is 0.36. In this case, the maximum NPF is at low frequencies and the desired angle of attack of  $3^\circ$ , where the dynamic stall creates a chaotic behavior. The gusts produced by the vane rotations defined by the proposed method have a mean NPF of 0.06. The results show a constant NPF for all cases except for high vane rotation amplitude at low frequency due to the dynamic stall.

---

## 5.5 Conclusions

---

A two vanes computer controlled GG was designed and successfully implemented in the Swansea University wind tunnel. A literature review was used as a guide for the

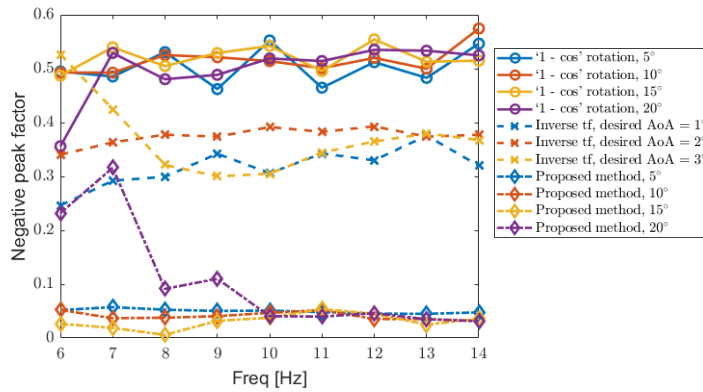


FIGURE 5.47: Negative peak factor using the three methods

design of the main components. Experimental data, collected from a cross hot-wire sensor, confirmed that the system is reliably capable of creating uniform discrete and continuous gusts. The results shown good repeatability and agree with previous similar work. Discrete gusts shown discrepancies between the desired and the measured gusts. Two techniques to improve the discrete gusts were proposed. Transfer functions were identified using periodic and impulsive vane oscillations and gave similar results. The transfer functions identified from impulsive vanes oscillation were used to calculate the vane rotation required to obtain an improved discrete gust. The results shown a reduction of the negative peaks, although the high nonlinearity due to the unsteady aerodynamic effects shown the limitation of this approach. The parametric study results shown that using a more complicated vane rotation function it is possible to obtain discrete gusts with negative peaks one order of magnitude smaller with respect to the previous cases.

# Chapter 6

---

## MODEL VALIDATION

The experimental validation of aeroelastic models is necessary to verify their accuracy. This chapter presents the design of a wing and different wingtips, the model structural characterisation, wind tunnel tests and results and the models' validation. The tests measured the static and dynamic behaviour of an aeroelastic straight untapered half-wing model equipped with either a fixed wingtip or a hinged wingtip. Static and dynamic wind tunnel tests were performed to prove the load alleviation concept and validate the aeroelastic models. The numerical models developed were based on the detailed model defined in Chapter 2 and used in Chapter 4. To improve the validation accuracy, the measurements from the gust generator in Chapter 5 were used as a disturbance to simulate the gust response.

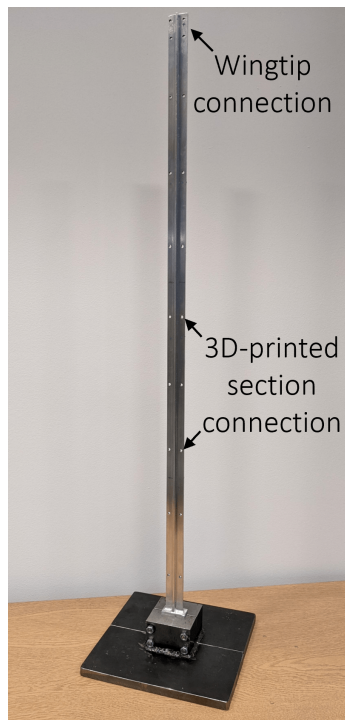
---

### 6.1 Wing and Wingtips Design

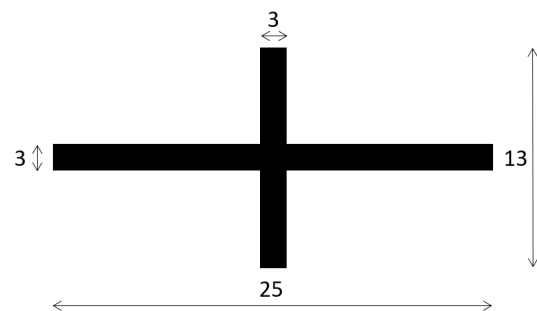
---

To experimentally prove the hinged wingtip device and validate aeroelastic models, a straight untapered half-wing with 1 m span and 0.134 m chord able to accommodate different wingtips was designed and manufactured. The wing comprises a 780 mm long aluminum spar with a cross cross-section and 3D-printed aerofoils connected to the spar. To minimise the wing thickness but allow the introduction of an aluminium spar, the

constant wing profile selected is the NACA0015 profile. Eight identical 3D-printed aerofoils are connected along the spar's span through two pairs of bolts and washers. The spar's tip is used to connect the wingtips through four pairs of bolts and washers. This design was selected to suit different wingtips without changing the rest of the wing. Figures 6.1a and 6.2 show the manufactured spar and one of the 3D-printed sections. Figure 6.1b shows the spar internal cross section. To facilitate the wing assembly, it

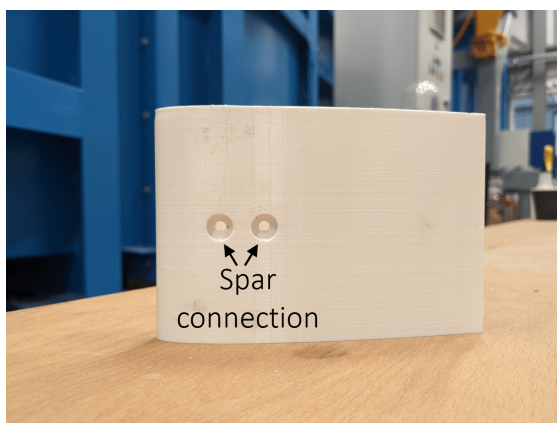


(a) Spar manufactured

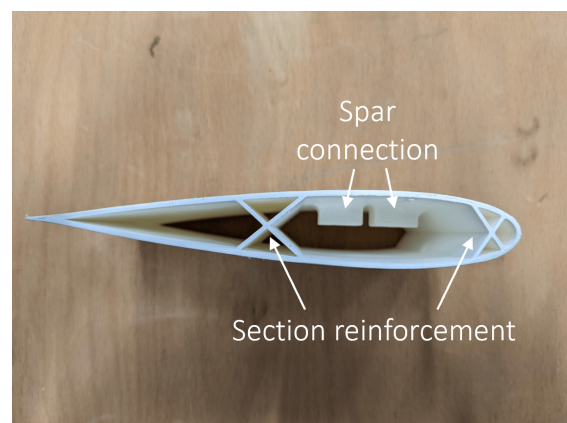


(b) Spar section

FIGURE 6.1: Aluminium spar



(a) Front view



(b) Top view

FIGURE 6.2: 3D printed section

was decided to connect each section to the spar from only the top face of the section

because a connection from both faces would require a precise clearance, challenging to ensure with a 3D-printed part. Figure 6.2b shows the material added to connect each section to the spar. Moreover, it also shows the reinforcement added to ensure higher torsional stiffness.

Three wingtips with the same span and weight were manufactured. The first wingtip is fixed, while in the other two, there is a hinge with an angle with respect to the free stream velocity (flare angle) of  $10^\circ$ . The hinge location is at 80% of the total wingspan. A  $0.35 \text{ mm} \times 25 \text{ mm} \times 100 \text{ mm}$  metal plate connects the wingtip root to the main wing in one of the two hinged wingtips to introduce a torsional stiffness on the hinge. Figure 6.3 shows the fixed and the hinged wingtips.

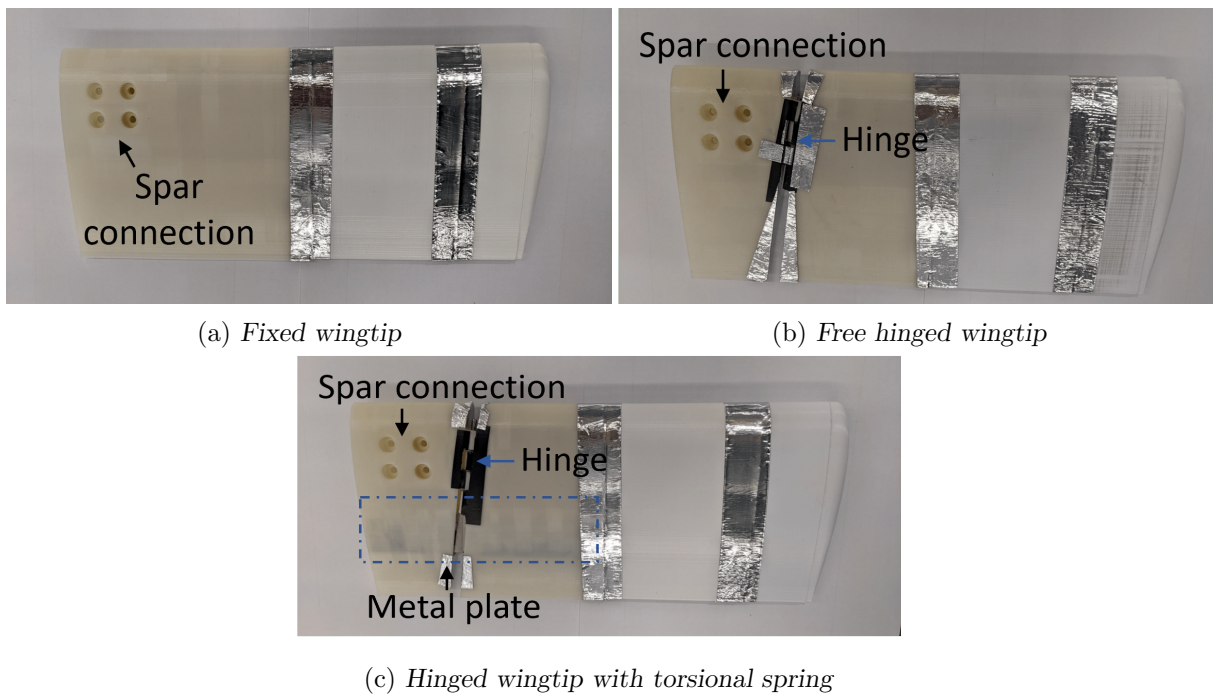
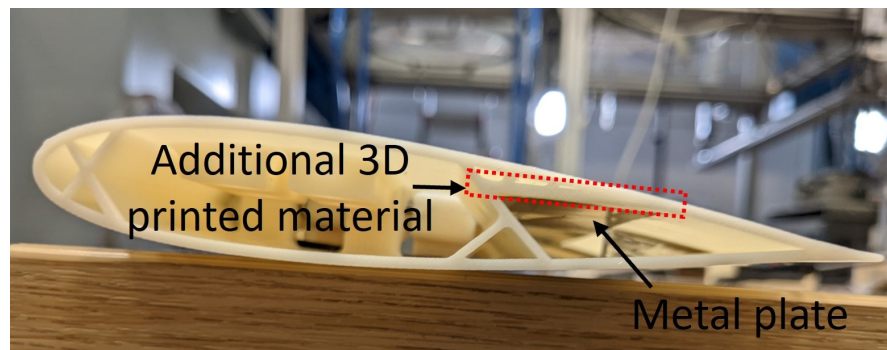


FIGURE 6.3: Wingtips manufactured

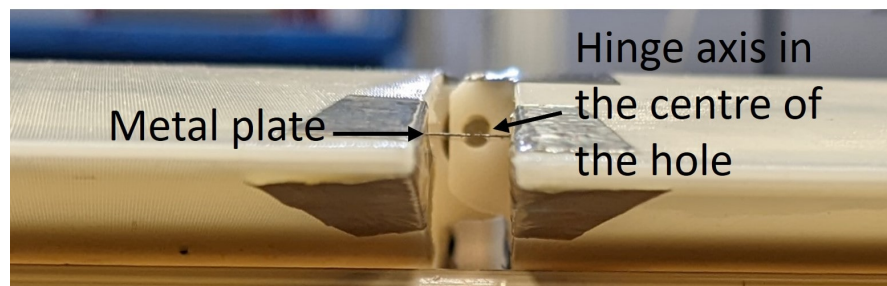
To make sure the metal plate is equivalent to a linear torsional spring at the hinge, 3D-printed material was added to ensure that the plate is aligned with the hinge axis for any fold angle. Figure 6.4 shows how the metal plate was added.

To facilitate assembly, the wingtip was divided into different sections. The first section is split into two parts for the hinged wingtip and connected through the hinge. The hinge comprises a steel shaft, a metal bush and two bearings assembled together. The hinge consists of a metal bush connected to a steel shaft rotating in two metal bearings. The shaft is bonded to a metal bush connected to the 3D-printed section, which is part of the wingtip. The bearings are bonded to the 3D-printed section, which is part of the





(a) Side view



(b) Rear view

FIGURE 6.4: Details of the hinged wingtip with torsional spring

main wing. Moreover, the bearings prevent the bush from moving in the hinge direction. The last three sections of all the wingtips have the same design. A threaded bar runs inside the wingtip and compress the different sections. Figure 6.5 shows the internal view of the fixed wingtip. Table 6.1 contains the weight of the wing components. Due to the accuracy of the 3D printer, the weight of the 3D-printed sections varies from the minimum value of 54.3 g and the maximum of 56.4 g. For the aeroelastic model, the average value of 55.2 g was used.

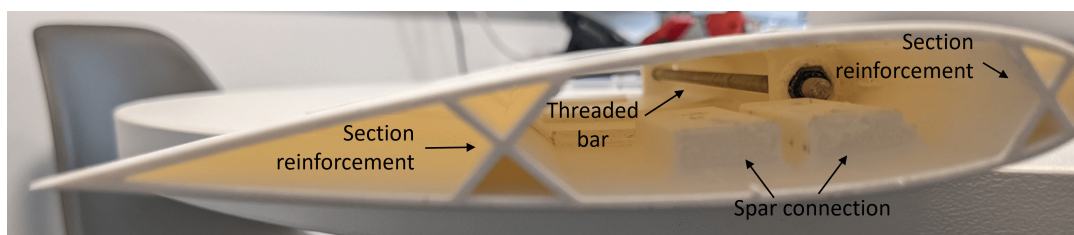


FIGURE 6.5: Wingtip threaded bar

The 3D-printed sections were manufactured in the laboratory of Swansea University by using two different materials: PLA and ABS-M30. PLA and ABS-M30 are both thermoplastic materials, and in Table 6.2, their properties are reported [152, 153]. For the printing, each material requires specific machine. 3D printing using ABS-M30 is more time-consuming but allows higher accuracy with respect to PLA. Due to the high

Component	Weight [kg]
Spar	0.292
Pair of bolt and washer	$1.9 \cdot 10^{-3}$
Wing 3D-printed section	$55.2 \cdot 10^{-3}$
Wingtip bearings and shaft	$3.8 \cdot 10^{-3}$
Wingtip threaded bar	$13.0 \cdot 10^{-3}$
Metal plate	$\approx 0$
Wingtip assembly	0.1938

TABLE 6.1: *Weight components*

precision required in manufacturing the hinge case, ABS-M30 was used. For consistency, the corresponding section for the fixed wingtip was also 3D-printed using ABS-M30. All the other parts were 3D-printed using PLA.

	ABS-M30	PLA	
Density	1040	1240	kg/m <sup>3</sup>
Young's modulus	2413	3120	MPa
Tensile stress	36	69.8	MPa

TABLE 6.2: *Properties of the 3D-printing materials*


---

## 6.2 Experimental Setup

---

The structural, aerodynamic and aeroelastic characterisation of a wing is performed using different sensors and equipment depending on the information to be extracted. Accelerometers, high-resolution cameras, and lasers are typically used for vibration measurement. High-resolution cameras and lasers have the advantage of being non-intrusive. Accelerometers were used for the impact hammer test and lasers to characterise the hinged wingtips and for the wind tunnel tests. A six-component force balance was used for the measurement of the wing root loads. This section shows the experimental setup, sensors used and the measurement procedure.

### 6.2.1 Accelerometer

Impact hammer tests were performed using the Data Physics Abacus 901 dynamic signal analyser [154] and accelerometers to identify mode shapes, natural frequencies and

damping ratios. Accelerometers can be considered as concentrated masses at their actual position. Table 6.3 shows the specifications of the accelerometers used [155, 156].

	PCB 352C03	PCB-352C22	
Sensitivity	( $\pm 10\%$ )10	( $\pm 15\%$ )10	mV/g
Frequency Range ( $\pm 5\%$ )	0.5 to 10000	1.0 to 10000	Hz
Broadband Resolution	0.0005	0.004	g rms
Sensing Element	Ceramic	Ceramic	
Weight	5.8	0.5	g

TABLE 6.3: Specifications of the accelerometers used

## 6.2.2 Displacement Sensor

Three LK-G507 Precision 1D Laser Triangulation sensors were used in the wind tunnel. Laser triangulation sensors include a detector (CMOS/CCD) and a solid-state laser light source. They operate on the basic principle wherein a laser beam is projected on the target under measurement, and a part of this beam is then reflected via focusing optics onto a detector. When the target shifts, the laser beam moves on the detector. Figure 6.6 shows the laser triangulation principle. The LK-G507 Precision 1D Laser Triangulation

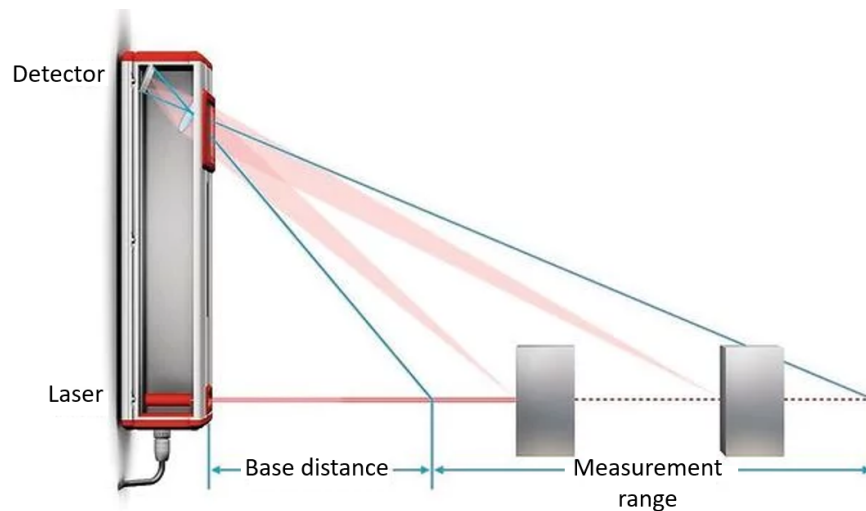


FIGURE 6.6: Laser triangulation principle (directly adapted from [22])

sensor can measure the distance of objects between 250 mm and 1000 mm from the laser with an accuracy of  $\pm 500 \mu\text{m}$  and sampling frequency up to 1 GHz [157]. The laser's output is a voltage proportional to the distance between the target and the laser. From the laser's controller, it is possible to modify the minimum and the maximum distance read for which the laser output is - 10 V and + 10 V, respectively. The laser's output is 0 V when the distance measure is 500 mm.

To record the voltages, the National Instrument NI-9231 module is used. The NI-9231 has eight analogue input channels, with 24 Bit resolution and  $\pm 5$  V range and is connected to the cDAQ-9189 [158]. The cDAQ-9189 is a CompactDAQ Ethernet chassis for distributed sensor measurement systems [159]. To ensure the maximum laser output voltage is within the safety limit and to have a linear relationship between the voltage ( $V_{laser}$ ) and the measured distance ( $d_{laser}$ ) in mm, the following conversion was used

$$d_{laser} = c_{laser} \cdot V_{laser} + 500 \quad (6.1)$$

where  $c_{laser} = 100$  mm/V.

The laser installation outside the wind tunnel with the laser case touching the plexiglass implies the laser beam has to pass through 25 mm of plexiglass, which deforms the beam's trajectory. To assess the effect of the plexiglass, static and dynamic tests were performed to characterise the sensors.

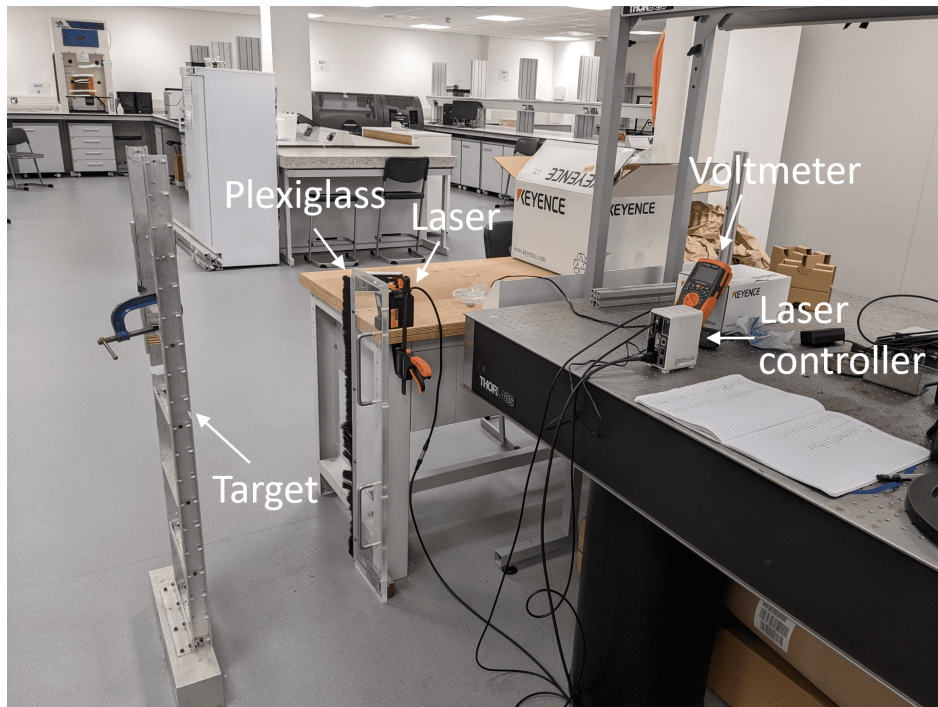
### 6.2.2.1 Static Test

Static tests were performed considering the target at a distance between 250 mm and 750 mm from the laser. Each measurement was performed with the plexiglass and without it to estimate the effect of the plexiglass on the laser's measurements. During the test, particular attention was taken to ensure the laser beam was perpendicular to the plexiglass. A digital voltmeter recorded the voltage of each measurement. Figure 6.7 shows the test setup and the measurement without and with the plexiglass.

Figure 6.8 shows the relation between the points measured with and without the plexiglass. The measurements without the plexiglass are considered as reference values. If the plexiglass was not introducing any measurement error, the measured data should be along the diagonal of Figure 6.8. Instead, the effect of the plexiglass is to overestimate the measured distances. Figure 6.9a shows that the identification error due to the plexiglass has a mean value of 8.0114 mm. To compensate for the error due to the plexiglass, Eq. (6.1) was modified as

$$d = c_{laser} \cdot V_{laser} + 500 - 8.0114 \quad (6.2)$$

where 8.0114 mm is the correction factor. Figure 6.9 shows that applying Eq. (6.2) the absolute and relative error in the distance identification is reduced.



(a) Test setup

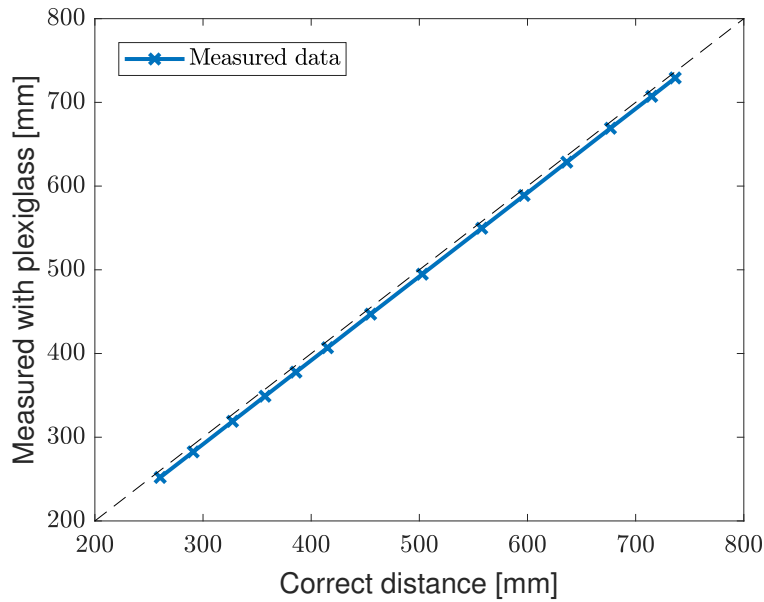
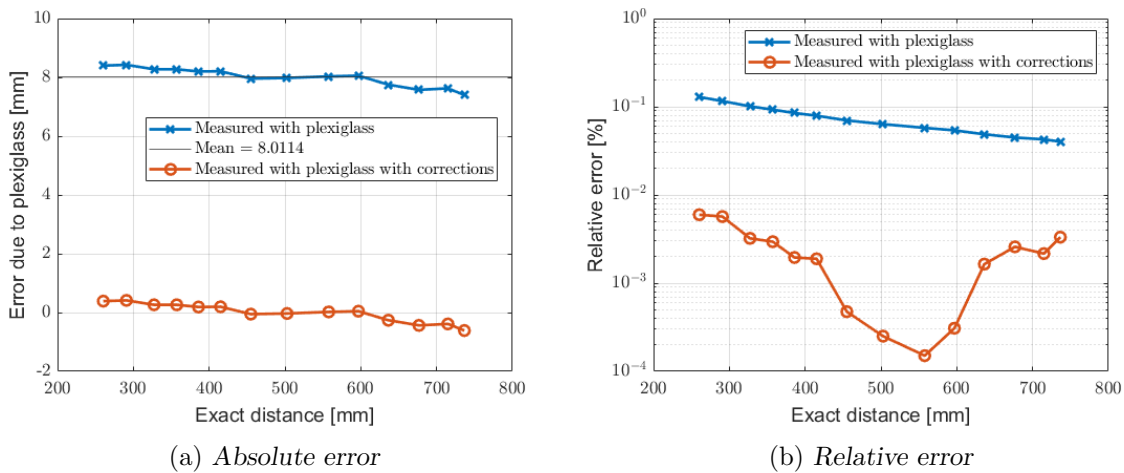


(b) Without plexiglass



(c) With plexiglass

FIGURE 6.7: Static test to measure the effect of the plexiglass on static laser measurements

FIGURE 6.8: *Static effect of the plexiglass*(a) *Absolute error*(b) *Relative error*FIGURE 6.9: *Error due to the plexiglass before and after corrections*

### 6.2.2.2 Dynamic Test

Two lasers measuring the spar tip oscillations were used to assess the effect of the plexiglass on dynamic measurements. One laser was located inside the wind tunnel and the other outside the wind tunnel with the plexiglass touching the laser case. Figure 6.10 shows the test setup. The two lasers measure the same point from the opposite sides of the spar. Figure 6.11 shows the measurements from the two lasers after subtracting the static value before the excitation. It also shows the measurement from the laser outside the wind tunnel multiplied by -1, which corresponds to the measurement inside

the wind tunnel. Therefore, the plexiglass does not introduce any further error in the laser measurements.

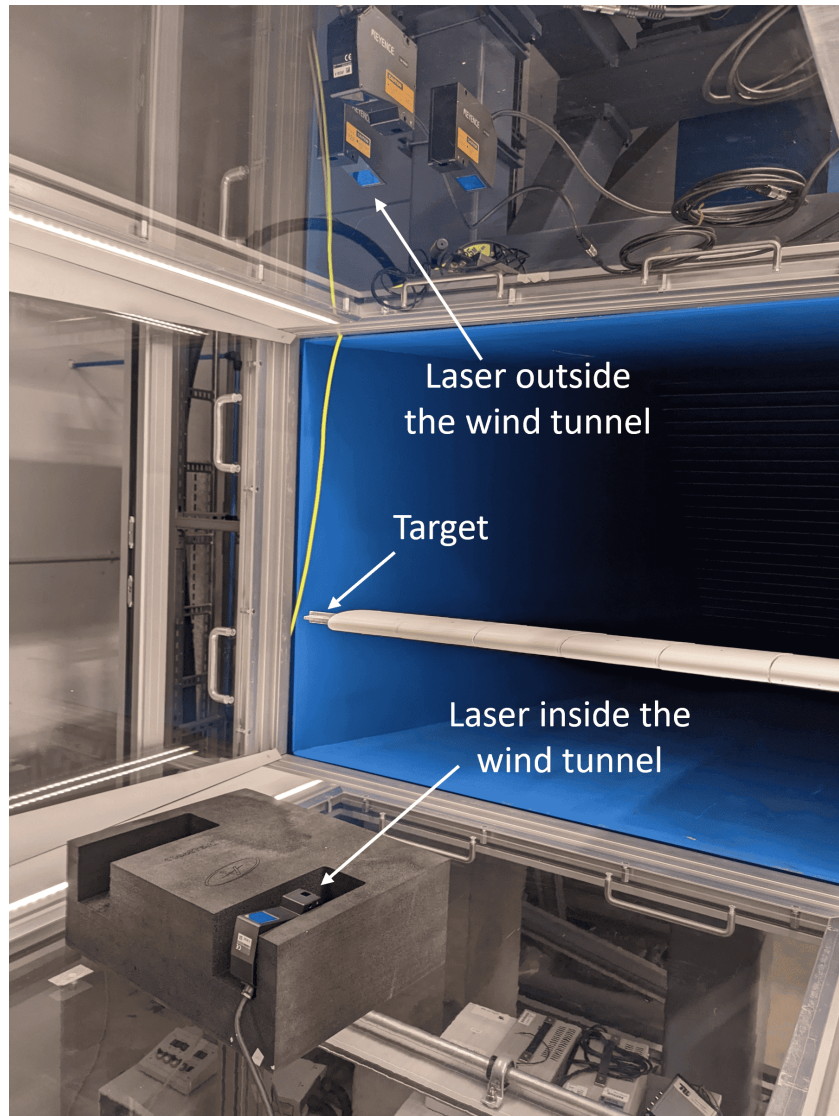


FIGURE 6.10: *Test setup for the dynamic effect of the plexiglass*

### 6.2.2.3 Fold Angle Identification

The laser displacement sensors were also used to identify the hinge fold angle by measuring the relative vertical displacement of a point on the hinge and a point on the wingtip. A test was performed to validate this technique. The wing with the free hinged wingtip was installed in the wind tunnel and a support structure was used to fix the position of the wing before the hinge. A movable bracket was used to support the wingtip at different heights and the correct fold angle was read by a protractor connected to the wingtip. Figure 6.12 shows the test setup. The identification of the fold angle  $\theta$  was

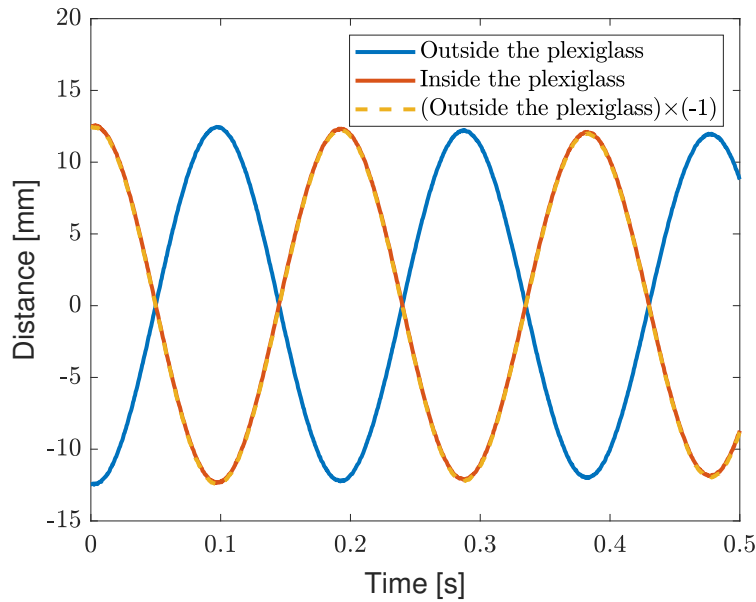


FIGURE 6.11: Measurement from sensors inside and outside the wind tunnel

performed using two lasers at the distance of 36.2 mm by using the relation

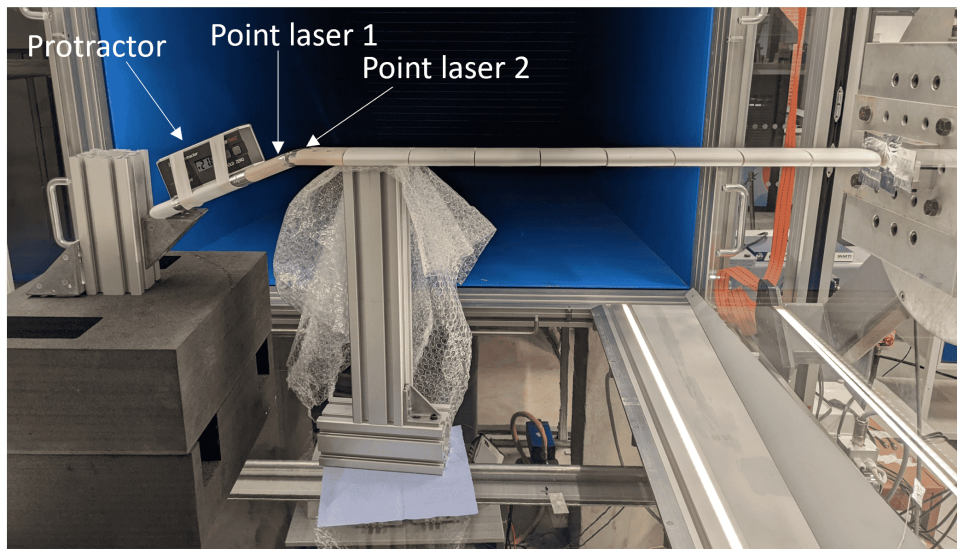
$$\theta = \text{atan}\left(\frac{d_2 - d_1}{36.2}\right) \quad (6.3)$$

where  $d_1$  and  $d_2$  are the vertical measurements of the point on the wingtip and on the hinge, respectively. Figure 6.13 shows the measured and identified fold angles. The maximum error in the identification was when the fold angle was  $29.9^\circ$  and the identified angle was  $31.0^\circ$  giving a  $1.1^\circ$  error which corresponds to 3.8% error. The error in the angle identification is lower than 5% so it is considered acceptable.

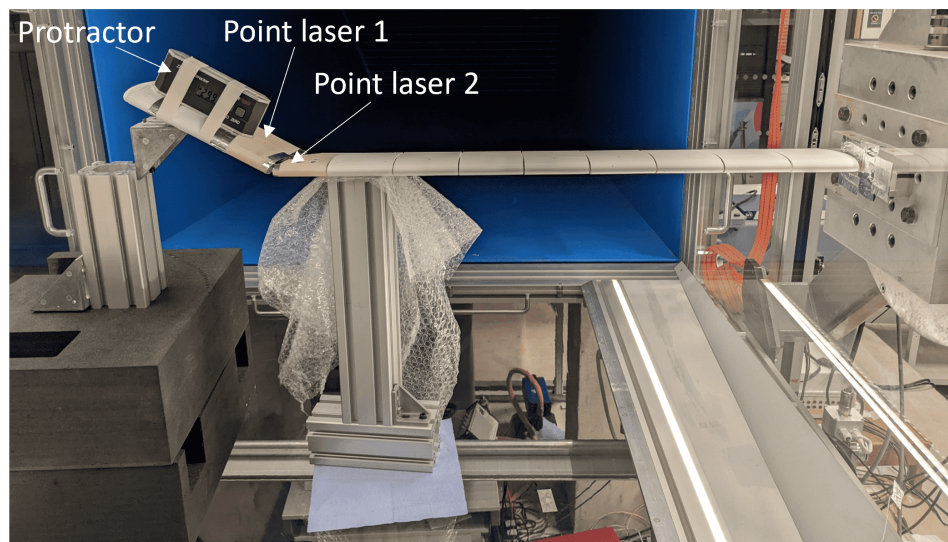
### 6.2.3 Balance

The Swansea University wind tunnel is equipped with AMTI GEN 5, a six-component force balance able to measure wing root force and moment [160]. Moreover, the balance can rotate to impose different wing root angles of attack. The balance has signal conditioning with a 1 kHz anti-aliasing filter, oversampling and digital signal processing. Each of the six analogue output channels has an independent 16-bit DAC conditioned by a low-pass reconstruction filter and amplifier. Each channel has a configurable gain to select the measurable maximum and minimum level load. Considering the wing dimensions, the gains were selected to the lower maximum and minimum load levels. Table 6.4 reports each channel's minimum, maximum and resolution level of load measurable. The z-axis is the one perpendicular to the balance.





(a) Negative fold angle

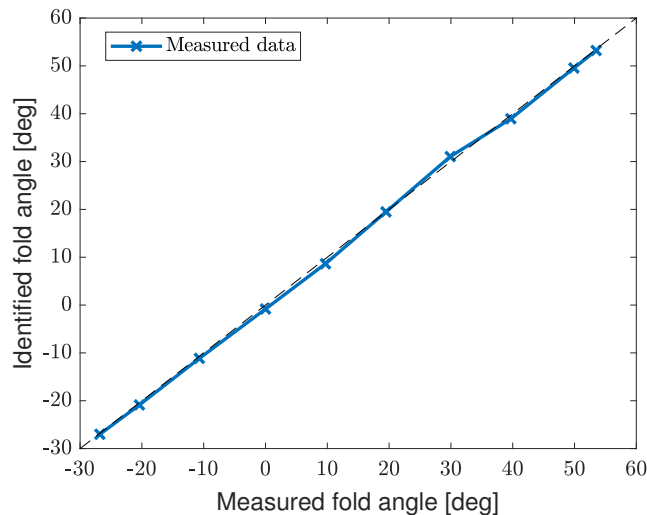


(b) Positive fold angle

FIGURE 6.12: Test setup for the identification of the fold angle

	Minimum	Maximum	Resolution
$F_x, F_y$	190.67 N	-190.67 N	5.8 mN
$F_z$	747.35 N	-747.35 N	22.8 mN
$M_x, M_y$	45.87 Nm	-45.87 Nm	1.4 mNm
$M_z$	21.83 Nm	-21.83 Nm	0.7 mNm

TABLE 6.4: Wind tunnel force balance minimum, maximum and resolution of each channel

FIGURE 6.13: *Measured vs identified fold angle*

Before and after each experiment, for all of the AoA considered during the test, measurements of the wing root loads were performed without any airspeed. These values were used to separate the aerodynamic loads from the loads due to gravity. Moreover, the linear time relation of the sensor drift was found from the difference in the measurements without airspeed before and after the wind tunnel test. To compensate for the drift effect, the hypothesis of linear drift with time was used, and a correction was added from the time information of each record.

---

### 6.3 Spar and Wing Structural Characterisation

---

Impact hammer tests were performed separately on the spar and the wing, considering all the wingtips, to assess their structural natural frequencies, mode shapes and damping ratios. Each Frequency Response Function (FRF) was calculated by the dynamic signal analyser Data Physics Abacus 901, taking the average from ten repetitions. The FRFs post-processing was performed in Matlab using the built-in function ‘modalfit’ to extract natural frequencies, damping ratio and modes shapes. The information extracted from the structural characterisation was used for the model validation. In each test, the impact force was applied at the accelerometers’ location on the opposite face with respect to the sensors. Moreover, impact hammer test were performed on the wing to ensure all the parts were well connected, and the system was linear. An impact hammer test was performed on the 3D-printed wing section to measure its first natural frequency.

### 6.3.1 Impact Hammer Test 3D-Printed Section

Firstly, an impact hammer test was performed to measure the first natural frequency of the 3D-printed sections bolted along the wing. Three PCB-352C22 accelerometers were used, and the impact force was applied only at the location of accelerometer one. Figure 6.14 shows the 3D-printed section during the impact hammer test. Figure 6.15 shows the frequency response functions of the 3D-printed airfoil section, and the first natural frequency is 509 Hz. The first natural frequency of the 3D-printed airfoil section was two orders of magnitude higher with respect to the expected first natural frequency of the wing, so at low frequency, there will be negligible interaction between the 3D-printed airfoil section deformation and the wing.

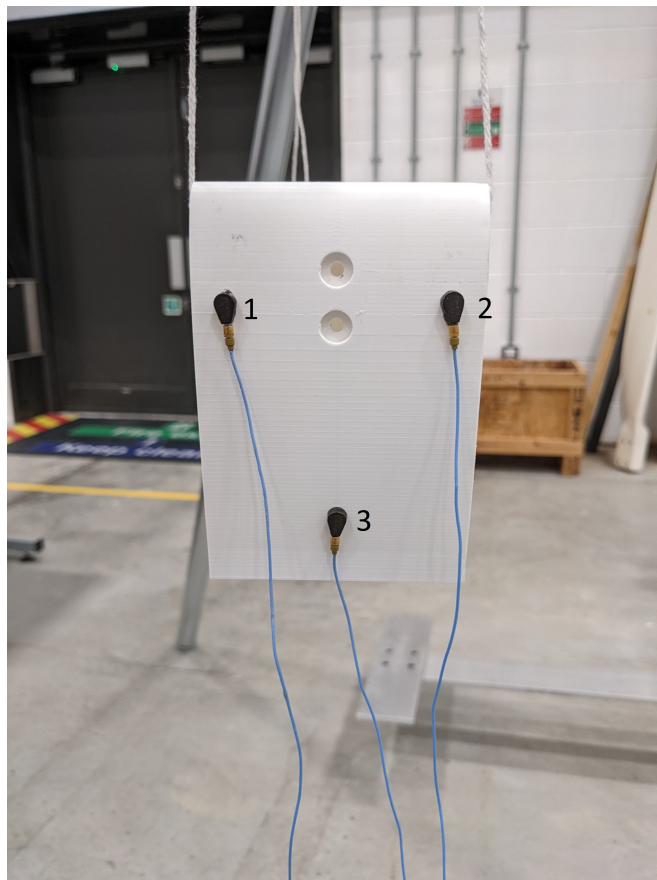
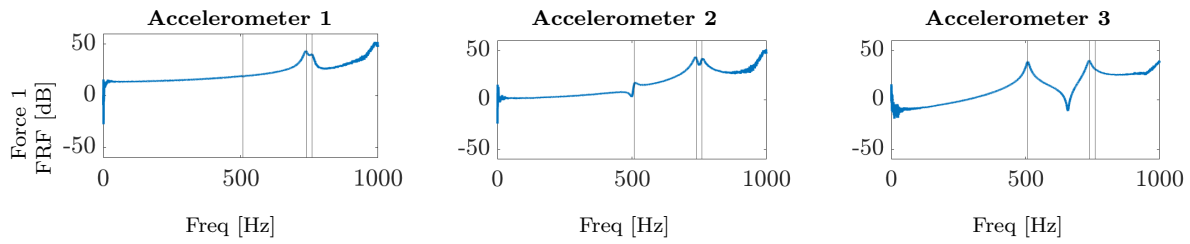


FIGURE 6.14: *Impact hammer test 3D-printed section*

### 6.3.2 Impact Hammer Test Wing Spar

Secondly, the impact hammer test on the spar was performed using four accelerometers uniformly distributed along the spar span. As accelerometers, three PCB-352C22 and one PCB 352C03 were used. Figures 6.16 and 6.17 show the test setup and the measured

FIGURE 6.15: *3D-printed airfoil section frequency response functions*

frequency response functions of the spar, respectively. Figure 6.17 shows the complete set of measured FRFs, which is symmetrical and with the main peaks well identifiable, confirming the system's linearity.

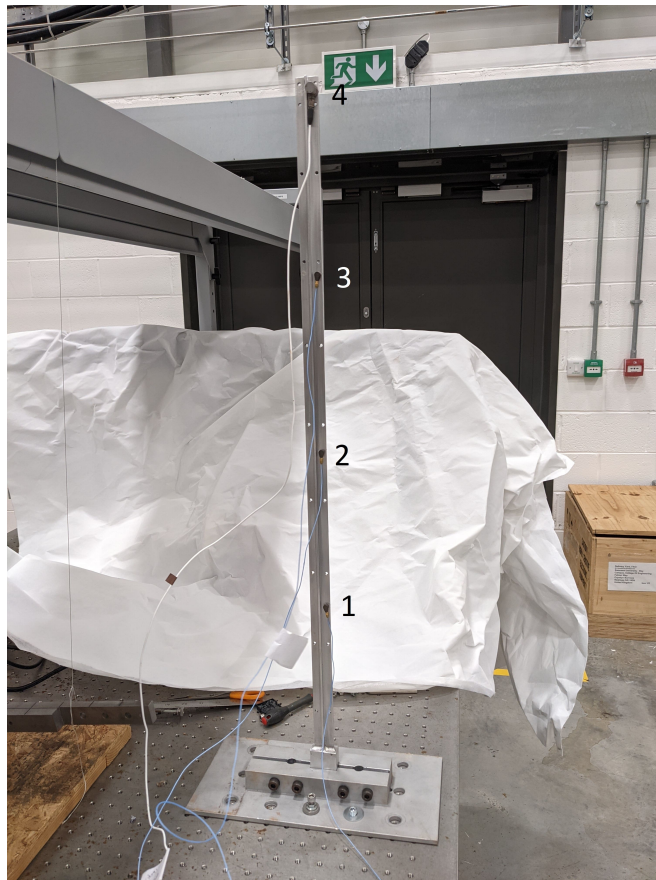
FIGURE 6.16: *Spar impact hammer test*

Table 6.5 reports the identified structural natural frequencies below 500 Hz and the corresponding mode shapes of the spar. Figure 6.18 shows the mode shapes reconstructed from the frequency response functions.

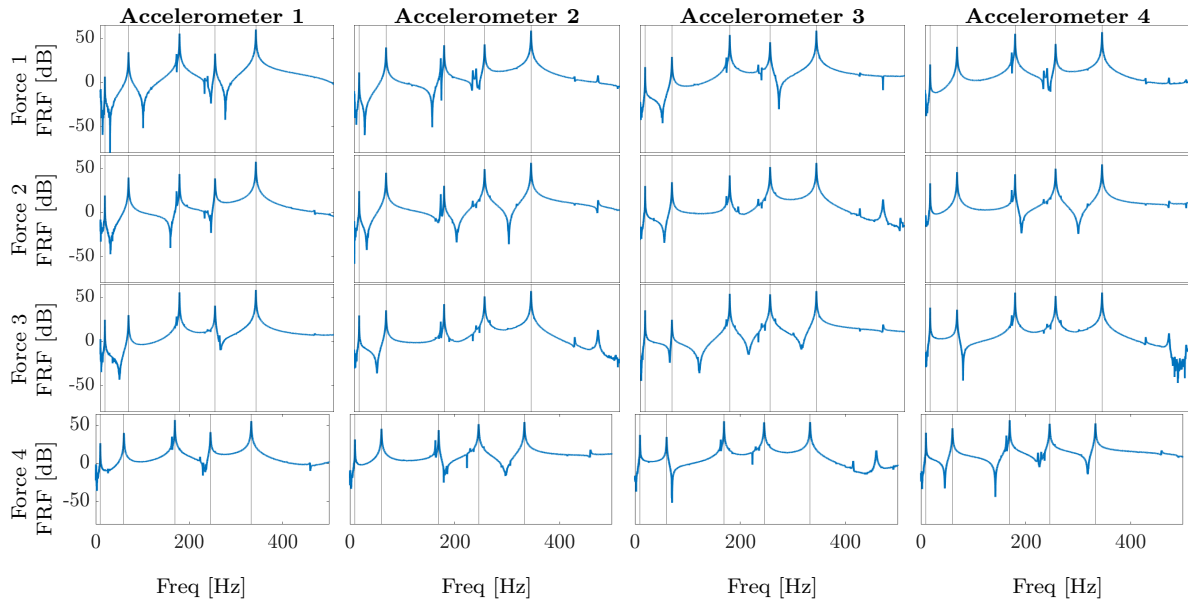


FIGURE 6.17: Spar frequency response functions

Frequency [Hz]	Damping ratio [%]	Mode shape
9.8	0.1	1 <sup>st</sup> out-of-plane bending
60.2	0.1	2 <sup>nd</sup> out-of-plane bending
169.4	0.05	3 <sup>rd</sup> out-of-plane bending
245.5	0.07	1 <sup>st</sup> torsion
332.8	1.0	4 <sup>th</sup> out-of-plane bending

TABLE 6.5: Spar measured natural frequencies, damping ratios and mode shapes

### 6.3.3 Impact Hammer Test of Wing with Different Wingtips

Finally, impact hammer tests were performed on the wing considering the three wingtips and using four PCB-352C22 accelerometers uniformly distributed along the wingspan and at the spar location, with the first accelerometer close to the wing root and the fourth on the wingtip. The wing was hung vertically with the wing root at the top to ensure the wingtip was parallel to the main wing. Figure 6.19 shows the impact hammer test setup in the cases considered. Figures 6.20, 6.21 and 6.22 show the FRFs of the wing with the fixed wingtip, the FRFs with the hinged wingtip and torsional spring and the FRFs with the free hinged wingtip. The excitation force was not applied at the fourth accelerometer location because, in the hinge cases, the high flexibility and low inertia made the excitation challenging. In the identified FRFs the main peaks are identifiable and the off-diagonal FRFs are symmetrical.

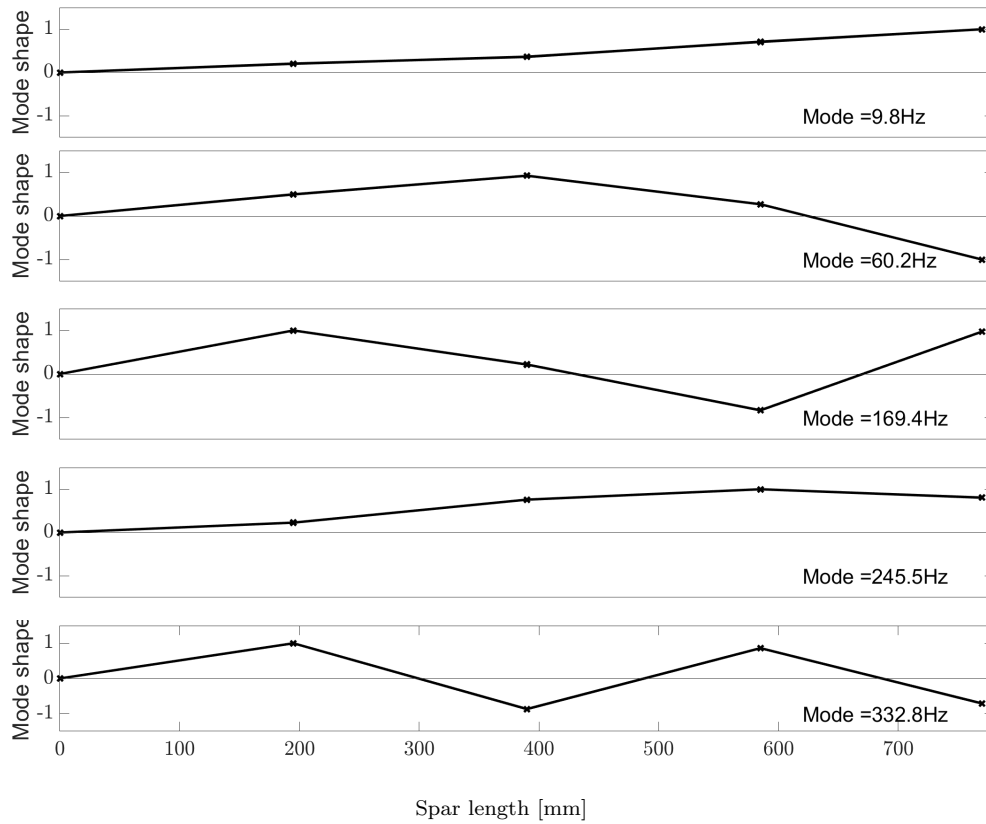


FIGURE 6.18: Spar mode shapes

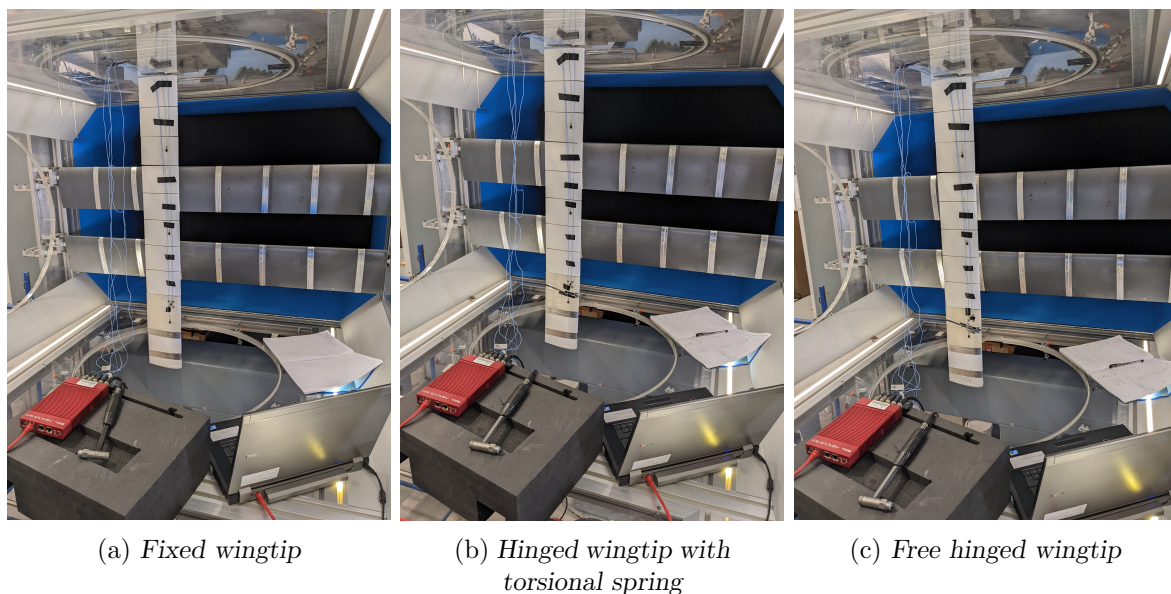
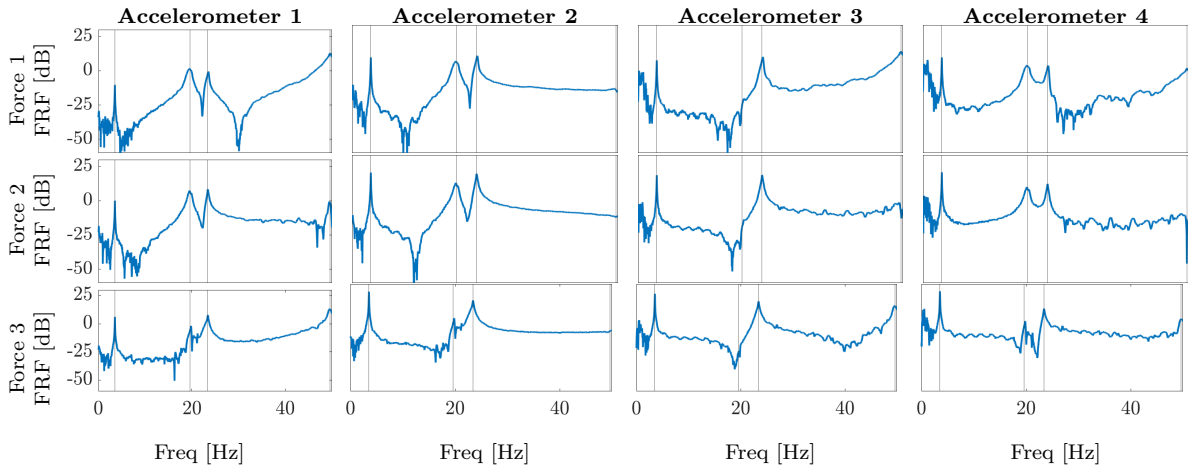
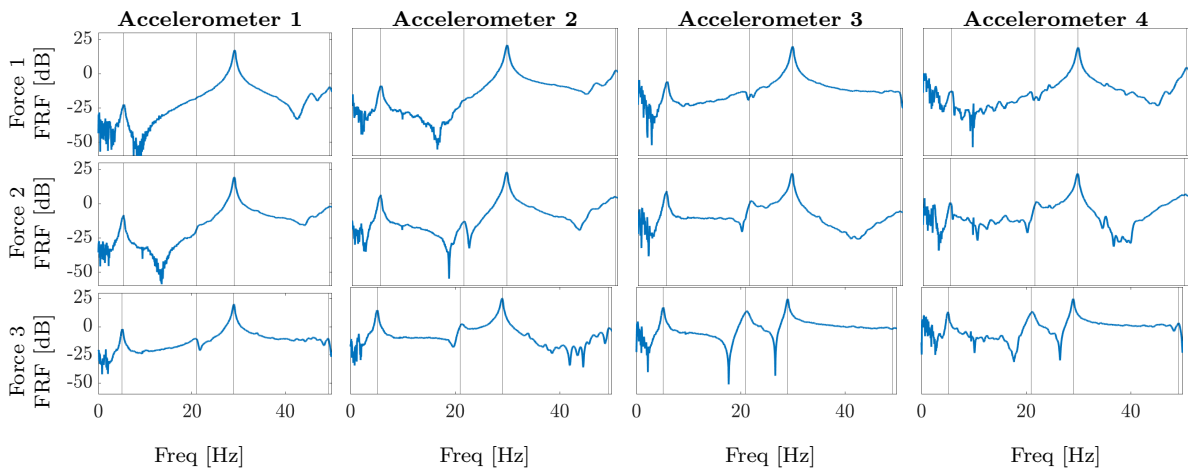


FIGURE 6.19: Impact hammer test of the wing with different wingtip

FIGURE 6.20: *Wing with fixed wingtip frequency response functions*FIGURE 6.21: *Wing with hinged wingtip and torsional spring frequency response functions*

Light accelerometers are not suitable to measure low frequency components. Indeed, Figures 6.20, 6.21 and 6.22 show high noise at low frequency. Hence, to identify the hinged wingtip's natural frequency and damping ratio, a laser was used to record the time history of vibration of a point on the wingtip when the wingtip was subjected to an initial displacement. Figure 6.23 shows the time history of the oscillations of the free hinged wingtip and the hinged wingtip with the torsional spring. Using the peak-to-peak and logarithmic decrement methods, the natural frequency and damping ratio in both cases were identified. Table 6.6 reports the measured structural natural frequencies below 50 Hz and the corresponding damping ratios of the wing with the different wingtips. The first natural frequency of the wing with the free hinged wingtip

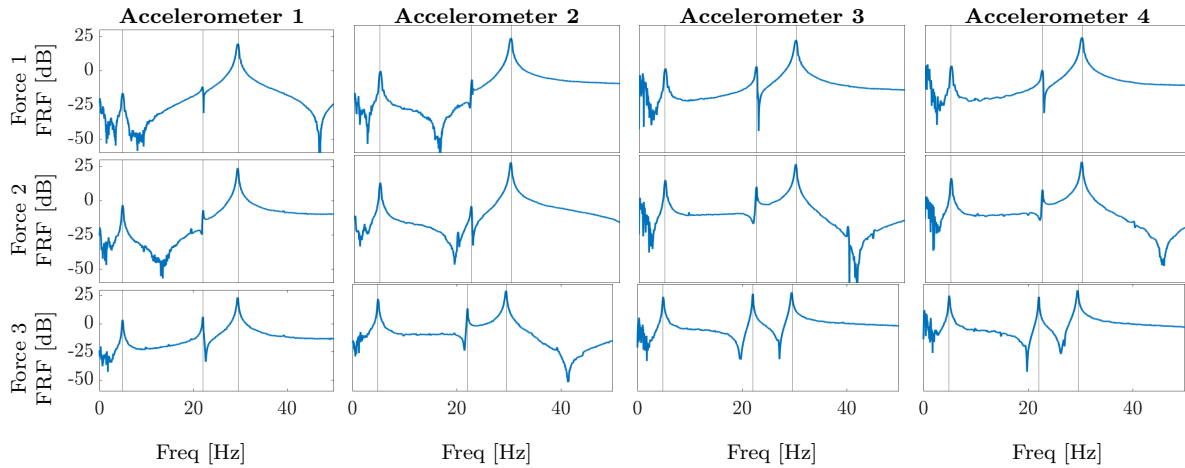


FIGURE 6.22: Wing with hinged wingtip frequency response functions

is not zero due to the gravitational effect. The metal plate on the hinge increases the wingtip's natural frequency of 0.2 Hz and decreases the damping ratio by four times. Due to the presence of the hinge and the consequent reduction in the main wing length, the natural frequency of the first out-of-plane bending mode increases from 3.5 Hz (fixed wingtip) to 4.9 Hz in the case of the free hinged wingtip and 5.1 Hz in the case of the hinged wingtip with the torsional spring.

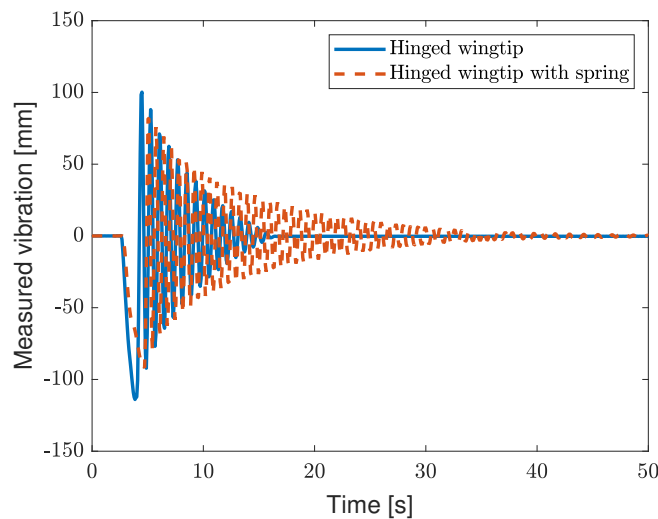


FIGURE 6.23: Identification wingtip natural frequency and damping ratio of the wing with hinged wingtip



Fixed Wingtip		Hinged wingtip with torsional spring		Hinged wingtip	
Frequency [Hz]	Damping ratio [%]	Frequency [Hz]	Damping ratio [%]	Frequency [Hz]	Damping ratio [%]
3.5	0.4	1.4	0.7	1.2	2.7
19.6	1.7	5.1	3.5	4.9	1.8
23.4	0.8	21.0	2.3	22.1	0.3
49.6	0.7	29.1	0.8	29.6	0.6
-	-	49.5	1.3	-	-

TABLE 6.6: Measured natural frequencies and damping ratios of the wing with different wingtips

## 6.4 Wind Tunnel Tests

Static and dynamic wind tunnel tests were performed to assess the static and dynamic performance of the wing with the manufactured wingtips. The wing root was connected to the six-component force balance to record the wing root loads. The wind tunnel was equipped with the gust generator to produce discrete gusts and three LK-G507 Precision 1D Lasers. Figure 6.24 shows the wing installed in the Swansea University wind tunnel, the balance and the gust generator.

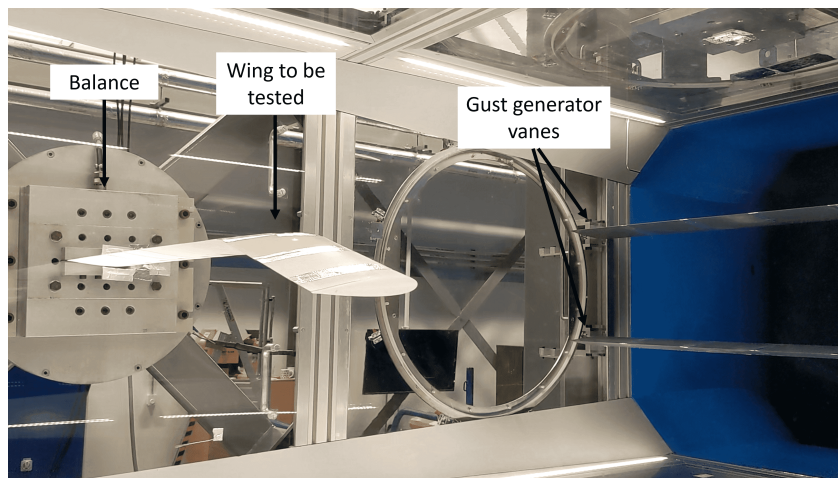


FIGURE 6.24: Wing installed in the wind tunnel

### 6.4.1 Static Test

A static wind tunnel test was performed, changing the wing root angle of attack (AoA) from  $0^\circ$  to  $12^\circ$  to  $-12^\circ$  and back to  $0^\circ$  with increments of  $1^\circ$ , recording with a sampling rate of 300 Hz for 20 seconds. Tests were performed at airspeeds of 10 m/s, 14 m/s, 18 m/s and 22 m/s. The wing performances were considered in terms of nondimensionalised coefficients. The nondimensionalization was performed considering a constant value for the wing dimension to ensure that a reduction in wing span, e.g. due to a significant wingtip rotation, did not increase the nondimensionalization coefficient.

From the measured lift  $L$ , the lift coefficient  $C_L$  was calculated as

$$C_L = \frac{L}{0.5\rho V^2 S} \quad (6.4)$$

where  $\rho$  is the air density calculated from the air temperature,  $V$  is the recorded free stream velocity, and  $S$  is the wing surface area given as  $0.134 \text{ m}^2$ . Figure 6.25 shows the  $C_L$  values at different AoA for the wing considered with the different wingtips.

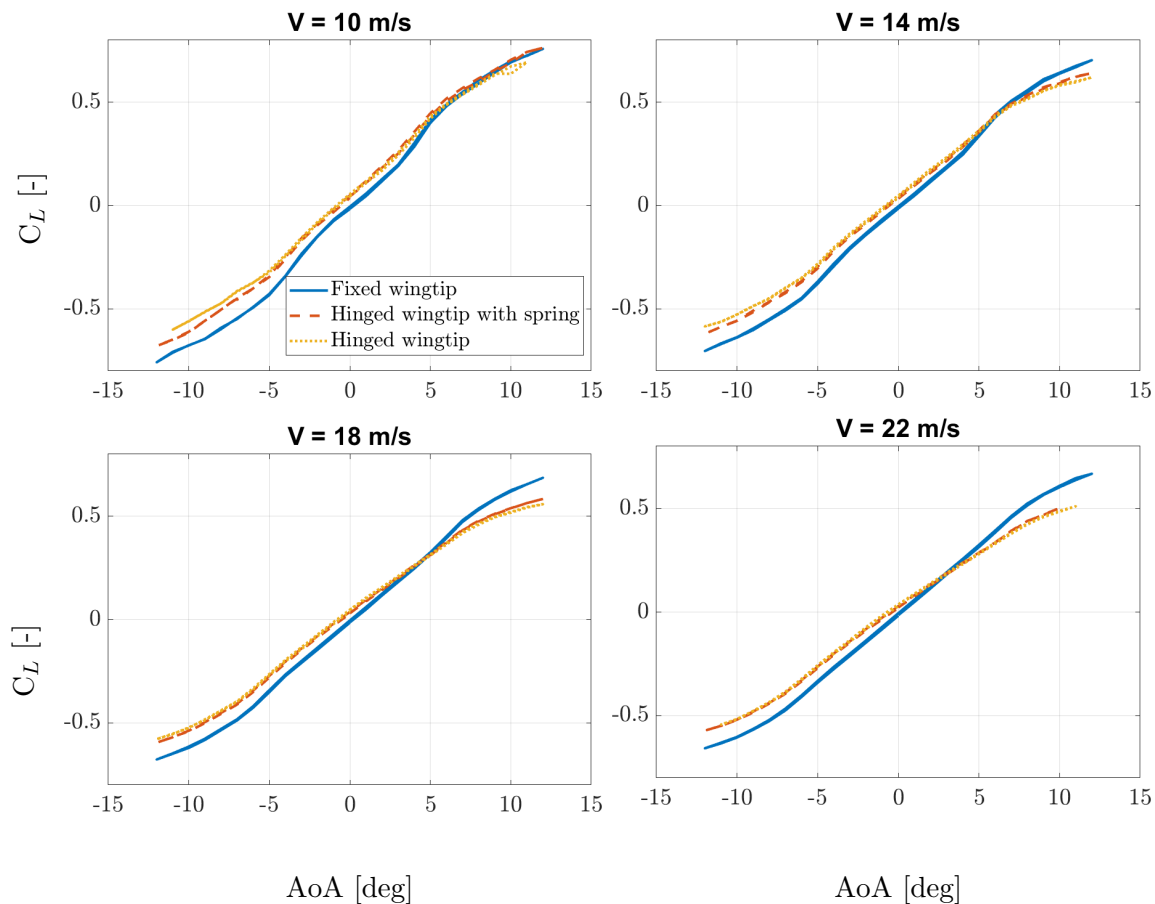


FIGURE 6.25: Lift coefficient at different angle of attack and airspeed

The  $C_L$  curve of the wing with the free hinged wingtip and the one with the hinged wingtip and a torsional spring have a similar trend. Indeed, Table 6.6 reports that the spring on the hinge only slightly modifies the natural frequencies due to its low stiffness. The  $C_L$  curve of the wing with a fixed wingtip and the one with a free wingtip intersect, representing the AoA for which the wingtip is parallel to the main wing. Figure 6.26 shows the intersection of the lift coefficient curves and define the intersection point as threshold. Indeed, Wing Root AoAs (WRAoAs) smaller than the threshold are asso-

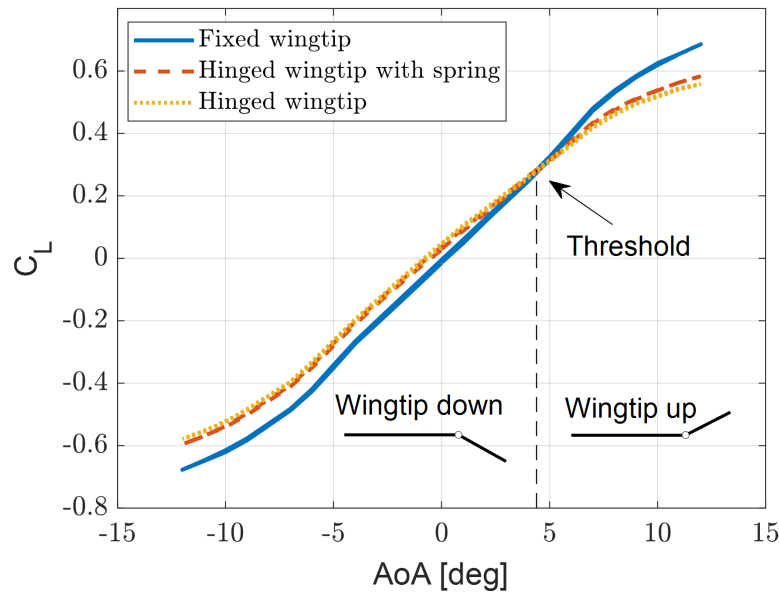


FIGURE 6.26: Lift coefficient at different angle of attack and 18 m/s

ciated with a negative fold angle (wingtip fold-down), and WRAoAs greater than the threshold are associated with a positive fold angle (wingtip fold-up). When the wingtip is fold-down, the wingtip AoA is higher than that of the main wing and vice-versa when the wingtip is fold-up. Increasing the airspeed, the AoA for which the wingtip is parallel to the main wing decreases. Indeed, for the same AoA and increasing the airspeed, the lift produced is higher; consequently, for a lower AoA, the wingtip can produce a lift able to balance its weight. For AoAs smaller than the threshold, the lift produced by a wing with a hinged wingtip is higher than the lift produced by a similar wing with a fixed wingtip due to the extra lift produced by the wingtip folded down. AoAs greater than the threshold are associated with higher lift for the wing with a fixed wingtip with respect to the wing with a hinged wingtip because the wingtip folded up produces less lift.

From the measured wing root out-of-plane bending moment  $M_{WRBM}$ , the rolling moment coefficient  $C_l$  was calculated as

$$C_l = \frac{M_{WRBM}}{0.5\rho V^2 S s} \quad (6.5)$$

where  $s$  is the wingspan. Figure 6.27 shows the rolling moment coefficient values at different AoA for the wing considered with all the wingtips.

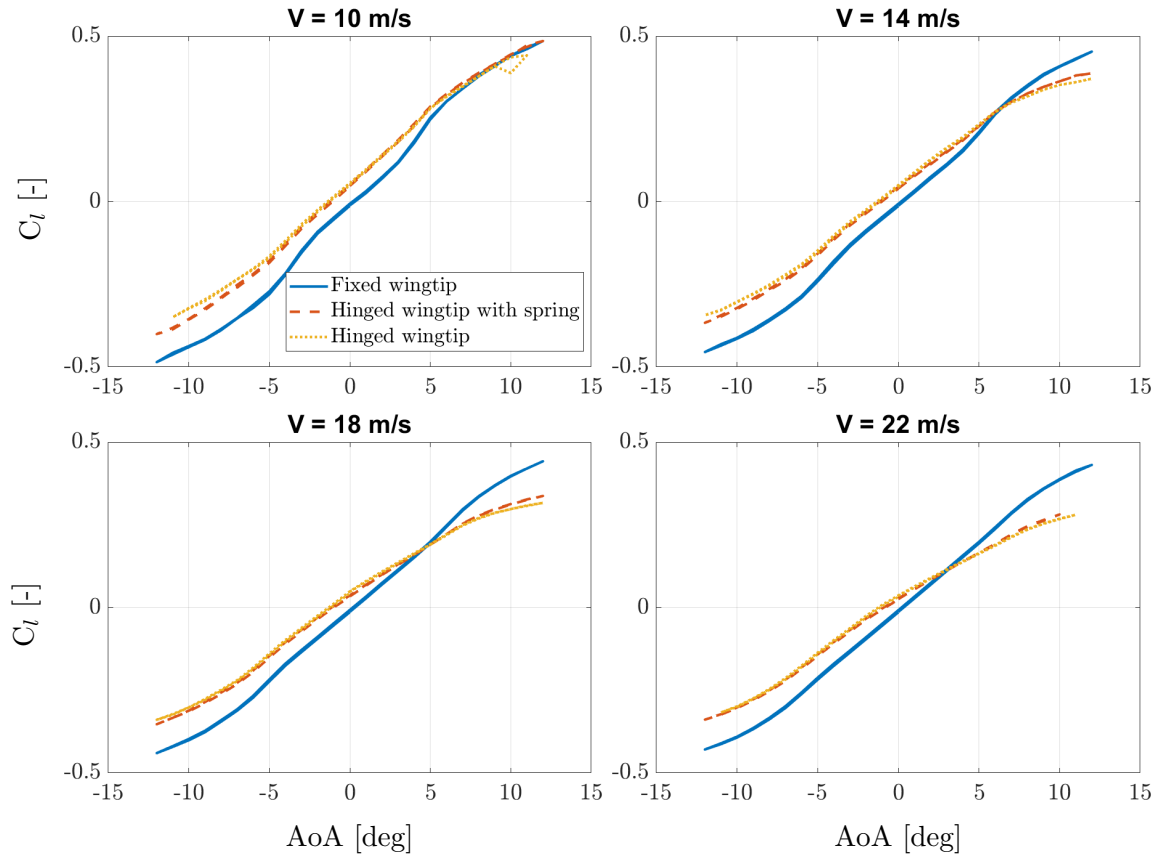


FIGURE 6.27: Rolling moment coefficient at different angle of attack and airspeed

As in the case of the  $C_L$  curves, the  $C_l$  of the wing with a fixed wingtip and the one with a hinged wingtip intersect.

Figures 6.25 and 6.27 show that the slope of the  $C_L$ -AoA and  $C_l$ -AoA curves for the wing with a hinged wingtip is lower with respect to the wing with a fixed wingtip. Gusts produce an increment of the wing AoA, which causes an increment in  $C_L$  and  $C_l$ . So, an AoA increment produces a smaller increment in lift and wing root out-of-plane bending moment in the wing with a hinged wingtip with respect to the wing with a fixed wingtip. Consequently, gusts cause a smaller load increment in the case of a wing with a hinged wingtip compared to a wing with a fixed wingtip. These results are in accordance with the literature and confirm the ability of a hinged wingtip to reduce gust loads [6].

Figure 6.28 shows the  $C_l$  and  $C_L$  curve plotted one against the other to compare the performance of the wingtips considered. Values of  $C_L$  smaller than the threshold are associated with higher  $C_l$  for the wing with a hinged wingtip with respect to the one with a fixed wingtip, and vice versa for  $C_L$  higher than the threshold.

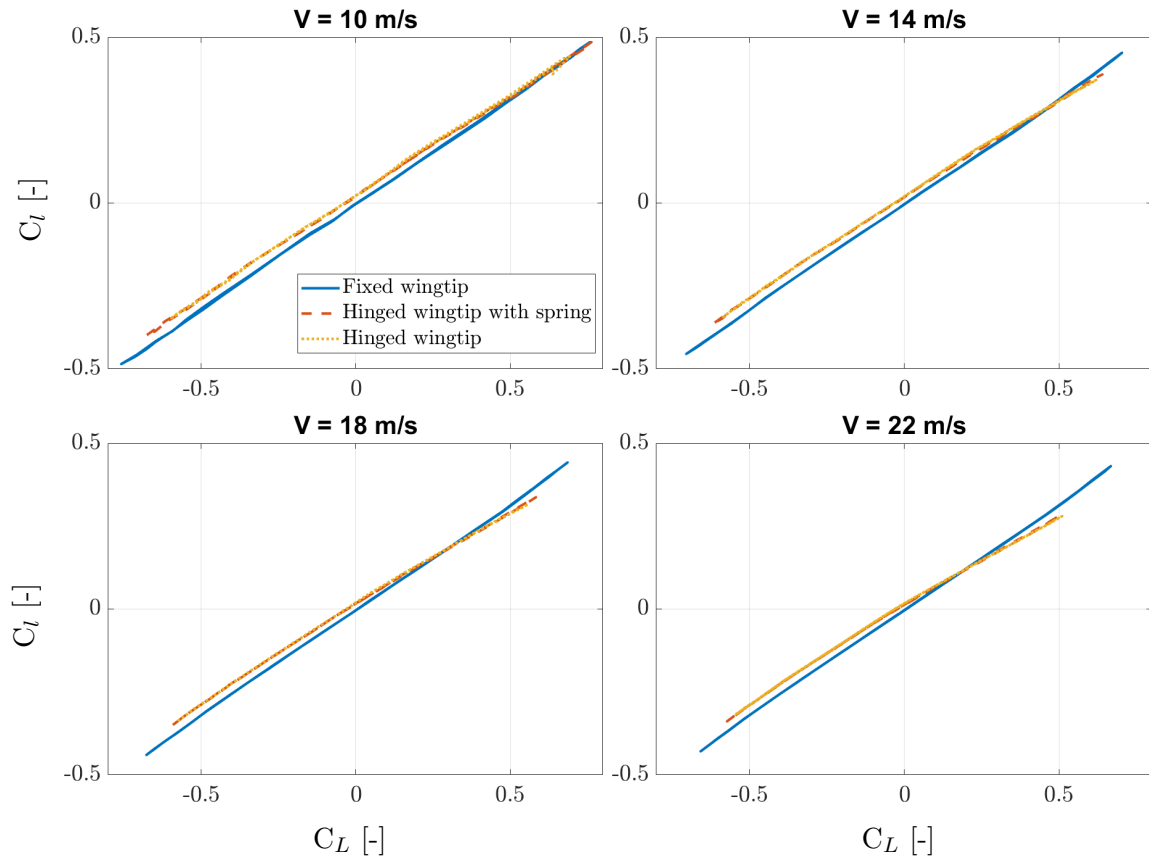


FIGURE 6.28: *Rolling moment coefficient at different lift coefficient and airspeed*

Figure 6.29 shows the fold angle for different AoA and airspeed of 10 m/s, 14 m/s, 18 m/s and 22 m/s. The identified fold angle from the measurements at 10 m/s is not reliable because at 10 m/s the lift produced is not enough to balance the weight. Indeed, the calibration has been performed keeping the wing straight. For low AoA and airspeed, the wingtip is not producing enough lift to balance the weight, and its fold angle is  $-27^\circ$ , the minimum negative angle achievable by the hinge. At low airspeed, the spring on the hinge can produce a moment able to rotate the wingtip. Increasing the airspeed, the effect of the spring decreases.

Figures 6.25, 6.27, 6.28 and 6.29 show that varying the airspeed and the AoA the results are consistent.

Figures 6.25, 6.27, 6.28 and 6.29 show that varying the airspeed and the AoA the results are consistent.

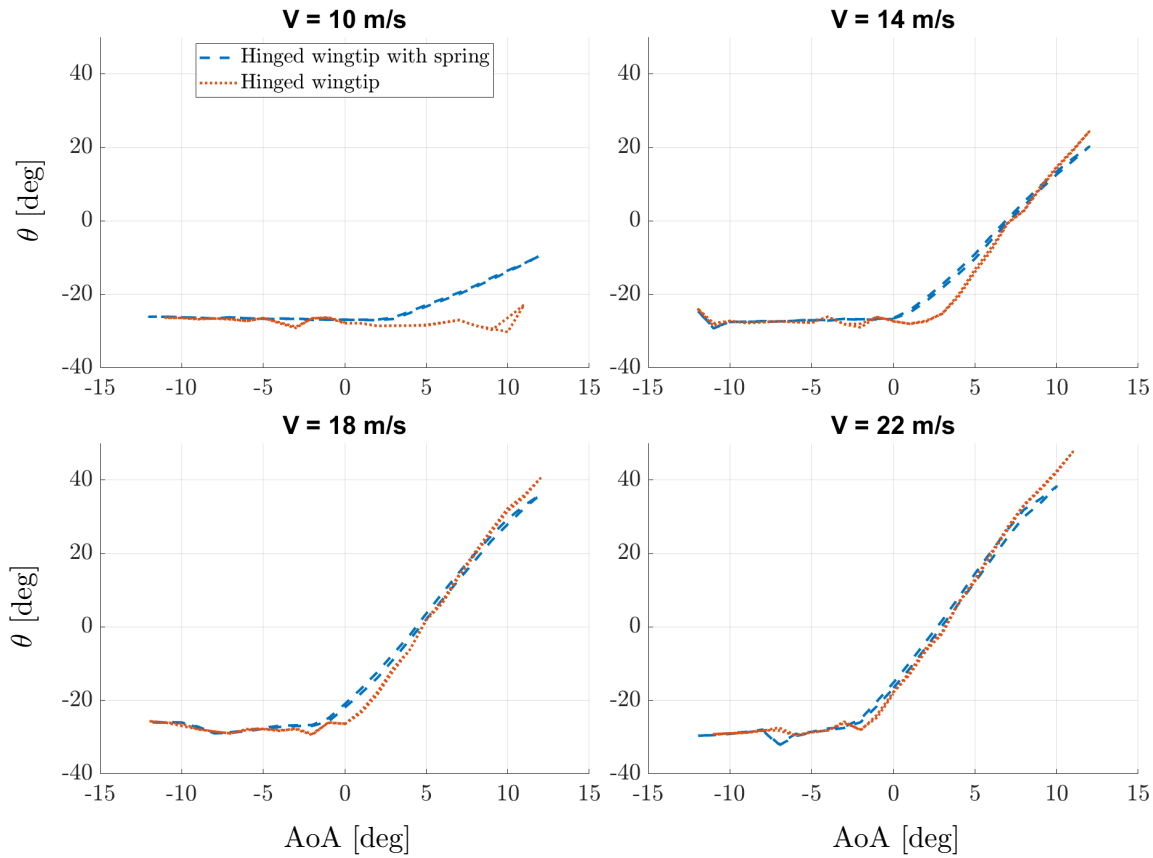


FIGURE 6.29: Wingtip fold angle at different angle of attack and airspeed

### 6.4.2 Dynamic Test

Discrete gusts, according to EASA, are described in terms of  $l_g$  and  $w_{g0}$  as in Eq. 2.7 while in Chapter 5 gusts were defined in terms of frequency of the ‘1 - cosine’ function. From the frequency of the ‘1 - cosine’ function is possible to find the  $l_g$  considering

$$\frac{V}{l_g} = f \quad (6.6)$$

and so

$$l_g = \frac{V}{f} \quad (6.7)$$

The wing with all the wingtips was subjected to discrete gusts with gust lengths from 1.29 m to 9 m and an airspeed of 18 m/s. Discrete gusts were obtained using the vane rotation defined after the parametric study of Section 5.4.2 considering  $A = 5^\circ$ ,  $A = 10^\circ$  and  $A = 15^\circ$ . Increasing the vane rotation, discrete gusts have a higher amplitude. In the following section, gusts produced by the three vane rotations are called small, medium and large discrete gusts (e.g. for  $l_g = 1.8$  m, vertical gust of 0.24 m/s, 0.46 m/s, and 0.63 m/s). To evaluate the effect of the WR AoA, the gust response was performed

at WRAoA of  $2^\circ$ ,  $4.4^\circ$  and  $6^\circ$ . Linear interpolation was performed on the  $C_L$  values at 18 m/s to find the WRAoA for which the hinged wingtip was parallel to the rest of the wing, and was estimated at  $4.4^\circ$ . A WRAoA of  $2^\circ$  was considered to ensure that during the gust response, any wingtip rotation was not hitting the lower hinge rotation limit. A WRAoA of  $6^\circ$  was considered to ensure that before the gust the wing with a hinged wingtip had a lower Wing Root Bending Moment WRBM with respect to the fixed wingtip.

Figure 6.30 shows the results of the same gust response repeated three times. In the three cases, the measurements are very similar showing a good repeatability.

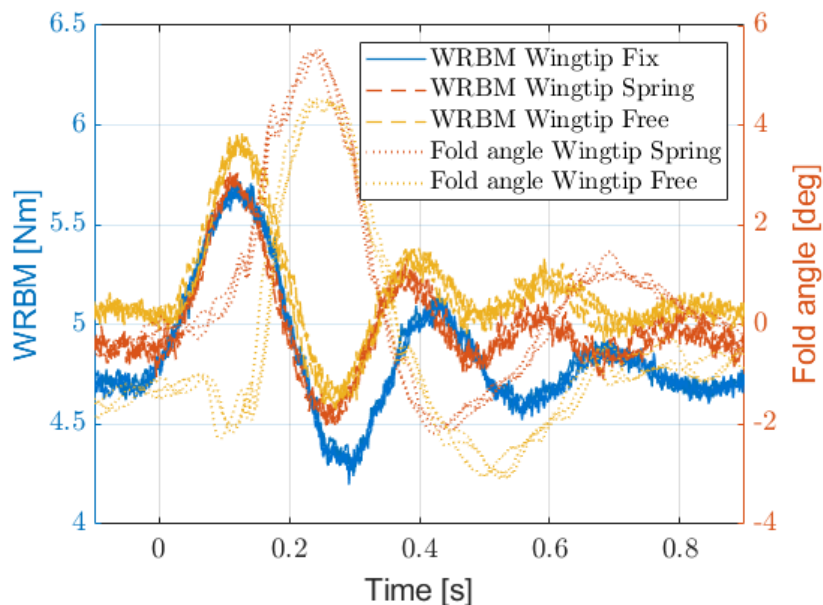


FIGURE 6.30: Typical gust response, each measurement is repeated three times to evaluate repeatability (gust length 9 m)

Figures 6.31, 6.32 and 6.33 show the measured time history gust response of the WRBM and fold angle for the small gust amplitude and the selected WRAoAs. Figures 6.34, 6.35 and 6.36 show the measured time history gust response of the WRBM and fold angle for the medium gust amplitude and the selected WRAoAs. Figures 6.37, 6.38 and 6.39 show the measured time history gust response of the WRBM and fold angle for the large gust amplitude and the selected WRAoAs. Figure 6.31 shows oscillation in the fold angle at around 10 Hz before the gust when the wingtip is free to rotate. It is conceivable that these oscillations are due to a coupling between the in-plane and the wingtip mode.

Before the gust, the WRBM of the wing with a hinged wingtip is higher than for the fixed wingtip for WRAoA of  $2^\circ$  and  $4.4^\circ$  and lower for a WRAoA of  $6^\circ$ , in accordance

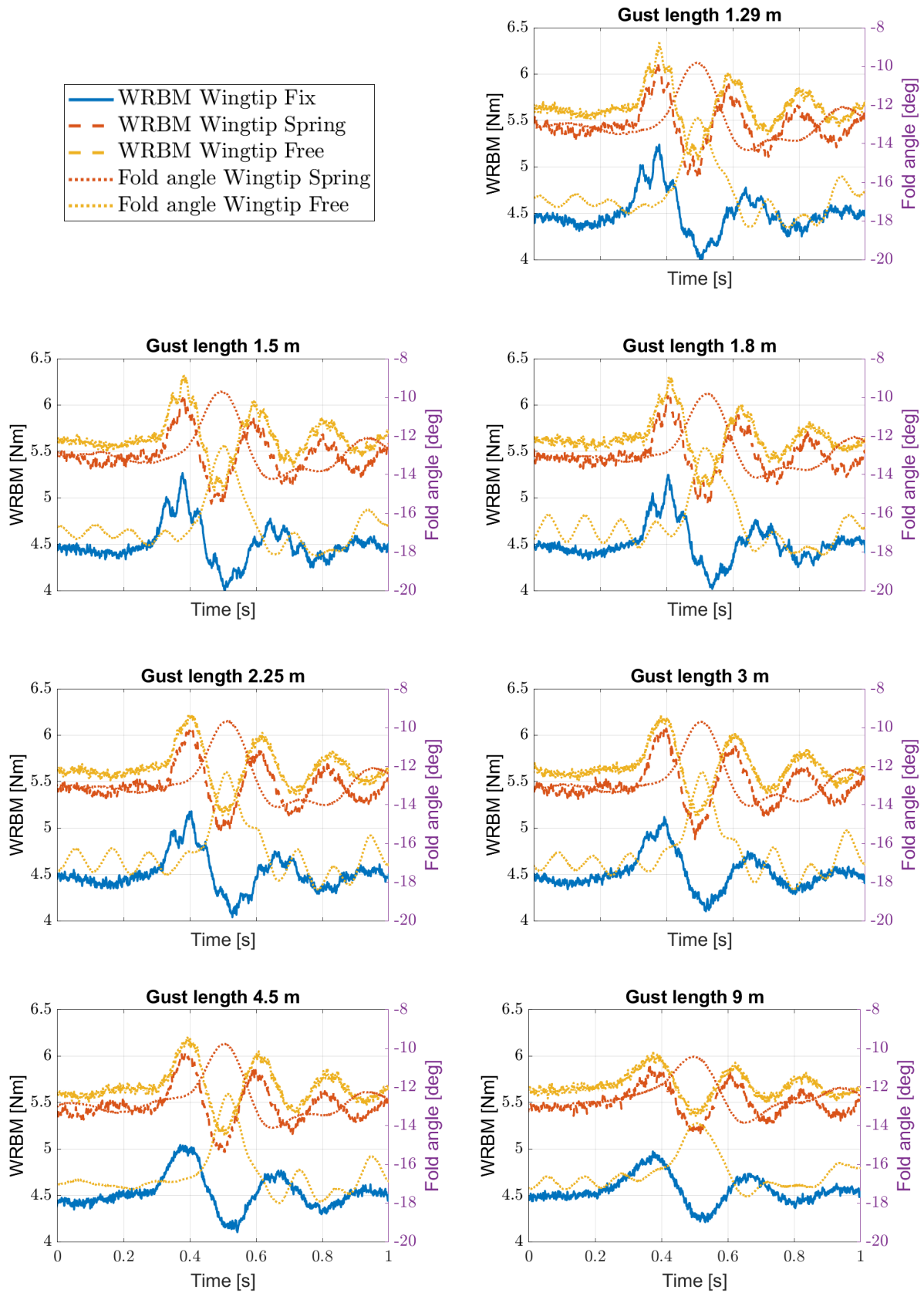


FIGURE 6.31: WRBM gust response for the wing with fixed wingtip, hinged wingtip and hinged wingtip with torsional spring and fold angle time history. Small discrete gust amplitude and wing root AoA  $2^\circ$



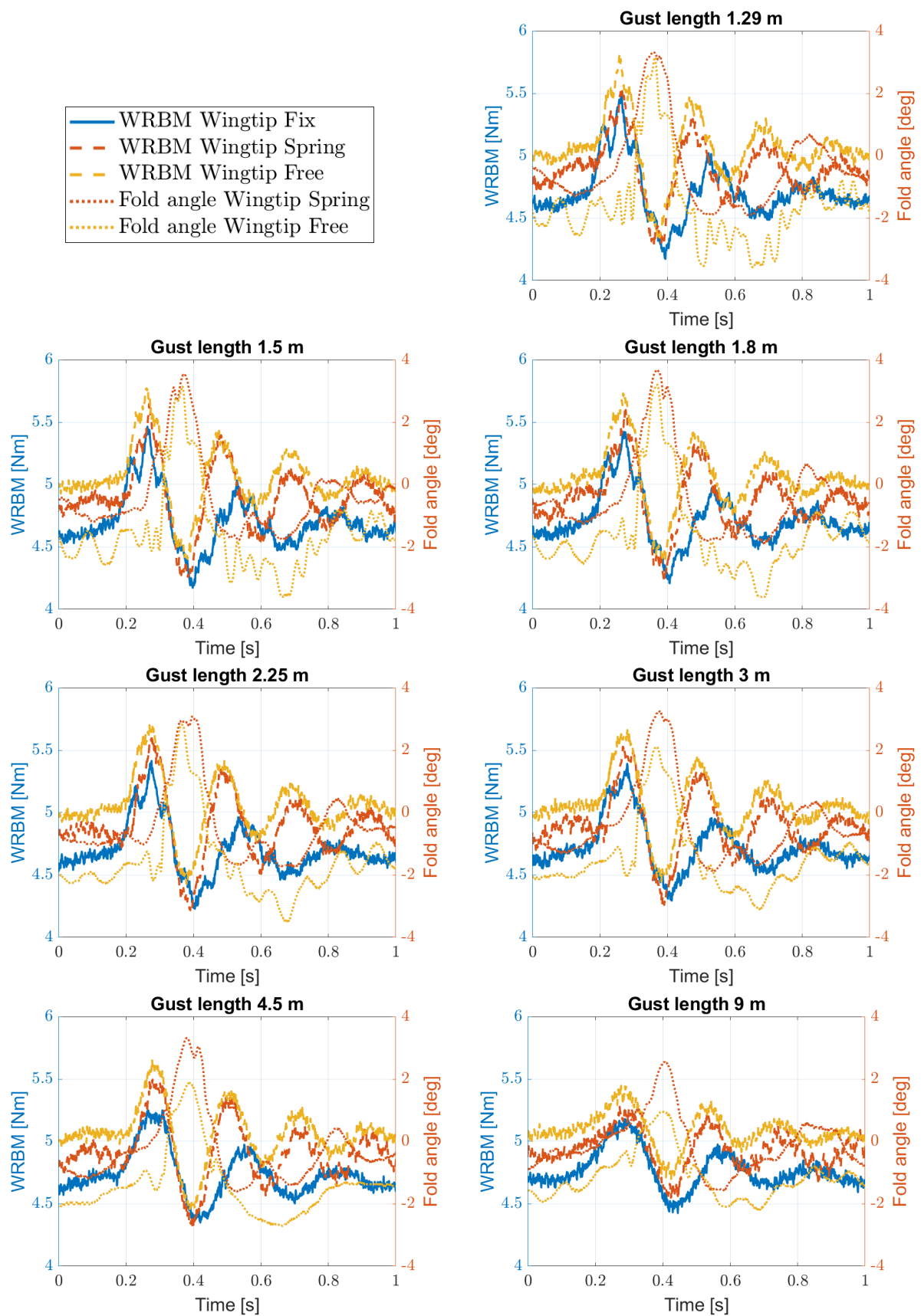


FIGURE 6.32: WRBM gust response for the wing with fixed wingtip, hinged wingtip and hinged wingtip with torsional spring and fold angle time history. Small discrete gust amplitude and wing root AoA  $4.4^\circ$

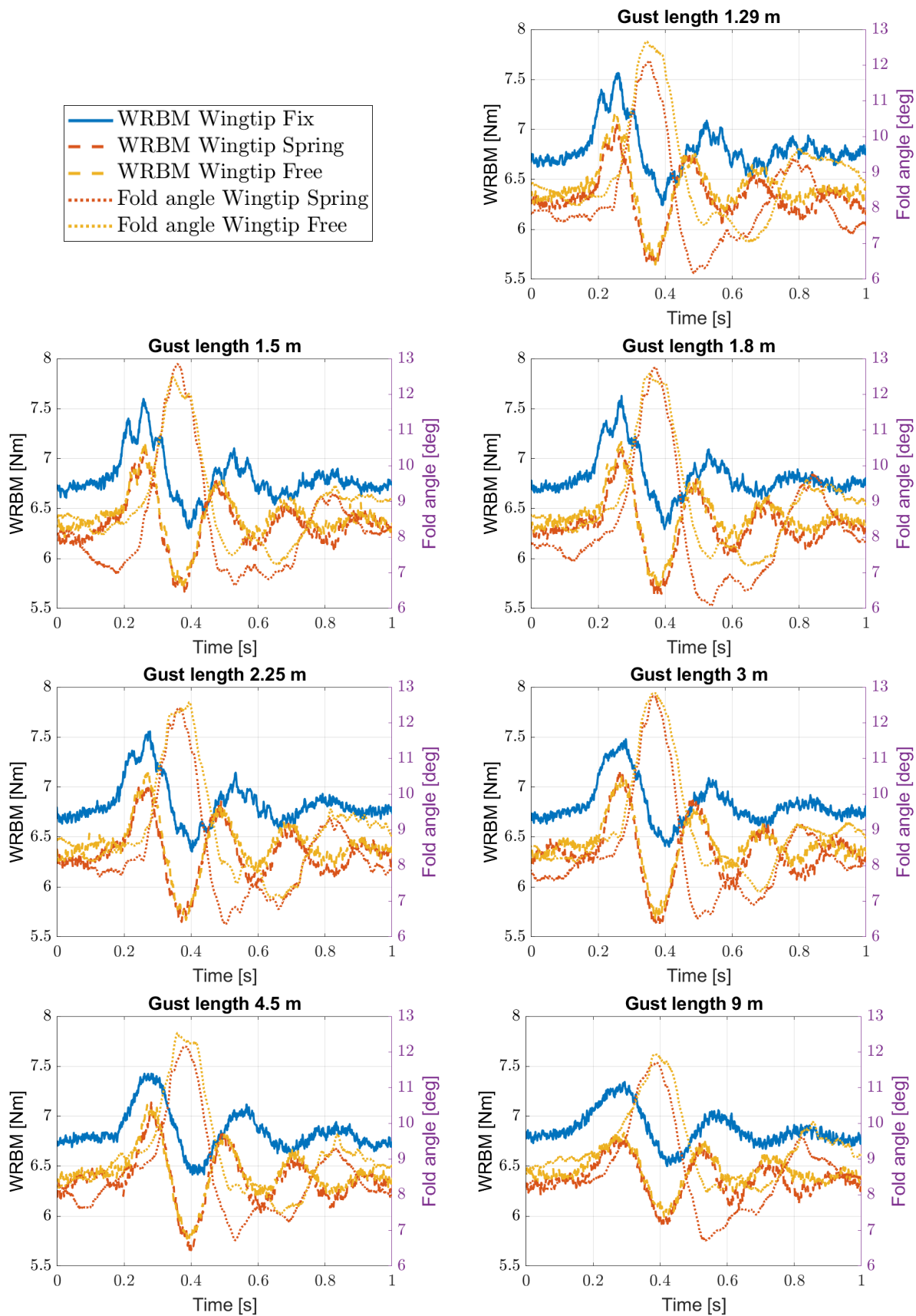


FIGURE 6.33: WRBM gust response for the wing with fixed wingtip, hinged wingtip and hinged wingtip with torsional spring and fold angle time history. Small discrete gust amplitude and wing root AoA  $6^\circ$

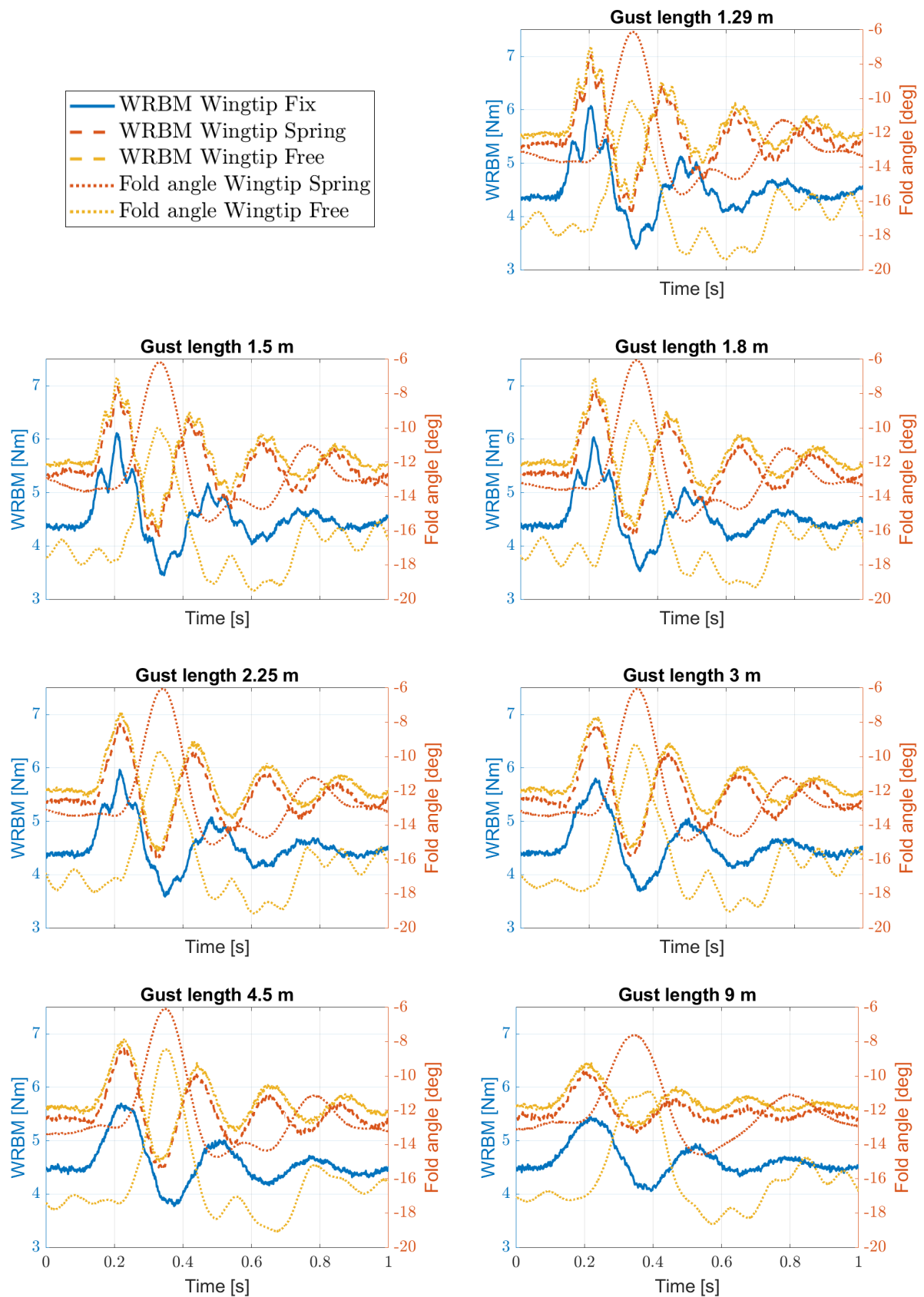


FIGURE 6.34: WRBM gust response for the wing with fixed wingtip, hinged wingtip and hinged wingtip with torsional spring and fold angle time history. Medium discrete gust amplitude and wing root AoA  $2^\circ$

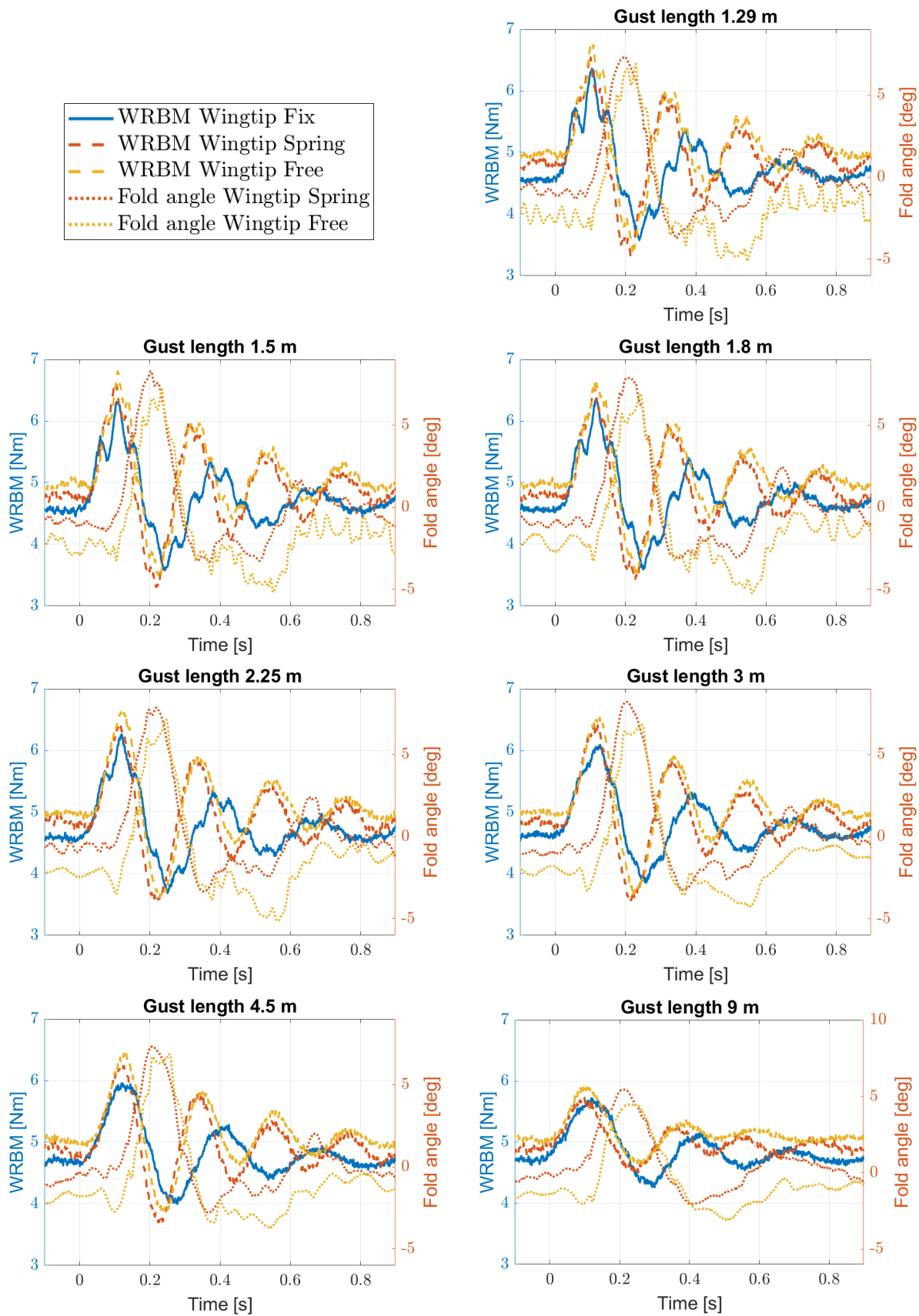


FIGURE 6.35: WRBM gust response for the wing with fixed wingtip, hinged wingtip and hinged wingtip with torsional spring and fold angle time history. Medium discrete gust amplitude and wing root AoA  $4.4^\circ$

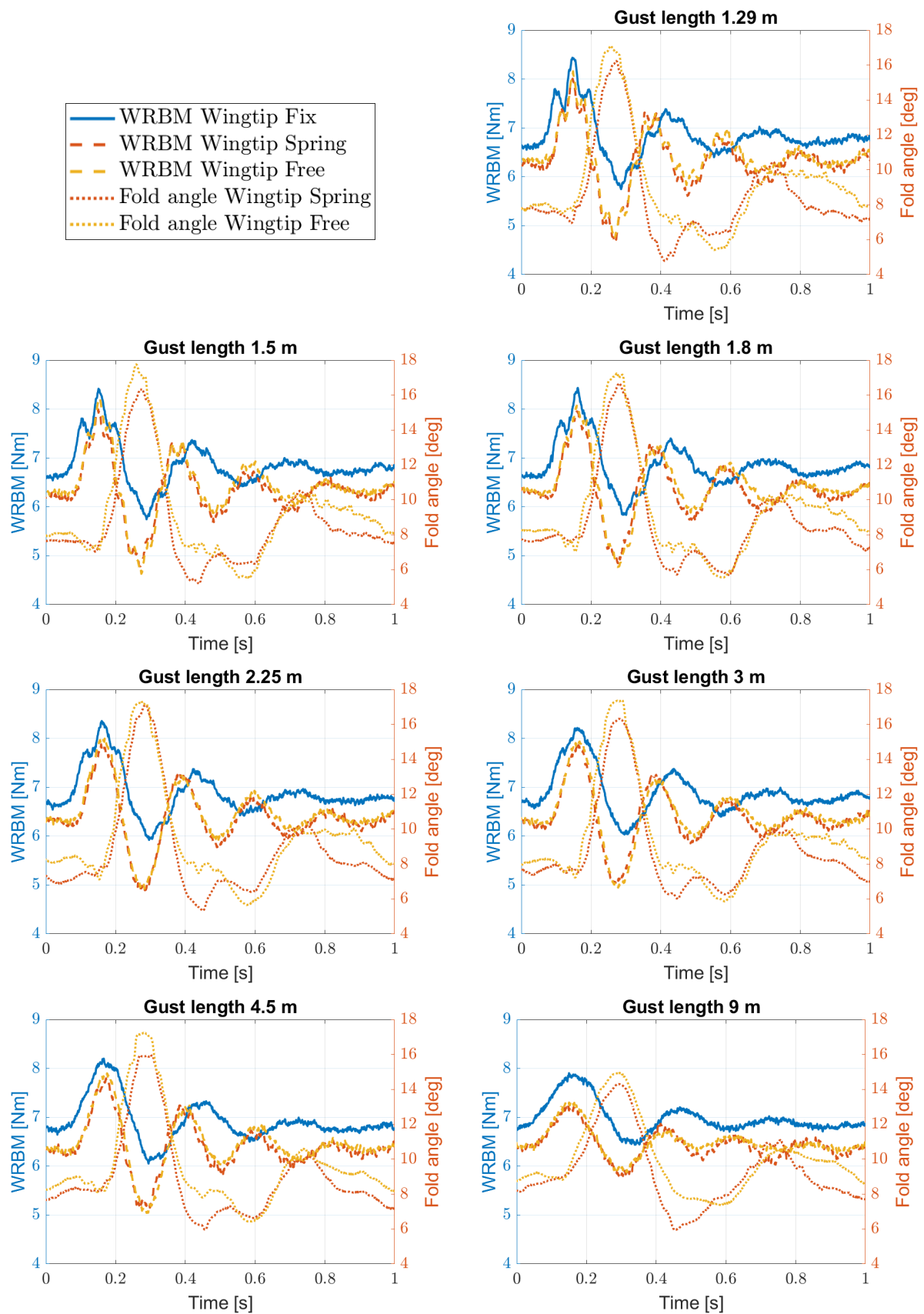


FIGURE 6.36: WRBM gust response for the wing with fixed wingtip, hinged wingtip and hinged wingtip with torsional spring and fold angle time history. Medium discrete gust amplitude and wing root AoA  $6^\circ$

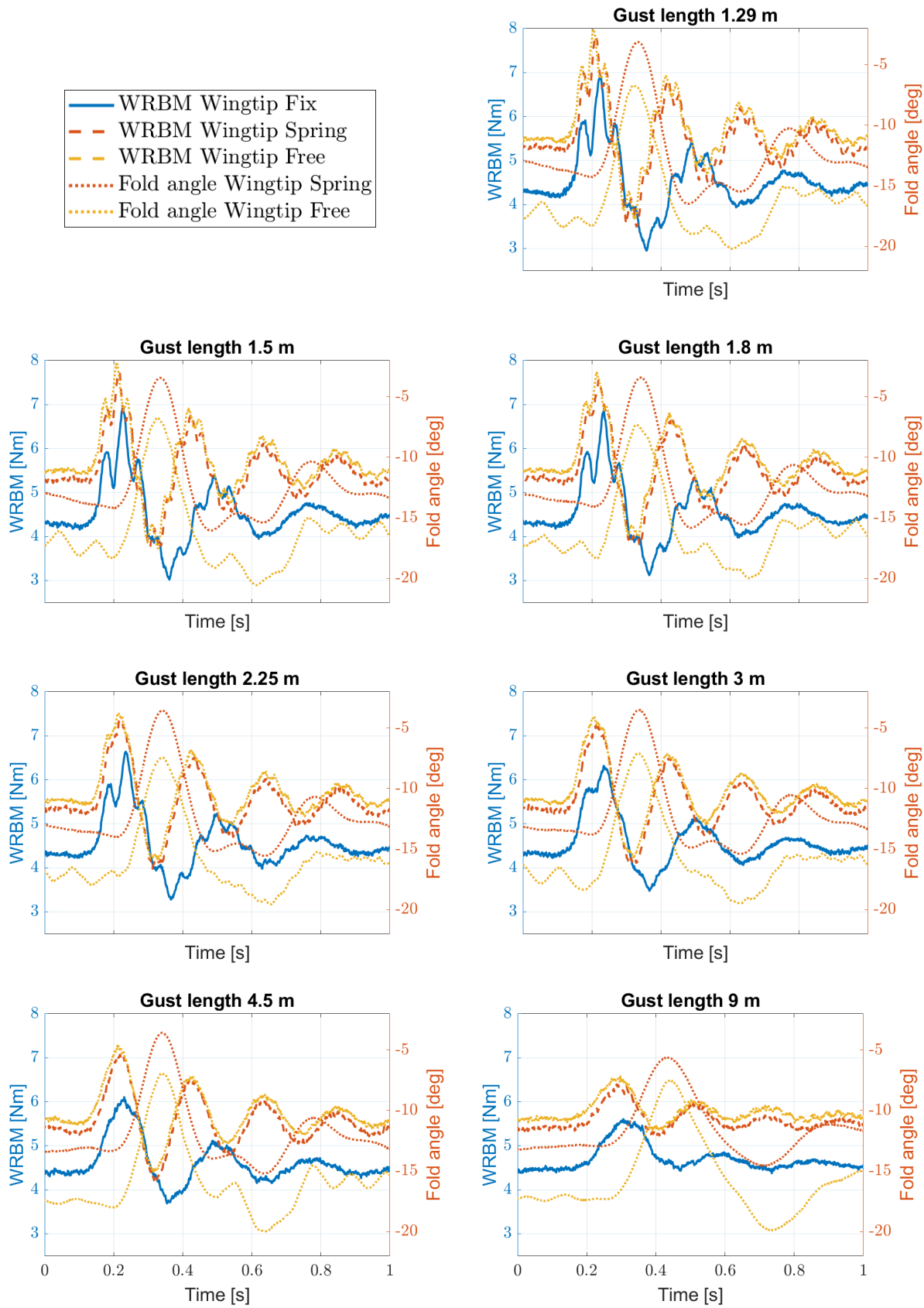


FIGURE 6.37: WRBM gust response for the wing with fixed wingtip, hinged wingtip and hinged wingtip with torsional spring and fold angle time history. Large discrete gust amplitude and wing root AoA  $2^\circ$

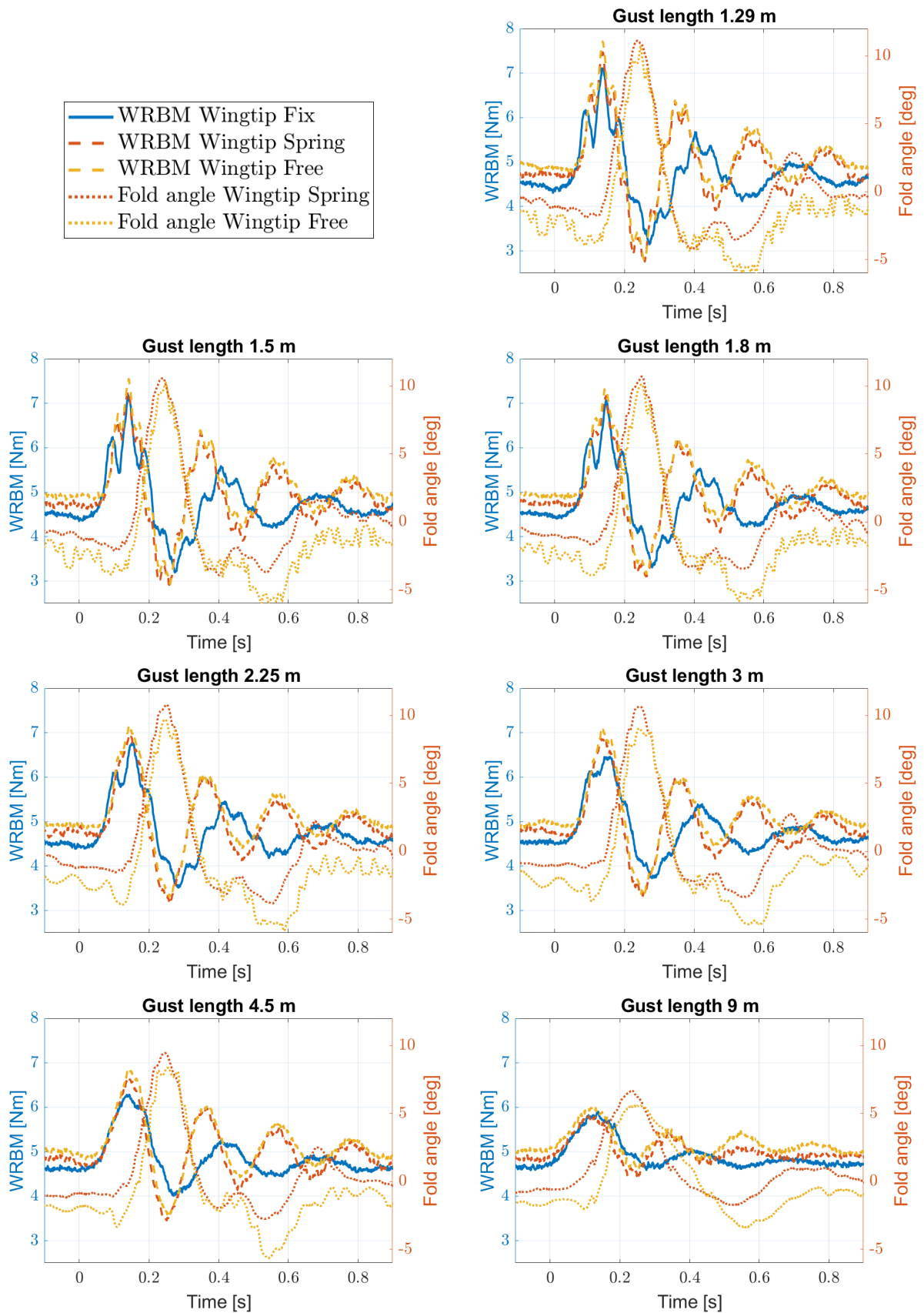


FIGURE 6.38: WRBM gust response for the wing with fixed wingtip, hinged wingtip and hinged wingtip with torsional spring and fold angle time history. Large discrete gust amplitude and wing root AoA  $4.4^\circ$

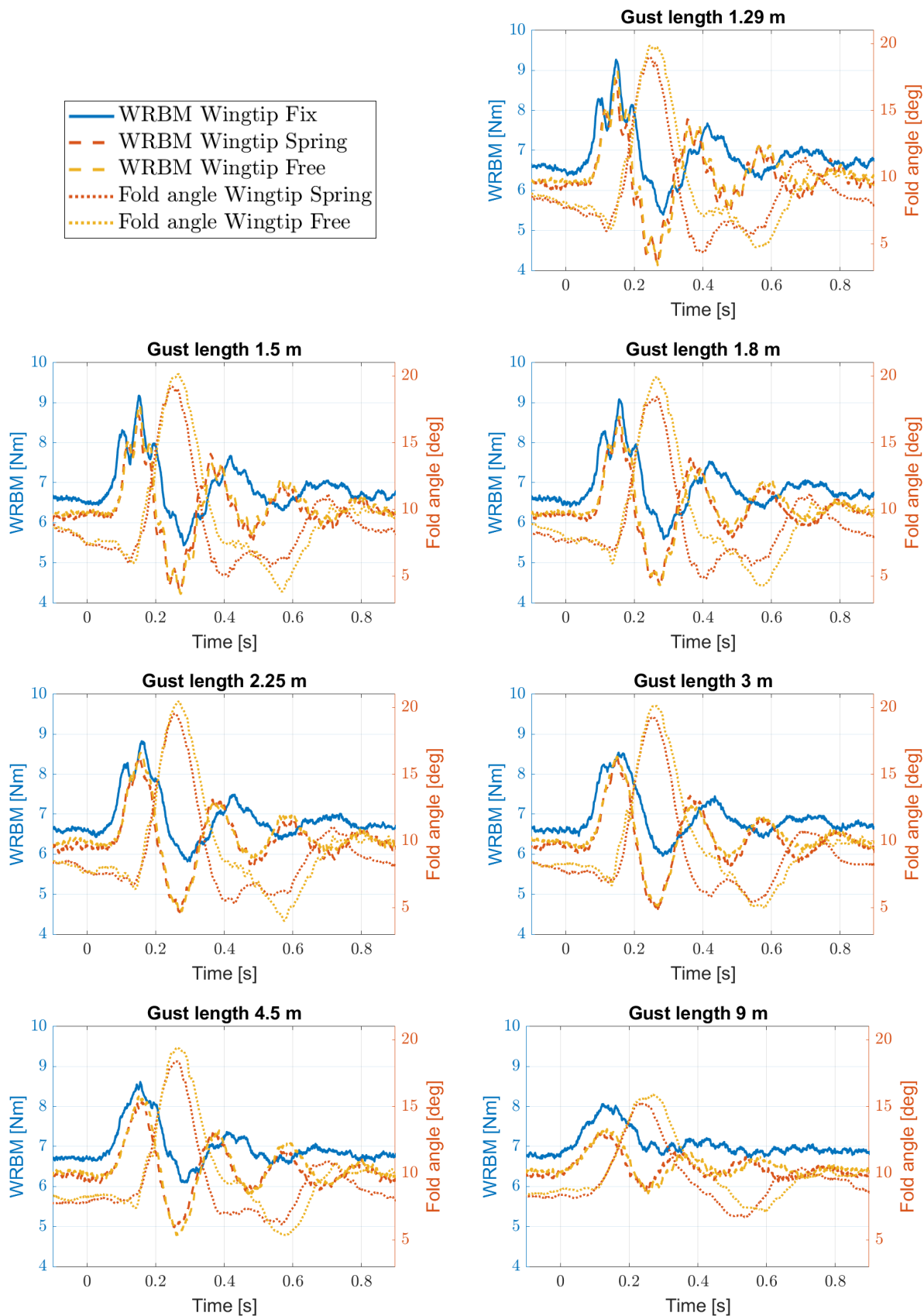


FIGURE 6.39: WRBM gust response for the wing with fixed wingtip, hinged wingtip and hinged wingtip with torsional spring and fold angle time history. Large discrete gust amplitude and wing root AoA  $6^\circ$



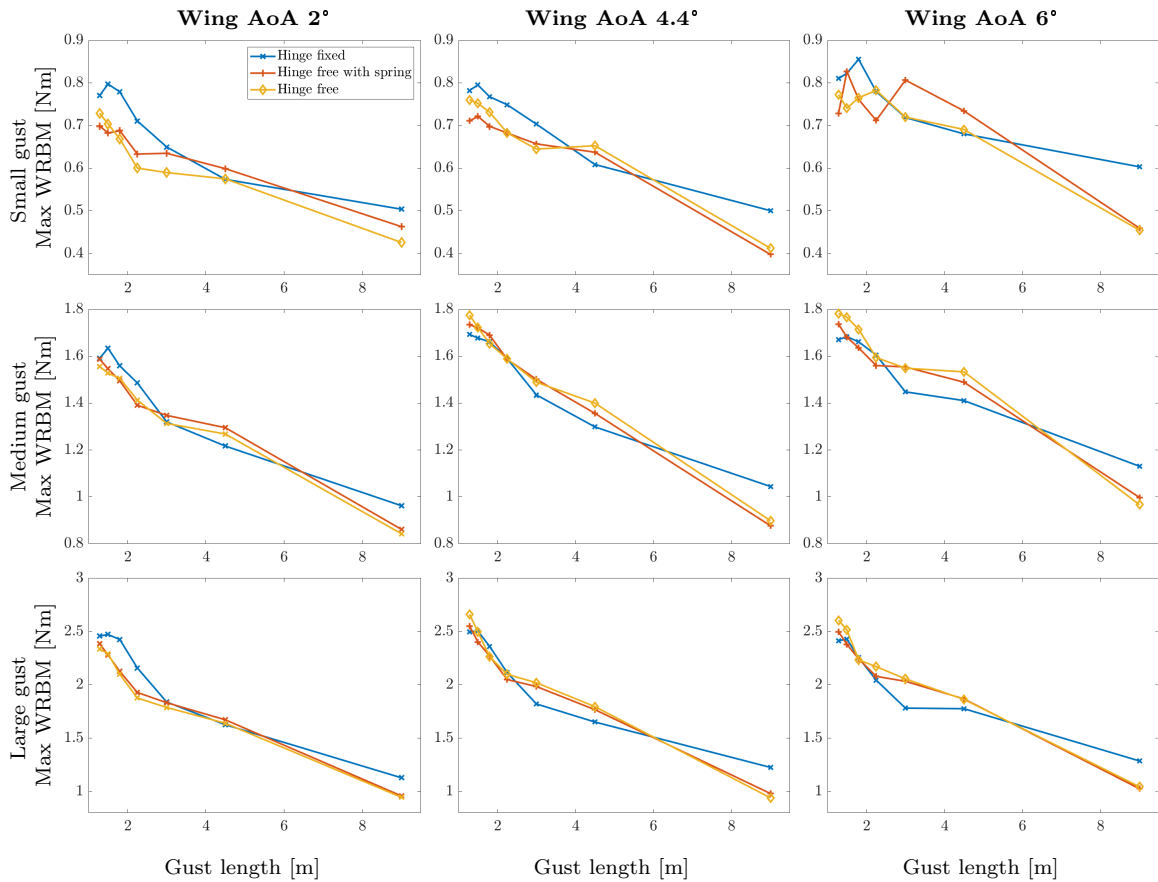


FIGURE 6.40: *WRBM maximum peak for all the cases considered*

with Figure 6.27. Indeed, before the gust, the wingtip is folded down in the cases of WRAoA  $2^\circ$  and  $4.4^\circ$  and fold up for a WRAoA of  $6^\circ$ .

When the gust reaches the wing, the WRBM increases for all the wingtips considered. In all the cases, except for the 9 m gust length, when the WRBM reaches its maximum value, the wingtip starts to rotate up until the WRBM reaches its minimum value. Indeed, in all the cases, the first negative peak is amplified by the wingtip folded up with respect to the case of the fixed wingtip.

For all tests considered, Figure 6.40 shows the absolute maximum WRBM increment from the trim value due to the gust for all the gusts considered. For a WRAoA of  $2^\circ$ , a free hinged wingtip is able to alleviate the maximum WRBM peaks for all the discrete gusts, except for a discrete gust of 4.5 m.

In the same configurations, the wing with a hinged wingtip and torsional spring have performace in between the case of wing with free hinged wingtip and fixed wingtip,

except for the case of 4.5 m gust length, where its maximum WRBM is amplified. A similar conclusion can be drawn in the case of WRAoAs of  $4.4^\circ$  and  $6^\circ$  for the small gust, with the difference that in the case of a WRAoA of  $4.4^\circ$ , the WRBM maximum peak for a discrete gust of 4.5 m is higher in the case of the free hinged wingtip with respect to the hinged wingtip with torsional spring and in the case of a WRAoA of  $6^\circ$ , the WRBM maximum peak for a discrete gust of 1.5 m, 3 m and 4.5 m is higher in the case of the hinged wingtip with the torsional spring with respect to the fixed wingtip. For medium and large discrete gusts and WRAoAs of  $4.4^\circ$  and  $6^\circ$ , the maximum peaks of the WRBM for the wing with a hinged wingtip have similar or higher values compared to the wing with a fixed wingtip. In all the cases, a hinged wingtip alleviates the maximum peak of the WRBM for a discrete gust with a gust length of 9 m. Indeed, in this case, the wingtip starts to rotate before the wingtip reaches its maximum value.

---

## 6.5 Numerical Model

---

The software MSC/Nastran [110] has been widely used to model aeroelastic systems and for modelling wings with hinged wingtips [43–45, 48, 51, 53, 55, 108, 161, 162]. The aeroelastic model representative of the manufactured wing with the fixed wingtip was developed in MSC/Nastran. The aluminium spar was modelled using beam elements. A convergence study was performed to assess the number of elements required to model the beam. A model with 200 elements was considered as a reference, and the first five natural frequencies were considered in each case. The convergence study terminated when there was no difference between the model and the reference, up to the first decimal point. Table 6.7 reports the results of the convergence study. The model with 100

	Number of elements						
	10	20	40	60	80	100	200
Mode 1 [Hz]	9.8	9.8	9.8	9.8	9.8	9.8	9.8
Mode 2 [Hz]	60.5	61.4	61.6	61.6	61.6	61.6	61.6
Mode 3 [Hz]	167.0	171.1	171.1	172.2	172.3	172.3	172.3
Mode 4 [Hz]	239.9	240.1	240.1	240.2	240.2	240.2	240.2
Mode 5 [Hz]	322.3	333.7	336.3	336.7	336.9	337.0	337.0

TABLE 6.7: Convergence study on the structural model of the spar

elements was considered for the gust response. The weight and inertia of each 3D printed wing and wingtip section and the metal bar were modelled as concentrated masses with

their correct inertia at their actual position. Inertia and centre of mass position were calculated by Solidworks [138] by correcting the mass density to match the weight of each manufactured part. To consider the plastic deformation, each concentrated mass was connected to the spar through a rigid beam and a spring via a CBUSH element. The DLM was used to model the aerodynamic forces and only quadratic aerodynamic panels were considered. After a convergence study performed considering the maximum tip vertical displacement due to a gust, 20 panels in chord and 150 panels in span were used. Figure 6.41 shows the results of the convergence study. From this aeroelastic

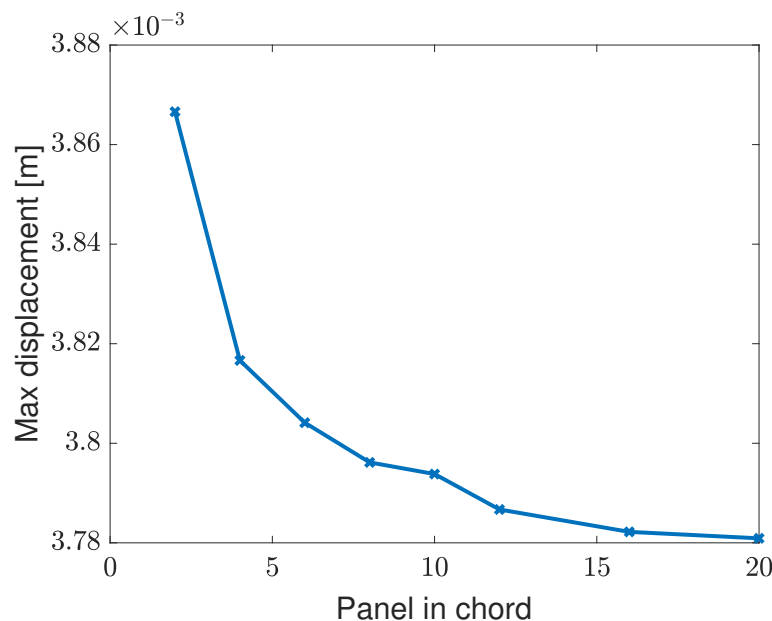


FIGURE 6.41: Convergence of the aerodynamic model of the wing with fixed wingtip

model, two aeroelastic models representative of the wing with the two manufactured hinged wingtips were obtained introducing a hinge at 80% of the wing span and with a fold angle of  $10^\circ$ . The hinge was modelled as two coincident nodes connected via a CBUSH element with the coordinate system aligned to the hinge axis. A PBUSH element introduced the stiffness on the hinge. The aerodynamic model was divided into two sections, the main wing section, from the wing root to the hinge, and the wingtip section, from the hinge to the tip [161]. Following the procedure used in the case of the wing with a fixed wingtip, a convergence study was performed to assess the number of panels required to model each section, considering only quadratic panels. Table 6.8 shows the number of panels considered in each case and the tip of the wing's maximum displacement due to a gust. As a result of the convergence study, 20 panels in chord were used for both sections. A total of 2400 aerodynamics panels were used to model the main wing, and 600 aerodynamics panels for the wingtip.

Case	Panels in chord wing	Panels in chord wingtip	Maximum peak [mm]
1	10	10	3.73
2	15	15	3.27
3	20	20	3.26
4	20	30	3.26
5	30	20	3.26

TABLE 6.8: Convergence of the aerodynamic model of the wing with hinged wingtip

Node	176
Beams elements	205
Concentrated masses	35
Rigid beams	56
Spring elements	14
Aerodynamic panels	3000

TABLE 6.9: Summary Nastran model

Table 6.9 summarises the Nastran model and Figure 6.42 shows the wing structural and aerodynamic models. Figure 6.42 also shows the position of the node on the spar at 0.78 m from the wing root used to compare numerical and experimental time responses.

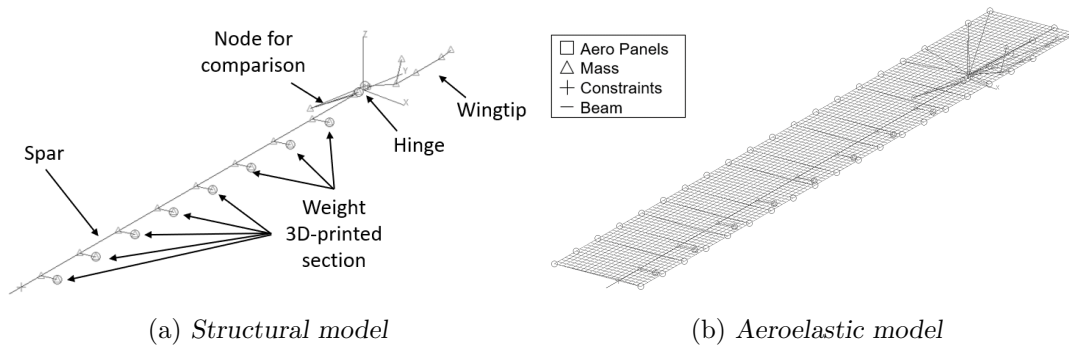


FIGURE 6.42: Nastran model

The models were tuned to obtain structural natural frequencies similar to the experimental frequencies given in Table 6.6. The structural damping, identified from the impact hammer test, was introduced in the model. Tables 6.10 and 6.11 report the comparison between the structural natural frequencies measured experimentally and calculated from the aeroelastic model for the spar alone and the wing with the different wingtips, respectively. In the case of only the spar, the first five structural natural frequencies calculated by the Nastran model have a maximum error of 5.1%. The good agreement between the numerical model and the experiment is due to the simplicity of the structure analysed. In all the wing cases, the measured first natural frequency perfectly matches the calculated first natural frequency due to an adjustment of the spar Young's modulus. For

the wing with the fixed wingtip, the first natural frequency is associated with the first out-of-plane bending mode, the second natural frequency is associated with the wing torsion, and the higher natural frequencies have contributions from both out-of-plane bending and torsion. For the wing with the hinged wingtip, the first natural frequency is associated with the wingtip mode, the second natural frequency is associated with the first out-of-plane bending mode, the third natural frequency is associated with the wing torsion, and the higher natural frequencies have contributions from both out-of-plane bending and torsion. In this case, a good match of the first natural frequency was obtained by introducing a suitable spring stiffness in the hinge.

Measured [Hz]	Calculated [Hz]	Error
9.8	9.8	0
62.0	60.2	3.0 %
175.0	169.4	3.3 %
258.1	245.5	5.1 %
344.8	332.8	3.6 %

TABLE 6.10: *First five structural natural frequencies of the spar measured experimentally and calculated from the Nastran model*

Fixed Wingtip			Hinged wingtip with torsional spring			Hinged wingtip		
Measured [Hz]	Calculated [Hz]	Error [%]	Measured [Hz]	Calculated [Hz]	Error [%]	Measured [Hz]	Calculated [Hz]	Error [%]
3.5	3.5	0	1.4	1.4	0	1.2	1.2	0
19.6	19.7	0.5	5.1	5.1	0	4.9	5.0	2.0
23.4	22.1	5.6	21.0	20.3	3.3	22.1	20.3	8.1
49.6	47.8	3.6	29.1	30.6	5.2	29.6	30.8	4.1
-	-	-	49.5	46.9	5.3	-	-	-

TABLE 6.11: *Structural natural frequencies below 50 Hz of the wing with the different wingtips measured experimentally and calculated from the Nastran models*

In the case of the wing with the different wingtips, the maximum error between measured and calculated structural natural frequencies was 8.1%. The mismatch between the calculated and measured wing natural frequencies was due to:

- Simplicity of the structural model: each 3D-printed section is considered as a lumped mass (considering the inertia values) and the connections are modelled as point connections. A detailed model could improve the accuracy of the model.

- Uncertainty in the mass proprieties: the weight, inertia and centre of mass position of each 3D-printed section were calculated by SOLIDWORKS [138], where the material density was imposed to match the manufactured one (the average weight in the case of multiple sections). For the wing 3D-printed sections, eight identical nominally copies were manufactured, but the difference between the lighter and the heavier sections was 3.1 g. The weight of the 3D-printed material was more than double that of the spar, and hence, due to the 3D printer inaccuracy, errors in the weight, inertia and centre of mass position can significantly impact the final results. Moreover, the wingtip was mainly made of 3D-printed sections, so the inertia imprecision at the tip of the wing can significantly alter the results.
- Uncertainty in the connection: all the 3D-printed sections were connected to the spar using bolts and washers which introduce friction in the system.
- Non-symmetrical connection: all the 3D-printed sections were connected to the spar only from the upper face. Figures 6.2b and 6.5 show the spar connection and the additional material added to transmit the load from the washer to the plastic. Due to the additional non-symmetrical plastic material added at the bolt location, the equivalent spar stiffness was non-symmetrical.

### 6.5.1 Comparison Between Numerical and Experimental Gust Responses

The numerical and experimental results were compared in terms of gust time history responses of the WRBM, vertical displacement of a point on the wing at 0.78 m from the wing root and hinge rotation. In the Natran model, due to the model linearity, the gust response is not affected by the WRAoA. To experimentally analyse the effect of different WRAoA, the responses were considered in the cases of WRAoA of 2°, 4.4° and 6°.

All the quantities of interest were compared in terms of the increment due to the gust. The numerical gust responses were obtained considering as gust input the respective gust time history measured in the previous campaign and reported in Section 5.4.2.

Figure 6.43 shows the comparison between the numerical and experimental gust response in the case of the fixed wingtip, Figures 6.43a and 6.43b, the hinged wingtip with torsional spring, Figures 6.43c and 6.43d, and the free hinged wingtip, Figures 6.43e and 6.43f.

Due to the record of the gust time history, the numerical model correctly predicts the oscillations before the main gust caused by the gust generator starting vortex. Moreover, the maximum peak prediction was correct for all the quantities of interest. In the case

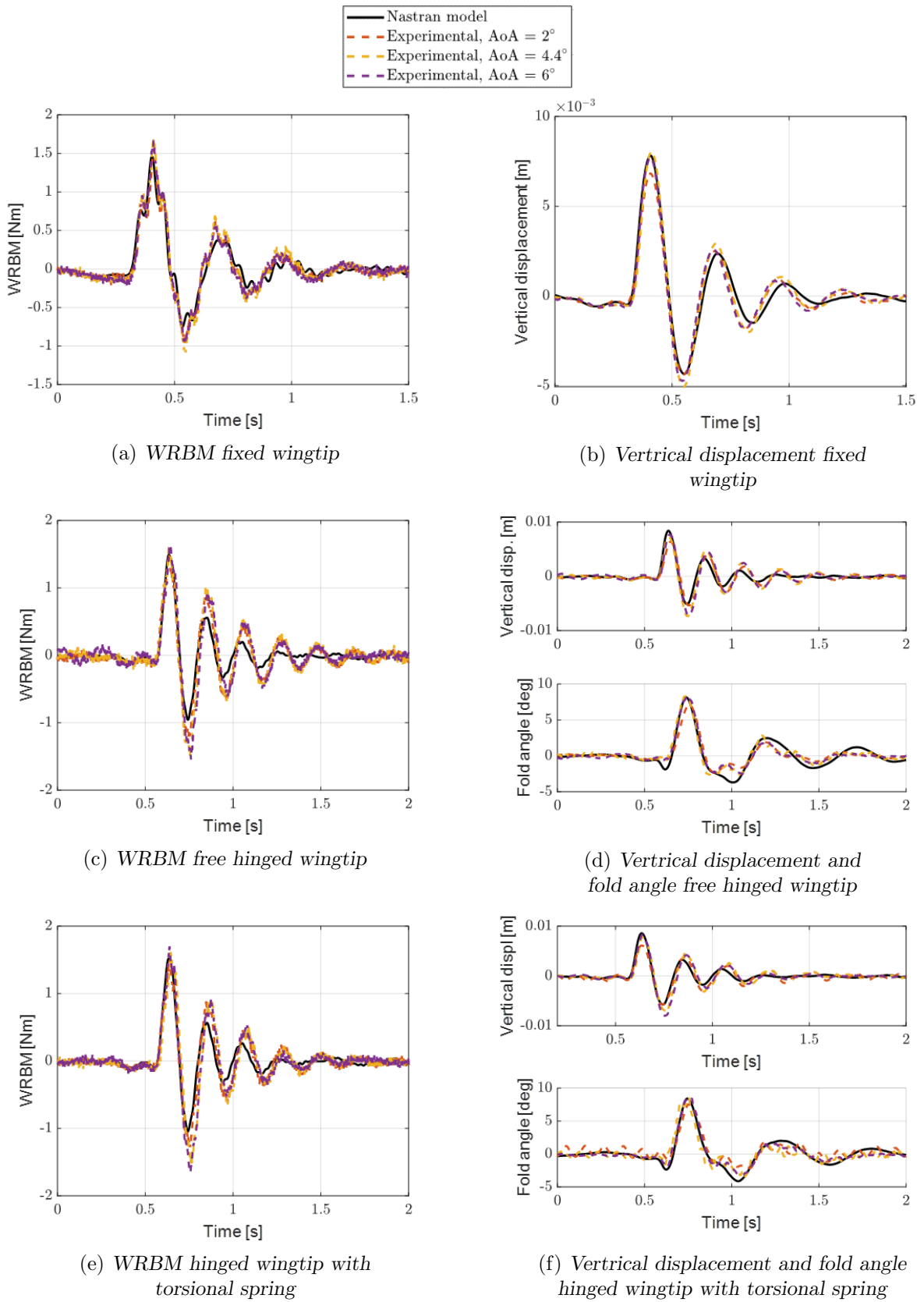


FIGURE 6.43: Comparison between numerical and experimental interesting quantities

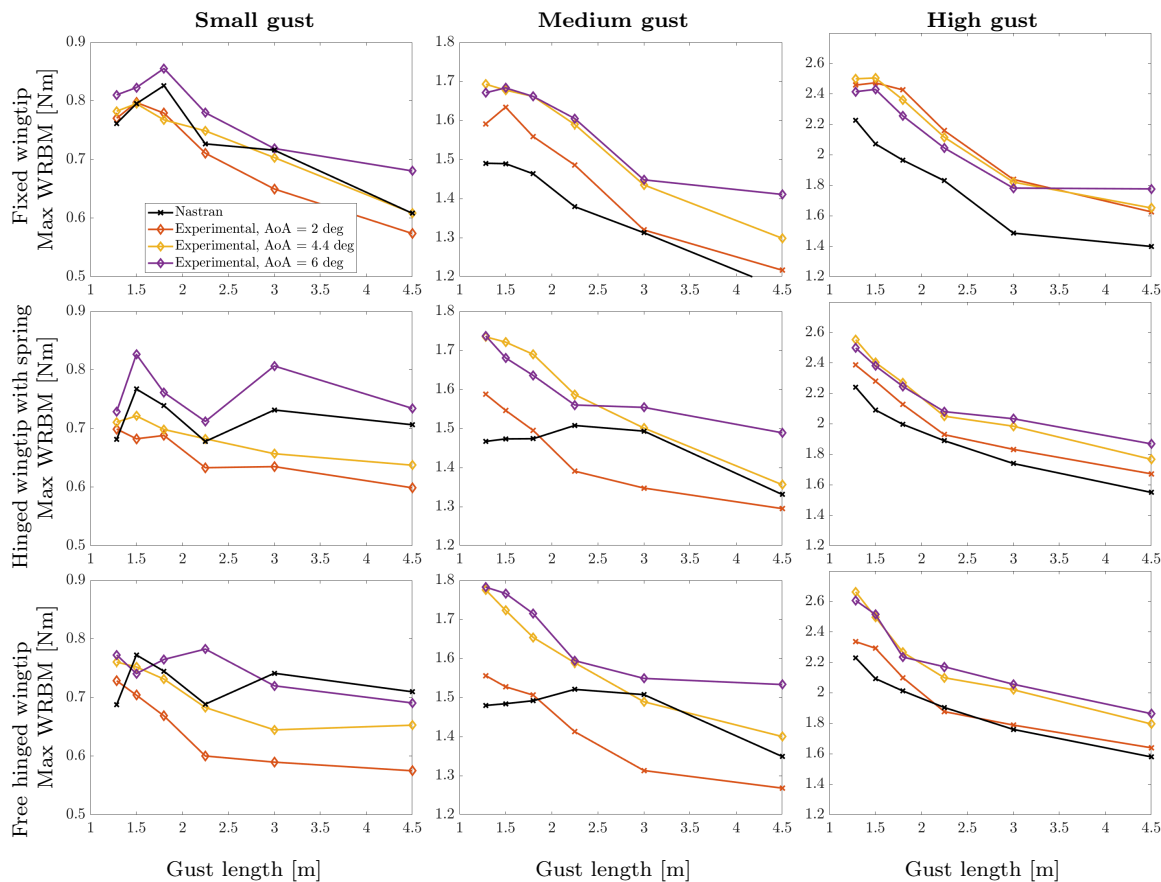


FIGURE 6.44: *WRBM maximum peak for all the cases considered*

of the wing with the fixed wingtip, the three experimental results have a similar time response in both quantities of interest. The Nastran model correctly predicts the time history response of both quantities of interest. However, the WRBM has a high-frequency oscillation at around 18 Hz with respect to the experimental results, suggesting lower aerodynamic torsional damping in the Nastran model than in the experiment. The results of the wing with both hinged wingtips have a similar trend and will be commented on together. The experimental results in the case of the wing with hinged wingtips are more affected by the WRAoA than the case of the wing with the fixed wingtip. Although the first structural natural frequency was correctly predicted in the case of the hinged wingtip with torsional spring and overpredicted by 0.1 Hz in the case of the free hinged wingtip, the main natural frequency for the numerical model time responses was at a higher frequency with respect to the experimental one. In both cases, the Nastran model correctly predicts the fold angle time history and overestimates the damping for the time history response of the WRBM and the vertical displacement of the point considered. The faster decay of the numerical model with respect to the experiments could be due



to an overestimation of the load alleviation due to the hinged wingtips.

In the design phase of an aircraft, great importance is given to the maximum peak because it is the most demanding case. So, the main aim of the aeroelastic models is to correctly capture the WRBM maximum peak. Figure 6.44 shows the WRBM comparison between the maximum increment due to the gust measured experimentally and calculated by the Nastran model considering the three wingtips, a discrete gust with gust lengths from 1.29 m to 4.5 m and the three-level of discrete gust intensity. In the case of the small discrete gust intensity, the Nastran model correctly predicts the maximum peaks for all the cases. Increasing the discrete gust intensity, the Nastran model underpredicts the maximum peaks. Moreover, Figure 6.44 shows the effect of the WRAoA. Indeed for the fixed wingtip, the maximum peaks are less affected by the WRAoA than the hinged wingtips.

---

## 6.6 Conclusion

---

In this chapter, the design of a wing and a fixed wingtip, a free hinged wingtip and a hinged wingtip with a torsional spring was performed. Static and dynamic wind tunnel tests were performed to assess their ability to alleviate gust loads and to validate the aeroelastic models. Static wind tunnel tests confirmed the ability of a hinged wingtip to alleviate gusts load. Gust responses shown the dynamic gust response of fixed and hinged wingtips. Aeroelastic models were developed in Nastran, and structural validations were performed. Moreover, the simulated gust responses were compared with the experimental responses in terms of time history response and WRBM peaks, and good agreement was found.

# Chapter 7

---

## CONCLUSIONS AND FUTURE WORK

---

### 7.1 Conclusions

---

This thesis presented numerical and experimental studies of aeroelastic hinged wingtips for aircraft loads alleviation. Numerical studies were performed considering simplified and detailed models. Both the models considered the same dimensions and weight distribution of a civil, commercial aircraft. The simplified model was obtained by adding a hinged wingtip to an existing model. Due to the low number of degrees of freedom and consequently the low time required for each simulation, the simplified model was used for the problem of worst-case identification and aeroelastic optimisation. Multi-objective optimisations were performed to explore the possible combinations of the wingtip's parameters. The results show a wide range of suitable combinations applicable to a detailed model when available. To overcome the reduction in the flutter speed, introducing a spring on the hinge that connects the wing with the wingtip and reducing the flare angle proved effective.

The problem of gust identification was studied considering the simplified and detailed model. The aircraft time history gust response was used with a model to identify the gust. Different regularisation methods were considered to solve the inverse problem,

including Tikhonov regularisation, truncated single value decomposition, and damped singular value decomposition. The results showed their inability to identify the gust in the case of noisy measurements. A robust technique for aircraft gusts identification based on cubic B-splines was proposed. The gust identification performed considering the detailed model for the generation of gust response time history and the simplified model for gust identification shown the potentiality of this technique.

To validate aeroelastic models, wind tunnel tests are required. Moreover, a gust generator is necessary to validate the gust response in the wind tunnel. Based on the dimensions of the Swansea University wind tunnel, a two vane-type gust generator was designed and characterised. The characterisation shown that the system can reliably produce uniform discrete and continuous sinusoidal gusts. The results exhibited good repeatability and concur with previous studies. The creation of discrete gusts shown discrepancies between the desired and the measured gusts. Experimental results reveal the complex dynamics of the airflow in the wake of the two gust generator vanes. More specifically, imposing ‘1-cos’ vane rotation does not produce an exact ‘1-cos’ gust. Two techniques were considered to improve the creation of discrete gusts. In the first case, the transfer functions between the vane rotation and the gust produced at the aircraft model location were identified, and its inverse was used to calculate the vane rotation. The strong aerodynamics nonlinearity limits the improvements of this method. A parametric study on vane rotation shown that a more complicated vane rotation function made it possible to obtain ‘1-cos’ gusts at the aircraft model location with a mean square error two orders of magnitude smaller than the initial case. Creating ‘1-cos’ gusts with similar frequency content as the regulations require will help design more efficient gust load alleviation systems.

A wing able to accommodate different wingtips, i.e. a fixed wingtip, a free hinged wingtip and a hinged wingtip with a torsional spring, was manufactured and tested in the Swansea University wind tunnel. Structural characterisation was performed on the wing spar and the wing with the manufactured wingtips. Static wind tunnel tests demonstrated the ability of the wing with a hinged wingtip to reduce the loads compared to a similar wing with a fixed wingtip. Gust loads measured at the wing root confirmed that in specific cases, the load increment due to gusts is smaller for a wing with a hinged wingtip with respect to the fixed wingtip. Aeroelastic models of the wing with manufactured wingtips were developed, and the structural natural frequencies are in accordance with the experimental ones. Comparisons were performed between experimental and simulated results in terms of wing root bending moment, fold angle and vertical displacement of a point along the wing.

---

## 7.2 Original Contributions

---

Original contributions from this PhD thesis are:

- The creation of an analytical model representing an aircraft with an elastic wing and hinged wingtips for the worst-case gust prediction and multi-objective optimisation.
- The development of a robust technique for aircraft gust and turbulence identification using B-Splines, considering models with different levels of fidelity.
- Design, install, commission, and characterise a gust generator for the Swansea University wind tunnel. Furthermore, the study of techniques to improve the creation of discrete gusts.
- Design of a wing able to accommodate a fixed wingtip and hinged wingtips. Creation of aeroelastic models representative of the manufactured wing with different wingtips. Static and dynamic wind tunnel tests prove the hinged wingtip's ability to reduce gust loads. Validation of the aeroelastic models through comparison of the experimental and simulated gust response time history.

---

## 7.3 Recommendations for Future Work

---

The topics discussed in this thesis introduce possible ideas for future research:

- Following the multi-objective optimisation procedure for the simplified model considering the worst gust case, the aeroelastic optimisation should be performed on a detailed aeroelastic model where design constraints drive the parameters limit.
- Introduction in the aeroelastic model of an aircraft flight control system to assess the interaction between the dynamic of the control system and the wingtip .
- Study of active control for the wingtip rotation. In addition, advance knowledge of the gust, e.g. through a Doppler LIDAR wind speed sensor, could be used to maximise the load alleviation.

- 
- Future work should also include real flight data to validate the proposed method for gust identification.
  - Improvement of the aerodynamic model near the hinge and on the wingtip. A validated CFD model can be used to improve the fidelity of aerodynamic model.
  - Improvement in the creation of discrete gusts. Nonlinear model identification can improve the model accuracy and further improve the creation of discrete gusts in the wind tunnel.
  - The validated aeroelastic model can be used as a reference model to perform optimisation to improve the load alleviation further.
  - Wind tunnel testing and model validation of wingtip with different wingspan and flare angle to understand if the same model strategy can be used and consequently perform numerical parameters optimisation.

# Appendix A

## DEVELOPMENT EQUATION OF MOTION FOR THE SIMPLIFIED MODEL

---

### A.1 Aeroelastic equation rigid aircraft with elastic wing

---

This section shows the steps required to obtain the aeroelastic equation of an aircraft with an elastic wing. The Lagrange's equation for a system with  $N$  degrees of freedoms may be written as

$$\frac{d}{dt} \left( \frac{\partial T}{\partial \dot{x}_i} \right) - \frac{\partial T}{\partial x_i} + \frac{\partial U}{\partial x_i} = Q_i = \frac{\partial(\delta W)}{\partial(\delta x_i)} \quad \text{for } i = 1, 2, \dots, N \quad (\text{AA.1.1})$$

where  $T$  is the kinetic energy,  $U$  the potential energy,  $Q_i$  is the generalised force and  $W$  is the work done by the generalised forces.

The total kinetic energy is

$$T = \frac{1}{2} m \dot{z}_c^2 + \frac{1}{2} I_y \dot{\alpha}^2 + \frac{1}{2} m_b \dot{q}_b^2 + \frac{1}{2} m_t \dot{q}_t^2 \quad (\text{AA.1.2})$$

The total elastic potential energy is

$$U = \frac{1}{2}k_b q_b^2 + \frac{1}{2}k_t q_t^2 \quad (\text{AA.1.3})$$

The total virtual work done by the external forces is

$$\begin{aligned} \delta W_E = & \int_0^s -dL \left\{ \delta z_c(t) - l_W \delta \alpha(t) + \left[ k_{e0} \left( 1 + A \left( \frac{y}{s} \right)^2 \right) - l_A \gamma_{e0} \right] \delta q_b(t) \right. \\ & \left. + \left[ k_{e0} - l_A \gamma_{e0} \left( 1 + B \left( \frac{y}{s} \right) \right) \right] \delta q_t(t) \right\} - L_T \left( \delta z_c(t) + l_T \delta \alpha(t) \right) \\ & \int_0^s -dL_{W_g} \left\{ \delta z_c(t) - l_W \delta \alpha(t) + \left[ k_{e0} \left( 1 + A \left( \frac{y}{s} \right)^2 \right) - l_A \gamma_{e0} \right] \delta q_b(t) \right. \\ & \left. + \left[ k_{e0} - l_A \gamma_{e0} \left( 1 + B \left( \frac{y}{s} \right) \right) \right] \delta q_t(t) \right\} - L_{T_g} \left( \delta z_c(t) + l_T \delta \alpha(t) \right) \\ & + M_{0W} \delta \alpha + mg \delta z_c \end{aligned} \quad (\text{AA.1.4})$$

Applying Lagrange's formulation for all the generalised coordinates gives

$$\frac{d}{dt} \left( \frac{\partial T}{\partial \dot{q}_b} \right) = m_b \ddot{q}_b \quad (\text{AA.1.5})$$

$$\frac{d}{dt} \left( \frac{\partial T}{\partial \dot{q}_t} \right) = m_t \ddot{q}_t \quad (\text{AA.1.6})$$

$$\frac{d}{dt} \left( \frac{\partial T}{\partial \dot{\alpha}} \right) = I_y \ddot{\alpha} \quad (\text{AA.1.7})$$

$$\frac{d}{dt} \left( \frac{\partial T}{\partial \dot{z}_c} \right) = m \ddot{z}_c \quad (\text{AA.1.8})$$

$$\frac{\partial T}{\partial q_b} = 0 \quad (\text{AA.1.9})$$

$$\frac{\partial T}{\partial q_t} = 0 \quad (\text{AA.1.10})$$

$$\frac{\partial T}{\partial \alpha} = 0 \quad (\text{AA.1.11})$$

$$\frac{\partial T}{\partial z_c} = 0 \quad (\text{AA.1.12})$$

$$\frac{\partial U}{\partial q_b} = k_b q_b \quad (\text{AA.1.13})$$

$$\frac{\partial U}{\partial q_t} = k_t q_t \quad (\text{AA.1.14})$$

$$\frac{\partial U}{\partial \alpha} = 0 \quad (\text{AA.1.15})$$

$$\frac{\partial U}{\partial z_c} = 0 \quad (\text{AA.1.16})$$

$$\begin{aligned} \frac{\partial(\delta W_E)}{\partial(\delta q_b)} = & - \int_0^s \left[ k_{e0} \left( 1 + A \left( \frac{y}{s} \right)^2 \right) - l_A \gamma_{e0} \right] dL \\ & - \int_0^s \left[ k_{e0} \left( 1 + A \left( \frac{y}{s} \right)^2 \right) - l_A \gamma_{e0} \right] dL_{W_g} \end{aligned} \quad (\text{AA.1.17})$$

$$\begin{aligned} \frac{\partial(\delta W_E)}{\partial(\delta q_t)} = & - \int_0^s \left[ k_{e0} - l_A \gamma_{e0} \left( 1 + B \left( \frac{y}{s} \right) \right) \right] dL \\ & - \int_0^s \left[ k_{e0} - l_A \gamma_{e0} \left( 1 + B \left( \frac{y}{s} \right) \right) \right] dL_{W_g} \end{aligned} \quad (\text{AA.1.18})$$

$$\frac{\partial(\delta W_E)}{\partial(\delta \alpha)} = \int_0^s l_W dL - l_T L_T + \int_0^s l_W dL_{W_g} - l_T L_{T_g} + M_{0W} \quad (\text{AA.1.19})$$

$$\frac{\partial(\delta W_E)}{\partial(\delta z_c)} = - \int_0^s dL - L_T - \int_0^s dL_{W_g} - l_T L_{T_g} + mg \quad (\text{AA.1.20})$$

Equations (AA.1.17), (AA.1.18), (AA.1.19), and (AA.1.20) have been solved using Wolfram Mathematica 12 [163].



---

## A.2 Aeroelastic equation rigid aircraft with elastic wing and hinged wingtip

---

This section shows the additional contributions due to the hinged wingtip.

The kinetic energy is

$$T = \frac{1}{2} m_{wt} \left[ k_{e0} (1 + A) \dot{q}_b - \left( x_f - \frac{\Gamma_x}{\cos(\gamma)} \right) \gamma_{e0} (1 + B) \dot{q}_t - \left( l_W + \frac{c}{4} - \frac{\Gamma_x}{\cos(\gamma)} \right) \dot{\alpha} + \dot{z}_c + \Gamma_y \dot{\theta} \right]^2 \quad (\text{AA.2.21})$$

The total elastic potential energy is

$$U = \frac{1}{2} k_\theta \theta^2 \quad (\text{AA.2.22})$$

The virtual work done by the external forces is

$$\begin{aligned} \delta W_{wt} = & -L_{wt} \left\{ \left[ k_{e0} (1 + A) - l_A \gamma_{e0} \right] \delta q_b + \left[ k_{e0} - l_A \gamma_{e0} (1 + B) \right] \delta q_t \right. \\ & + \left. \delta z_c - l_w \delta \alpha + \frac{s_3}{2} \delta \theta \right\} + m_{wt} g \left[ k_{e0} (1 + A) \delta q_b \right. \\ & - \left. \left( x_f - \frac{\Gamma_x}{\cos(\gamma)} \right) \gamma_{e0} (1 + B) \delta q_t \right. \\ & \left. - \left( l_W + \frac{c}{4} - \frac{\Gamma_x}{\cos(\gamma)} \right) \delta \alpha + \delta z_c + \Gamma_y \delta \theta \right] \quad (\text{AA.2.23}) \end{aligned}$$

Applying Lagrange's formulation for all the generalised coordinates gives

$$\begin{aligned} \frac{d}{dt} \left( \frac{\partial T}{\partial \dot{q}_b} \right) = & m_{wt} \left\{ \left[ k_{e0} (1 + A) \right]^2 \ddot{q}_b - k_{e0} (1 + A) \left( x_f - \frac{\Gamma_x}{\cos(\gamma)} \right) \gamma_{e0} (1 + B) \ddot{q}_t \right. \\ & - k_{e0} (1 + A) \left( l_W + \frac{c}{4} - \frac{\Gamma_x}{\cos(\gamma)} \right) \ddot{\alpha} \\ & \left. + k_{e0} (1 + A) \ddot{z}_c + k_{e0} (1 + A) \Gamma_y \ddot{\theta} \right\} \quad (\text{AA.2.24}) \end{aligned}$$

$$\begin{aligned}
\frac{d}{dt} \left( \frac{\partial T}{\partial \dot{q}_t} \right) = & m_{wt} \left\{ - \left( x_f - \frac{\Gamma_x}{\cos(\gamma)} \right) \gamma_{e0} (1+B) k_{e0} (1+A) \ddot{q}_b \right. \\
& + \left[ \left( x_f - \frac{\Gamma_x}{\cos(\gamma)} \right) \gamma_{e0} (1+B) \right]^2 \ddot{q}_t \\
& + \left( x_f - \frac{\Gamma_x}{\cos(\gamma)} \right) \gamma_{e0} (1+B) \left( l_W + \frac{c}{4} - \frac{\Gamma_x}{\cos(\gamma)} \right) \ddot{\alpha} \\
& - \left( x_f - \frac{\Gamma_x}{\cos(\gamma)} \right) \gamma_{e0} (1+B) \ddot{z}_c \\
& \left. - \left( x_f - \frac{\Gamma_x}{\cos(\gamma)} \right) \gamma_{e0} (1+B) \Gamma_y \ddot{\theta} \right\}
\end{aligned} \tag{AA.2.25}$$

$$\begin{aligned}
\frac{d}{dt} \left( \frac{\partial T}{\partial \dot{\alpha}} \right) = & m_{wt} \left\{ - \left( l_W + \frac{c}{4} - \frac{\Gamma_x}{\cos(\gamma)} \right) k_{e0} (1+A) \ddot{q}_b \right. \\
& + \left( l_W + \frac{c}{4} - \frac{\Gamma_x}{\cos(\gamma)} \right) \left( x_f - \frac{\Gamma_x}{\cos(\gamma)} \right) \gamma_{e0} (1+B) \ddot{q}_t \\
& + \left( l_W + \frac{c}{4} - \frac{\Gamma_x}{\cos(\gamma)} \right)^2 \ddot{\alpha} - \left( l_W + \frac{c}{4} - \frac{\Gamma_x}{\cos(\gamma)} \right) \ddot{z}_c \\
& \left. - \left( l_W + \frac{c}{4} - \frac{\Gamma_x}{\cos(\gamma)} \right) \Gamma_y \ddot{\theta} \right\}
\end{aligned} \tag{AA.2.26}$$

$$\begin{aligned}
\frac{d}{dt} \left( \frac{\partial T}{\partial \dot{z}_c} \right) = & m_{wt} \left[ k_{e0} (1+A) \ddot{q}_b - \left( x_f - \frac{\Gamma_x}{\cos(\gamma)} \right) \gamma_{e0} (1+B) \ddot{q}_t \right. \\
& \left. - \left( l_W + \frac{c}{4} - \frac{\Gamma_x}{\cos(\gamma)} \right) \ddot{\alpha} + \ddot{z}_c + \Gamma_y \ddot{\theta} \right]
\end{aligned} \tag{AA.2.27}$$

$$\begin{aligned}
\frac{d}{dt} \left( \frac{\partial T}{\partial \dot{\theta}} \right) = & m_{wt} \left[ \Gamma_y k_{e0} (1+A) \ddot{q}_b - \Gamma_y \left( x_f - \frac{\Gamma_x}{\cos(\gamma)} \right) \gamma_{e0} (1+B) \ddot{q}_t \right. \\
& \left. - \Gamma_y \left( l_W + \frac{c}{4} - \frac{\Gamma_x}{\cos(\gamma)} \right) \ddot{\alpha} + \Gamma_y \ddot{z}_c + \Gamma_y^2 \ddot{\theta} \right]
\end{aligned} \tag{AA.2.28}$$

$$\frac{\partial T}{\partial q_b} = 0 \tag{AA.2.29}$$

$$\frac{\partial T}{\partial q_t} = 0 \tag{AA.2.30}$$

$$\frac{\partial T}{\partial \alpha} = 0 \tag{AA.2.31}$$

$$\frac{\partial T}{\partial z_c} = 0 \tag{AA.2.32}$$

$$\frac{\partial T}{\partial \theta} = 0 \tag{AA.2.33}$$

$$\frac{\partial U}{\partial q_b} = 0 \tag{AA.2.34}$$

$$\frac{\partial U}{\partial q_t} = 0 \quad (\text{AA.2.35})$$

$$\frac{\partial U}{\partial \alpha} = 0 \quad (\text{AA.2.36})$$

$$\frac{\partial U}{\partial z_c} = 0 \quad (\text{AA.2.37})$$

$$\frac{\partial U}{\partial \theta} = k_\theta \theta \quad (\text{AA.2.38})$$

$$\frac{\partial(\delta W_{wt})}{\partial(\delta q_b)} = -L_{wt} \left[ k_{e_0} (1 + A) - l_A \gamma_{e_0} \right] + m_{wt} g k_{e_0} (1 + A) \quad (\text{AA.2.39})$$

$$\frac{\partial(\delta W_{wt})}{\partial(\delta q_t)} = -L_{wt} \left[ k_{e_0} - l_A \gamma_{e_0} (1 + B) \right] - m_{wt} g \left( x_f - \frac{\Gamma_x}{\cos(\gamma)} \right) \gamma_{e_0} (1 + B) \quad (\text{AA.2.40})$$

$$\frac{\partial(\delta W_{wt})}{\partial(\delta \alpha)} = l_w L_{wt} - m_{wt} g \left( l_W + \frac{c}{4} - \frac{\Gamma_x}{\cos(\gamma)} \right) \quad (\text{AA.2.41})$$

$$\frac{\partial(\delta W_{wt})}{\partial(\delta z_c)} = -L_{wt} + m_{wt} g \quad (\text{AA.2.42})$$

$$\frac{\partial(\delta W_{wt})}{\partial(\delta \theta)} = -L_{wt} \frac{s_3}{2} + m_{wt} g \Gamma_y \quad (\text{AA.2.43})$$

Equations (AA.2.39), (AA.2.40), (AA.2.41), (AA.2.42), and (AA.2.43) have been solved using Wolfram Mathematica 12 [163].

---

### A.3 Modification of the orthogonality condition for an engine on the elastic wing

---

In this section the procedure utilized to calculate the modal masses and the coefficients ( $A$ ,  $B$ ,  $k_{e0}$  and  $\gamma_{e0}$ ) of the bending and torsional degrees of freedoms when the wing includes a concentrated mass representative of an engine is presented. The engine is modelled as a concentrated mass ( $m_M$ ) at the longitudinal distance  $x_M$  from the elastic axis (positive aft) and  $y_M$  from the symmetric axis. The procedure to find the seven unknowns ( $k_{eF}$ ,  $k_{eC}$ ,  $k_{eT}$ ,  $k_{e0}$ ,  $\gamma_{e0}$ ,  $A$  and  $B$ ) can be found in Appendix C of Wright et. al [20]. The orthogonality condition has to be modified to give:

$$\begin{aligned}
& m_F k_{eF} + m_W \left(1 + \frac{A}{3}\right) k_{e0} + m_W l_E \left(1 + \frac{B}{2}\right) \gamma_{e0} + m_C k_{eC} + m_T k_{eT} \\
& + m_M k_{e0} \left(1 + A \left(\frac{y_M}{s}\right)^2\right) - m_M x_M \gamma_{e0} \left(1 + B \frac{y_M}{s}\right) = 0
\end{aligned} \tag{AA.3.44}$$

$$\begin{aligned}
& -m_F k_{eF} l_F - m_W \left(1 + \frac{A}{3}\right) k_{e0} l_{WM} + (I_W - m_W l_E l_{WM}) \left(1 + \frac{B}{2}\right) \gamma_{e0} + m_T k_{eT} l_T \\
& + m_M k_{e0} \left(1 + A \left(\frac{y_M}{s}\right)^2\right) (x_M + l_E + l_{WM}) \\
& - m_M x_M \gamma_{e0} \left(1 + B \frac{y_M}{s}\right) (x_M + l_E + l_{WM}) = 0
\end{aligned} \tag{AA.3.45}$$

The modal mass equation has to be modified in order to take into account the contribution of the engine as:

$$\begin{aligned}
m_e = & m_F k_{eF}^2 + m_W \left(1 + \frac{2A}{3} + \frac{A^2}{5}\right) k_{e0}^2 + (I_W + m_W l_E^2) \left(1 + B + \frac{B^2}{3}\right) \gamma_{e0}^2 \\
& + 2m_W l_E \left(1 + \frac{A}{3} + \frac{B}{2} + \frac{AB}{4}\right) k_{e0} \gamma_{e0} + m_C k_{eC}^2 + m_T k_{eT}^2 \\
& + m_M \left[ k_{e0} \left(1 + A \left(\frac{y_M}{s}\right)^2\right) - x_M \gamma_{e0} \left(1 + B \frac{y_M}{s}\right) \right]^2
\end{aligned} \tag{AA.3.46}$$

---

## A.4 Quantities of interest

---

Expressions of the interesting quantities are given in this section. The vertical shear force (positive upwards) is

$$S_{wr}(t) = \int_0^s dL(t) + L_{wt}(t) + \int_0^s (\ddot{z}_{WM}(t) - g) dm_w + m_{wt}(\ddot{z}_\Gamma(t) - g) - m_M(\ddot{z}_M(t) - g) \quad (\text{BA.4.47})$$

The bending moment (positive to the rear) is

$$M_{wr}(t) = \int_0^s y dL(t) + sL_{wt}(t) + \int_0^s y(\ddot{z}_{WM}(t) - g) dm_w + m_{wt}(\ddot{z}_\Gamma(t) - g)s + m_M(\ddot{z}_M(t) - g)y_M \quad (\text{BA.4.48})$$

The torsional moment (positive towards the tip of the wing) is

$$T_{wr}(t) = \int_0^s l_A dL(t) + l_A L_{wt}(t) - \int_0^s l_E (\ddot{z}_{WM}(t) - g) dm_w - m_{wt}(\ddot{z}_\Gamma(t) - g) \left( \frac{\Gamma_x}{\cos(\gamma)} - \frac{c}{4} - l_A \right) - m_M x_M (\ddot{z}_M(t) - g) \quad (\text{BA.4.49})$$

where the acceleration of the wing mass is

$$\ddot{z}_{WM}(y, t) = \ddot{z}_c(t) - l_{WM} \ddot{\alpha}(t) + \left[ k_{e_0} \left( 1 + A \left( \frac{y}{s} \right)^2 \right) + l_E \gamma_{e_0} \right] \ddot{q}_b(t) + \left[ k_{e_0} + l_E \gamma_{e_0} \left( 1 + B \left( \frac{y}{s} \right) \right) \right] \ddot{q}_t(t) \quad (\text{BA.4.50})$$

and the acceleration of the wingtip centre of mass is

$$\ddot{z}_M(t) = \ddot{z}_c(t) - (x_M + l_E + l_{WM}) \ddot{\alpha}(t) + \left[ k_{e_0} \left( 1 + A \left( \frac{y_M}{s} \right)^2 \right) - x_M \gamma_{e_0} \right] \ddot{q}_b(t) + \left[ k_{e_0} - x_M \gamma_{e_0} \left( 1 + B \left( \frac{y_M}{s} \right) \right) \right] \ddot{q}_t(t) \quad (\text{BA.4.51})$$

# BIBLIOGRAPHY

- [1] E. E. Agency. European aviation environmental report 2019, 2019. [https://www.easa.europa.eu/eaer/system/files/usr\\_uploaded/219473\\_EASA\\_EAER\\_2019\\_WEB\\_LOW-RES.pdf](https://www.easa.europa.eu/eaer/system/files/usr_uploaded/219473_EASA_EAER_2019_WEB_LOW-RES.pdf), Last accessed on 22-02-2022.
- [2] Christine V Jutte and Bret K Stanford. *Aeroelastic tailoring of transport aircraft wings: state-of-the-art and potential enabling technologies*. NASA TM-2014-218252, 2014.
- [3] Boeing website. 777x gallery. <https://www.boeing.com/commercial/777x#/gallery>, Last accessed on 24-01-2022.
- [4] John B Allen. Articulating winglets, November 23 1999. US Patent 5,988,563.
- [5] Dale Pitt. Static and dynamic aeroelastic analysis of structural wing fold hinges that are employed as an aeroelastic tailoring tool. In *45th AIAA/ASME/ASCE/AHS/ASC Structures, Structural Dynamics & Materials Conference*, page 1754, 2004.
- [6] Ronald Cheung, Djamel Rezgui, Jonathan E Cooper, and Thomas Wilson. Testing of a hinged wing-tip device for gust loads alleviation. *Journal of Aircraft*, 2018.
- [7] Ronald C Cheung, Djamel Rezgui, Jonathan E Cooper, and Thomas Wilson. Analyzing the dynamic behavior of a high aspect ratio wing incorporating a folding wingtip. In *AIAA Scitech 2020 Forum*, page 2290, 2020.
- [8] Fintan Healy, Alessandro Pontillo, Djamel Rezgui, Jonathan E Cooper, James Kirk, Thomas Wilson, and Andrea Castrichini. Experimental analysis of the dynamics of flared folding wingtips via a novel tethered flight test. In *AIAA SCITECH 2022 Forum*, page 1757, 2022.
- [9] John C Houbolt. Atmospheric turbulence. *AIAA Journal*, 11(4):421–437, 1973.

- 
- [10] Simone Simeone, Andrea Da Ronch, and T Rendall. A gust reconstruction framework applied to a nonlinear reduced order model of a wing typical section. In *58th AIAA/ASCE/AHS/ASC Structures, Structural Dynamics, and Materials Conference*, page 0634, 2017.
- [11] H Makita and K Sassa. Active turbulence generation in a laboratory wind tunnel. In *Advances in turbulence 3*, pages 497–505. Springer, 1991.
- [12] Richard E. Thomas. Progress report gust simulation in a wind tunnel. Technical report, NASA CR-66235, 1966.
- [13] Donald A Buell. An experimental investigation of the velocity fluctuations behind oscillating vanes. 1969.
- [14] Federico Fonte, Luca Riccobene, Sergio Ricci, Stephan Adden, Matteo Martegani, et al. Design, manufacturing and validation of a gust generator for wind tunnel test of a large scale aeroelastic model. In *30th Congress of the International Council of the Aeronautical Science, Daejeon*, pages 25–30, 2016.
- [15] Paul MGJ Lancelot, Jurij Sodja, Noud PM Werter, and Roeland De Breuker. Design and testing of a low subsonic wind tunnel gust generator. *Advances in aircraft and spacecraft science*, 4(2):125, 2017.
- [16] Jens Neumann and Holger Mai. Gust response: Simulation of an aeroelastic experiment by a fluid–structure interaction method. *Journal of Fluids and Structures*, 38:290–302, 2013.
- [17] Wilmer H Reed III. *Aeroelasticity matters: Some reflections on two decades of testing in the NASA Langley transonic dynamics tunnel*. NASA TM-83210, 1981.
- [18] DM Tang, Paul GA Cizmas, and EH Dowell. Experiments and analysis for a gust generator in a wind tunnel. *Journal of Aircraft*, 33(1):139–148, 1996.
- [19] Naomi J Allen and Mark Quinn. Development of a transonic gust rig for simulation of vertical gusts on half-models. In *31st AIAA Aerodynamic Measurement Technology and Ground Testing Conference*, page 2403, 2015.
- [20] Jan Robert Wright and Jonathan Edward Cooper. *Introduction to aircraft aeroelasticity and loads*, volume 20. John Wiley & Sons, 2008.
- [21] Christian Willert and Jürgen Kompenhans. Piv analysis of ludwig prandtl’s historic flow visualization films. *arXiv preprint arXiv:1010.3149*, 2010.

- [22] KEM Konstruktion. Prinzip der lasertriangulation, 2012. <https://kem.industrie.de/sensoren/prinzip-der-lasertriangulation/>, Last accessed on 08-02-2022.
- [23] Acares. Aeronautics and air transport: Beyond vision 2020 (towards 2050). *Advisory Council for Aeronautics Research in Europe*, 2010.
- [24] International Air Transport Association et al. Iata forecast predicts 8.2 billion air travelers in 2037. *Retrieved July, 1:2019*, 2018.
- [25] Frederic M Hoblit. *Gust loads on aircraft: concepts and applications*. American Institute of Aeronautics and Astronautics, 1988.
- [26] European Aviation Safety Agency. Certification specifications and acceptable means of compliance for large aeroplanes cs25, 2020. <https://www.easa.europa.eu/sites/default/files/dfu/CS-25%20Amendment%2024.pdf>, Last accessed on 08-11-2021.
- [27] Christopher D Regan and Christine V Jutte. Survey of applications of active control technology for gust alleviation and new challenges for lighter-weight aircraft. *NASA TM-2012-216008*, 04 2012.
- [28] William J Hargrove. The c-5a active lift distribution control system. Technical report, NASA N76-31148, 1976.
- [29] E. RYNASKI, II D. ANDRISANI, and B. EULRICH. Gust alleviation using direct turbulence measurements. In *5th Atmospheric Flight Mechanics Conference for Future Space Systems*, page 1674, 1979.
- [30] Guillermo Jenaro Rabadan, Nikolaus P. Schmitt, Thomas Pistner, and Wolfgang Rehm. Airborne lidar for automatic feedforward control of turbulent in-flight phenomena. *Journal of Aircraft*, 47(2):392–403, 2010.
- [31] C Besson, A Dolfi-Bouteyre, G Canat, N Cézard, B Augère, A Durecu, L Lombard, M Valla, and A Hallermeyer. Doppler lidar developments for aeronautics. *Aerospace Lab*, 08(12):pages–1, 2016.
- [32] Nicolas Fezans and Hans-Dieter Joos. Combined feedback and lidar-based feedforward active load alleviation. In *AIAA Atmospheric Flight Mechanics Conference*, page 3548, 2017.
- [33] H-G Giessler, Michael Kopf, Paolo Varutti, Timm Faulwasser, and Rolf Findeisen. Model predictive control for gust load alleviation. *IFAC Proceedings Volumes*, 45(17):27–32, 2012.



- 
- [34] Hugo Fournier, Paolo Massioni, Minh Tu Pham, Laurent Bako, Robin Vernay, and Michele Colombo. Robust gust load alleviation of flexible aircraft equipped with lidar. *Journal of Guidance, Control, and Dynamics*, 45(1):58–72, 2022.
- [35] Nicolas Fezans, Hans-Dieter Joos, and Christoph Deiler. Gust load alleviation for a long-range aircraft with and without anticipation. *CEAS Aeronautical Journal*, 10(4):1033–1057, 2019.
- [36] Michael H Shirk, Terrence J Hertz, and Terrence A Weisshaar. Aeroelastic tailoring-theory, practice, and promise. *Journal of Aircraft*, 23(1):6–18, 1986.
- [37] Max M Munk. Propeller containing diagonally disposed fibrous material, October 11 1949. US Patent 2,484,308.
- [38] Terrence Weisshaar, Changho Nam, and Alicia Batista-Rodriguez. Aeroelastic tailoring for improved uav performance. In *39th AIAA/ASME/ASCE/AHS/ASC Structures, Structural Dynamics, and Materials Conference and Exhibit*, page 1757, 1998.
- [39] Silvestro Barbarino, Onur Bilgen, Rafic M Ajaj, Michael I Friswell, and Daniel J Inman. A review of morphing aircraft. *Journal of intelligent material systems and structures*, 22(9):823–877, 2011.
- [40] Thomas Wilson, Andrea Castrichini, Alvaro Azabal, Je Cooper, Rafic Ajaj, and Martin Herring. Aeroelastic behaviour of hinged wing tips. In *International Forum on Aeroelasticity and Structural Dynamics, IFASD 2017*. Royal Aeronautical Society, 06 2017.
- [41] Anon. Knee-action wings cushion ride in french plane. *Popular Science Magazine*, 158:150, 1951.
- [42] John Pattinson, Thomas Wilson, and Martin Herring. High fidelity simulation of the folding wing tip for loads alleviaton. In *International Forum on Aeroelasticity and Structural Dynamics, (IFASD 2015)*, 08 2015.
- [43] A Castrichini, V H Siddaramaiah, D E Calderon, J E Cooper, T Wilson, and Y Lemmens. Preliminary investigation of use of flexible folding wing tips for static and dynamic load alleviation. *The Aeronautical Journal*, 121(1235):73–94, 2017.
- [44] Andrea Castrichini, V H Siddaramaiah, D E Calderon, Jonathan E Cooper, Thomas Wilson, and Yves Lemmens. Nonlinear folding wing tips for gust loads alleviation. *Journal of Aircraft*, 53(5):1391–1399, 2016.

- [45] Andrea Castrichini, Jonathan E Cooper, Thomas Wilson, Alessandro Carrella, and Yves Lemmens. Nonlinear negative stiffness wingtip spring device for gust loads alleviation. *Journal of Aircraft*, 54(2):627–641, 2017.
- [46] C Valente, A Castrichini, A Landi, JE Cooper, D Jones, A Gaitonde, F Mastroddi, and T Wilson. High fidelity cfd/csm analysis of a folding wing-tip device for aircraft loads alleviation. In *RAeS 6th Aircraft Structural Design Conference*, 2018.
- [47] Ronald C Cheung, Djamel Rezgui, Jonathan E Cooper, and Thomas Wilson. Testing of folding wing-tip for gust load alleviation in high aspect ratio wing. In *AIAA Scitech 2019 Forum*, page 1863, 2019.
- [48] Andrea Castrichini, Tom Wilson, F Saltari, F Mastroddi, Nicola Viceconti, and Jonathan E Cooper. Aeroelastics flight dynamics coupling effects of the semi-aeroelastic hinge device. *Journal of Aircraft*, 57(2):333–341, 2020.
- [49] Rafic M Ajaj. Flight dynamics of transport aircraft equipped with flared-hinge folding wingtips. *Journal of Aircraft*, 58(1):98–110, 2021.
- [50] Fintan Healy, Ronald C Cheung, Theodor Neofet, Mark H Lowenberg, Djamel Rezgui, Jonathan E Cooper, Andrea Castrichini, and Tom Wilson. Folding wingtips for improved roll performance. In *AIAA Scitech 2021 Forum*, page 1153, 2021.
- [51] Fintan Healy, Ronald C Cheung, Djamel Rezgui, Jonathan E Cooper, Thomas Wilson, and Andrea Castrichini. On the nonlinear geometric behaviour of flared folding wingtips. In *AIAA Scitech 2022 Forum*, page 0656, 2022.
- [52] Fintan Healy, Ronald C Cheung, Djamel Rezgui, and Jonathan E Cooper. Nonlinear stability analysis and experimental exploration of limit cycle oscillations with flared folding wingtips. In *AIAA SCITECH 2022 Forum*, page 0657, 2022.
- [53] Claudio Conti, Francesco Saltari, Franco Mastroddi, Thomas Wilson, and Andrea Castrichini. Quasi-steady aeroelastic analysis of the semi-aeroelastic hinge including geometric nonlinearities. *Journal of Aircraft*, pages 1–11, 2021.
- [54] Xavier Carrillo, Christoph Mertens, Andrea Sciacchitano, Bas van Oudheusden, Roeland De Breuker, and Jurij Sodja. Wing stiffness and hinge release threshold effects on folding wingtip gust load alleviation. In *AIAA SCITECH 2022 Forum*, page 1559, 2022.
- [55] Andrea Castrichini, Thomas Wilson, and Je Cooper. On the dynamic release of the semi aeroelastic wing-tip hinge device. 10 2018.

- [56] Andrea Castrichini, Thomas Wilson, and Alvaro Azabal. Apparatus, aircraft comprising an apparatus and method of performing a descent in an aircraft, 10 2018.
- [57] Thomas Wilson, Andrea Castrichini, and Alvaro Azabal. Apparatus, aircraft and method of moving a movably mounted wing tip device, October 24 2019. US Patent App. 16/386,675.
- [58] Thomas Wilson, Martin Herring, John PATTINSON, Je Cooper, Andrea Castrichini, Rafic Ajaj, and Hitul DHORU. An aircraft wing with a moveable wing tip device for load alleviation, 05 2021.
- [59] AIRBUS. Albatrossone achieves proof-of-concept on a small scale. <https://www.airbus.com/en/innovation/disruptive-concepts/biomimicry/albatrossone>, Last accessed on 02-02-2022.
- [60] Thomas Wilson, James Kirk, John Hobday, and Andrea Castrichini. Small scale flying demonstration of semi aeroelastic hinged wing tips. In *International Forum on Aeroelasticity and Structural Dynamics, (IFASD 2019)*, 06 2019.
- [61] D. J. Wagg, K. Worden, R. J. Barthorpe, and P. Gardner. Digital Twins: State-of-the-Art and Future Directions for Modeling and Simulation in Engineering Dynamics Applications. *ASCE-ASME J Risk and Uncert in Engrg Sys Part B Mech Engrg*, 6(3), 05 2020. 030901.
- [62] Timothy D West and Mark Blackburn. Is digital thread/digital twin affordable? a systemic assessment of the cost of DoD's latest Manhattan project. *Procedia Computer Science*, 114:47–56, 2017.
- [63] Eric J Tuegel, Anthony R Ingraffea, Thomas G Eason, and S Michael Spottswood. Reengineering Aircraft Structural Life Prediction Using a Digital Twin. *International Journal of Aerospace Engineering*, 2011:154798, 2011.
- [64] Lars Bensch, Hermann Henrichfreise, Juergen Jusseit, and Ludger Merz. Method for reconstructing gusts and structural loads at aircraft, in particular passenger aircraft, June 26 2012. US Patent 8,209,159.
- [65] John C Houbolt. Design manual for vertical gusts based on power spectral techniques. Technical report, Aeronautical Research Associates of Princeton Inc NJ, 1970.

- [66] JK Zbrozek. The relationship between the discrete gust and power spectra presentations of atmospheric turbulence, with a suggested model of low-altitude turbulence. Technical Report R. & M. No. 3216, Aeronautical Research Council Reports and Memoranda, 1961.
- [67] MC Kim, AM Kabe, and SS Lee. Atmospheric flight gust loads analysis. *Journal of Spacecraft and Rockets*, 37(4):446–452, 2000.
- [68] H Henrichfreise, L Bensch, J Jusseit, L Merz, and M Gojny. Estimation of gusts and structural loads for commercial aircraft. In *International Forum on Aeroelasticity and Structural Dynamics (IFASD)*, Seattle, 2009.
- [69] Aristeidis Antonakis, Mudassir Lone, and Alastair Cooke. Neural network based dynamic model and gust identification system for the Jetstream G-NFLA. *Proceedings of the Institution of Mechanical Engineers, Part G: Journal of Aerospace Engineering*, 231(6):1138–1153, 2017.
- [70] B-T Wang. Prediction of impact and harmonic forces acting on arbitrary structures: theoretical formulation. *Mechanical Systems and Signal Processing*, 16(6):935–953, 2002.
- [71] Henrik Hesse and Rafael Palacios. Dynamic load alleviation in wake vortex encounters. *Journal of Guidance, Control, and Dynamics*, 39(4):801–813, 2016.
- [72] Mordechai Karpel, Alexander Shousterman, Hector Climent, and Manuel Reyes. *Dynamic Response to Wake Encounter*, page 1921. 2013.
- [73] K Wilhelm and B Gmelin. Dynamic wind tunnel testing for active control research. *AGARD Ground and Flight Testing for Aircraft Guidance and Control*, pages 793–807, 1984.
- [74] Sergio Ricci, Alessandro De Gaspari, Luca Riccobene, and Federico Fonte. Design and wind tunnel test validation of gust load alleviation systems. In *58th AIAA/ASCE/AHS/ASC Structures, Structural Dynamics, and Materials Conference*, page 1818, 2017.
- [75] Pedro Pereira, Luis Almeida, Afzal Suleman, Vanessa Bond, Robert Canfield, and Maxwell Blair. Aeroelastic scaling and optimization of a joined-wing aircraft concept. In *48th AIAA/ASME/ASCE/AHS/ASC Structures, Structural Dynamics, and Materials Conference*, page 1889, 2007.
- [76] Laurent Mydlarski. A turbulent quarter century of active grids: from makita (1991) to the present. *Fluid Dynamics Research*, 49(6):061401, 2017.

- [77] Dustin Grissom and William Devenport. Development and testing of a deterministic disturbance generator. In *10th AIAA/CEAS Aeroacoustics Conference*, page 2956, 2004.
- [78] Svetlana Kuzmina, Fanil Ishmuratov, Mikhail Zichenkov, and Vasily Chedrik. Analytical-experimental study on using different control surfaces to alleviate dynamic loads. In *47th AIAA/ASME/ASCE/AHS/ASC Structures, Structural Dynamics, and Materials Conference 14th AIAA/ASME/AHS Adaptive Structures Conference 7th*, page 2164, 2006.
- [79] Sergio Ricci and Alessandro Scotti. Wind tunnel testing of an active controlled wing under gust excitation. In *49th AIAA/ASME/ASCE/AHS/ASC Structures, Structural Dynamics, and Materials Conference, 16th AIAA/ASME/AHS Adaptive Structures Conference, 10th AIAA Non-Deterministic Approaches Conference, 9th AIAA Gossamer Spacecraft Forum, 4th AIAA Multidisciplinary Design Optimization Specialists Conference*, page 1727, 2008.
- [80] V Brion, A Lepage, Y Amosse, D Soulevant, P Senecat, JC Abart, and P Paillart. Generation of vertical gusts in a transonic wind tunnel. *Experiments in Fluids*, 56(7):1–16, 2015.
- [81] AJ Saddington, MV Finnis, and K Knowles. The characterisation of a gust generator for aerodynamic testing. *Proceedings of the Institution of Mechanical Engineers, Part G: Journal of Aerospace Engineering*, 229(7):1214–1225, 2015.
- [82] Kieran Wood, Ronald Cheung, Thomas Richardson, Je Cooper, Oliver Darbyshire, and Clyde Warsop. A new gust generator for a low speed wind tunnel: Design and commissioning. In *55th AIAA Aerospace Sciences Meeting*, 01 2017.
- [83] Naresh Poudel, Meilin Yu, Zachary F Smith, and John T Hrynyuk. A combined experimental and computational study of a vertical gust generator in a wind tunnel. In *AIAA Scitech 2019 Forum*, page 2166, 2019.
- [84] David A Olson, Ahmed M Naguib, and Manoochehr M Koochesfahani. Development of a low-turbulence transverse-gust generator in a wind tunnel. *AIAA Journal*, 59(5):1575–1584, 2021.
- [85] San Technologies. Gust generator. [https://www-en.santech.co.jp/business/test-research/dounyurei#h.p\\_lzrblfq2zJAv](https://www-en.santech.co.jp/business/test-research/dounyurei#h.p_lzrblfq2zJAv), Last accessed on 22-01-2022.
- [86] ND Ham, PH Bauer, and TL Lawrence. Wind tunnel generation of sinusoidal lateral and longitudinal gusts by circulation of twin parallel airfoils. *NASA STI/Recon Technical Report N*, 75:29351, 1974.

- [87] Sudarshan Koushik and Fredric Schmitz. *A New Experimental Approach to Study Helicopter Blade-Vortex Interaction Noise*. 2008.
- [88] Jason Roadman and Kamran Mohseni. Gust characterization and generation for wind tunnel testing of micro aerial vehicles. In *47th AIAA aerospace sciences meeting including the new horizons forum and aerospace exposition*, page 1290, 2009.
- [89] Raymond L Bisplinghoff, Holt Ashley, and Robert L Halfman. *Aeroelasticity*. Courier Corporation, 2013.
- [90] E Carson Yates Jr. Modified-strip-analysis method for predicting wing flutter at subsonic to hypersonic speeds. *Journal of Aircraft*, 3(1):25–29, 1966.
- [91] Yinan Wang, Xiaowei Zhao, Rafael Palacios, and Keisuke Otsuka. Aeroelastic simulation of high-aspect ratio wings with intermittent leading-edge separation. *AIAA Journal*, pages 1–14, 2021.
- [92] Qi Yan and Zhiqiang Wan. A highly efficient aeroelastic analysis method based on external aerodynamic force and strip theory. In *2018 AIAA Aerospace Sciences Meeting*, page 2068, 2018.
- [93] Adriana V Martínez, Pedro J Boschetti, and Pedro J González Ramirez. Dynamic stability and flying qualities of an unmanned airplane as a flexible body. In *AIAA Scitech 2020 Forum*, page 1268, 2020.
- [94] Zhenjun Zhao and Gexue Ren. Multibody dynamic approach of flight dynamics and nonlinear aeroelasticity of flexible aircraft. *AIAA journal*, 49(1):41–54, 2011.
- [95] Wolf R Krüger. Multibody dynamics for the coupling of aeroelasticity and flight mechanics of highly flexible structures. In *Proceedings of the International Forum on Elasticity and Structural Dynamics*, 2007.
- [96] Edward Albano and William P Rodden. A doublet-lattice method for calculating lift distributions on oscillating surfaces in subsonic flows. *AIAA journal*, 7(2):279–285, 1969.
- [97] Max Blair. A compilation of the mathematics leading to the doublet lattice method. Technical report, WRIGHT LAB WRIGHT-PATTERSON AFB OH, 1992.
- [98] P Konstadinopoulos, DF Thrasher, DT Mook, AH Nayfeh, and L Watson. A vortex-lattice method for general, unsteady aerodynamics. *Journal of aircraft*, 22(1):43–49, 1985.

- [99] Luigi Morino. Steady, oscillatory, and unsteady subsonic and supersonic aerodynamics-production version (soussa-p 1.1), volume i-theoretical manual. *NASA CR-159130*, 1980.
- [100] Thiemo M Kier. Integrated flexible dynamic maneuver loads models based on aerodynamic influence coefficients of a 3d panel method. In *56th AIAA/ASCE/AHS/ASC Structures, Structural Dynamics, and Materials Conference*, page 0185, 2015.
- [101] Kenneth L Roger and ROGER KL. Airplane math modeling methods for active control design. Technical report, AGARD-CP-228, 19661977.
- [102] SHERWOODH TIFFANY, WILLI ADAMS, and JR A M M. Nonlinear program-ping extensions to rational function approximation methods for unsteady aerodynamic forces. Technical report, NASA TP-2766, 1988.
- [103] Walter Eversman and Ashish Tewari. Consistent rational-function approximation for unsteady aerodynamics. *Journal of Aircraft*, 28(9):545–552, 1991.
- [104] Mordechai Karpel and Sherwood Tiffany Hoadley. *Physically weighted approximations of unsteady aerodynamic forces using the minimum-state method*, volume 3025. NASA, Report n. 3025, 1991.
- [105] Mouti Karpel, Boris Moulin, and P C Chen. Dynamic response of aeroservoelastic systems to gust excitation. *Journal of Aircraft*, 42(5):1264–1272, 2005.
- [106] Matteo Ripepi and Paolo Mantegazza. Improved matrix fraction approximation of aerodynamic transfer matrices. *AIAA journal*, 51(5):1156–1173, 2013.
- [107] Lawrence F Shampine and Mark W Reichelt. The matlab ode suite. *SIAM journal on scientific computing*, 18(1):1–22, 1997.
- [108] Paolo Mastracci, Francesco Saltari, Franco Mastroddi, Thomas Wilson, and Andrea Castrichini. Unsteady aeroelastic analysis of the semi aeroelastic hinge including local geometric nonlinearities. *AIAA Journal*, 01 2022.
- [109] H Haddad Khodaparast and Jonathan E Cooper. Rapid prediction of worst-case gust loads following structural modification. *AIAA journal*, 52(2):242–254, 2014.
- [110] MSC Nastran et al. Quick reference guide. *MSC. SOFTWARE*, 1, 2019.
- [111] William P Rodden and Erwin H Johnson. *MSC/NASTRAN aeroelastic analysis: user’s guide; Version 68*. MacNeal-Schwendler Corporation, 1994.

- [112] V Hodigere Siddaramaiah, DE Calderon, JE Cooper, and T Wilson. Preliminary studies in the use of folding wing tips for loads alleviation. In *Royal Aeronautical Society Applied Aerodynamics Conference*, 2014.
- [113] Mathworks. *Optimization toolbox user's guide*. March, 2020.
- [114] Kalyanmoy Deb. *Multi-objective optimization using evolutionary algorithms*, volume 16. John Wiley & Sons, 2001.
- [115] Janusz Mroczka and Damian Szczuczyński. Inverse problems formulated in terms of first-kind Fredholm integral equations in indirect measurements. *Metrol. Meas. Syst.*, 16(3):333–357, 2009.
- [116] Richard C Aster, Brian Borchers, and Clifford H Thurber. *Parameter estimation and inverse problems*. Elsevier, 2018.
- [117] Per Christian Hansen. Regularization tools: a matlab package for analysis and solution of discrete ill-posed problems. *Numerical algorithms*, 6(1):1–35, 1994.
- [118] Khosrow Maleknejad and Taher Lotfi. Using wavelet for numerical solution of Fredholm integral equations. In *Proceedings of the World Congresson Engineering, London*, pages 876–879, 01 2007.
- [119] K. Maleknejad and F. Mirzaee. Using rationalized Haar wavelet for solving linear integral equations. *Applied Mathematics and Computation*, 160(2):579–587, 2005.
- [120] J. Rashidinia and M. Zarebnia. Numerical solution of linear integral equations by using Sinc-collocation method. *Applied Mathematics and Computation*, 168(2):806–822, 2005.
- [121] Fergyanto E. Gunawan, Hiroomi Homma, and Yasuhiro Kanto. Two-step b-splines regularization method for solving an ill-posed problem of impact-force reconstruction. *Journal of Sound and Vibration*, 297(1):200–214, 2006.
- [122] Hirotaka Shiozaki, Theo Geluk, Frank Daenen, Yoshihisa Iwanaga, and Joris Van Herbruggen. Time-domain transfer path analysis for transient phenomena applied to tip-in/tip-out (shock & jerk). Technical report, jun 2012.
- [123] M Ghajari, Z Sharif-Khodaei, MH Aliabadi, and A Apicella. Identification of impact force for smart composite stiffened panels. *Smart Materials and Structures*, 22(8):085014, 2013.
- [124] James F Doyle. A wavelet deconvolution method for impact force identification. *Experimental mechanics*, 37(4):403–408, 1997.



- [125] N. Hu, H. Fukunaga, S. Matsumoto, B. Yan, and X.H. Peng. An efficient approach for identifying impact force using embedded piezoelectric sensors. *International Journal of Impact Engineering*, 34(7):1258–1271, 2007.
- [126] Baijie Qiao, Xuefeng Chen, Xiaofeng Xue, Xinjie Luo, and Ruonan Liu. The application of cubic b-spline collocation method in impact force identification. *Mechanical Systems and Signal Processing*, 64:413–427, 2015.
- [127] Baijie Qiao, Xingwu Zhang, Xinjie Luo, and Xuefeng Chen. A force identification method using cubic b-spline scaling functions. *Journal of Sound and Vibration*, 337:28–44, 2015.
- [128] Lei Wang, Yaru Liu, and Yisi Liu. An inverse method for distributed dynamic load identification of structures with interval uncertainties. *Advances in Engineering Software*, 131:77–89, 2019.
- [129] Jie Liu, Xingsheng Sun, Xu Han, Chao Jiang, and Dejie Yu. Dynamic load identification for stochastic structures based on Gegenbauer polynomial approximation and regularization method. *Mechanical Systems and Signal Processing*, 56-57:35–54, 2015.
- [130] Anas Batou and Christian Soize. Identification of stochastic loads applied to a nonlinear dynamical system using an uncertain computational model and experimental responses. *Computational Mechanics*, 43(4):559–571, 2009.
- [131] Lei Wang and Yaru Liu. A novel method of distributed dynamic load identification for aircraft structure considering multi-source uncertainties. *Structural and Multidisciplinary Optimization*, 61(5):1929–1952, 2020.
- [132] Per Christian Hansen. The truncated SVD as a method for regularization. *BIT Numerical Mathematics*, 27(4):534–553, 1987.
- [133] Gene H Golub, Per Christian Hansen, and Dianne P O’Leary. Tikhonov regularization and total least squares. *SIAM journal on matrix analysis and applications*, 21(1):185–194, 1999.
- [134] Grace Wahba. *Spline models for observational data*. SIAM, 1990.
- [135] Carl De Boor, Carl De Boor, Etats-Unis Mathématicien, Carl De Boor, and Carl De Boor. *A practical guide to splines*, volume 27. springer-verlag New York, 1978.
- [136] J Rashidinia, E Babolian, and Z Mahmoodi. Spline collocation for Fredholm integral equations. *Mathematical Sciences*, 5:147–158, 2011.

- [137] JA Adams. Cubic spline curve fitting with controlled end conditions. *Computer-Aided Design*, 6(1):2–9, 1974.
- [138] Dassault Systèmes. Solidworks education edition 2019/2020, 2019.
- [139] E Jogensen Finn. How to measuer turbulence with hot-wire anemometers. *Dantec Dynamics*, 2002.
- [140] Dantec Dynamics. Miniature x wire probe, straight (55p61). <https://www.dantecdynamics.com/components/hot-wire-and-hot-film-probes/dual-sensor-probe/miniature-wire/>, Last accessed on 07-02-2022.
- [141] MH Akbari and SJ Price. Simulation of dynamic stall for a naca 0012 airfoil using a vortex method. *Journal of fluids and structures*, 17(6):855–874, 2003.
- [142] W.J. McCroskey, L.W. Carr, and K.W. McAlister. Dynamic stall experiments on oscillating airfoils. *AIAA Journal*, 14(1):57–63, 1976.
- [143] Amanullah Choudhry, Ryan Leknys, Maziar Arjomandi, and Richard Kelso. An insight into the dynamic stall lift characteristics. *Experimental Thermal and Fluid Science*, 58:188–208, 2014.
- [144] Gordon J Leishman. *Principles of helicopter aerodynamics with CD extra*. Cambridge university press, 2006.
- [145] Robert E Sheldahl and Paul C Klimas. Aerodynamic characteristics of seven symmetrical airfoil sections through 180-degree angle of attack for use in aerodynamic analysis of vertical axis wind turbines. Technical report, SAND 80–2114, Unlimited Release, UC-60, 1981.
- [146] Marinos Manolesos, Giorgos Papadakis, and S Voutsinas. An experimental and numerical investigation on the formation of stall-cells on airfoils. In *Journal of Physics: Conference Series*, volume 555, page 012068. IOP Publishing, 2014.
- [147] Kenneth W McAlister, Lawrence W Carr, and William J McCroskey. *Dynamic stall experiments on the NACA 0012 airfoil*. NASA TP 1100, 1978.
- [148] DI Pullin and AE Perry. Some flow visualization experiments on the starting vortex. *Journal of Fluid Mechanics*, 97(2):239–255, 1980.
- [149] Debopam Das, M Bansal, and A Manghnani. Generation and characteristics of vortex rings free of piston vortex and stopping vortex effects. *Journal of Fluid Mechanics*, 811:138–167, 2017.

- [150] Arthur M Jaffe. The millennium grand challenge in mathematics. *Notices of the AMS*, 53(6):652–660, 2006.
- [151] Mathworks. *Signal Processing Toolbox user’s guide*. March, 2022a.
- [152] Materialise Manufacturing. Datasheets 3d printing materials, 2021. [https://www.materialise.com/system/files/resources/materialise\\_datasheets\\_25\\_01\\_2022.pdf](https://www.materialise.com/system/files/resources/materialise_datasheets_25_01_2022.pdf), Last accessed on 20-06-2022.
- [153] Materialise Manufacturing.
- [154] Data Physics.
- [155] PCB PIEZOTRONICS. Icp  $\text{\textcircled{R}}$ accelerometer, 2013. [https://www.pcb.com/contentStore/docs/pcb\\_corporate/vibration/products/specsheets/352c22\\_h.pdf](https://www.pcb.com/contentStore/docs/pcb_corporate/vibration/products/specsheets/352c22_h.pdf), Last accessed on 21-06-2022.
- [156] PCB PIEZOTRONICS. Icp  $\text{\textcircled{R}}$ accelerometer, 2006. [https://www.pcb.com/contentStore/docs/pcb\\_corporate/vibration/products/specsheets/352c03\\_e.pdf](https://www.pcb.com/contentStore/docs/pcb_corporate/vibration/products/specsheets/352c03_e.pdf), Last accessed on 21-06-2022.
- [157] Keyence. Sensor head: Ultra long distance, wide beam, 2022. <https://www.keyence.com/products/measure/laser-1d/lk-g3000/models/lk-g507//>, Last accessed on 08-02-2022.
- [158] National Instruments. Ni-9231 datasheet, 2022. <https://www.ni.com/docs/en-US/bundle/ni-9231-specs/page/specs.html>, Last accessed on 21-06-2022.
- [159] National Instruments. cdaq tm-9185/9189, 2019. <https://www.ni.com/docs/en-US/bundle/cdaq-9185-9189-features/resource/376610b.pdf>, Last accessed on 21-06-2022.
- [160] AMTI.
- [161] Andrea Castrichini. *Parametric Assessment of a Folding Wing-Tip Device for Aircraft Loads Alleviation*. PhD thesis, University of Bristol, 2017.
- [162] Thomas Wilson, Andrea Castrichini, John Paterson, and Raul Arribas Ardura. Non-linear aeroelastic behaviour of hinged wing tips. In *RAeS 6th Aerospace Structures Design Conference*, 10 2018.
- [163] Stephen Wolfram. The mathematica book. *Assembly Automation*, 1999.